Energy Efficient Massive MIMO and Beamforming for 5G Communications

A thesis submitted for the degree of Doctor of Philosophy

(Ph.D.)

by

Jun Qian

Communications and Information Systems Research Group

Department of Electronic and Electrical Engineering

University College London

March 16, 2022

I, Jun Qian, confirm that the work presented in this thesis is my own. Where information has been derived from other sources, I confirm that this has been indicated in the thesis.

Sign:

Date:

Abstract

Massive multiple-input multiple-output (MIMO) has been a key technique in the next generation of wireless communications for its potential to achieve higher capacity and data rates. However, the exponential growth of data traffic has led to a significant increase in the power consumption and system complexity. Therefore, we propose and study wireless technologies to improve the trade-off between system performance and power consumption of wireless communications.

This Thesis firstly proposes a strategy with partial channel state information (CSI) acquisition to reduce the power consumption and hardware complexity of massive MIMO base stations. In this context, the employment of partial CSI is proposed in correlated communication channels with user mobility. By exploiting both the spatial correlation and temporal correlation of the channel, our analytical results demonstrate significant gains in the energy efficiency of the massive MIMO base station.

Moreover, relay-aided communications have experienced raising interest; especially, two-way relaying systems can improve spectral efficiency with short required operating time. Therefore, this Thesis focuses on an uncorrelated massive MIMO two-way relaying system and studies power scaling laws to investigate how the transmit powers can be scaled to improve the energy efficiency up to several times the energy efficiency without power scaling while approximately maintaining the system performance.

In a similar line, large antenna arrays deployed at the space-constrained relay would give rise to the spatial correlation. For this reason, this The-

sis presents an incomplete CSI scheme to evaluate the trade-off between the spatial correlation and system performance. In addition, the advantages of linear processing methods and the effects of channel aging are investigated to further improve the relay-aided system performance.

Similarly, large antenna arrays are required in millimeter-wave communications to achieve narrow beams with higher power gain. This poses the problem that locating the best beam direction requires high power and complexity consumption. Therefore, this Thesis presents several low-complexity beam alignment methods with respect to the state-of-the-art to evaluate the trade-off between complexity and system performance.

Overall, extensive analytical and numerical results show an improved performance and validate the effectiveness of the proposed techniques.

Impact Statement

This Thesis contributes to designing and analysing energy-efficient schemes in fifth-generation (5G) and beyond wireless communication networks. The research of energy-efficient schemes is motivated by the increasing power consumption of mobile devices and base stations due to the satisfaction of the unprecedentedly growing data rates achieved by serving a significantly increasing number of mobile devices. Besides meeting the demands of high data rates, lowering the power consumption and computational loads is also crucial for practical resource-limited mobile devices.

The attractive advantages of energy-efficient schemes in 5G and beyond communications have drawn significant attention from both academia and industry. From Ericsson's 2020 report "Breaking the energy curve: how to roll out 5G without increasing energy consumption", it is known that mobile devices might double their energy consumption in the coming years due to network densification and increasing demands of data rates. Moreover, previous studies have shown that global carbon emissions and global power consumption are expected to increase, which is not sustainable for business and environmental perspectives. Some countries have already considered energy rationing for power savings. Therefore, it is crucial to evolve wireless networks towards nationwide 5G while reducing power consumption. However, there are several challenges to enhance the network energy efficiency: i) Limited battery technologies for mobile devices to scale up with the higher energy requirements, and this harms the battery lifetime; ii) The Excessive number of antennas deployed in massive MIMO systems inevitably applies

additional radio frequency (RF) chains and introduces increasing power consumption and hardware complexity; iii) The increased inter-antenna correlation due to insufficient antenna separation in constrained physical spaces may also affect the system capacity. The research in this Thesis studies novel solutions explicitly designed for massive MIMO systems to overcome these challenges and provides system design guidelines from the perspective of academia. The incomplete channel state information technology can attain power savings at the base stations. The technologies of relay-aided cooperative communication can achieve shorter operating time while increasing the data rates and improving the energy efficiency up to several times when power scaling is applied. Also, it is illustrated that low-complexity beam alignment in millimeter-wave communications can improve the received level of the system and achieve complexity, even power consumption reduction.

The research in this Thesis also provides theoretical support for the characterization and development of energy-efficient schemes in the industry. The energy-efficient schemes studied in this Thesis are promising to provide system design guidelines for power savings in 5G wireless communications. Energy efficiency is a huge opportunity but also a design constraint and challenge for future communications. It is known that Nokia, in their 2021 report "Successfully monetizing 5G requires a RAN that efficiently scales up capacity", highlighted the importance of 5G radio access network (RAN) technology with the potential to save energy, while further actions to enhance energy efficiency and minimize CO2 emissions are required to guarantee the exponentially increased data traffic. Also, Ericsson announced their Ericsson Spectrum Sharing and leaner, versatile 5G-ready radio systems such as Ericsson Radio Systems that will have the benefits of reducing energy costs while, at the same time, serving more traffic for 5G communications and beyond.

Acknowledgements

When I look back at the years that led to the construction of this Thesis, there are many people that I would like to mention and express my thanks to.

First, I would like to express my special thanks to my Ph.D. supervisor, Prof. Christos Masouros, for offering me this excellent opportunity to pursue my Ph.D. degree at UCL. I have been profoundly encouraged by his attitude and enthusiasm for research, and I appreciate his generous support in every paper we have produced together. It is his insightful guidance and detailed advice that have helped me to achieve my accomplishments. The past four years may be the most important period of my life, and I am grateful that I have spent these years at UCL under his supervision.

Then, I would like to thank Mr. Tanabe Kosuke, Mr. Ichikawa Masaki, Mr. Sasaki Eisaku, Mr. Marumoto Tsuehisa, Mr. Nader Zein and Prof. Izzat Darwazeh. We have completed an academic-industrial project together and made some achievements. I really appreciate them for their valuable suggestions and comments on the project.

I would like to further express my appreciation to Prof. Michail Matthaiou and Dr. Adrian Garcia-Rodriguez for their insightful and valuable remarks in the papers we have co-authored. I also appreciate Prof. Kai-kit Wong and Dr. Chin-Pang Liu for attending my MPhil to Ph.D. transfer, and providing helpful advice on my presentation skills and research topics. I would also like to show my appreciation to Prof. Nathan Gomes and Dr. Zeeshan Shakir for attending my Ph.D. viva and providing insightful comments on my research.

Moreover, I am also thankful to my UCL colleagues, including but not limited to: Dr. Ang Li, Dr. Lifeng Wang, Dr. Fan Liu, Dr. Xiaoyan Hu, Dr. Jialing Liao, Dr. Yin Bi, Dr. Zhongxiang Wei, Dr. Jianjun Zhang, Dr. Abdelhamid Albaraesi, Dr. Aryan Kaushik, Mr. Jingsong Sun, Miss. Nanchi Su, Miss. Xiaoye Jing, Mr. Mohammad Abdullahi and Mr. Iman Valiulahi.

Finally, I acknowledge the financial support provided by my parents and their unconditional love. I deeply appreciate their understanding, encouragement, and supports for me to pursue my Ph.D. degree at UCL.

Contents

List of Abbreviations

5G	Fifth Generation
AF	Amplify-and-Forward
AoA	Angle of Arrival
AoD	Angle of Departure
AWGN	Additive White Gaussian Noise
BC	Broadcast Channel
BS	Base station
CSI	Channel State Information
D2D	Device-to-Device
DAC	Digital-to-Analog Converter
DoD	Direction of Departure
DF	Decode-and-Forward
DSP	Digital Signal Processor
EE	Energy Efficiency
FDD	Frequency-Division Duplex
FNBW	First-Null Beamwidth
HPBW	Half-Power Beamwidth
IF	Intermediate Frequency

IoT	Internet of Things
LMI	Linear Matrix Inequality
LOS	Line-of-Sight
LTE	Long Term Evolution
MAC	Multiple Access Channel
MF	Matched Filtering
MIMO	Multiple-Input Multiple-Output
mmWave	Millimeter-Wave
MRC	Maximum Ratio Combining
MRT	Maximum Ratio Transmission
MSE	Mean Squared Error
MMSE	Minimum Mean Squared Error
NLOS	Non-Line-of-Sight
OFDM	Orthogonal Frequency-Division Multiplexing
PA	Power Amplifier
QCQP	quadratically constrained quadratic program
QP	Quadratic Programming
RAN	Radio Access Network
RF	Radio Frequency
RZF	Regularized Zero-Forcing
Rx	Receiver
SER	Symbol Error Rate
SINR	Signal-to-Interference-plus-Noise Ratio
SNR	Signal-to-Noise Ratio

SVD	Singular Value Decomposition
TDD	Time-Division Duplex
Tx	Transmitter
ULA	Uniform Linear Array
UPA	Uniform Planar Array
URA	Uniform Rectangular Array
ZF	Zero-Forcing
ZFR	Zero-Forcing Reception
ZFT	Zero-Forcing Transmission

List of Notations

a	Scalar
$\mathbf{a}$	Vector
$\mathbf{A}$	Matrix
j	Imaginary unit
$\mathscr{O}(\cdot)$	Order of numerical operations
$\mathbb{C}^{m\times n}$	A $m \times n$ matrix in the complex set
$\mathbb{CN}(\alpha, \beta)$	Complex normal distribution
$\mathbb{R}$	Set of real numbers
$\mathbb{E}\{\cdot\}$	Expectation of a random variable
$(\cdot)^T$	Transpose
$(\cdot)^*$	Conjugate
$(\cdot)^H$	Conjugate transpose
$(\cdot)^{-1}$	Inverse of a square matrix
$(\cdot)^\dagger$	Moore-Penrose inverse
$\mathrm{tr}\{\cdot\}$	Trace of a matrix
$\det(\cdot)$	The determinant of a square matrix
$\mathrm{diag}(\mathbf{a})$	Transformation of the vector $\mathbf{a}$ into a diagonal matrix
$\mathrm{vec}(\cdot)$	Vectorisation operation
$\mathrm{var}(\cdot)$	Variance of random variables

$\min(\cdot)$	Minimum entry of a vector
$\max(\cdot)$	Maximum entry of a vector
∞	Infinity
$\in$	$\mathrm{X} \in \mathrm{Y}$ indicates that X takes values from the set Y
$\forall$	For all
$\sim$	Indicates "distributed as"
$\lvert\cdot\rvert$	Absolute value or modulus
$\lVert\cdot\rVert$	Standard norm
$\lVert\cdot\rVert_2$	Euclidian form
$\lVert\cdot\rVert_F$	Frobenius norm
$[\mathbf{A}]_{m,n}$	The element in the m-th row and n-th column of $\mathbf{A}$
$[\mathbf{a}]_m$	The m-th entry in the vector $\mathbf{a}$
$\lfloor\cdot\rfloor$	Floor function
$\lceil\cdot\rceil$	Ceiling function
$x = \mathrm{find}\{a = \mathbf{b}\}$	Find function, $[\mathbf{b}]_x = a$
$J_0(\cdot)$	Zeroth-order Bessel function of the first kind
$Q_1(\cdot)$	First-order Marcum Q function

List of Figures

List of Tables

Chapter 1

Introduction

The design of energy-efficient wireless communications has become a crucial focus of both academia and industry for the past generations of mobile communications due to the need of serving a significantly increasing number of mobile devices simultaneously to satisfy the high data rate requirements [1]. However, the increased energy consumption of mobile devices and base stations due to the increasingly attainable data rate has been one of the open questions in developing next-generation communications. Explicitly, the power consumption of mobile devices has been often neglected in the past researches and has become a significant concern since current battery technologies lack the ability to satisfy the scale-up energy requirements and maintain battery lifetime simultaneously [2]. Information and communication technologies account for approximately 2% of global carbon emissions, and communication networks also currently account for up to $2\% - 3\%$ of global power consumption. Both values are expected to keep increasing each year [3, 4, 5]. For this reason, fifth-generation (5G) communication systems and beyond must provide a high data rate in an energy-efficient manner [2, 4, 6]. To assess the trade-off between power consumption and achievable data rates, the researchers focused on a combination of these two factors, that is the energy efficiency [2].

Energy efficiency essentially refers to the trade-off between the spectral efficiency of a communication system and its total power consumption.

Therefore, it is expected that the energy efficiency maximization will determine the characteristics of future wireless communication systems, which is commonly referred to as green communication [7, 8]. Indeed, because of the importance of green communication, new technologies to improve the energy efficiency of wireless communication systems have been developed. Among these, the use of multiple antennas, or multiple-input multiple-output (MIMO) communications, has been introduced to satisfy future energy efficiency requirements while maximizing the achievable rates [2]. Furthermore, massive or large-scale MIMO technologies incorporating a large number of antennas have been developed to increase achievable rates and maintain the constrained power consumption [9, 10]. This is possible because large antenna arrays at the base stations can achieve unprecedented spatial resolutions and alleviate detrimental effects including channel noise and interference [9, 10].

The theoretical advantages of massive MIMO systems are very appealing. However, the practical implementation with dedicating one radio frequency (RF) chain per antenna is challenging due to the enormous complexity of both hardware requirements and signal processing, and power consumption of the related circuitry [11, 12]. Because of these considerations, technologies such as hybrid precoding and detection [13], spatial modulation (SM) [14] and antenna selection (AS) [15] have been proposed and modified to promote both the practicable implementation and energy efficiency of massive MIMO systems. These techniques aim to improve energy efficiency and reduce the number of RF chains implemented on transmitters and receivers to achieve a low-complexity implementation while exploiting the feasibility of the massive MIMO systems [16, 17]. According to these considerations mentioned above and the importance of green communications, the characterization and development of energy-efficient schemes in future wireless communications are under consideration since energy efficiency plays a vital role as a design constraint for 5G communications.

Overall, this Thesis focuses on interesting open-ended questions related to energy-efficient transmission systems and approaches.

1.1 Aim and Motivation

Despite a number of technologies and realistic implementations considered for future energy-efficient communications, several aspects involved in the multiple-antenna system design present a significant number of open questions.

Channel propagation and the design of massive MIMO systems lead to research aimed at improving their performance and exploring system-level differences compared to conventional communication systems [10]. Among these essential differences, the higher power consumption caused by dedicating one RF chain to each antenna, and the increasing size of the physical structure required to implement a significant number of antennas, are significantly relevant. These impacts are driving the development of new approaches to improve the performance of massive MIMO systems that could meet the satisfaction of practical systems [9, 18].

Similarly, the specific problems of massive MIMO systems such as the enormous complexity of hardware and signal processing significantly interfere with their energy efficiency [12, 18]. In this case, the implementation of strategies applied on MIMO systems such as antenna selection, first introduced as a tool for complexity reduction, might diminish the above problems [15, 19]. However, the techniques resulting from these studies were not directly adaptable to massive MIMO systems [18]. Compared to conventional communication systems, exceeding a large number of antennas in massive MIMO systems causes enormous complexity and power consumption, interfering with analog-digital data transmission [12]. As a result, the design of novel solutions or modifications to existing schemes explicitly designed for massive MIMO systems is particularly crucial because it is intended to facilitate the practical deployment of massive MIMO systems.

Finally, the application of massive MIMO systems to millimeter-wave (mmWave) communications makes it possible to explore large bandwidths and enhance antenna gains. This motivates the development of techniques that may achieve close-to-optimal beam alignment for promising gains [20]. However, most studies focus exclusively on line-of-sight (LOS) scenarios with potential high path loss exponent [21, 22]. It is of great interest to study potential solutions of high-gain beamforming to compensate for this path loss, and take advantage of the spatial diversity by exploring the multi-path effects and interference among the terminals.

1.2 Main Contributions

This Thesis aims at enhancing the energy efficiency and practicability of massive MIMO systems by introducing and analyzing various transmission schemes and improving the existing approaches with this objective. The main contributions of this Thesis can be highlighted and summarized in the following list:

- Design of a scheme to reduce the signal processing and hardware complexity of massive MIMO systems deployed in confined physical spaces with user mobility by partial CSI acquisition (Chapter 3). The designed strategy exploits both the spatial correlation experienced between the channels of adjacent antennas and the temporal correlation between transmission frames determined by user mobility for the CSI relaxation. The results obtained for space-constrained massive MIMO systems demonstrate that the number of RF components and the digital signal processing complexity can be reduced at a moderate spectral efficiency loss but an improved energy efficiency.

- Performance analyses for relay-aided massive MIMO systems in the scenario of the half-duplex decode-and-forward protocol with zero-forcing processing (Chapter 4). Robust max-min optimization problems accounting for effective power distribution are also designed.

The analytical results are shown to match the simulated results. The proposed method is shown to be capable of significantly improving the energy efficiency performance by distributing the transmit powers properly while alleviating the moderate spectral efficiency performance loss.

- Extension of the relay-aided massive MIMO systems to the space-constrained structure with path loss model and incomplete CSI acquisition (Chapter 5). The proposed system exploits the spatial correlation generated at the relay to release the CSI acquisition and reduce the complexity of massive antenna arrays. Relevant technical specifications such as channel aging and the impact of steering matrices for correlated channels are analyzed. The results show that exploiting the spatial correlation at the relay can improve the energy efficiency while preserving the system performance.

- Development of two-stage beam alignment methods exploiting an antenna deactivating approach and the knowledge of beam patterns in mmWave communication systems (Chapter 6). Analytical and numerical results are evaluated in terms of achievable antenna gains and total measurements/complexity to show that the proposed two-stage beam alignment methods can improve the performance-complexity trade-off compared to the existing exhaustive scheme while maintaining the fundamental antenna gain requirement. Moreover, the potential complexity reduction can further benefit in reducing power consumption due to the necessity of high-performance computing flops.

1.3 Thesis Organisation

Subsequent to this introductory chapter, this Thesis is organised according to the structure depicted in Fig. 1.1 and described in the sequel.

Chapter 2 provides a thorough review of multiple-antenna systems that constitute the basis of this Thesis. In particular, this chapter focuses on

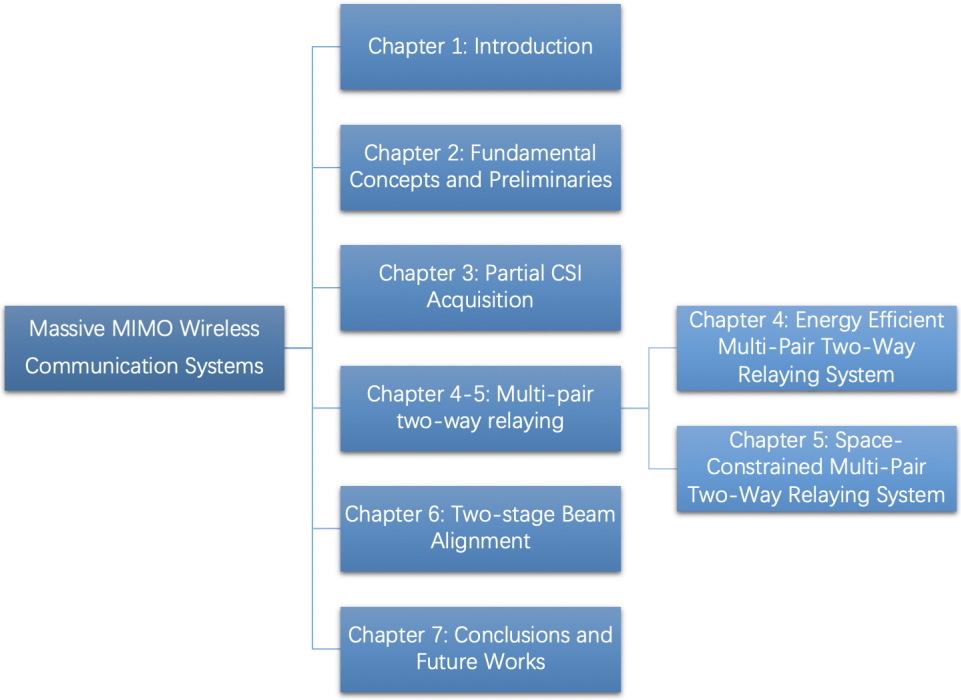

Figure 1.1: Thesis Organisation

the principles of MIMO systems, emphasising the state-of-the-art precoding techniques. The specifications of system characteristics of massive MIMO systems, the introduction of typical relaying methods and antenna array characteristics are also identified since they form the foundation of this Thesis.

Chapter 3 aims to reduce the hardware and signal processing complexity in space-constrained massive MIMO systems. The proposed strategy exploits the spatial correlation that occurs in physically constrained arrays and the temporal correlation that occurs in the time-varying channel to reduce the complexity and improve the energy efficiency. These objectives can be achieved by collecting CSI for a subset of antennas and a subset of transmission frames, subsequently, deriving the CSI of the remaining antennas and frames by simple linear interpolation. The resulting performance-complexity trade-off is evaluated in this chapter.

Chapter 4 proposes to analyze the relay-aided massive MIMO system in the scenario of the half-duplex decode-and-forward protocol with zero-

forcing processing. Different power scaling laws are presented, and max-min optimization is also analyzed. These results show that the proposed system has the potential to improve the energy efficiency performance by proper transmit power allocation while maintaining a desired spectral efficiency.

Chapter 5 extends the relay-aided massive MIMO system with the space-constrained structure and path loss model. The effects of linear processing methods have been carefully studied to confirm their benefits in massive MIMO regimes. Incomplete CSI acquisition based on spatial correlation is applied to improve the performance-complexity trade-off, while the outdated CSI caused by channel aging can be tolerated in the proposed system without significant performance degradation.

Chapter 6 presents several novel two-stage beam alignment methods exploiting an antenna deactivating approach and the theoretical beam patterns in mmWave communications. The benefits of the proposed methods are evaluated by introducing the achievable antenna gain, the number of measurements and total complexity, and the misalignment probability. These metrics show that the proposed methods can achieve significant measurement/complexity reductions compared to the existing exhaustive method, while maintaining the required gain performance.

Chapter 7 concludes this Thesis with a summary of all the contributions presented in the previous chapters, and future research work within the framework of this Thesis is also discussed.

1.4 List of Publications

The above-mentioned contributions in this Thesis have resulted in the following publications.

Journal Papers:

[J1] **J. Qian**, C. Masouros and A. Garcia-Rodriguez, "Partial CSI Acquisition for Size-Constrained Massive MIMO Systems With User Mobility", *IEEE Transactions on Vehicular Technology*, vol. 67, no. 9, pp. 9016-9020, Sept. 2018, doi:

10.1109/TVT.2018.2849263.

[J2] **J. Qian**, C. Masouros and M. Matthaiou, "Multi-Pair Two-Way Massive MIMO Relaying With Zero Forcing: Energy Efficiency and Power Scaling Laws", *IEEE Transactions on Communications*, vol. 68, no. 3, pp. 1417-1431, March 2020, doi: 10.1109/TCOMM.2019.2959329.

[J3] **J. Qian**, C. Masouros, "Multipair Relaying with Space-Constrained Large-Scale MIMO Arrays: Spectral and Energy Efficiency Analysis with Incomplete CSI", *accepted by IEEE Open Journal of Communications Society*, September 2021.

Conference Papers:

[C1] **J. Qian**, C. Masouros, "On the Performance of Physically Constrained Multi-Pair Two-Way Massive MIMO Relaying with Zero Forcing", *2019 IEEE 30th Annual International Symposium on Personal, Indoor and Mobile Radio Communications* (*PIMRC*), 2019, pp. 1-6, doi: 10.1109/PIMRC.2019.8904163.

[C2] **J. Qian**, C. Masouros, "On the Effects of Channel Aging in D2D Two-Way Relaying with Space-Constrained Massive MIMO", *2020 IEEE Globecom Workshops* (*GC Wkshps*, 2020, pp. 1-6, doi: 10.1109/GCWkshps50303.2020.9367524.

[C3] **J. Qian**, C. Masouros, K. Tanabe, E. Sasaki, N. Zein and T. Marumoto, " Beam-Pattern Assisted Low-Complexity Beam Alignment for Fixed Wireless mmWave xHaul", *Accepted by IEEE International Conference on Communications* (*ICC*) *2022*.

Chapter 2

Multiple-Antenna Wireless Communication Systems

This chapter presents basic concepts and techniques with regard to multiple antenna systems that are relevant to this Thesis. This chapter focuses on channel models, imperfect CSI models, performance metrics and multiple antenna strategies for improving wireless communication system performance. Because of the wide reach of the work, this introductory chapter provides an overview of the areas of research relevant to the contributions of this Thesis. Each chapter comprises a detailed analysis of the specific state of the art.

2.1 Multiple-input Multiple-output (MIMO) Communications

2.1.1 Fundamentals and Preliminaries

Multiple-Input Multiple-Output (MIMO) technologies have appeared and received strengthened research interest due to the increasing demand of scaling up the data rates and improving the reliability of wireless networks [23, 24, 25]. Multiple antennas deployed at the base stations (BSs) can transmit parallel data streams which are spatially multiplexed. Fig. 2.1 displays a block diagram illustrating the fundamental wireless channels of MIMO

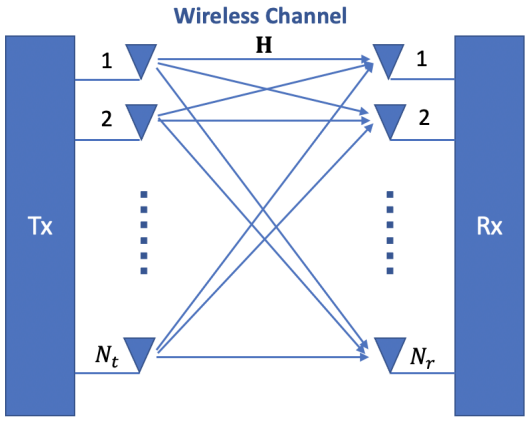

Figure 2.1: Block diagram of MIMO communication systems

communication systems. Formally, a downlink MIMO transmission channel with N_t transmit antennas on the BS and N_r receive antennas can be generally represented by a the channel matrix $\mathbf{H} \in \mathbb{C}^{N_r \times N_t}$. This results in a received signal vector $\mathbf{y} \in \mathbb{C}^{N_r \times 1}$ with the math form

$$\mathbf{y} = \mathbf{H}\mathbf{x} + \mathbf{n}, \tag{2.1}$$

where $\mathbf{x} \in \mathbb{C}^{N_t \times 1}$ denotes the transmit signal vector, and $\mathbf{n} \in \mathbb{C}^{N_r \times 1}$ is additive white Gaussian noise (AWGN), i.e., $\mathbf{n} \sim \mathbb{CN}\left(\mathbf{0}, \sigma^2 \cdot \mathbf{I}_{N_r}\right)$ with noise variance σ^2. Here, $\mathbf{I}_{N_r}$ denotes the $N_r \times N_r$ identity matrix and the symbol $\sim$ indicates "distributed as". Alternatively, (2.1) may be extended mathematically to

$$\begin{bmatrix} y_1 \\ y_2 \\ \vdots \\ y_{N_r} \end{bmatrix} = \begin{bmatrix} h_{1,1} & h_{1,2} & \cdots & h_{1,N_t} \\ h_{2,1} & h_{2,2} & \cdots & h_{2,N_t} \\ \vdots & \vdots & \ddots & \vdots \\ h_{N_r,1} & h_{N_r,2} & \cdots & h_{N_r,N_t} \end{bmatrix} \begin{bmatrix} x_1 \\ x_2 \\ \vdots \\ x_{N_t} \end{bmatrix} + \begin{bmatrix} n_1 \\ n_2 \\ \vdots \\ n_{N_r} \end{bmatrix}, \tag{2.2}$$

where the element $h_{i,j}$ represents the complex channel gain between the j-th transmit antenna and the i-th receive antenna; meanwhile, each y_i and x_j represent the received and transmit signal on the i-th receive antenna and j-th transmit antenna $(i = 1, ..., N_r,\ j = 1, ..., N_t)$, respectively. Each n_k denotes the AWGN on the k-th receive antenna $(k = 1, ..., N_r)$.

2.1.2 Linear Precoding in MIMO systems

Intuitively, MIMO technologies require extra signal processing techniques at the transmitter, the receiver, or both sides. These signal processing techniques can be divided and classified into precoding for the transmitter, detection for the receiver, and joint transmitter-receiver techniques depending on where the signal processing is carried out. Typically, precoding techniques are preferred in the downlink of multi-user MIMO systems with a single base station (BS), while receive detection schemes are employed in the uplink to separate data streams. Additionally, precoding techniques can transfer the signal processing load of users to the BS to reduce the computing load of users. This is essential because the BS is typically characterized with greater power and complexity constraints and has reliable channel state information (CSI) [26]. Because of the above-mentioned considerations and importance, precoding techniques are introduced in this chapter.

In this chapter, we focus on the introduction of existing linear precoding techniques. It is well-known that linear precoding techniques are low complexity schemes to achieve multi-user interference cancellation at the BS since the BS has both knowledge of the channel and the transmit symbols [23, 27, 28, 29, 30]. In general, the linear precoding process can be mathematically expressed as

$$\mathbf{x} = \mathbf{F}\mathbf{s} = \frac{1}{w} \cdot \mathbf{W}\mathbf{s}, \tag{2.3}$$

where $\mathbf{F} = \frac{1}{w} \cdot \mathbf{W} \in \mathbb{C}^{N_t \times N_r}$ is the precoding matrix with w representing the normalization factor to ensure that the transmission power of the precoded signals $\mathbf{x}$ is constrained to $\mathbb{E}\{\mathbf{x}^H\mathbf{x}\} \leq P_t$. $\mathbf{s} \in \mathbb{C}^{N_r \times 1}$ is the vector of input symbols. The short term normalization factor w can be given by

$$w = \|\mathbf{W}\|_F = \sqrt{\mathrm{tr}\{\mathbf{W}\mathbf{W}^H\}}. \tag{2.4}$$

This is also known as the amplification factor. Subsequently, we present typical linear precoding methods computationally efficient for multiple-antenna

systems, including matched filtering (MF), zero forcing (ZF) and regularized zero forcing (RZF).

Matched Filtering (MF), also known as maximum ratio transmission (MRT), is the simplest precoding method [31]. This method maximizes the received signal-to-noise ratio (SNR) but ignoring the multi-user interference. The precoding matrix is formulated as

$$\mathbf{F}_{MF} = \frac{1}{w_{MF}} \cdot \mathbf{H}^H = \frac{\mathbf{H}^H}{\sqrt{\mathrm{tr}\left\{\mathbf{H}\mathbf{H}^H\right\}}}. \tag{2.5}$$

MF precoding can achieve promising performance in massive MIMO regimes or low SNR scenarios, which are noise-limited. Its performance is significantly degraded as the multi-user interference is not explicitly mitigated in interference-limited scenarios [23].

Zero-Forcing (ZF) is also a simple precoding method which has been widely studied [32, 33]. This precoding method forces to eliminate the multi-user interference fully for each user; however, raising the pre-detection noise at the receivers. The precoding matrix is formulated by employing the Moore-Penrose inverse and the mathematical expression can be given by

$$\mathbf{F}_{ZF} = \frac{1}{w_{ZF}} \cdot \mathbf{H}^{\dagger} = \frac{1}{w_{ZF}} \cdot \mathbf{H}^H \left(\mathbf{H}\mathbf{H}^H\right)^{-1} = \frac{\mathbf{H}^H \left(\mathbf{H}\mathbf{H}^H\right)^{-1}}{\sqrt{\mathrm{tr}\left\{\left(\mathbf{H}\mathbf{H}^H\right)^{-1}\right\}}}. \tag{2.6}$$

Generally, ZF precoding method can achieve a better performance than MF precoding in the high SNR regimes.

Regularised Zero-Forcing (RZF) improves the performance of ZF precoding, while requiring a similar computational cost. This is achieved by introducing a regularisation factor to maximize the signal-to-interference-plus-noise ratio (SINR) rather than just achieving the interference cancella-

tion [33]. The RZF precoding matrix is given by

$$\mathbf{F}_{RZF} = \frac{1}{w_{RZF}} \cdot \mathbf{H}^H \left(\mathbf{H}\mathbf{H}^H + \vartheta \cdot \mathbf{I}\right)^{-1} = \frac{\mathbf{H}^H \left(\mathbf{H}\mathbf{H}^H + \vartheta \cdot \mathbf{I}\right)^{-1}}{\sqrt{\mathrm{tr}\left\{(\mathbf{H}\mathbf{H}^H + \vartheta \cdot \mathbf{I})^{-1}\mathbf{H}\mathbf{H}^H(\mathbf{H}\mathbf{H}^H + \vartheta \cdot \mathbf{I})^{-1}\right\}}}, \tag{2.7}$$

where the optimal regularisation factor is $\vartheta = N_r\sigma^2$, set to satisfy the minimum mean square error (MMSE) criterion for the considered system [33].

The main differences between linear precoding techniques are summarized in the table 2.1.

2.2 Massive MIMO Systems

Massive MIMO systems are becoming increasingly important because of the exciting advantages of improving the spectral efficiency and data rate demands by employing a great number of antennas simultaneously in microwave communication systems [9, 10, 12, 34, 35]. These systems rely on the deployment of excessive antenna arrays at the base stations and also become crucial for millimeter wave (mmWave) frequencies to improve the system performance [36]. This chapter gives a brief overview of the key characteristics of massive MIMO systems. Specifically, we envision a time-division duplexing (TDD) system, as it is commonly used in massive MIMO systems, thanks to its simplification characterized by channel reciprocity [9]. These peculiarities constitute one of the major research areas of this Thesis.

Linear Precoding			
Name	Closed-form Expression	Complexity	Performance
MF	$\mathbf{F}_{MF} = \frac{1}{w_{MF}} \cdot \mathbf{H}^H$	Simplest	Lowest
ZF	$\mathbf{F}_{ZF} = \frac{1}{w_{ZF}} \cdot \mathbf{H}^H \left(\mathbf{H}\mathbf{H}^H\right)^{-1}$	Higher than MF	Better than MF
RZF	$\mathbf{F}_{RZF} = \frac{1}{w_{RZF}} \cdot \mathbf{H}^H \left(\mathbf{H}\mathbf{H}^H + \vartheta \cdot \mathbf{I}\right)^{-1}$	Comparable complexity to ZF	Better than ZF

Table 2.1: Summary of linear precoding methods

2.2.1 System Model of Massive MIMO

A general single cell scenario is considered, where the BS is equipped with N_t antennas and serves $N_r \ll N_t$ single-antenna users, the uplink channel can be represented as the Hermitian transpose of the downlink channel under TDD operation due to channel reciprocity [9, 37]. In this case, the uplink channel matrix $\mathbf{H}_u \in \mathbb{C}^{N_t \times N_r}$ can be expressed as

$$\mathbf{H}_u = \mathbf{H}^H = \mathbf{Z}\mathbf{D}_\beta^{1/2}. \tag{2.8}$$

Here, $\mathbf{Z} \in \mathbb{C}^{N_t \times N_r}$ represents the complex fast-small fading effect, typically assumed as independent and identically distributed (i.i.d.) when Rayleigh fading is assumed. $\mathbf{D}_\beta \in \mathbb{R}^{N_r \times N_r}$ is a diagonal matrix representing the slow-large fading coefficients composing path loss and shadowing effect. The slow-large fading coefficient β_k of the k-th user in $\mathbf{D}_\beta$ is defined as

$$\beta_k = (\frac{\kappa}{D_k^\nu})^{\frac{1}{2}}, \tag{2.9}$$

where κ represents the standard shadowing effect with typical values ranging from 2 to 6, D_k is the distance between the BS and k-th user ($k = 1, ..., N_r$), and ν is the path loss exponent [38, 39]. Consequently, $\mathbf{y}_u \in \mathbb{C}^{N_t \times 1}$, the signal vector received at the BS in the uplink transmission, can be defined as

$$\mathbf{y}_u = \sqrt{p_u} \cdot \mathbf{H}_u \cdot \mathbf{x}_u + \mathbf{n}_u, \tag{2.10}$$

where, $\mathbf{x}_u \in \mathbb{C}^{N_r \times 1}$ is the signal vector from the users to the BS, p_u is the uplink transmit power and $\mathbf{n}_u \in \mathbb{C}^{N_t \times 1}$ is additive white Gaussian noise [9].

2.2.2 Achievable Sum Rates in massive MIMO

The deployment of massive MIMO at the transmitter results in significant benefits in terms of attainable sum rates and signal processing for uplink and downlink transmissions. Without losing generality, this chapter focuses on uplink channels, similar results are available for downlink channels thanks

to the channel reciprocity of TDD operation. The achievable sum rate in the uplink of a massive MIMO system is given by [9]

$$R_u = \log_2 \det(\mathbf{I}_{N_r} + p_u \mathbf{H}_u^H \mathbf{H}_u), \tag{2.11}$$

where $\det(\cdot)$ denotes the determinant of the square matrix. In fact, as a consequence of $N_r \ll N_t$ and large to infinite N_t in massive MIMO systems, the channel responses for different users become orthogonal, namely, the columns of the channel matrix $\mathbf{H}_u$ are orthogonal under favorable propagation conditions, if the elements of $\mathbf{Z}$ are all independent [29]. With this channel orthogonality, the following expression can be achieved [9]

$$\mathbf{H}_u^H \mathbf{H}_u = \mathbf{D}_\beta^{1/2} \mathbf{Z}^H \mathbf{Z} \mathbf{D}_\beta^{1/2} \approx N_t \mathbf{D}_\beta^{1/2} \mathbf{I}_{N_r} \mathbf{D}_\beta^{1/2} = N_t \mathbf{D}_\beta. \tag{2.12}$$

Therefore, only the slow-large scale fading determined by $\mathbf{D}_\beta$ has a direct effect on the communication between the users and the BS. Consequently, incorporating this result into (2.11), the achievable sum rate can be simplified as

$$R_u \approx \log_2 \det(\mathbf{I}_{N_r} + N_t p_u \mathbf{D}_\beta) = \sum_{k=1}^{N_r} \mathbf{log}_2(1 + N_t p_u \beta_k). \tag{2.13}$$

This computation provides an intuitive interpretation that the transmission channel of massive MIMO systems can be broken down into N_r parallel additive white Gaussian noise channels, where k-th equivalent link has the received SNR $N_t p_u \beta_k$.

2.2.3 Energy Efficiency in Massive MIMO

The trade-off between system performance and power consumption can be analyzed as a parameter referred to as energy efficiency. The need to exponentially increase achievable rates while controlling power consumption makes it crucial to optimise energy efficiency [2, 4, 40]. The energy efficiency is analytically defined as

$$\varepsilon = \frac{R}{P_{tot}}. \tag{2.14}$$

Here, R refers to the sum rates, the spectral efficiency, or the throughput, and P_{tot} is the total system power consumption. In this case, if R refers to the sum rates (bit/s) [4, 41], the energy efficiency will be defined in terms of (bits/Joule). If R refers to the spectral efficiency (bit/s/Hz) [4], the energy efficiency will be defined in terms of (bits/Joule/Hz). Typically, there exist several models for the total power consumption. In this chapter, we briefly introduce the models that are relevant to the contributions of this Thesis to be employed for the analysis of total power consumption and energy efficiency, including

$$P_{\text{tot}} = \frac{P_{\text{PA}} + P_{\text{RF}} + P_{\text{BB}}}{(1-\sigma_{\text{DC}})(1-\sigma_{\text{MS}})(1-\sigma_{\text{cool}})}. \tag{2.15}$$

Here, $\sigma_{\text{DC}}, \sigma_{\text{MS}}$ and $\sigma_{\text{cool}} \in (0,1)$ are the parameters representing DC-DC loss, power supplies loss and active cooling loss respectively. Moreover, P_{PA} represents the power consumed by power amplifiers (PA) and it is given by

$$P_{\text{PA}} = \frac{P_t}{\zeta}, \tag{2.16}$$

where ζ is the power amplifier efficiency and P_t is the power required at the output of the power amplifiers. P_{RF} refers to the power consumption of other electronic components in the radio frequency (RF) chains. Generally, each antenna is connected to one RF chain [17] and P_{RF} can be expressed as

$$P_{RF} = N(P_{DAC} + P_{mix} + P_{filt}) + P_{syn}, \tag{2.17}$$

where P_{syn} is the power consumption of the frequency synthesizer, P_{DAC}, P_{mix} and P_{filt} are the power consumed by the digital-to-analog converters (DACs), signal mixers and filters in all N RF chains at the transmitter respectively [17]. Additionally,

$$P_{\text{BB}} = p_c C. \tag{2.18}$$

Here, P_{BB} denotes the power consumption of digital signal processor (DSP) where p_c determines the power consumption per real flop and C refers to the average number of real flops per second [17, 42].

Another commonly used power consumption model in the two-way relay channel model can be given by [43],

$$P_{\text{tot}} = \sum_{i=1}^{N_r} P_{tot,i} + P_{tot,r} + P_{\text{static}}, \tag{2.19}$$

where P_{static} is the power of all the static circuits [44]. $P_{tot,i}$ is the total power at i-th user and $P_{tot,r}$ denotes the total power at the relay [44], which can be expressed as

$$P_{\text{tot,x}} = \frac{P_{t,x}}{\zeta} + P_{\text{RF,x}}, x = i, r. \tag{2.20}$$

Here, $P_{t,x}$ represents the power required at the power amplifiers of the BS or users; ζ denotes the power amplifier efficiency referring to (2.16). The power consumption of the RF components at the i-th user or the relay is $P_{\text{RF,x}}$ ($x = i, r$, $i = 1, ..., N_r$) referring to (2.17) where N is the number of antennas at the user or relay terminal.

Energy efficiency optimization has become a crucial topic in the 5G wireless communications and beyond. [45, 46] consider the optimization of the resulting energy efficiency and [40, 45] investigate the effects of the power consumption of RF chains on energy efficiency. In general, the impact of the incorporation of an excessive number of antennas and equally large number of analogue hardware components in massive MIMO BSs on the power consumption and energy efficiency becomes a major concern. This is because the circuit power consumption is increasing to degrade the energy efficiency. Meanwhile, the hardware complexity of massive MIMO is exponentially increasing due to the large number of required RF components. As a result of these considerations, these massive MIMO systems to achieve energy-efficient and low-complexity communications are the focus of the following chapter.

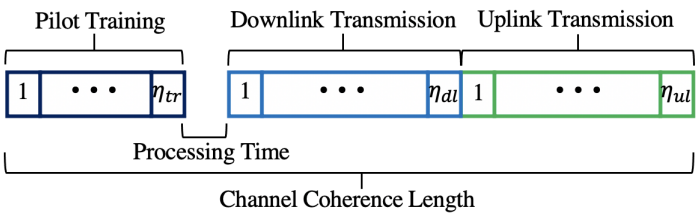

Figure 2.2: TDD Operation Protocol

2.2.4 Acquisition of Channel State Information (CSI)

It is introduced in Chapter 2.1.2 that the employment of linear precoding and detection requires the knowledge of the channel state information (CSI) at the BS. Typically, the channel coherence interval can be divided into two phases: pilot training, and data transmission and reception, under TDD operation [9, 47]. Fig. 2.2 shows the TDD operation protocol, and illustrates the distribution of CSI acquisition sequence, where the BS first acquires the CSI by uplink pilots in the pilot training phase with η_{tr} time/frequency symbol slots, and then the BS transmits or receives data in the transmission phase with available CSI for downlink precoding and uplink detection.

In general, the pilot training phase starts with users transmitting their own pilot signals to the BS over η_{tr} symbols, typically, $\eta_{tr} \geq N_r$. This allows the orthogonality between the pilot vector of the k-th user and the pilot signals of the remaining users. The received signal at the BS after pilot training is given by

$$\mathbf{Y}_{tr} = \sqrt{p_{ul}}\mathbf{H}_u\mathbf{Q} + \mathbf{N}, \tag{2.21}$$

where $\mathbf{Y}_{tr} \in \mathbb{C}^{N_t \times \eta_{tr}}$, $\mathbf{Q} \in \mathbb{C}^{N_r \times \eta_{tr}}$ is the pilot signal matrix, in which all rows are independent due to the orthogonality introduced above. p_{ul} is the uplink transmit power and $\mathbf{N} \in \mathbb{C}^{N_t \times \eta_{tr}}$ is an AWGN matrix [17, 37]. Correlating the received signals after the pilot training phase with the pilot sequences available at the BS yields the decision metric, and the least square channel estimate $\hat{\mathbf{H}}_u$ can be mathematically given by

$$\hat{\mathbf{H}}_u = \mathbf{Y}_{tr}\mathbf{Q}^H = (\sqrt{p_{ul}}\mathbf{H}_u\mathbf{Q} + \mathbf{N})\mathbf{Q}^H = \sqrt{p_{tr}}\mathbf{H}_u + \mathbf{N}\mathbf{Q}^H. \tag{2.22}$$

where p_{tr} is the power consumption of pilot symbols [17, 37]. Moreover, thanks to the channel reciprocity of TDD operation, the downlink channel estimate can be straightforwardly obtained as the conjugate transpose of the uplink estimate. Usually, the necessity of $\eta_{tr} \geq N_r$ in the CSI acquisition may limit the performance of practical massive MIMO systems and increase the operating time or the complexity of CSI acquisition [48]. Another challenge in the CSI acquisition process is pilot contamination, in which the length of pilot sequences is limited by the channel coherence time in realistic multi-cell massive MIMO; therefore, the orthogonality between the pilots of neighbouring cells cannot be guaranteed and can cause inter-cell interference and degrade the system performance [9, 29]. These challenges entail a crucial area of research to reduce the CSI acquisition load and mitigate pilot contamination in massive MIMO.

2.2.5 Modelling of Imperfect CSI

According to the studies in Chapter 2.2.4, a statistical CSI error model that is relevant to the contributions of this Thesis has been derived subsequently. The minimum mean square error (MMSE) uplink channel estimation is performed deriving from (2.22) [37, 49], and the imperfect channel model can be expressed as

$$\mathbf{H}_u = \tau \cdot \hat{\mathbf{H}}_u + \sqrt{1-\tau^2}\mathbf{E}. \tag{2.23}$$

Here $\mathbf{H}_u$ represents the actual wireless propagation channel, and $\hat{\mathbf{H}}_u$ is the imperfect channel estimate. $\tau \in [0,1]$ denotes the factor modelling the quality of acquired CSI. $\mathbf{E}$ denotes the corresponding estimation error matrix, where all entries are independent and distributed as $\mathbb{CN}(0,1)$ [17, 50].

This imperfect channel model is motivated by the actuality that the perfect acquisition of CSI is difficult in cellular communication systems, and this makes it crucial to study the system performance with imperfect CSI [37]. (2.22)-(2.23) announce that the CSI acquisition can limit the practical performance of massive MIMO systems due to the requirement $\eta_{tr} \geq N_r$

and the quality of acquired CSI. Therefore, reducing the channel estimation complexity and preserving the practical system performance becomes an important topic [48], and this aspect is also analyzed in this Thesis.

2.3 Channel Modelling

Chapter 2.1 and Chapter 2.2 introduce the importance of the knowledge of the channel for all linear precoding techniques, and therefore it is necessary to study the channel modelling. In this chapter, we briefly introduce the channel models that are relevant to this Thesis. In general, we consider the non-line-of-sight (NLoS) propagation channel models, unless specifically stated.

2.3.1 Uncorrelated Rayleigh Channel

The most common and widely used channel model is the uncorrelated Rayleigh channel. This model is a typical multi-path fading channel model commonly used in 5G communications assuming that the independent reflectors and scatters are in the wireless environment. When the number of propagation paths is large, a statistical model with complex random distribution can be applied. Subsequently, the channel gain can be considered as approximately complex Gaussian distributed according to the central limit theorem [23, 38]. In general, each channel coefficient can be modelled as

$$\mathbf{H}_{m,n} \sim \mathbb{CN}(0,1). \tag{2.24}$$

According to this modelling, the magnitude of each channel follows a Rayleigh distribution resulting from the multiple NLoS paths of the signal propagating from transmitter to receiver [51, 52], which names this channel model.

2.3.2 Correlated Rayleigh Channel

The uncorrelated Rayleigh channel model assumes that the channels between different antennas are independent without spatial correlation effect.

However, for a practical antenna array with limited spaces, the channels between adjacent antennas are spatially correlated, especially when the inter-antenna distance is smaller than the carrier wavelength, usually, smaller than half carrier wavelength [23, 53, 54]. In this sub-chapter, statistical model of spatially-correlated Rayleigh Fading Channel will be briefly introduced.

Separately-Correlated Rayleigh Channel: When a massive MIMO system with a base station of N_t antennas and N_r single-antenna users is considered, the spatial correlation exists at both the transmitter and receiver. According to [54, 55], we model the channel $\mathbf{H}$ as

$$\mathbf{H} = \mathbf{A}_r \mathbf{G} \mathbf{A}_t^H. \tag{2.25}$$

In (2.25), $\mathbf{G} = 1/\sqrt{L} \cdot \mathrm{diag}(g_1, g_2, ..., g_L) \in \mathbb{C}^{L \times L}$ is a diagonal matrix representing the independent and identically distributed Rayleigh fading channel, where L is the number of independent paths and each element satisfies (2.24). In general, it is assumed that the correlation matrices for the transmitter and receiver can be separated. $\mathbf{A}_r \in \mathbb{C}^{N_r \times L}$ and $\mathbf{A}_t \in \mathbb{C}^{N_t \times L}$ are the correlation matrices for the receive antennas and transmit antennas containing L steering vectors, respectively [54]. When the uniform linear array (ULAs) topology is applied, $\mathbf{A}_r$ and $\mathbf{A}_t$ can be decomposed into [17, 34]

$$\mathbf{A}_r = \left[\mathbf{a}_r{}^T \left(\theta_1^r\right), \mathbf{a}_r{}^T \left(\theta_2^r\right), \cdots, \mathbf{a}_r{}^T \left(\theta_L^r\right) \right], \tag{2.26}$$

$$\mathbf{A}_t = \left[\mathbf{a}_t{}^T \left(\theta_1^t\right), \mathbf{a}_t{}^T \left(\theta_2^t\right), \cdots, \mathbf{a}_t{}^T \left(\theta_L^t\right) \right]. \tag{2.27}$$

The corresponding steering vectors of ULA topology, $\mathbf{a}_r\left(\theta_m^r\right) \in \mathbb{C}^{1 \times N_r}$ and $\mathbf{a}_t\left(\theta_m^t\right) \in \mathbb{C}^{1 \times N_t}$ are in terms of [56]

$$\mathbf{a}_r(\theta_m^r) = [1, e^{j2\pi d_r sin(\theta_m^r)}, ..., e^{j2\pi(N_r-1)d_r sin(\theta_m^r)}], \tag{2.28}$$

$$\mathbf{a}_t(\theta_m^t) = [1, e^{j2\pi d_t sin(\theta_m^t)}, ..., e^{j2\pi(N_t-1)d_t sin(\theta_m^t)}], \tag{2.29}$$

where θ_m^t and θ_m^r $(m = 1, ..., L)$ represents the angles of departure (AoDs) and the angles of arrival (AoAs) respectively [57]. d_t and d_r denote the inter-antenna distance normalized by the carrier wavelength λ for the transmit and receive antenna arrays respectively. Similarly, $\mathbf{A}_r$ and $\mathbf{A}_t$ can be decomposed into [17, 34]

$$\mathbf{A}_r = \left[\mathbf{a}_r{}^T\left(\theta_1^r, \phi_1^r\right), \mathbf{a}_r{}^T\left(\theta_2^r, \phi_2^r\right), \cdots, \mathbf{a}_r{}^T\left(\theta_L^r, \phi_L^r\right)\right], \tag{2.30}$$

$$\mathbf{A}_t = \left[\mathbf{a}_t{}^T\left(\theta_1^t, \phi_1^t\right), \mathbf{a}_t{}^T\left(\theta_2^t, \phi_2^t\right), \cdots, \mathbf{a}_t{}^T\left(\theta_L^t, \phi_L^t\right)\right], \tag{2.31}$$

where for uniform rectangular arrays (URAs). In general, the respective horizontal and vertical array steering vectors can be characterized as [56]

$$\mathbf{a}_{x,h}(\theta_m^x, \phi_m^x) = [1, e^{j2\pi[d_x^h sin(\phi_m^x) sin(\theta_m^x)]}, \ldots, e^{j2\pi[(N_x^h - 1) d_x^h sin(\phi_m^x) sin(\theta_m^x)]}], \tag{2.32}$$

$$\mathbf{a}_{x,v}(\theta_m^x, \phi_m^x) = [1, e^{j2\pi[d_x^v sin(\theta_m^x) cos(\phi_m^x)]}, \ldots, e^{j2\pi[(N_x^v - 1) d_x^v sin(\theta_m^x) cos(\phi_m^x)]}], \tag{2.33}$$

where θ_m^x and ϕ_m^x $(m = 1, ..., L,\ x = t, r)$ denote the elevation and azimuth directions of AoDs and AoAs respectively [57]. The steering vectors $\mathbf{a}_r\left(\theta_m^r, \phi_m^r\right) \in \mathbb{C}^{1\times N_r}$ and $\mathbf{a}_t\left(\theta_m^t, \phi_m^t\right) \in \mathbb{C}^{1\times N_t}$ can be expressed as [55, 56]

$$\begin{aligned}\mathbf{a}_r\left(\theta_m^r, \phi_m^r\right) &= \mathrm{vec}\big(\mathbf{a}_h(\theta_m^r, \phi_m^r)^{\mathrm{T}} \mathbf{a}_v(\theta_m^r, \phi_m^r)\big) \\ &= \Big[1, e^{j2\pi[d_r^h sin(\phi_m^r) sin(\theta_m^r)]}, \ldots, e^{j2\pi[(N_r^h - 1) d_r^h sin(\phi_m^r)) sin(\theta_m^r)) + (N_r^v - 1) d_r^v sin(\theta_m^r)) cos(\phi_m^r))]}\Big]\end{aligned} \tag{2.34}$$

$$\begin{aligned}\mathbf{a}_t\left(\theta_m^t, \phi_m^t\right) &= \mathrm{vec}\big(\mathbf{a}_h(\theta_m^t, \phi_m^t)^{\mathrm{T}} \mathbf{a}_v(\theta_m^t, \phi_m^t)\big) \\ &= \Big[1, e^{j2\pi[d_t^h sin(\phi_m^t) sin(\theta_m^t)]}, \ldots, e^{j2\pi[(N_t^h - 1) d_t^h sin(\phi_m^t)) sin(\theta_m^t)) + (N_t^v - 1) d_t^v sin(\theta_m^t)) cos(\phi_m^t))]}\Big],\end{aligned} \tag{2.35}$$

where the vector valued operator $\mathrm{vec}(\cdot)$ can map a $m \times n$ matrix to a $mn \times 1$ column vector. N_x^h and N_x^v $(x = t, r)$ represent the number of antennas deployed in the horizontal and vertical directions respectively. In this case, the total number of antennas can be redefined as $N_x = N_x^h \times N_x^v$ $(x = t, r)$ under the URA scenario. $d_x^{\{h,v\}} = \frac{D_x^{\{h,v\}}}{N_x^{\{h,v\}} - 1}$ is the normalized inter-antenna distance where $D_x^{\{h,v\}}$ is the respective horizontal and vertical lengths of the antenna

arrays, d_x^h and d_x^v $(x = t, r)$ denote the respective horizontal and vertical inter-antenna distance normalized by the carrier wavelength for the receive and transmit antenna arrays.

Semi-Correlated Rayleigh Channel: In general, when a multi-user MIMO system is considered, users are uncorrelated because they are considered as perfectly separated. Therefore, a semi-correlated channel model will be considered with only the spatial correlation existing at the transmitter. As a result, each channel response vector $\mathbf{h}_k \in \mathbb{C}^{1\times N_t}$, $(k = 1, ..., N_r)$, for the users can be modified as [17, 50]

$$\mathbf{h}_k = \mathbf{g}_k \mathbf{A}_k, \ \forall k \in \{1, 2, \cdots, N_r\}, \tag{2.36}$$

where $\mathbf{g}_k \in \mathbb{C}^{1\times L}$ comprises all entries following the standard complex Gaussian distribution, modelling the Rayleigh components. $\mathbf{A}_k \in \mathbb{C}^{L\times N_t}$ contains L steering vectors to model the transmit correlation, where L is the number of directions of departure (DoDs). For ULAs, $\mathbf{A}_k$ can be modelled as

$$\mathbf{A}_k = \frac{1}{\sqrt{L}} \cdot \left[\mathbf{a}^T\left(\theta_{k,1}\right), \mathbf{a}^T\left(\theta_{k,2}\right), \cdots, \mathbf{a}^T\left(\theta_{k,L}\right)\right]^T, \tag{2.37}$$

where each steering vector $\mathbf{a}\left(\theta_{k,i}\right) \in \mathbb{C}^{1\times N_t}$ can be given by

$$\mathbf{a}(\theta_{k,i}) = [1, e^{j2\pi d sin(\theta_{k,i})}, ..., e^{j2\pi(N_t-1)d sin(\theta_{k,i})}], \tag{2.38}$$

where d denotes the equidistant inter-antenna distance normalised by the carrier wavelength. Similarly, for URAs, $\mathbf{A}_k$ can be modelled as

$$\mathbf{A}_k = \frac{1}{\sqrt{L}} \cdot \left[\mathbf{a}^T\left(\theta_{k,1}, \phi_{k,1}\right), \mathbf{a}^T\left(\theta_{k,2}, \phi_{k,2}\right), \cdots, \mathbf{a}^T\left(\theta_{k,L}, \phi_{k,L}\right)\right]^T, \tag{2.39}$$

where each $\mathbf{a}\left(\theta_{k,i}, \phi_{k,i}\right) \in \mathbb{C}^{1\times N_t}$, supported by the respective horizontal and vertical array steering vectors modelled for separately-correlated channels,

is given by

$$\begin{aligned}\mathbf{a}(\theta_{k,i},\phi_{k,i}) &= \mathrm{vec}\big(\mathbf{a}_h(\theta_{k,i},\phi_{k,i})^{\mathrm{T}}\mathbf{a}_v(\theta_{k,i},\phi_{k,i})\big)\\ &= \Big[1, e^{j2\pi[d_h sin(\phi_{k,i})sin(\theta_{k,i})]}, \dots, e^{j2\pi[(N_h-1)d_h sin(\phi_{k,i})sin(\theta_{k,i})+(N_v-1)d_v sin(\phi_{k,i})cos(\theta_{k,i})]}\Big].\end{aligned} \tag{2.40}$$

In (2.40), $d_{\{h,v\}}$ denotes the equidistant inter-antenna distance normalised by the carrier wavelength in the horizontal and vertical directions. N_h and N_v are the number of antennas deployed in the horizontal and vertical directions respectively. In this URA scenario, the total number of antennas can be redefined as $N_t = N_h \times N_v$. This can be considered as a derivation of the modelling for separately-correlated channels [55].

2.4 Cooperative Communication

2.4.1 Two-way Relay Channel Model

Typically, wireless communication networks are exposed to various channel problems such as fading and path loss; a relay can be applied to overcome these problems and can enhance cellular coverage and improve network capacity and throughput [44, 58]. Moreover, a relay-aided channel model can be referred to as a probability model of the communication between transmitters and receivers with one or more intermediate relays in information theory [58]. In this chapter, we briefly present the single-relay cooperative communication relevant to the contributions of this Thesis. As such, we focus on the single massive MIMO relay network where the relay is equipped with N_R antennas. The source terminal can only transmit its information to the destination terminal through the relay.

In general, a two-way massive MIMO relay system with two groups of terminals and a relay T_R is considered. Each group includes K terminals, and each terminal in one group is paired to a separate terminal in the other group. For convenience, the set of terminals in one group is denoted as T_A, and the other set is denoted as T_B. All terminals would exchange information

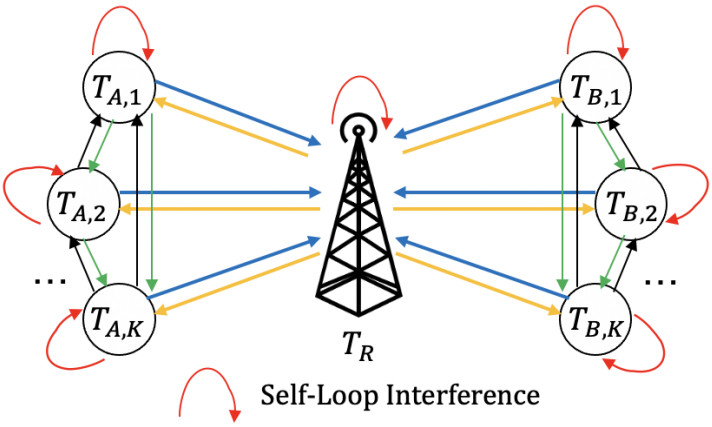

Figure 2.3: Full-Duplex Two-Way Relay System

through a relay. No direct link exists between the terminals of the two groups because of the long transmission distance [59].

2.4.1.1 Full-Duplex Two-way Relaying

In full-duplex mode, the relay can receive and transmit simultaneously. However, it results in the self-loop interference, as shown in Fig. 2.3. The relay's n_R antennas are used for transmission; the remaining $N_R - n_R$ antennas can be used for reception. Similarly, each terminal is equipped with N_T antennas, where n_T antennas are used for transmission, and the rest $N_T - n_T$ antennas are for reception [60, 61, 62].

At the n-th time instant, each terminal transmits their own signal $\mathbf{s}_{X,i}(n) \in \mathbb{C}^{n_T}$ with power $p_{X,i}$ $(X = A, B,\ i = 1, \ldots, K)$ to the relay. The relay broadcasts signal $\mathbf{x}_R(n) \in \mathbb{C}^{n_R}$ to all terminals with power of p_R. The transmitted signals from the terminals will be received at the relay, and the broadcast signal from the relay will also be leaked back to the relay itself. This leaked signal is considered as self-loop interference [62]. Although several cancellation methods are applied to cancel the self-loop interference, it is challenging to achieve perfect cancellation; in this case, residual self-loop interference still remains [62, 63]. Therefore, after the certain cancellation of

the self-loop interference, the signal received to the relay may be given by

$$\mathbf{y}_R(n) = \sum_{X=A,B} \sum_{i=1}^{K} \sqrt{p_{X,i}} \mathbf{H}_{T_{X,i}R} \mathbf{s}_{X,i}(n) + \mathbf{H}_{RR} \mathbf{x}_R(n) + \mathbf{n}_R(n), \tag{2.41}$$

where $\mathbf{H}_{T_{X,i}R} \in \mathbb{C}^{(N_R - n_R) \times n_T}$ is the channel response matrix from the terminal $T_{X,i}$, $X = A, B$, $i = 1, ..., K$, to the relay T_R, $\mathbf{H}_{RR} \in \mathbb{C}^{(N_R - n_R) \times n_R}$ represents the channel response matrix for the self-loop link at the relay after certain self-loop interference cancellation and $\mathbf{H}_{RR}\mathbf{x}_R(n)$ characterizes the residual self-loop interference remaining at the relay, and $\mathbf{n}_R(n)$ satisfying $\mathbb{CN}(0, \sigma^2 \mathbf{I}_{N_R - n_R})$ is the complex Gaussian noise at the relay. Similarly, the received signal at the terminal $T_{X,i}$ after self-loop interference cancellation can be expressed as

$$\begin{aligned} \mathbf{y}_{T_{X,i}}(n) = {} & \mathbf{H}_{RT_{X,i}} \mathbf{x}_R(n) + \sqrt{p_{X,i}} \mathbf{H}_{T_{X,i}T_{X,i}} \mathbf{s}_{X,i}(n) \\ & + \sum_{j=1, j \neq i}^{K} \sqrt{p_{X,j}} \mathbf{H}_{T_{X,j}T_{X,i}} \mathbf{s}_{X,j}(n) + \mathbf{n}_{T_{X,i}}(n). \end{aligned} \tag{2.42}$$

Here, $\mathbf{H}_{RT_{X,i}} \in \mathbb{C}^{(N_T - n_T) \times n_R}$ characterizes the channel response matrix from the relay to the terminal $T_{X,i}$, $X = A, B$, $i = 1, ..., K$, $\mathbf{H}_{T_{X,i}T_{X,i}} \in \mathbb{C}^{(N_T - n_T) \times n_T}$ represents the channel response matrix for the self-loop link at the terminal $T_{X,i}$, and $\mathbf{H}_{T_{X,j \neq i}T_{X,i}} \in \mathbb{C}^{(N_T - n_T) \times n_T}$ is the inter-user channel in the group T_X. $\mathbf{n}_{T_{X,i}}(n)$ satisfying $\mathbb{CN}(0, \sigma^2 \mathbf{I}_{N_T - n_T})$ is the complex Gaussian noise at the terminal. The broadcast signal of the relay $\mathbf{x}_R(n)$ is generated by $\mathbf{y}_R(n - \delta)$, where $\delta \geq 1$ is the processing delay. Incorporating (2.41) with (2.42), the received signal $\mathbf{y}_{T_{X,i}}(n)$ can be re-written as

$$\begin{aligned} \mathbf{y}_{T_{X,i}}(n) = {} & \mathbf{H}_{RT_{X,i}} \Big[\sum_{X=A,B} \sum_{i=1}^{K} \sqrt{p_{X,i}} \mathbf{H}_{T_{X,i}R} \mathbf{s}_{X,i}(n - \delta) + \mathbf{H}_{RR} \mathbf{x}_R(n - \delta) + \mathbf{n}_R(n - \delta) \Big] \\ & + \sqrt{p_{X,i}} \mathbf{H}_{T_{X,i}T_{X,i}} \mathbf{s}_{X,i}(n) + \sum_{j=1, j \neq i}^{K} \sqrt{p_{X,j}} \mathbf{H}_{T_{X,j}T_{X,i}} \mathbf{s}_{X,j}(n) + \mathbf{n}_{T_{X,i}}(n). \end{aligned} \tag{2.43}$$

Note that relaying schemes introduced in Chapter 2.4.2 will be applied at the relay to generate the broadcast signal.

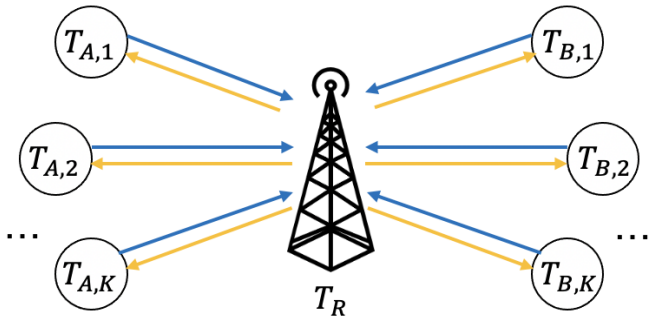

Figure 2.4: Half-Duplex Two-Way Relay System

2.4.1.2 Half-Duplex Two-way Relaying

When the relay operates in the half-duplex mode, it can transmit and receive separately. When the relay receives the signal from the source terminals, it uses all its N_R antennas for the receive diversity, and it uses the same N_R antennas to transmit the information to the destination terminals for the transmit diversity [61, 64]. Similar with Chapter 2.4.1.1, each terminal is equipped with N_T antennas and transmits independent signal $\mathbf{s}_{X,i} \in \mathbb{C}^{N_T}$ with power $p_{X,i}$, $X = A, B$, $i = 1, \ldots, K$. The relay broadcasts the signal $\mathbf{x}_R \in \mathbb{C}^{N_R}$ to all terminals with power of p_R. In the first time slot, the received signal at the relay can be given by

$$\mathbf{y}_R = \sum_{X=A,B} \sum_{i=1}^{K} \sqrt{p_{X,i}} \mathbf{H}_{T_{X,i}R} \mathbf{s}_{X,i} + \mathbf{n}_R, \tag{2.44}$$

where $\mathbf{H}_{T_{X,i}R} \in \mathbb{C}^{N_R \times N_T}$ denotes the channel response matrix from the terminal $T_{X,i}$, $X = A, B$, $i = 1, \ldots, K$, to the relay T_R, and $\mathbf{n}_R$ satisfying $\mathbb{CN}(0, \sigma^2 \mathbf{I}_{N_R})$ is the complex Gaussian noise at the relay. In the second time slot, the relay broadcasts $\mathbf{x}_R \in \mathbb{C}^{N_R}$ as a combination of all received signals from terminals [64]; therefore, the received signals at the terminal $T_{X,i}$ is

$$\mathbf{y}_{T_{X,i}} = \mathbf{H}_{RT_{X,i}} \mathbf{x}_R + \mathbf{n}_{T_{X,i}}. \tag{2.45}$$

Here, $\mathbf{H}_{RT_{X,i}} \in \mathbb{C}^{N_T \times N_R}$ represents the channel response matrix from the relay to the terminal $T_{X,i}$, $X = A, B$, $i = 1, \ldots, K$, $\mathbf{n}_{T_{X,i}}$ satisfying $\mathbb{CN}(0, \sigma^2 \mathbf{I}_{N_T})$ is the

complex Gaussian noise at the terminal.

Similarly, the relaying schemes introduced in Chapter 2.4.2 will be applied at the relay to generate the broadcast signal.

2.4.2 Relaying Schemes

There exist three main relaying schemes: Amplify-and-Forward, Decode and-Forward and Compress-and-Forward.

Amplify-and-Forward (AF): In this amplify-and-forward (AF) method, the relay receives a noisy version of the signals transmitted by source terminals. The relay amplifies the received signals by multiplication with an amplifying matrix and then re-transmits them to the destination terminals of the transmission [65, 66]. Inevitably, the AF method transmits both the desired signals and the noise. This results in an SNR loss that reduces the system performance, especially in multi-hop networks [65, 67]. However, the AF method is generally assumed to achieve a low complexity because it does not decode the signals from the source terminals, which is "non-regenerative" [65, 66]. This means that even a relay without the ability to separate the streams of multiple source terminals, can still help the communication between multiple source-destination terminal pairs. This characteristic makes the AF method a popular option for practical cooperative communications.

Decode-and-Forward (DF): In the decode-and-forward (DF) method, the relay detects and decodes the received signals from source terminals. It then retransmits the signal to the destination terminals of the transmission. Different from the AF method, this is called "regenerative" [65, 66]. The process of DF can be briefly introduced as: the received signals are decoded by multiplying by a linear receiver matrix and then re-encoded with a linear precoding matrix at the relay. The need to decode the received signals and the necessary signal processing is generally more complex than the AF method. However, the re-transmitted data is usually considered to be perfectly restored at the relay and therefore noiseless since the DF method does

not suffer from the problem of noise amplification, especially at low signal-to-noise ratios (SNRs) [65, 68, 69].

Compress-and-Forward (CF): The received signal is quantized at the relay by the compress-and-forward (CF) method and then forwarded to the destination terminal instead of decoding [65, 70]. This CF method is also called "quantize-and-forward" [65]. The CF method is the most efficient one if the source-relay and the source-destination channels are of good quality, and the relay-destination link is reliable. In this case, the relay without decoding the source signal still has an independent signal observation to give assistance to the decoding at the destination terminals [65, 70, 71].

Briefly summarized, the relay transmits the amplified received signals in the last time slot in the AF scheme. In the DF scheme, the relay decodes the received signals in one time slot and re-transmits the re-encoded signals in the next slot. In the CF scheme, the relay quantizes the received signal in one time slot and re-transmits the encoded quantized received signals in the following time slot [58]. Compared with DF and CF, AF requires minor delay and less computing power since no decoding or quantizing is applied at the relay; nevertheless, CF and DF can outperform AF in performance [58, 72]. In our Thesis, the performance of decode-and-forward relay is detailedly studied in Chapter 4 and Chapter 5.

2.5 Millimeter-Wave Channel and Antenna Array

2.5.1 Millimeter-Wave Channel Model

In addition to the channel models introduced in Chapter 2.3, we also introduce the mmWave channel model in this chapter. mmWave communications have experienced an increasing interest due to its ample frequency spectrum availability, the throughput enhancements and the potential of limited scattering [21, 73, 74]. Because of these considerations, the mmWave channel model with both LOS term and multi-path component [75, 76, 77], is math-

ematically presented as

$$\mathbf{H} = \alpha_0 \mathbf{a}_r(\theta_{r,0}, \phi_{r,0}) \mathbf{a}_t^H(\theta_{t,0}, \phi_{t,0}) + \sum_{m=1}^{N_p} \alpha_m \mathbf{a}_r(\theta_{r,m}, \phi_{r,m}) \mathbf{a}_t^H(\theta_{t,m}, \phi_{t,m}). \quad (2.46)$$

In (2.46), the first term accounts for the LOS component with α_0, the path gain. Similarly, the second term models the N_p multi-path components with standard complex Gaussian distribution path gains, α_m, $m \in [1, ..., N_p]$. Moreover, $\mathbf{a}_r(\theta_{r,m}, \phi_{r,m})$ and $\mathbf{a}_t(\theta_{t,m}, \phi_{t,m})$, $m \in [0, ..., N_p]$, are the receive and transmit array steering vectors, respectively [75, 77]. $\theta_{r,m}(\phi_{r,m})$ and $\theta_{t,m}(\phi_{t,m})$, $m \in [0, ..., N_p]$, model the elevation (azimuth) angles of arrival and departure (AoA/AoD) respectively. For ULAs, the transmit/receive steering vector can be expressed as

$$\mathbf{a}_x(\theta_{x,m}) = [1, e^{j2\pi d_x sin(\theta_{x,m})}, ..., e^{j2\pi(N_x-1)d_x sin(\theta_{x,m})}]^T, \quad (2.47)$$

where d_x, $x = t, r$, $m \in [0, ..., N_p]$, is the physical inter-antenna distance normalized by carrier wavelength. Similarly, for URAs, the transmit/receive steering vector can be modelled as

$$\mathbf{a}_x(\theta_{x,m}, \phi_{x,m}) = \Big[1, e^{j2\pi[d_x^h sin(\phi_m^r) sin(\theta_{x,m})]}, \dots, \\ e^{j2\pi[(N_x^h-1)d_x^h sin(\phi_{x,m}))sin(\theta_{x,m}))+(N_x^v-1)d_r^v sin(\theta_{x,m}))cos(\phi_{x,m}))]}\Big]^T, \quad (2.48)$$

where $N_x^h \times N_x^r = N_x$, d_x^h and d_x^v are the respective horizontal and vertical inter-antenna distance normalized by carrier wavelength, $x = t, r$, $m \in [0, ..., N_p]$.

The study of mmWave communication propagation characteristics has become more popular in the past years [73]. Due to the LOS nature of mmWave communication [75], the most significant assumption is a clear LOS path modelled by free-space conditions with no secondary wave paths caused by reflections [78, 79]. It is crucial to evaluate the role of antennas in their primary application of communication links. The basic communication link model is shown in Fig. 2.5. In general, the available received power

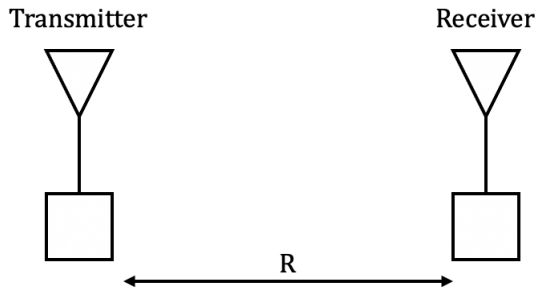

Figure 2.5: Communication Link

P_r of the communication link can be given by the Friis transmission equation [73, 78, 79, 80, 81]

$$P_r = P_t \frac{G_t G_r \lambda^2}{(4\pi\mathfrak{R})^2}, \tag{2.49}$$

where P_t is the transmit power of the antenna, G_t and G_r are the transmit and receive antenna gains, $\mathfrak{R}$ is the distance between the transmitter and receiver, and λ is the carrier wavelength. The Friis transmission equation is the basis of communication analysis in free space propagation model [73, 79], and a convenient dB-form of (2.49) can be obtained by taking 10 log of both sides:

$$\begin{aligned} P_r(\text{dBm}) = P_t(\text{dBm}) + G_t(\text{dB}) + G_r(\text{dB}) \\ - 20\log_{10}\mathfrak{R}(\text{km}) - 20\log_{10} f(\text{MHz}) - 32.44. \end{aligned} \tag{2.50}$$

The unit dBm is power in decibels above a milliwatt. Typically, the term $\frac{\lambda^2}{(4\pi\mathfrak{R})^2}$ in (2.49) is defined as free space loss to describe the quadratic attenuation growth with the mmWave frequency [78, 82]. The dB-form of free space loss is

$$L_{\text{fs}} = -20\log_{10}\mathfrak{R}(\text{km}) - 20\log_{10} f(\text{MHz}) - 32.44. \tag{2.51}$$

Consequently, from (2.51), it can be observed that if two separate systems operating at two different frequencies with the same gains are compared, the system with a lower frequency will achieve better performance.

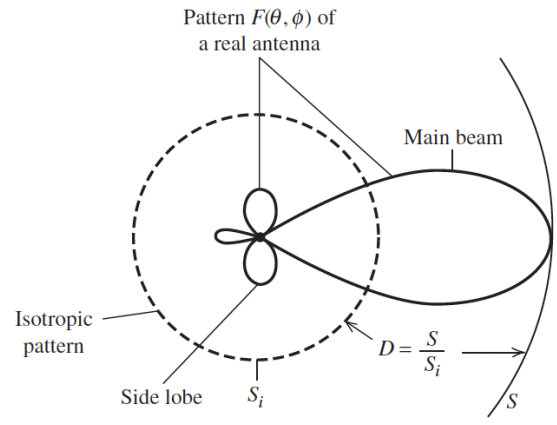

Figure 2.6: Illustration of radiation pattern $F(\theta,\phi)$ and directivity D [78]

2.5.2 Fundamentals of Antennas

2.5.2.1 Radiation Pattern

An antenna radiation pattern or antenna pattern is a mathematical function or a graphical representation of the radiation properties of the antenna as a function of directional coordinates [78, 80]. A general radiation pattern example is presented in Fig. 2.6 [78]. The radiation pattern describes the angular variation of the radiation level around an antenna, where an antenna aims to transmit, or receive signals in different desired directions [78]. The radiation pattern of an antenna may be one of its most important characteristics, and the complete pattern can be written as

$$F(\theta,\phi) = g(\theta,\phi)f(\theta,\phi). \tag{2.52}$$

where $g(\theta,\phi)$ is the element factor and $f(\theta,\phi)$ is the pattern factor, (θ,ϕ) denotes the angle coordinates. The pattern factor relies on the integral over the current and is strictly based on the current distribution. The element pattern is the pattern of an infinitesimal current element in the current distribution [78]. The descriptions of these factors are presented in the following. Formally, the directional properties of an antenna's radiation can be described by the power pattern, which is considered as another form of the radiation

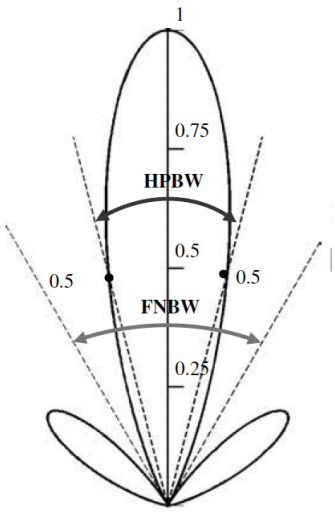

Figure 2.7: Typical radiation pattern [80]

pattern. The general power pattern is

$$P(\theta,\phi) = |F(\theta,\phi)|^2. \tag{2.53}$$

It is obvious to recognize that the radiation pattern and power pattern are the same in decibels.

$$|F(\theta,\phi)|_{dB} = 20\log|F(\theta,\phi)| = P(\theta,\phi)_{dB}. \tag{2.54}$$

2.5.2.2 Beamwidth

As shown in Fig. 2.6, various parts of a radiation pattern are considered as lobes, classified into the main, minor, side, and back lobes. A radiation lobe represents the portion of the radiation pattern bounded by comparatively weak radiation intensity regions. [78]. The main lobe is defined as the radiation lobe pointing to the maximum radiation direction.

Associated with the antenna pattern is a parameter called beamwidth. One of the most widely used beamwidths is the Half-Power Beamwidth (HPBW), which is defined as the angular separation between two points

on the opposite side of the pattern with half of the maximum value,

$$\text{HPBW} = |\theta_{\text{HPBW left}} - \theta_{\text{HPBW right}}|, \tag{2.55}$$

here $\theta_{\text{HPBW left}}$ and $\theta_{\text{HPBW right}}$ are the left and right points of the main lobe maximum for which the power pattern has a value of one-half. An example demonstrated by Fig. 2.7 [80]. Another important beamwidth is the separation between the first nulls of the pattern, namely, First-Null Beamwidth (FNBW). Both HPBW and FNBW are demonstrated in Fig. 2.7. In general, half of FNBW is used to approximate HPBW, with $FNBW \approx 2HPBW$ [80, 82]. Subsequently, a measure of the power concentration in the main lobe is the sidelobe level (SLL). SLL is defined as the ratio between the radiation pattern value of the greatest side lobe and the pattern value of the main lobe. In decibels, it is given by [78]

$$\text{SLL}_{\text{dB}} = 20\log\frac{|F(\text{greatest side lobe})|}{|F(\text{main lobe})|}. \tag{2.56}$$

2.5.2.3 Radiation Intensity

The radiation intensity as a far-field parameter, can be defined as the radiated power in a particular direction per unit of solid angle [78, 82]. Mathematically, it is expressed as

$$U(\theta,\phi) = |F(\theta,\phi)|^2, \tag{2.57}$$

where the radiation intensity unit is W/unit solid angle, the total radiated power (unit: W) is achieved by integrating the radiation intensity at all angles around the antenna. Thus, the total radiated power can be expressed as [78]

$$P_{rad} = \int_0^{2\pi}\int_0^{\pi} U(\theta,\phi)\sin(\theta)d\theta d\phi. \tag{2.58}$$

Here, $\sin(\theta)d\theta d\phi$ is the element of solid angle.

2.5.2.4 Directivity and Gain

In general, an antenna can be primarily considered as a spatial amplifier. An essential description of an antenna is the energy concentration level in one direction taking precedence over radiation in other directions, and this characteristic is directivity [78, 80]. Fig. 2.6 shows the radiation pattern of a real antenna compared to an isotropic spatial distribution.

The directivity of an antenna corresponds to the ratio between the radiation intensity in a particular direction and the average radiation intensity. The average radiation intensity is equal to the total radiated power divided by 4π, which can also be considered as the radiation intensity of an isotropic source [78, 80]. The mathematical form of directivity can be written as

$$D = \frac{U}{U_0} = \frac{4\pi U}{P_{rad}}, \tag{2.59}$$

where U is the radiation intensity of the given direction. $U_0 = \frac{P_{rad}}{4\pi}$ is the average radiation intensity. If the direction is not specified, the reference direction of the maximum radiation is taken into consideration, and the maximum directivity value will be assumed as [78, 80]

$$D_{max} = \frac{4\pi U_{max}}{P_{rad}}. \tag{2.60}$$

Here, directivity is dimensionless. A more general expression of the directivity can be expanded to include sources with radiation patterns defined in Chapter 2.5.2.1 and Chapter 2.5.2.3, which are the functions of angle coordinates (θ, ϕ). The general expression of the directivity defined in (2.59) can be rewritten as

$$D(\theta, \phi) = \frac{4\pi U(\theta, \phi)}{\int_0^{2\pi} \int_0^{\pi} U(\theta, \phi) \sin(\theta) d\theta d\phi}. \tag{2.61}$$

In general, it is desirable and convenient to express directivity in decibels (dB) instead of dimensionless quantities. The conversion of non-

dimensional directivity into decibels (dB) can be given by

$$D(dB) = 10\log_{10}[D(dimensionless)]. \tag{2.62}$$

According to the above expressions, directivity is determined by the radiation pattern of an antenna directly [78, 80, 81]. When an antenna is used in a system, we focus on the efficiency showing how much the antenna can transform the available input power into radiated power; therefore, the antenna gain is defined to indicate these directive properties. The antenna gain, also applied in the communication link by (2.50), is defined as 4π times the ratio of the radiation intensity in a given direction to the power accepted (input) by the antenna [78, 80]. In the form of an equation that is expressed as

$$\text{Gain}(\theta,\phi) = 4\pi\frac{\text{radiation intensity}}{\text{total input (accepted) power}} = 4\pi\frac{U(\theta,\phi)}{P_{in}}. \tag{2.63}$$

Here, the power accepted (input) by the antenna P_{in} is related to total radiated power P_{rad}, according to

$$P_{rad} = e_r P_{in}. \tag{2.64}$$

where $e_r \in (0.1)$ is the efficiency of the antenna radiation (dimensionless). Then, the relationship between antenna gain and directivity can be given by

$$\text{Gain}(\theta,\phi) = e_r D(\theta,\phi). \tag{2.65}$$

If the antenna is 100% efficient, namely, $e_r = 1$, we can find that the antenna directivity is equal to the antenna gain [78, 80]. Similar to (2.62), the expression to convert dimensionless gain into decibels (dB) is

$$\text{Gain}(dB) = 10\log_{10}[\text{Gain}(dimensionless)]. \tag{2.66}$$

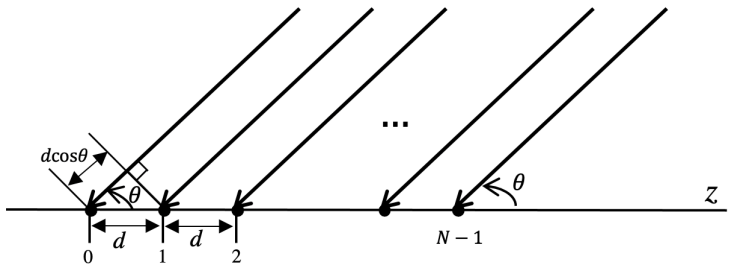

Figure 2.8: Equally spaced N-element linear array

2.5.3 Antenna Arrays

The enhancement of the single antenna-element dimensions often results in more directive characteristics. One way to achieve the dimension enlargement of the antenna without increasing the size of the individual elements is to form an assembly of radiating elements in an electrical and geometrical configuration. This new multi-element structure is referred to as the antenna array [80, 83]. Antenna arrays are popular because of the ability to shape the pattern through spacing and phase excitation adjustment, and the capability to scan the pattern by dynamically adjusting the phase excitation electronically in angular space [78].

2.5.3.1 N-Element Linear Array

Referring to the geometry of Fig. 2.8, we consider linear arrays with uniformly spaced antenna elements. We assume that all the antenna elements are isotropic and response equally in all directions to an incoming plane wave [78]. When the outputs from all receiver antenna elements are summed, the total array response depends on θ, the angle for the line of antenna elements (the Z-axis in Fig. 2.8). Additionally, we assume that all the antenna elements experience identical amplitudes, but each antenna element has a linear phase progression β. The amplitude and phase shift are used to weight the response of each antenna element. The phase of the arriving wave is set to zero at the origin for convenience. As shown in Fig. 2.8, the phase of each antenna element leads its nearest neighbor on the left by the same amount of $kd\cos\theta$ in the antenna array [78, 80, 82]. Thus, the array

factor is

$$\begin{aligned} AF &= 1 + e^{j(kd\cos\theta+\beta)} + e^{j2(kd\cos\theta+\beta)} + \ldots + e^{j(N-1)(kd\cos\theta+\beta)} \\ &= \sum_{n=1}^{N} e^{j(n-1)(kd\cos\theta+\beta)}. \end{aligned} \tag{2.67}$$

k measures the shift in phase per unit distance of wave travel. Theoretically, a wave shifts 2π radians of phase for one full cycle, namely, one wavelength, thus

$$k = \frac{2\pi}{\lambda}. \tag{2.68}$$

Therefore, it can be assumed that the maximum radiation can be directed to form a scanning array; this is called the phased (scanning) array. Generally, by tuning β, we can achieve beam steering or alignment. If the maximum radiation of the antenna array is oriented at an angle to θ_0 [78, 80], to accomplish the steering, the phase excitation β can be adjusted and expressed as

$$\beta = -kd\cos\theta_0. \tag{2.69}$$

In this case, the adjusted array factor can be given by

$$AF = \sum_{n=1}^{N} e^{j(n-1)(kd\cos\theta - kd\cos\theta_0)}. \tag{2.70}$$

As a result, the maximum radiation can be achieved in any desired direction by controlling the progressive phase difference between the antenna elements to form a phased scanning array. This is the basic principle of electronic scanning phased array operation, and can be considered as fundamentals of beam alignment in the experimental scenarios.

2.5.3.2 Multidimensional Arrays

In practice, only two-dimensional patterns can be measured; nevertheless, a collection of these can reconstruct the three-dimensional characteristics of an antenna array. In general, multidimensional arrays can be applied for scenarios requiring a narrower beam, higher gain, or main beam scanning in

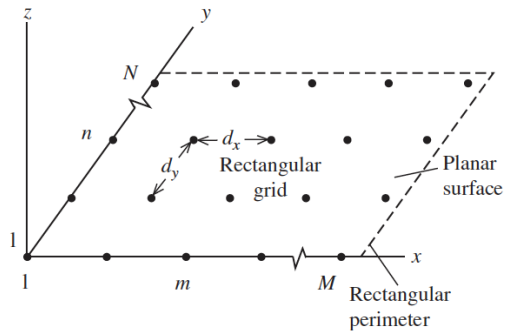

Figure 2.9: Example Planar Array [78]

desired direction [78]. First, the array factor of the $N \times M$ three-dimensional array shown in Fig. 2.9 can be expressed as [78, 83]

$$AF(\theta,\phi) = \sum_{n=1}^{N}\sum_{m=1}^{M} e^{j(k\hat{\mathbf{r}}\cdot\mathbf{r}_{mn}+\beta_{mn})}. \tag{2.71}$$

Here, $\hat{\mathbf{r}}$ is the unit vector pointing in the direction of interest [78, 82]:

$$\hat{\mathbf{r}} = \sin\theta\cos\phi\hat{\mathbf{x}} + \sin\theta\sin\phi\hat{\mathbf{y}} + \cos\theta\hat{\mathbf{z}}. \tag{2.72}$$

The antenna elements of a three-dimensional array are located with position vectors from the origin to the mn-th element,

$$\mathbf{r}_{mn} = x_{mn}\hat{\mathbf{x}} + y_{mn}\hat{\mathbf{y}} + z_{mn}\hat{\mathbf{z}}. \tag{2.73}$$

An example of a planar array, in which the antenna elements are uniformly arranged along a rectangular grid in the xy-plane, is displayed in Fig. 2.9 [78, 82]. The array factor follows (2.71), can be expressed as

$$AF(\theta,\phi) = \sum_{n=1}^{N}\sum_{m=1}^{M} e^{jk(x_{mn}\sin\theta\cos\phi + y_{mn}\sin\theta\sin\phi+\beta)}, \tag{2.74}$$

where $\beta = -x_{mn}\sin\theta_0\cos\phi_0 - y_{mn}\sin\theta_0\sin\phi_0$ is the phase excitation to achieve the maximum radiation direction (θ_0,ϕ_0) derived from (2.69). Similarly, the array factor of planar arrays in other planes can be directly derived from

above-mentioned equations.

Based on the above-mentioned introduction, we have defined the radiation pattern of a single antenna as a product of an element factor and a pattern factor in (2.52). For the antenna array, we can expand this concept and obtain the complete array pattern by pattern multiplication as the product of the element pattern and the array factor [78, 80, 82]. Then the mathematical calculation of characteristics including but not limited to radiation intensity, directivity and antenna gain for antenna arrays can be achieved by (2.52)-(2.66) in Chapter 2.5.1 straightforwardly.

Chapter 3

Large Scale Antenna Systems: Partial Channel State Information

This chapter is based on our works published in [J1].

3.1 Introduction

In this chapter, we focus on a low-complexity approach in the physically constrained massive MIMO systems with user mobility. This is inspired by the concern that when employing large-scale antenna arrays in confined physical spaces with user mobility, the spatial correlation due to insufficient inter-antenna distance and the temporal correlation due to user mobility become determinants for the resulting performance [17, 84, 85]. Recent studies have shown that these correlations can be exploited. For instance, temporal channel correlation and the detected data symbols can be leveraged in time division duplex (TDD) massive MIMO systems to address pilot contamination [84]. The spatial correlation between antennas is employed to optimize the CSI acquisition stage in frequency division duplex (FDD) systems [86]. Moreover, the spatial correlation in TDD massive MIMO systems can achieve mean square error (MSE) enhancement while reducing the overall; this gives rise to the requirement for developing a robust interference management technique to avoid the spectral efficiency (SE) degradation [87]. In this case, the joint spatial-temporal correlation scenario introduces an open

question of the trade-off between correlations and achievable sum rate in massive MIMO systems [88].

The effect of nonisotropic scattering and user mobility on channel capacity is studied in [89]. Measured results with moderate user mobility in a line-of-sight (LOS) scenario are presented in [90]. Most relevant to this chapter, space-constrained antenna deployments are studied in [56, 76]. Similarly, low-complexity strategies to preserve the performance of space-constrained massive MIMO are presented in [17, 34, 91].

This chapter proposes to exploit temporal and spatial correlation jointly for size-constrained massive MIMO base stations (BSs). Specifically, instantaneous CSI is acquired for a subset of BS antennas and time frames. For those antennas without CSI, channel estimates are obtained by exploiting spatial correlation among adjacent antennas. For those frames without an explicit CSI acquisition phase, the channel coefficients are estimated from the CSI previously available by exploiting the channel's temporal correlation related to user mobility. This chapter therefore extends the study of [17] where only spatial correlation is exploited in scenarios without user mobility. Our strategy leads to reduced complexity for CSI acquisition, at the expense of CSI quality and the resulting performance. Accordingly, we study the channel estimation error introduced by the proposed approach with respect to the perfect and frequent CSI acquisition. In this setting, our work shows an overall favourable trade-off for the proposed strategy with partial CSI.

3.2 System Model and Partial CSI Acquisition

We begin with the description of the system model, followed by the introduction of the partial CSI acquisition.

3.2.1 Physically-constrained Channel Model

We consider a general massive MIMO system with N_t antennas at the BS and N_r single-antenna users ($N_t \geq N_r$). The BS antennas are arranged in a uniform rectangular array (URA) topology. As shown in Fig. 3.1, N_h and N_v

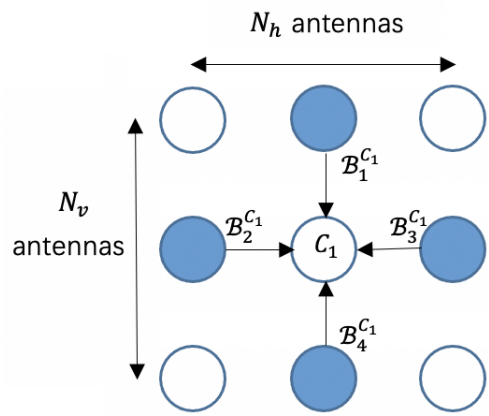

Figure 3.1: Example CSI distribution pattern for a URA with $N_t = 9$, $N_c = 4$. Colored and white elements represent antennas with and without CSI acquisition respectively.

denote the number of antennas deployed horizontally and vertically respectively with $N_t = N_h \times N_v$. Similar to (2.1), the signal received during downlink transmission at the k-th user is given by [17]

$$\mathrm{y}_k = \sqrt{\rho_{\mathrm{f}}}\mathbf{h}_k\mathbf{x} + n_k, \tag{3.1}$$

where $\mathbf{x} \in \mathbb{C}^{N_t \times 1}$ represents the transmitted symbols from the BS, $\mathbf{h}_k \in \mathbb{C}^{1 \times N_t}$ denotes the k-th row of the downlink communication channel matrix $\mathbf{H} \in \mathbb{C}^{N_r \times N_t}$ from the BS to the k-th user, ρ_{f} denotes the SNR, and $n_k \sim \mathbb{CN}(0, 1)$ is the standard additive white Gaussian noise. The transmit signal can be further decomposed as $\mathbf{x} = w \cdot \mathbf{Fs}$, where $\mathbf{s} \in \mathbb{C}^{N_r \times 1}$ denotes the conveyed user symbols, $\mathbf{F} \in \mathbb{C}^{N_t \times N_r}$ represents a linear precoding matrix, and $w = 1/\sqrt{\{\mathrm{Tr}[\mathbf{FF}^{\mathrm{H}}]\}}$ is a normalization constant guaranteeing the average transmission power $P_t = \mathbb{E}\{\mathbf{x}^{\mathrm{H}}\mathbf{x}\} = 1$. In the following, we concentrate on zero-forcing (ZF) precoding for which

$$\mathbf{F} = \widetilde{\mathbf{H}}^{\mathrm{H}}(\widetilde{\mathbf{H}}\widetilde{\mathbf{H}}^{\mathrm{H}})^{-\mathbf{1}}, \tag{3.2}$$

where $\widetilde{\mathbf{H}}$ represents the downlink channel estimate. In this chapter, we consider that the BS has to be deployed in a confined physical space and assume

an impedance matching network that resolves any mutual coupling effects at the transmitter [92]. Thus, by particularizing (2.36), the downlink propagation channel to k-th user is modeled as [49, 76]

$$\mathbf{h}_k = \mathbf{g}_k \mathbf{A}_k, \tag{3.3}$$

where $\mathbf{g}_k \sim \mathbb{CN}(0, \mathbf{I}_{L_k})$, L_k denotes the number of signal propagation paths with different angles of departure. For simplicity, $L_k = L$, $k = 1, ..., N_r$, is assumed. $\mathbf{A}_k \in \mathbb{C}^{L \times N_t}$ is the transmit steering matrix of the k-th user given by [17, 34]

$$\mathbf{A}_k = \frac{1}{\sqrt{L}} [\mathbf{a}^{\mathrm{T}}(\theta_{k,1}, \phi_{k,1}), ..., \mathbf{a}^{\mathrm{T}}(\theta_{k,L}, \phi_{k,L})]^{\mathrm{T}}. \tag{3.4}$$

Here, $\theta_{k,i}$ and $\phi_{k,i}$ represent the elevation and azimuth angles describing the directions of departure respectively. The steering vectors $\mathbf{a}$ for the URA topology adopt the form [56, 93]

$$\begin{aligned} \mathbf{a}(\theta_{k,i}, \phi_{k,i}) = [1, e^{j2\pi[d_h sin(\theta_{k,i}) sin(\phi_{k,i})]}, ..., \\ e^{j2\pi[(N_h-1)d_h sin(\theta_{k,i}) sin(\phi_{k,i}) + (N_v-1)d_v sin(\theta_{k,i}) cos(\phi_{k,i})]}], \end{aligned} \tag{3.5}$$

where d_h and d_v represent the horizontal and vertical inter-antenna spacing normalized by the carrier wavelength λ respectively. Note that, receive correlation is not considered, since the inter-user spacing is significantly greater than λ [34].

We further consider a model accounting for the temporal correlation among the channels of adjacent frames with user mobility. Let l represent the index of the frame sample with CSI collection. In the following we adopt the autoregressive model AR(1) for temporal correlation studied in [94]. The actual channel for the $(l+1)$-th frame without pilot training stage for CSI acquisition can be expressed as [94, 95]

$$\mathbf{H}_{l+1} = \rho \mathbf{H}_l + \sqrt{1 - \rho^2} \cdot \mathbf{E}, \tag{3.6}$$

where ρ represents the correlation coefficient computed by the zeroth-order Bessel function of the first kind $\rho = J_0(2\pi f_d t)$ with t, the time interval and Doppler spread $f_d = f_c \frac{v}{c}$. Here, f_c is the carrier frequency, v is the user speed and c is the speed of light [94, 96]. Moreover, the rows of $\mathbf{E} \in \mathbb{C}^{N_r \times N_t}$ is expressed as $\mathbf{e}_k = \mathbf{z}_k \mathbf{A}_k$, where $\mathbf{z}_k \sim \mathbb{CN}(0, \mathbf{I}_L)$ is uncorrelated with $\mathbf{g}_k$, $k = 1, ..., N_r$ [94].

3.2.2 Distribution of the CSI Acquisition

The presence of temporal correlation between transmitted frames for low and moderate user velocities motivates us to consider the probability of collecting CSI for only a subset of frames. We employ antenna activation pattern such as the one studied in detail in [17] to distribute the CSI. We only consider an elementary example, as shown in Fig. 3.1 for a model with 3×3 URA. Here, the $N_c = 4$ active antennas are denoted by the shaded elements.

More generally, in this chapter, we study a model comprised of N_{total} frames. In this system, CSI is acquired in a subset $N_a \leq N_{\text{total}}$ of these frames and solely for a reduced number $N_c \leq N_t$ of antennas. The CSI distribution pattern in Fig. 3.1 is employed for N_a frames with CSI. To prevent extensive repetition, the systematic study of the antenna activation patterns is shown by leaning on the general case from [17]. First, let $\mathscr{B}$ and $\mathscr{C}$ denote the subsets of indices for active and inactive antennas during the CSI acquisition stage respectively. The channel estimate for active antennas in $\mathscr{B}$ is

$$\widetilde{\mathbf{h}}_k|_{[\mathscr{B}]} = \left(\sqrt{1 - \tau_k^2} \mathbf{h}_k + \tau_k \mathbf{q}_k \mathbf{A}_k \right) \Big|_{[\mathscr{B}]}, \tag{3.7}$$

where $\tau_k \in [0, 1]$ models the quality of acquired CSI, $\mathbf{q}_k \sim \mathbb{CN}(0, \mathbf{I}_L)$ is uncorrelated with $\mathbf{g}_k$ [17, 76]. The CSI of inactive antennas in $\mathscr{C}$ is obtained by averaging the CSI of adjacent active antennas

$$\widetilde{\mathbf{h}}_{k,\mathscr{C}_n} = \frac{1}{N_{\mathscr{C}_n}} \sum_{i \in N_{\mathscr{C}_n}} \widetilde{\mathbf{h}}_{k,\mathscr{B}_i^{\mathscr{C}_n}}. \tag{3.8}$$

where $N_{\mathscr{C}_n}$ represents the number of antennas with available CSI that are used to approximate the CSI of a specific antenna $\mathscr{C}_n$. Intuitively, the CSI of the $\mathscr{C}_n$-th antenna is computed through an average of the CSI from its closest antennas, $B_i^{\mathscr{C}_n}$. An example of the distribution is shown in Fig. 3.1. This approach has been selected for its low computational complexity, as analyzed in Chapter 3.3.2. Note that (3.7)-(3.8) are used to estimate the channel during N_a frames with CSI, while the channel estimates of other frames are obtained by using the previous CSI. For completeness, the pseudocode of the frame distribution algorithm with the computation of estimated channels following (3.7)-(3.8) is presented in Algorithm 3.1.

Algorithm 3.1 Pseudocode of the frame distribution algorithm

1: **input** : N_{total}, N_a
2: **output** : N_{active}, $\widetilde{\mathbf{H}}_l$
3: $N_{\text{active}} = \text{zeros}\ (1, N_{\text{total}})$ (Initialization)
4: $\lceil N_{\text{total}}/N_a \rceil = N_g \leftarrow$ { The largest interval between adjacent frames with CSI acquisition, which are equally spaced }
5: { ***First stage***: The distribution of the first $N_a \leq 0.5N_{\text{total}}$ frames where CSI is acquired }
6: **for** $i = 1 : N_g : N_{\text{total}}$ **do**
7: $\quad N_{\text{active}}(1, i) = 1 \leftarrow$ { To equally space the frames to acquire CSI from the first transmitted frame }
8: **end for**
9: { ***Second stage***: When $N_a > 0.5N_{\text{total}}$, the distribution of the rest $(N_a - \lceil 0.5N_{\text{total}} \rceil)$ frames where CSI is acquired }
10: **if** $N_a > 0.5N_{\text{total}}$ **then**
11: $\quad a = 2 : N_g : N_{\text{total}}$;
12: $\quad$ **for** $j = 1 \rightarrow (N_a - \lceil N_{\text{total}}/N_g \rceil)$ **do**
13: $\quad\quad N_{\text{active}}(1, a(j)) = 1 \leftarrow$ { To equally space the rest $(N_a - \lceil 0.5N_{\text{total}} \rceil)$ frames with CSI acquisition }
14: $\quad$ **end for**
15: **end if**
16: { 17 – 23: The channel estimate for each frame }
17: **for** $l = 1 \rightarrow N_{\text{total}}$ **do**
18: $\quad$ **if** $N_{\text{active}}(1, l) == 1$ **then**
19: $\quad\quad \widetilde{\mathbf{H}}_l \leftarrow$ { Channel estimate following Eq. (3.7)-(3.8) }
20: $\quad$ **else**
21: $\quad\quad \widetilde{\mathbf{H}}_l = \widetilde{\mathbf{H}}_{l-1}$;
22: $\quad$ **end if**
23: **end for**

3.3 System Performance Analysis

3.3.1 Channel Estimation Error under Partial CSI

We concentrate on the channel estimation error introduced by the proposed strategy in this chapter. The channel estimation error $\widehat{\mathbf{h}}_k$ for the k-th user in a frame duration is given by

$$\widehat{\mathbf{h}}_k = \mathbf{h}_k - \widetilde{\mathbf{h}}_k. \tag{3.9}$$

In the following we use the mean square error (MSE) to calculate the channel estimation error factor of the l-th frame, which is given by [17]

$$\delta_k^l = \frac{\mathbb{E}\left\{\|\widehat{\mathbf{h}}_k\|_2^2\right\}}{\mathbb{E}\left\{\|\mathbf{h}_k\|_2^2\right\}} = \frac{\mathbb{E}\left\{\|\mathbf{h}_k - \widetilde{\mathbf{h}}_k\|_2^2\right\}}{\mathbb{E}\left\{\|\mathbf{h}_k\|_2^2\right\}}, \tag{3.10}$$

According to Chapter 3.2, the distribution of frames with CSI acquisition are defined by Algorithm 3.1. If the index of the frame with CSI is l, the indices of following frames without CSI can be $[l+1, l+2, ..., l+m]$. In view of the analysis in [17], in this chapter, the channel estimation error factor generated by the proposed strategy with temporal correlation for the k-th user in the $(l+m)$-th frame is defined in the following. First, δ_k^{l+m} following (3.10) can be decomposed as

$$\delta_k^{l+m} = \frac{\mathbb{E}\left\{\sum_{n\in\mathscr{B}} |\widehat{\mathrm{h}}_{k,n}^{l+m}|^2 + \sum_{n\in\mathscr{C}} |\widehat{\mathrm{h}}_{k,n}^{l+m}|^2\right\}}{\mathbb{E}\left\{\sum_{N_t} |\mathrm{h}_{k,n}^{l+m}|^2\right\}}, \tag{3.11}$$

where $\widehat{\mathrm{h}}_{k,n}^{l+m}$ is the channel estimation error from the n-th BS antenna to the k-th user in the $(l+m)$-th frame. Following the physical channel model defined in (3.3), we have $\mathbb{E}\left\{\sum_{N_t} |\mathrm{h}_{k,n}|^2\right\} = N_t$ and $\mathbb{E}\left\{|\widehat{\mathrm{h}}_{k,n}|^2\right\} = \mathrm{var}\,(\widehat{\mathrm{h}}_{k,n})$. Therefore, in (3.11), the factors in the first part involving the subset $\mathscr{B}$ of active antennas

in the l-th frame referring to (3.6) can be expressed as

$$\begin{aligned}
&\mathbb{E}\left\{|\widehat{\mathrm{h}}_{k,n}^{l+m}|^2\right\} = \mathbb{E}\left\{|\mathrm{h}_{k,n}^{l+m} - \widetilde{\mathrm{h}}_{k,n}^{l+m}|^2\right\} \\
&= \mathbb{E}\Bigg\{\Big|\rho^{l+m-1}\mathrm{h}_{k,n} + \frac{(1-\rho^{l+m-1})\sqrt{1-\rho^2}}{1-\rho}\mathrm{e}_{k,n} - \rho^{l-1}\sqrt{1-\tau_k^2}\cdot\mathrm{h}_{k,n} \\
&- \frac{(1-\rho^{l-1})\sqrt{1-\rho^2}\sqrt{1-\tau_k^2}}{1-\rho}\mathrm{e}_{k,n} - \tau_k\mathbf{q}_k\mathbf{A}_k|_{[n]}\Big|^2\Bigg\}, n \in \mathscr{B},
\end{aligned} \tag{3.12}$$

Here, $e_{k,n} = \mathbf{z}_k\mathbf{A}_k|_{[n]}$, where $\mathbf{z}_k\mathbf{A}_k$ represents the vectors of $\mathbf{E}$ defined in Chapter 3.2.1. The computation of $\widetilde{\mathrm{h}}_{k,n}|_{[\mathscr{B}]}$ for active antennas in the l-th frame follows (3.7). For the second part with the subset $\mathscr{C}$ of inactive antennas in (3.11), the factors introduced by averaging approach and partial channel estimate can be computed as

$$\begin{aligned}
&\mathrm{var}\left(\widehat{\mathrm{h}}_{k,n}^{l+m}\right) = \mathrm{var}\left(\mathrm{h}_{k,n}^{l+m} - \frac{1}{N_n}\sum_{i=1}^{N_n}\widetilde{\mathrm{h}}_{k,\mathscr{B}_i^n}^{l+m}\right) \\
&= \mathrm{var}\Bigg(\rho^{l+m-1}\mathrm{h}_{k,n} + \frac{(1-\rho^{l+m-1})\sqrt{1-\rho^2}}{1-\rho}e_{k,n} \\
&- \frac{1}{N_n}\sum_{i=1}^{N_n}\Big[\rho^{l-1}\sqrt{1-\tau_k^2}\cdot\mathrm{h}_{k,\mathscr{B}_i^n} + \frac{(1-\rho^{l-1})\sqrt{1-\rho^2}\sqrt{1-\tau_k^2}}{1-\rho}\mathrm{e}_{k,\mathscr{B}_i^n} \\
&+ \tau_k\mathbf{q}_k\mathbf{A}_k|_{[\mathscr{B}_i^n]}\Big]\Bigg), n \in \mathscr{C},
\end{aligned} \tag{3.13}$$

where $\frac{1}{N_n}\sum_{i=1}^{N_n}\widetilde{\mathrm{h}}_{k,\mathscr{B}_i^n}$ computes the channel estimate for inactive antennas in l-th frame with CSI following (3.7)-(3.8). Based on the above-mentioned expressions, the channel estimation error factor for $(l+m)$-th frame can be

given by

$$\delta_k^{l+m} = \frac{1}{\sum_{n=1}^{N_t}\left[\rho^{2(l+m-1)} + (\frac{(1-\rho^{l+m-1})\sqrt{1-\rho^2}}{1-\rho})^2\right]\Theta_k|_{[n,n]}} \times \Bigg\{ \sum_{n\in\mathscr{B}} \Bigg[\Big(\rho^{l-1}(\rho^m - \sqrt{1-\tau_k^2})\Big)^2$$
$$+ \Big(\frac{[(1-\rho^{l+m-1}) - (1-\rho^{l-1})\sqrt{1-\tau_k^2}]\sqrt{1-\rho^2}}{1-\rho}\Big)^2 + \tau_k^2\Bigg]\Theta_k|_{[n,n]}$$
$$+ \sum_{n\in\mathscr{C}} \Bigg[\Big(\rho^{2(l+m-1)} + (\frac{(1-\rho^{l+m-1})\sqrt{1-\rho^2}}{1-\rho})^2\Big)\Theta_k|_{[n,n]}$$
$$+ \frac{1}{N_n^2}\sum_{i\in\mathscr{B}^n}\Big[(\rho^{l-1}\sqrt{1-\tau_k^2})^2 + (\frac{(1-\rho^{l-1})\sqrt{1-\rho^2}\sqrt{1-\tau_k^2}}{1-\rho})^2 + \tau_k^2\Big]\Theta_k|_{[i,i]}$$
$$- \frac{2\sqrt{1-\tau_k^2}}{N_n}\mathrm{Re}\Bigg(\sum_{i\in\mathscr{B}^n}\Big[\rho^{2l+m-2} + \frac{(1-\rho^{l+m-1})(1-\rho^{l-1})(1-\rho^2)}{(1-\rho)^2}\Big]\Theta_k|_{[n,i]}\Bigg)$$
$$+ \frac{2}{N_n^2}\mathrm{Re}\Bigg(\sum_{i,j\in\mathscr{B}^n, i>j}\Big[(\rho^{l-1}\sqrt{1-\tau_k^2})^2 + (\frac{(1-\rho^{l-1})\sqrt{1-\rho^2}\sqrt{1-\tau_k^2}}{1-\rho})^2 + \tau_k^2\Big]\Theta_k|_{[j,i]}\Bigg)\Bigg]\Bigg\}. \tag{3.14}$$

In (3.14), $\Theta_k = \mathbb{E}\left\{\mathbf{h}_k^{\mathrm{H}}\mathbf{h}_k\right\} = \mathbf{A}_k^{\mathrm{H}}\mathbf{A}_k$ is the channel correlation matrix of k-th user. Meanwhile, $\mathscr{B}^n$ and N_n denote the indices and the number of adjacent antennas for CSI computation of n-th antenna respectively. m can be considered as the index of frame without CSI when l-th frame with CSI is set to be initial. When $m = 0$, channel estimation error factor for the l-th frame with CSI acquisition can be obtained. In the proposed N_{total}-frame model, each frame has its own δ_k^l for k-th user; therefore, the average channel estimation error factor for k-th user is computed as

$$\overline{\delta}_k = \frac{1}{N_{\text{total}}}\sum\nolimits_{l=1}^{N_{\text{total}}}\delta_k^l. \tag{3.15}$$

3.3.2 Complexity Analysis

In this sub-chapter, the signal processing complexity of the proposed strategy is studied, while the proposed technique could also be applied to massive MIMO systems operating in FDD; nevertheless, in the following, we focus on the more practical TDD systems [9]. The global complexity is com-

puted based on the three phases of TDD communication system, including CSI acquisition, downlink transmission and uplink reception following the analysis in [17, 97].

The complexity for each phase is shown in Table 3.1 [17, 97], where η_{tr}, η_{dl} and η_{ul} represent the time resources allocated to each phase respectively. The process of generating the channel estimate from the received pilot signals determines the complexity C^{tr} during the CSI acquisition stage [97]. The downlink stage comprising the precoding matrix and transmit signals generator results in the complexity

$$C^{\text{d}} = C^{\text{d}}_{\text{inv}} + C^{\text{d}}_{\text{d}}, \tag{3.16}$$

where $C^{\text{d}}_{\text{inv}}$ accounts for computing the ZF precoding matrix, whereas C^{d}_{d} accounts for computing precoded signals obtained via the strategy studied in [17, 97]. In TDD systems, the uplink detection matrix can be obtained at no cost due to channel reciprocity, and C^{u} stands for the operations related to data reception [17].

For the proposed temporally-spatially correlated channel model, only N_a frames perform the pilot correlation process during the CSI acquisition stage. The remaining frames only implement data transmission and reception using previous CSI. Therefore, the complexity for frames where CSI is acquired can be expressed as

$$C^{A}_{\text{total}} = C^{\text{tr}} + C^{\text{d}} + C^{\text{u}}. \tag{3.17}$$

Instead, for the rest of the frames we have

$$C^{I}_{\text{total}} = C^{\text{d}} + C^{\text{u}}. \tag{3.18}$$

Accordingly, the average total complexity per frame in the N_{total}-frame model

can be expressed as

$$\overline{C}_{\text{total}} = \frac{1}{N_{\text{total}}}\left[N_a \cdot C^A_{\text{total}} + (N_{\text{total}} - N_a) \cdot C^I_{\text{total}}\right]. \tag{3.19}$$

3.3.3 Achievable Ergodic Rates and Energy Efficiency

In this sub-chapter, the effects of partial CSI acquisition on the ergodic sum rate (spectral efficiency) and energy efficiency of the massive MIMO system are studied.

3.3.3.1 Ergodic Downlink Sum Rates

The downlink ergodic sum rates of the communication system for the l-th frame can be defined as

$$\mathrm{R}^l_{\text{sum}} = \eta_{\text{dl}}/\eta_{\text{coh}} \cdot B \sum_{k=1}^{N_r} \log_2(1+\gamma^l_k), \tag{3.20}$$

where η_{coh} is the number of coherence symbols of the channel, and $\eta_{\text{dl}}/\eta_{\text{coh}}$ represents the proportion of the time allocated to downlink transmission. B denotes the system bandwidth, and S^l_k refers to the spectral efficiency of k-th user in l-th frame, can be given by

$$S^l_k = \log_2(1+\gamma^l_k). \tag{3.21}$$

Communication Phase	*Complexity in flops*
CSI acquisition phase (only for N_a frames)	$C^{\text{tr}} = 8N_cN_r\eta_{\text{tr}} = 8N_cN_r^2$
Downlink phase – Signal generation – Precoding matrix	$C^{\text{d}} = C^{\text{d}}_{\text{inv}} + C^{\text{d}}_{\text{d}}$ $C^{\text{d}}_{\text{d}} = 8N_cN_r\eta_{\text{dl}}$ $C^{\text{d}}_{\text{inv}} = \left(24N_r^3 + 16N_r^2N_t\right) + N_r + \left(2N_rN_t + 8N_r^2N_t\right)$
Uplink phase	$C^{\text{u}} = 8N_tN_r\eta_{\text{ul}}$

Table 3.1: Computational complexity (flops) at the Base Station

Moreover, γ_k^l stands for the associated SINR [17]

$$\gamma_k^l = \frac{w^2 |\,\mathbb{E}\left\{\mathbf{h}_k^{\mathrm{H}}\mathbf{f}_k\right\}|^2}{\frac{1}{\rho_{\mathrm{f}}} + w^2 \mathrm{var}\left(\mathbf{h}_k^{\mathrm{H}}\mathbf{f}_k\right) + w^2 \sum_{i\neq k} \mathbb{E}\left\{|\mathbf{h}_k^{\mathrm{H}}\mathbf{f}_i|^2\right\}}, \tag{3.22}$$

where $\mathbf{f}_k$ is the k-th column of the precoding matrix defined in Chapter 3.2, which follows (3.2), (3.6)-(3.8) for the examined l-th frame. Moreover, for the proposed N_{total}-frame model, the average spectral efficiency achievable for each user in each frame can be computed as

$$\overline{S}_k = \frac{1}{N_{\mathrm{total}}} \sum\nolimits_{l=1}^{N_{\mathrm{total}}} \{\frac{1}{N_r} \sum\nolimits_{k=1}^{N_r} S_k^l\}. \tag{3.23}$$

3.3.3.2 Energy Efficiency

The resulting energy efficiency for downlink transmission in the l-th frame is given as [42]

$$\varepsilon_l = \frac{R_{\mathrm{sum}}^l}{P_{\mathrm{tot}}}, \tag{3.24}$$

where P_{tot} represents the total power consumption during the transmission referring to (2.15). All power consumption terms are following (2.16)-(2.18). Moreover, in the power consumption term P_{BB}, C, the number of real floating point operations per second, is determined by (3.17)-(3.18) for frames with and without CSI acquisition, respectively [17, 42]. Therefore, considering the computational complexity, the total transmission power consumption P_{tot} can be further decomposed as

$$P_{\mathrm{tot}} = \begin{cases} P_{\mathrm{tot}}^A & \propto C_{\mathrm{total}}^A \text{ for frames with CSI,} \\ P_{\mathrm{tot}}^I & \propto C_{\mathrm{total}}^I \text{ for frames without CSI.} \end{cases} \tag{3.25}$$

For the N_{total}-frame model, each frame displays different energy efficiency due to varying complexity and channel estimate. The resulting energy effi-

ciency ε_l for the l-th frame can be re-expressed as

$$\varepsilon_l = \begin{cases} R^l_{\text{sum}}/P^A_{\text{tot}}, & \text{if the } l\text{-th frame is with CSI,} \\ R^l_{\text{sum}}/P^I_{\text{tot}}, & \text{if the } l\text{-th frame is without CSI.} \end{cases} \tag{3.26}$$

Accordingly, the average energy efficiency per frame in the N_{total}-frame model can be obtained by

$$\overline{\varepsilon} = \frac{1}{N_{\text{total}}} \sum\nolimits_{l=1}^{N_{\text{total}}} \varepsilon_l. \tag{3.27}$$

3.4 Simulation Results

We compare our approach to full CSI based on numerical results, for a common massive MIMO scenario with $N_t = 144$, $N_r = 12$, $L = 50$, and varying number of active antennas N_c [17]. The angle spread of the azimuth and elevation angles is fixed to be $\pi/5$ and π respectively [80]. Imperfect CSI estimation parameter is considered with $\tau_k = 0.1$. In previous studies [17], when inter-antenna spacing is smaller than a wavelength, the system is correlated. In order to study the role of high correlations, the inter-antenna spacing in our study is fixed to $d_v = d_h = 0.3\lambda$. Moreover the total system bandwidth is $B = 20$ MHz, which is a normal bandwidth in massive MIMO systems. The standard Long-term evolution (LTE) frame with a time duration of 10 ms containing 140 orthogonal frequency-division multiplexing (OFDM) symbols in total ($\eta_{\text{coh}} = 140$) is considered, where 70% symbols are assigned to downlink transmission [17]. We assume that the channel matrix stays constant for the frame duration with the time interval $t = 1$ ms [94], and consider a carrier frequency of $f_c = 2.5$GHz. The total number of LTE frames examined for the temporal correlated model is $N_{\text{total}} = 10$. We consider a femtocell base station for defining the power consumption parameters [17].

The evolution of average channel estimation error factor per user per frame $\overline{\delta}_k$ for varying number of frames with CSI is shown in Fig. 3.2 (a) for

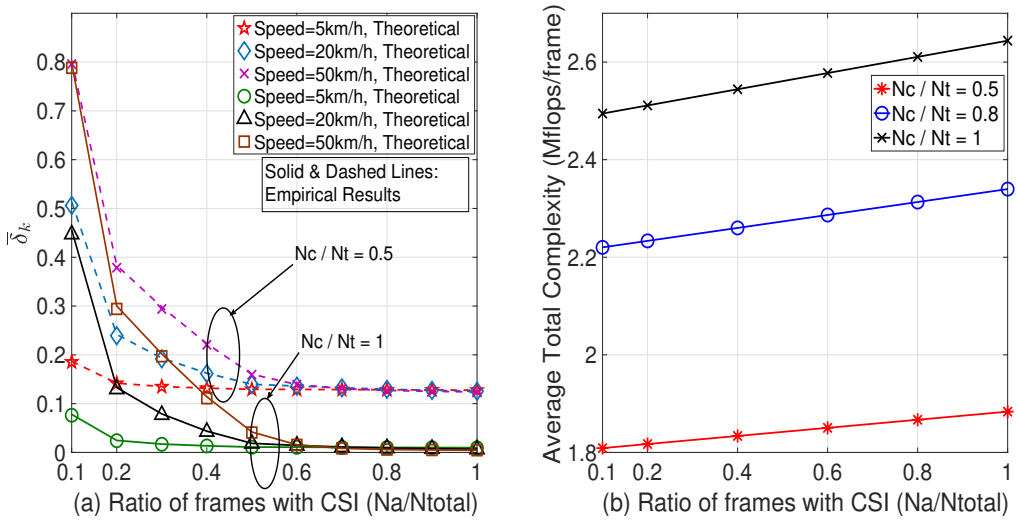

Figure 3.2: Average (a) channel estimation error factor per user per frame $\overline{\delta}_k$ and (b) total complexity per frame with increasing N_a. $\eta_{\text{coh}} = 140$, $\eta_{\text{tr}} = N_r = 12$, $\eta_{\text{dl}} = 7 \times 14$ per frame. SNR =15 dB.

three scenarios with user velocities of 5, 20, and 50 km/h. The results of this figure corroborate the intuition that the channel estimation error factor increases with user mobility. Moreover, a close match between the theoretical error (markers) following (3.14) and the empirical error (solid and dashed lines) can be observed. Fig. 3.2 (a) also shows that in most cases the channel estimation error becomes significant for $N_a/N_{\text{total}} \leq 1/2$ since CSI becomes highly outdated. The average total complexity per frame following (3.19) can be observed in Fig. 3.2 (b), for increasing number N_a of frames with CSI. By employing the proposed approach, complexity savings can be further achieved when both spatial and temporal correlations are jointly exploited with smaller number of active antennas N_c and frames N_a dedicated to CSI acquisition.

The effect of N_a on the average spectral efficiency per user per frame is shown in Fig. 3.3 (a). The results of this figure show that an increasing number of frames with CSI is required when the user velocity increases, which results in diminishing temporal correlation, to reach the performance obtained when $N_a = N_{\text{total}}$. Still, for low and moderate user velocities, close to optimal SE can be obtained with a reduced N_a. The benefits of acquiring CSI

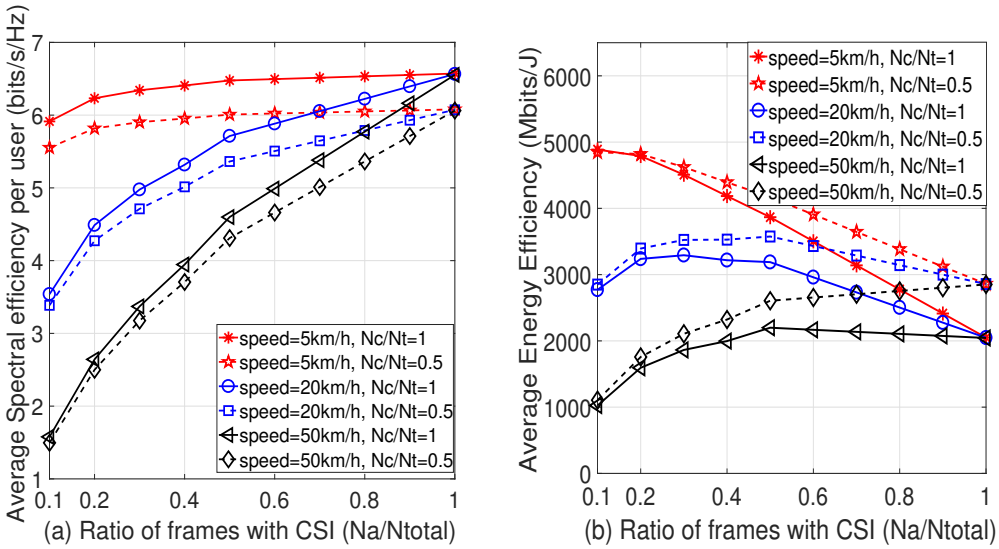

Figure 3.3: Average (a) spectral efficiency per user per frame and (b) energy efficiency per frame with increasing N_a for a femtocell scenario and varying user velocity. SNR =15 dB.

for a subset of time frames and antennas are further highlighted in Fig. 3.3 (b), where the energy efficiency is shown for increasing N_a. We note that the EE captures the trade-off between SE performance and complexity. Fig. 3.3 (b) shows that reducing the number of frames with CSI can be beneficial to EE for low and moderate user velocities. Especially, when $v = 20\,\text{km/h}$, the EE of the massive MIMO system considered can be maximized when $N_a \approx 0.5N_{\text{total}}$ and $N_c = 0.5N_t$, while even smaller N_a is optimal for lower mobility. Clearly, this shows that joint spatial-temporal correlation is beneficial to the EE performance and this occurs because the reduced power consumption in the RF chains compensates for the loss in the achievable data rates.

3.5 Conclusions

In this chapter, we have proposed a CSI acquisition model making use of temporal and spatial correlations for size-constrained massive MIMO systems with user mobility. We exploit partial CSI acquisition and obtain significant complexity and power consumption gains. The numerical results presented in this chapter demonstrate that the proposed scheme exploiting the spatial and temporal correlations jointly can achieve an energy efficiency

enhancement while preserving the performance of size-constrained massive MIMO systems with complete CSI, especially for low and moderate user mobility scenarios.

Chapter 4

Energy Efficient Multi-Pair Two-Way Relaying System

This chapter is based on our works published in [J2].

4.1 Introduction

Inspired by the potential of relay-aided systems to compensate for fading and path loss, we investigate a multi-pair two-way massive MIMO relaying system in this chapter. In general, the application of massive MIMO techniques in a multi-pair relaying system, where users can exchange information via a shared relay, has attracted great attention due to the potential of improving the network capacity, cellular coverage, system throughput, and enhancing the service quality for cell edge users [98, 99]. Moreover, by deploying a large number of antennas at the relay, the spatial diversity can be amplified while boosting the achievable performance [9]. Initially, one-way relaying systems were studied for multi-pair massive MIMO relaying. For amplify-and-forward (AF) protocol, the power control problem was studied in [100]. In addition, for decode-and-forward (DF) protocol, the comparison of the achievable SE with different linear processing methods has been studied in [99], while [101] has investigated the outage performance of one-way DF relaying. However, one-way relaying might incur spectral efficiency (SE) loss [102, 103]. In order to reduce the SE loss, two-way relaying is introduced

to improve the SE and extend the communication range while enabling bidirectional communication [104, 105, 106]. Theoretically, in two-way relaying systems, user pairs can exchange information via a shared relay in only two time slots, and the required time is much shorter than that in one-way relaying system [62, 107]. To this end, multi-pair two-way relaying with massive arrays has been widely studied in previous studies, where more than one pair of users can be served to exchange information [104, 108].

Normally, the AF protocol is investigated in most studies of multi-pair two-way massive MIMO relaying, while the DF protocol is typically overlooked. However, the AF relaying might suffer from noise amplification [69]. In this case, DF two-way relaying is proposed as it can achieve better performance than AF relaying at low signal-to-noise ratios (SNRs) without noise propagation at the relay [68, 69]. Also, we recall that DF two-way relaying has the ability to perform separate precoding and power allocation on each relaying communication direction, at the cost of higher complexity [109]. In some previous studies with two-way relaying, full-duplex has been adopted [62, 106]. However full-duplex operation may not be practically feasible due to the huge intensity difference in near/far field of the transmitted/received signals. In this case, half-duplex operation, in which the relay transmits and receives in orthogonal frequency or time resources, has practical relevance and is considered in this chapter [68, 110].

In the light of above, we study a multi-pair two-way half-duplex DF relaying system with zero-forcing (ZF) processing and imperfect channel state information (CSI) [69, 111]. This chapter refers to the work of [69], where only maximum ratio combining/maximum ratio transmission (MRC/MRT) is considered. A detailed analysis of the sum SE is presented and we characterize a practical power consumption model to analyze the energy efficiency (EE) performance of the proposed relaying system. Additionally, power scaling laws have been investigated in previous studies to show the trade-off between the transmit powers and system performance [44, 69, 104]. Based

on this trade-off, several new power scaling laws are introduced to improve the EE while maintaining the desired SE for a large number of relay antennas [44] are studied in detail. Specifically, the main contributions of this chapter can be summarized as

- With a general multi-pair massive MIMO two-way relaying system employing the DF protocol, we present a new large-scale approximation of the SE with ZF processing and imperfect CSI when the number of relay antennas approaches infinity. Deriving these expressions is overlooked in the specific relaying system due to the difficulty in manipulating matrix inverses, which inherently kick in ZF type of analysis.

- We characterize a practical power consumption model derived from the relevant models in [17, 43]. It is utilized to analyze the EE performance of the proposed multi-pair two-way relaying system.

- We investigate three power scaling laws inspired from [69, 104] to indicate the trade-off between the transmit powers of each user, each pilot symbol and the relay. The same SE, even the same EE, can be achieved with different configurations of the power-scaling parameters. This provides great flexibility in practical system design and forms a roadmap to select the optimal parameters to maximize the EE performance in particular scenarios.

- Motivated by the Max-Min fairness studies in [105, 112], we formulate an optimization problem to maximize the minimum achievable SE among all user pairs with imperfect CSI in order to improve the sum SE and achieve fairness across all user pairs. The complexity analysis of the proposed optimization problem has been investigated.

4.2 System Model

As shown in Fig. 4.1, we investigate a multi-pair two-way half-duplex DF relaying system, in which K pairs of single-antenna users, defined as $\mathrm{T}_{A,i}$ and

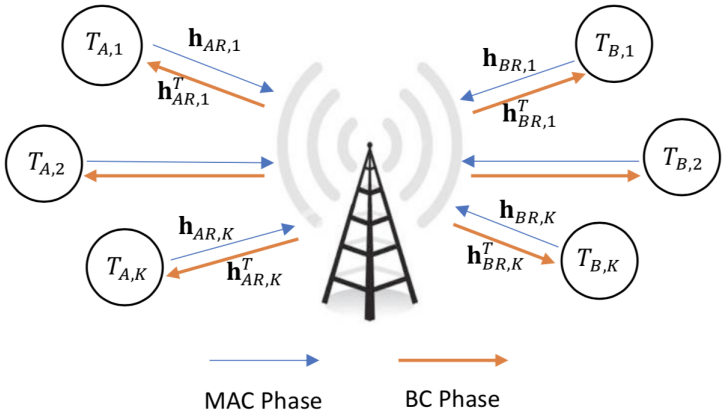

Figure 4.1: Multi-pair two-way DF relaying system.

$\mathrm{T}_{B,i}, i = 1, \ldots, K$, exchange information via a shared relay T_R with N_R antennas, generally, $N_R \gg K$. Moreover, we assume that there are no direct transmission links between user pairs. Normally, it is assumed that massive MIMO system operates in a time-division duplexing (TDD) mode [102, 103]. To this end, we assume that the proposed system is modelled as uncorrelated Rayleigh fading in coherence with the channel model introduced in Chapter 2.3.1, works under TDD protocol, and channel reciprocity holds [114, 115]. The uplink and downlink channels between $\mathrm{T}_{X,i}, X = A, B$ and T_R are denoted as $\mathbf{h}_{XR,i} \sim \mathbb{CN}(\mathbf{0}, \beta_{XR,i}\mathbf{I}_{N_R})$ and $\mathbf{h}^T_{XR,i}$, $i = 1, \ldots, K$, respectively, while $\beta_{AR,i}$ and $\beta_{BR,i}$ represent the large-scale fading parameters which are considered to be constant in this chapter for simplicity. Additionally, the uplink channel matrix can be formed as $\mathbf{H}_{XR} = [\mathbf{h}_{XR,1}, \ldots, \mathbf{h}_{XR,K}] \in \mathbb{C}^{N_R \times K}$, $X = A, B$.

For the proposed relaying system, the data transmission process can be divided into two phases with equal time slots. Generally, this two-phase protocol can be named as Multiple Access Broadcast (MABC) protocol [68]. In the first Multiple Access Channel (MAC) phase, all users transmit their signals to the relay simultaneously. Therefore, the received signal at the relay can be expressed as [43]

$$\mathbf{y}_r = \sum_{i=1}^{K} \left(\sqrt{p_{A,i}} \mathbf{h}_{AR,i} x_{AR,i} + \sqrt{p_{B,i}} \mathbf{h}_{BR,i} x_{BR,i} \right) + \mathbf{n}_R, \tag{4.1}$$

where $x_{XR,i}$ is the Gaussian signal transmitted by the i-th user $\mathrm{T}_{X,i}$ with zero mean and unit power, $p_{X,i}$ is the average transmit power of $\mathrm{T}_{X,i}, X = A, B$. $\mathbf{n}_R$ is the vector of additive white Gaussian noise (AWGN) at the relay whose elements are independent and identically distributed (i.i.d) satisfying $\mathbb{CN}(0,1)$. For low-complexity transmission, linear processing is applied at the relay. Thus, the transformed signal can be given by

$$\mathbf{z}_r = \mathbf{F}_{MAC}\mathbf{y}_r \ , \tag{4.2}$$

with $\mathbf{F}_{MAC} \in \mathbb{C}^{2K \times N_R}$, the linear receiver matrix in the MAC phase.

In the second Broadcast Channel (BC) phase, the relay first decodes the received information and then re-encodes and broadcasts it to users [69]. The linear precoding matrix $\mathbf{F}_{BC} \in \mathbb{C}^{N_R \times 2K}$ in the BC phase is applied to obtain the transmit signal of the relay as

$$\mathbf{y}_t = \rho_{DF}\mathbf{F}_{BC}\mathbf{x}, \tag{4.3}$$

where $\mathbf{x} = \left[\mathbf{x}_A^T, \mathbf{x}_B^T\right]^T$ represents the decoded signal and ρ_{DF} is the normalization coefficient determined by the average relay power constraint $\mathbb{E}\left\{||\mathbf{y}_t||^2\right\} = p_r$. Therefore, the received signals at $\mathrm{T}_{X,i}, X = A, B$ is given by

$$z_{X,i} = \mathbf{h}_{XR,i}^T\mathbf{y}_t + n_{X,i}, \tag{4.4}$$

with the standard AWGN at $\mathrm{T}_{X,i}$, $n_{X,i} \sim \mathbb{CN}(0,1)$, $X = A, B$.

4.2.1 Linear Processing

Generally, the inter-pair interference and inter-user interference can be eliminated by linear processing in massive MIMO systems [43, 116]. In this chapter, the fundamental linear processing scheme, ZF processing, is applied at the relay to achieve low-complexity transmission. Thus, the linear processing matrices $\mathbf{F}_{MAC} \in \mathbb{C}^{2K \times N_R}$ and $\mathbf{F}_{BC} \in \mathbb{C}^{N_R \times 2K}$ for the proposed system de-

fined above can be given by [98, 117]

$$\mathbf{F}_{MAC} = \left(\left[\hat{\mathbf{H}}_{AR}, \hat{\mathbf{H}}_{BR}\right]^H \left[\hat{\mathbf{H}}_{AR}, \hat{\mathbf{H}}_{BR}\right] \right)^{-1} \left[\hat{\mathbf{H}}_{AR}, \hat{\mathbf{H}}_{BR}\right]^H, \tag{4.5}$$

$$\mathbf{F}_{BC} = \left[\hat{\mathbf{H}}_{BR}, \hat{\mathbf{H}}_{AR}\right]^* \left(\left[\hat{\mathbf{H}}_{BR}, \hat{\mathbf{H}}_{AR}\right]^T \left[\hat{\mathbf{H}}_{BR}, \hat{\mathbf{H}}_{AR}\right]^* \right)^{-1}, \tag{4.6}$$

respectively. In (4.5)-(4.6) above, $\hat{\mathbf{H}}_{XR}$ are the estimated channels, $X = A, B$. To simplify the mathematical expressions in the following, we assume that $\mathbf{F}_{MAC}^{AR} \in \mathbb{C}^{K \times N_R}$, $\mathbf{F}_{MAC}^{BR} \in \mathbb{C}^{K \times N_R}$ represent the first K rows and the remaining K rows of $\mathbf{F}_{MAC}$, respectively. Meanwhile, $\mathbf{F}_{BC}^{RB} \in \mathbb{C}^{N_R \times K}$, $\mathbf{F}_{BC}^{RA} \in \mathbb{C}^{N_R \times K}$ stand for the first K columns of and the remaining K columns of $\mathbf{F}_{BC}$, respectively.

4.2.2 Channel Estimation

In massive MIMO systems, it is important to consider imperfect CSI since it is difficult to acquire perfect channel knowledge in practical scenarios [99]. In TDD systems, the standard way to estimate channels at the relay is to transmit pilots in coherence with the CSI acquisition introduced in Chapter 2.2.4 [17, 29].

In this case, among the coherence interval with length η_{coh} (in symbols), η_p symbols are applied as pilot symbols for channel estimation [69]. Generally, we assume that all pilot sequences are mutually orthogonal and $\eta_p \geq 2K$ is required. Moreover, we assume that the minimum mean square error (MMSE) estimator is employed at the relay to estimate channels [17, 50, 99]. Therefore, we can have the channel estimates as

$$\mathbf{h}_{XR,i} = \hat{\mathbf{h}}_{XR,i} + \Delta\mathbf{h}_{XR,i}, \tag{4.7}$$

where $\hat{\mathbf{h}}_{XR,i}$ and $\Delta\mathbf{h}_{XR,i}$ are the i-th columns of the estimated matrix $\hat{\mathbf{H}}_{XR}$ and estimation error matrix $\Delta\mathbf{H}_{XR}$, respectively, while $\hat{\mathbf{H}}_{XR}$ and $\Delta\mathbf{H}_{XR}$ are statistically independent, $X = A, B$. p_p represents the transmit power of each pilot symbol used for channel estimation, the elements in $\hat{\mathbf{h}}_{XR,i}$ and $\Delta\mathbf{h}_{XR,i}$ are Gaussian random variables with zero mean and variance $\sigma_{XR,i}^2 = \frac{\eta_p p_p \beta_{XR,i}^2}{1+\eta_p p_p \beta_{XR,i}}$,

$\tilde{\sigma}^2_{XR,i} = \frac{\beta_{XR,i}}{1+\eta_p p_p \beta_{XR,i}}$, $X = A, B$, respectively [99].

4.3 Performance Analysis

4.3.1 Spectral Efficiency

In this sub-chapter, we focus on the SE performance of the proposed half-duplex DF two-way relaying system. Generally, the large-scale approximation of the SE can be derived when $N_R \to \infty$.

4.3.1.1 Exact Expressions

In the MAC phase, according to (4.1)-(4.2), the transformed signal at the relay determined by the i-th user pair can be expressed as

$$z_{r,i} = z^A_{r,i} + z^B_{r,i}, \tag{4.8}$$

where $z^X_{r,i}$ can be obtained by

$$\begin{aligned} z^X_{r,i} = & \underbrace{\sqrt{p_{X,i}} \left(\mathbf{F}^{AR}_{MAC,i} + \mathbf{F}^{BR}_{MAC,i} \right) \hat{\mathbf{h}}_{XR,i} x_{X,i}}_{\text{desired signal}} \\ & + \underbrace{\sqrt{p_{X,i}} \left(\mathbf{F}^{AR}_{MAC,i} + \mathbf{F}^{BR}_{MAC,i} \right) \Delta\mathbf{h}_{XR,i} x_{X,i}}_{\text{estimation error}} \\ & + \underbrace{\sum_{j \neq i} \sqrt{p_{X,j}} \left(\mathbf{F}^{AR}_{MAC,i} + \mathbf{F}^{BR}_{MAC,i} \right) \mathbf{h}_{XR,j} x_{X,j}}_{\text{inter-user interference}} + \underbrace{\mathbf{F}^{XR}_{MAC,i} \mathbf{n}_R}_{\text{noise}}, \end{aligned} \tag{4.9}$$

and $\mathbf{z}_r = \mathbf{z}^A_r + \mathbf{z}^B_r \in \mathbb{C}^{K \times 1}$, with $\mathbf{z}^X_r \in \mathbb{C}^{K \times 1}$, $X = A, B$. With the assistance of (4.8)-(4.9), when we take the i-th pair of users into consideration, the power of estimation error, inter-user interference and compound noise in $z_{r,i}$ can be given by

$$\begin{aligned} A_i = & \, p_{A,i} \left(\left| \mathbf{F}^{AR}_{MAC,i} \Delta\mathbf{h}_{AR,i} \right|^2 + \left| \mathbf{F}^{BR}_{MAC,i} \Delta\mathbf{h}_{AR,i} \right|^2 \right) \\ & + p_{B,i} \left(\left| \mathbf{F}^{AR}_{MAC,i} \Delta\mathbf{h}_{BR,i} \right|^2 + \left| \mathbf{F}^{BR}_{MAC,i} \Delta\mathbf{h}_{BR,i} \right|^2 \right), \end{aligned} \tag{4.10}$$

$$\begin{aligned} B_i = &\sum_{j\neq i} p_{A,j}\left(\left|\mathbf{F}_{MAC,i}^{AR}\mathbf{h}_{AR,j}\right|^2 + \left|\mathbf{F}_{MAC,i}^{BR}\mathbf{h}_{AR,j}\right|^2\right) \\ &+ \sum_{j\neq i} p_{B,j}\left(\left|\mathbf{F}_{MAC,i}^{AR}\mathbf{h}_{BR,j}\right|^2 + \left|\mathbf{F}_{MAC,i}^{BR}\mathbf{h}_{BR,j}\right|^2\right), \end{aligned} \tag{4.11}$$

$$C_i = \left|\left|\mathbf{F}_{MAC,i}^{AR}\right|\right|^2 + \left|\left|\mathbf{F}_{MAC,i}^{BR}\right|\right|^2, \tag{4.12}$$

respectively. With the expressions of desired signals in (4.9) for $z_{r,i}^{A}$ and $z_{r,i}^{B}$, the SE of the specified user $\mathrm{T}_{X,i}$ $(X = A, B)$ to the relay with the signal-to-noise- plus-interference ratio (SINR), can be expressed as

$$R_{XR,i} = \frac{\eta_{coh} - \eta_p}{2\eta_{coh}}\mathbb{E}\left\{\log_2(1 + \mathrm{SINR}_{XR,i})\right\}, \tag{4.13}$$

where $\mathrm{SINR}_{XR,i}$ can be expressed as

$$\mathrm{SINR}_{XR,i} = \frac{p_{X,i}\left(\left|\mathbf{F}_{MAC,i}^{AR}\hat{\mathbf{h}}_{XR,i}\right|^2 + \left|\mathbf{F}_{MAC,i}^{BR}\hat{\mathbf{h}}_{XR,i}\right|^2\right)}{A_i + B_i + C_i}. \tag{4.14}$$

Additionally, the standard lower capacity bound associated with the worst-case uncorrelated additive noise is considered in this chapter [37, 69]; therefore, the achievable SE of the i-th user pair in the MAC phase can be expressed as

$$\begin{aligned} R_{1,i} = &\frac{\eta_{coh} - \eta_p}{2\eta_{coh}} \times \\ &\mathbb{E}\left\{\log_2\left(1 + \frac{p_{A,i}\left(\left|\mathbf{F}_{MAC,i}^{AR}\hat{\mathbf{h}}_{AR,i}\right|^2 + \left|\mathbf{F}_{MAC,i}^{BR}\hat{\mathbf{h}}_{AR,i}\right|^2\right) + p_{B,i}\left(\left|\mathbf{F}_{MAC,i}^{AR}\hat{\mathbf{h}}_{BR,i}\right|^2 + \left|\mathbf{F}_{MAC,i}^{BR}\hat{\mathbf{h}}_{BR,i}\right|^2\right)}{A_i + B_i + C_i}\right)\right\}. \end{aligned} \tag{4.15}$$

In the BC phase, via applying $\mathbf{F}_{BC}$ to generate the relay's transmit signal, the received signal at $\mathrm{T}_{X,i}$ can be calculated by (4.4). Take $z_{A,i}$ as an example,

$$\begin{aligned} z_{A,i} = &\underbrace{\rho_{DF}\hat{\mathbf{h}}_{AR,i}^{T}\mathbf{F}_{BC,i}^{RA}x_{B,i}}_{\text{desired signal}} + \underbrace{\rho_{DF}\Delta\mathbf{h}_{AR,i}^{T}\mathbf{F}_{BC,i}^{RA}x_{B,i}}_{\text{estimation error}} \\ &\underbrace{+\rho_{DF}\sum_{j=1}^{K}\mathbf{h}_{AR,i}^{T}\mathbf{F}_{BC,j}^{RB}x_{A,j} + \rho_{DF}\sum_{j\neq i}\mathbf{h}_{AR,i}^{T}\mathbf{F}_{BC,j}^{RA}x_{B,j}}_{\text{inter-user interference}} + \underbrace{n_{A,i}}_{\text{noise}}, \end{aligned} \tag{4.16}$$

while $z_{B,i}$ can be obtained by replacing the subscripts "AR", "BR" in the channel vectors and corresponding vectors, the subscripts "RA", "RB" in linear precoding vectors, and "A", "B" in signal and noise terms with the subscripts "BR", "AR", the subscripts "RB", "RA", and "B", "A" in $z_{A,i}$, respectively. To this end, we can obtain the SE of the relay to the i-th user $\mathrm{T}_{X,i}$, $X = A, B$ by

$$R_{RX,i} = \frac{\eta_{coh} - \eta_p}{2\eta_{coh}} \times \mathbb{E}\Big\{\log_2(1 + \mathrm{SINR}_{RX,i})\Big\}, \tag{4.17}$$

where $\mathrm{SINR}_{RX,i}$ can be expressed as

$$\mathrm{SINR}_{RX,i} = \frac{\left|\hat{\mathbf{h}}_{XR,i}^T \mathbf{F}_{BC,i}^{RX}\right|^2}{\left|\Delta\mathbf{h}_{XR,i}^T \mathbf{F}_{BC,i}^{RX}\right|^2 + \sum\limits_{j=1}^{K}\left(\left|\mathbf{h}_{XR,i}^T \mathbf{F}_{BC,j}^{RA}\right|^2 + \left|\mathbf{h}_{XR,i}^T \mathbf{F}_{BC,j}^{RB}\right|^2\right) - \left|\mathbf{h}_{XR,i}^T \mathbf{F}_{BC,i}^{RX}\right|^2 + \frac{1}{\rho_{DF}^2}}. \tag{4.18}$$

Meanwhile, the achievable SE of the i-th user pair in the BC phase is defined as the sum of the end-to-end SE from $\mathrm{T}_{A,i}$ to $\mathrm{T}_{B,i}$ and from $\mathrm{T}_{B,i}$ to $\mathrm{T}_{A,i}$ [43, 69],

$$R_{2,i} = \min\left(R_{AR,i}, R_{RB,i}\right) + \min\left(R_{BR,i}, R_{RA,i}\right). \tag{4.19}$$

Therefore, the sum SE of the multi-pair two-way DF relaying system can be expressed as

$$R = \sum_{i=1}^{K} R_i = \sum_{i=1}^{K} \min\left(R_{1,i}, R_{2,i}\right), \tag{4.20}$$

where R_i is the achievable SE of the i-th user pair for the proposed system determined by the minimum SE in MAC and BC phases [103, 109].

4.3.1.2 Approximations

Practically, the large-scale approximation of the SE for the i-th user pair studied in the following can be derived when the relay employs a great number of antennas, i.e., $N_R \to \infty$.

Lemma 1: When $N_R \to \infty$, the inner product of any two columns in the

estimated channel matrix $\hat{\mathbf{H}}_{XR}$ can be defined as [98, 118]

$$\frac{1}{N_R} \cdot \hat{\mathbf{h}}_{XR,i}^H \hat{\mathbf{h}}_{XR,j} \rightarrow \begin{cases} \sigma_{XR,i}^2, & i = j \\ 0, & i \neq j \end{cases}. \tag{4.21}$$

Proof: Please see Appendix A.

With an increasing number of relay antennas, the channel vectors within $\hat{\mathbf{H}}_{XR}$ become asymptotically mutually orthogonal. As such, $\hat{\mathbf{H}}_{XR}^H \hat{\mathbf{H}}_{XR}$ can be assumed to approach a diagonal matrix [76]. Thus, according to **Lemma 1**, we can obtain

$$\frac{1}{N_R} \cdot \hat{\mathbf{H}}_{XR}^H \hat{\mathbf{H}}_{XR} \rightarrow \mathrm{diag}\left\{\sigma_{XR,1}^2, \sigma_{XR,2}^2, ..., \sigma_{XR,K}^2\right\}, \tag{4.22}$$

$X = A, B$. Furthermore, the matrix inversion in (4.5)-(4.6) can be simplified by the above-mentioned calculations,

$$\left(\hat{\mathbf{H}}_{XR}^H \hat{\mathbf{H}}_{XR}\right)^{-1} \rightarrow \mathrm{diag}\left\{\frac{1}{N_R \cdot \sigma_{XR,1}^2}, \frac{1}{N_R \cdot \sigma_{XR,2}^2}, ..., \frac{1}{N_R \cdot \sigma_{XR,K}^2}\right\}, \tag{4.23}$$

$X = A, B$. Therefore, the linear processing matrices $\mathbf{F}_{MAC}$ and $\mathbf{F}_{BC}$ can be simplified when $N_R \rightarrow \infty$ as follows

$$\mathbf{F}_{MAC} \rightarrow \begin{bmatrix} \left(\hat{\mathbf{H}}_{AR}^H \hat{\mathbf{H}}_{AR}\right)^{-1} \hat{\mathbf{H}}_{AR}^H \\ \left(\hat{\mathbf{H}}_{BR}^H \hat{\mathbf{H}}_{BR}\right)^{-1} \hat{\mathbf{H}}_{BR}^H \end{bmatrix}, \tag{4.24}$$

$$\mathbf{F}_{BC} \rightarrow \left[\hat{\mathbf{H}}_{BR}^* \left(\hat{\mathbf{H}}_{BR}^T \hat{\mathbf{H}}_{BR}^*\right)^{-1}, \hat{\mathbf{H}}_{AR}^* \left(\hat{\mathbf{H}}_{AR}^T \hat{\mathbf{H}}_{AR}^*\right)^{-1}\right], \tag{4.25}$$

respectively, while the normalization coefficient ρ_{DF} defined in (4.3) can be given by

$$\rho_{DF} = \sqrt{\frac{p_r}{E\left\{\left|\left|\mathbf{F}_{BC}\right|\right|_{\mathrm{F}}^2\right\}}} = \sqrt{\frac{N_R \cdot p_r}{\sum_{i=1}^{K}\left(\frac{1}{\sigma_{AR,i}^2} + \frac{1}{\sigma_{BR,i}^2}\right)}}. \tag{4.26}$$

Corollary 1: With the DF protocol and the properties of ZF processing [119], when $N_R \rightarrow \infty$, the large-scale approximations associated with $\hat{R}_i$ ($R_i -$

$\hat{R}_i \to 0$) can be given by

$$\hat{R} = \sum_{i=1}^{K} \hat{R}_i = \sum_{i=1}^{K} \min\left(\hat{R}_{1,i}, \hat{R}_{2,i}\right). \tag{4.27}$$

The approximations of the achievable SE in MAC and BC phases can be given by

$$\hat{R}_{1,i} = \frac{\eta_{coh} - \eta_p}{2\eta_{coh}} \times \log_2 \left(1 + \frac{N_R(p_{A,i} + p_{B,i})}{\left(\frac{1}{\sigma^2_{AR,i}} + \frac{1}{\sigma^2_{BR,i}}\right) \left[\sum_{j=1}^{K} \left(p_{A,j}\tilde{\sigma}^2_{AR,j} + p_{B,j}\tilde{\sigma}^2_{BR,j} \right) + 1 \right]} \right), \tag{4.28}$$

$$\hat{R}_{2,i} = \min\left(\hat{R}_{AR,i}, \hat{R}_{RB,i}\right) + \min\left(\hat{R}_{BR,i}, \hat{R}_{RA,i}\right). \tag{4.29}$$

Meanwhile, the SE from the user pair/relay to the relay/user pair can be expressed as

$$\hat{R}_{AR,i} = \frac{\eta_{coh} - \eta_p}{2\eta_{coh}} \times \log_2 \left(1 + \frac{N_R p_{A,i}}{\left(\frac{1}{\sigma^2_{AR,i}} + \frac{1}{\sigma^2_{BR,i}}\right) \left[\sum_{j=1}^{K} \left(p_{A,j}\tilde{\sigma}^2_{AR,j} + p_{B,j}\tilde{\sigma}^2_{BR,j} \right) + 1 \right]} \right), \tag{4.30}$$

$$\hat{R}_{RA,i} = \frac{\eta_{coh} - \eta_p}{2\eta_{coh}} \times \log_2 \left(1 + \frac{N_R \cdot p_r}{(p_r\tilde{\sigma}^2_{AR,i} + 1) \sum_{j=1}^{K} \left(\frac{1}{\sigma^2_{AR,j}} + \frac{1}{\sigma^2_{BR,j}} \right)} \right). \tag{4.31}$$

$\hat{R}_{BR,i}$ and $\hat{R}_{RB,i}$ can be obtained by replacing the transmit powers $p_{A,i}$, $p_{B,i}$, and the subscripts "AR", "BR" with the transmit powers $p_{B,i}$, $p_{A,i}$, and the subscripts "BR", "AR" in $\hat{R}_{AR,i}$ and $\hat{R}_{RA,i}$, respectively.

Proof: Please see Appendix B.

4.3.2 Energy Efficiency

Generally, the EE is defined as the ratio of the sum SE to the total power consumption of the proposed system. Improving the EE performance is critical in large-scale antenna arrays. The mathematical form of the energy efficiency

can be given by [17, 44, 120],

$$\varepsilon = \frac{R}{P_{\text{total}}}, \tag{4.32}$$

where R denotes the sum SE defined in (4.20), P_{total} represents the total power consumption. In a practical two-way relay system, the total power consumption introduced in (2.19) consists of the transmitted signal power, the powers of operating static circuits and the radio frequency (RF) components in each RF chain. Normally, each antenna is connected to one RF chain [17]. Therefore, the power consumption model for the users and the relay referring to (2.20) can be defined as [43],

$$\begin{aligned} P_{tot,i} &= \frac{1}{2\eta_{coh}}\left[\frac{(\eta_{coh}-\eta_p)p_u+\eta_p p_p}{\zeta_i}+\eta_{coh}\cdot P_{RF,i}\right] \\ &= \frac{1}{2\eta_{coh}}\left[\frac{(\eta_{coh}-\eta_p)p_u+\eta_p p_p}{\zeta_i}\right]+\frac{1}{2}P_{RF,i}, \end{aligned} \tag{4.33}$$

$$P_{tot,r} = \frac{1}{2\eta_{coh}}\left[\frac{\eta_{coh}p_r}{\zeta_r}+\eta_{coh}\cdot P_{RF,r}\right] = \frac{1}{2}\left(\frac{p_r}{\zeta_r}+P_{RF,r}\right), \tag{4.34}$$

respectively. Note that $P_{tot,i}$ represents the total power at i-th user and $P_{tot,r}$ indicates the total power at the relay; ζ_r and ζ_i denote the power amplifier efficiency for the relay and i-th user, respectively. The power consumption of the RF components for single-antenna users and the relay with N_R antennas referring to (2.17) can be defined as

$$P_{RF,i} = P_{DAC,i}+P_{mix,i}+P_{filt,i}+P_{syn,i}, \tag{4.35}$$

$$P_{RF,r} = N_R(P_{DAC,r}+P_{mix,r}+P_{filt,r})+P_{syn,r}, \tag{4.36}$$

respectively. All power consumption terms are introduced and defined in (2.17). We refer readers to Chapter 2.2.3 for a more detailed study to avoid duplication. Based on the above expressions, the total power consumption

P_{total} defined in (2.19) for the system can be re-expressed as

$$P_{total} = 2K \cdot P_{tot,i} + P_{tot,r} + P_{static}, \tag{4.37}$$

where P_{static} is the power of all the static circuits [44]. To simplify the power consumption model in the simulation, we assume that $\zeta_i = \zeta_r = \zeta$, $P_{DAC,i} = P_{DAC,r} = P_{DAC}$, $P_{mix,i} = P_{mix,r} = P_{mix}$, $P_{filt,i} = P_{filt,r} = P_{filt}$ and $P_{syn,i} = P_{syn,r} = P_{syn}$ for $i = 1, 2, ..., K$.

4.4 Power Scaling Laws

This sub-chapter investigates how the power-scaling laws affect the achievable SE, particularly how power reductions with N_R maintain a desired SE. We consider three power-scaling cases: a) only the transmit power of each pilot symbol is scaled; b) the transmit powers of data transmission at each user and the relay are scaled; c) all transmit powers are scaled, to demonstrate the interplay among the transmit power of each pilot symbol p_p, the transmit power of each user p_u and the relay p_r.

For simplicity, we assume that $p_{A,i} = p_{B,i} = p_u$, $i = 1, ..., K$. We define that $\bar{R}_{1,i}$, $\bar{R}_{2,i}$, $\bar{R}_i$, $\bar{R}_{XR,i}$ and $\bar{R}_{RX,i}$, $X = A, B$, are asymptotic expressions of the achievable SE; additionally, without loss of generality in the following, we define that

$$\bar{R} = \sum_{i=1}^{K} \bar{R}_i = \sum_{i=1}^{K} \min\left(\bar{R}_{1,i}, \bar{R}_{2,i}\right), \tag{4.38}$$

$$\bar{R}_{2,i} = \min\left(\bar{R}_{AR,i}, \bar{R}_{RB,i}\right) + \min\left(\bar{R}_{BR,i}, \bar{R}_{RA,i}\right). \tag{4.39}$$

4.4.1 Pilot Symbol Transmit Power Scaling

Only the transmit power of the pilot symbol is scaled by N_R with $p_p = \frac{E_p}{N_R^{\gamma}}$, where E_p is a constant and $\gamma > 0$. This case is said to achieve power savings in the channel training stage.

Corollary 2: For $p_p = \frac{E_p}{N_R^{\gamma}}$, with fixed p_u, p_r, E_p and $\gamma > 0$, when $N_R \to \infty$, we can present the asymptotic results as

$$R_i - \min\left(\bar{R}_{1,i}, \bar{R}_{2,i}\right) \to 0. \tag{4.40}$$

with

$$\bar{R}_{1,i} = \frac{\eta_{coh} - \eta_p}{2\eta_{coh}} \log_2 \left(1 + \frac{2\frac{\eta_p E_p}{N_R^{\gamma-1}}}{\left(\frac{1}{\beta_{AR,i}^2} + \frac{1}{\beta_{BR,i}^2}\right)\left(\sum_{j=1}^{K}\left(\beta_{AR,j} + \beta_{BR,j}\right) + \frac{1}{p_u}\right)} \right), \tag{4.41}$$

$$\bar{R}_{AR,i} = \frac{\eta_{coh} - \eta_p}{2\eta_{coh}} \log_2 \left(1 + \frac{\frac{\eta_p E_p}{N_R^{\gamma-1}}}{\left(\frac{1}{\beta_{AR,i}^2} + \frac{1}{\beta_{BR,i}^2}\right)\left(\sum_{j=1}^{K}\left(\beta_{AR,j} + \beta_{BR,j}\right) + \frac{1}{p_u}\right)} \right), \tag{4.42}$$

$$\bar{R}_{RA,i} = \frac{\eta_{coh} - \eta_p}{2\eta_{coh}} \log_2 \left(1 + \frac{\frac{\eta_p E_p}{N_R^{\gamma-1}} p_r}{\sum_{j=1}^{K}\left(p_r \beta_{AR,i} + 1\right)\left(\frac{1}{\beta_{AR,j}^2} + \frac{1}{\beta_{BR,j}^2}\right)} \right), \tag{4.43}$$

and $\bar{R}_{BR,i}$ and $\bar{R}_{RB,i}$ can be obtained by replacing the subscripts "AR", "BR" in $\bar{R}_{AR,i}$ and $\bar{R}_{RA,i}$ with the subscripts "BR", "AR", respectively.

We can observe that the pilot symbol transmit power scaling depends on the choice of γ to scale the transmit power of each pilot symbol. From (4.41)-(4.43), we can know that when we reduce p_p aggressively with $\gamma > 1$, $\bar{R}_i$ approaches zero. In contrast, when $0 < \gamma < 1$, $\bar{R}_i$ grows unboundedly. Additionally, when $\gamma = 1$, $\bar{R}_i$ converges to a non-zero limit.

4.4.2 Relay and User Transmit Power Scaling

The transmit power of each pilot symbol p_p is fixed, while other transmit powers are scaled with $p_u = \frac{E_u}{N_R^{\alpha}}$, $p_r = \frac{E_r}{N_R^{\beta}}$, where $\alpha \geq 0$ and $\beta \geq 0$, and E_u, E_r are constants. In this case, the potential power savings in data transmission are studied.

Corollary 3: For $p_u = \frac{E_u}{N_R^{\alpha}}$, $p_r = \frac{E_r}{N_R^{\beta}}$, with fixed p_p, E_u, E_r and $\alpha \geq 0$, $\beta \geq 0$, when $N_R \to \infty$, we can obtain

$$R_i - \min(\bar{R}_{1,i}, \bar{R}_{2,i}) \to 0. \tag{4.44}$$

with

$$\bar{R}_{1,i} = \frac{\eta_{coh} - \eta_p}{2\eta_{coh}} \log_2 \left(1 + \frac{2 \times \frac{E_u}{N_R^{\alpha-1}}}{\left(\frac{1}{\sigma_{AR,i}^2} + \frac{1}{\sigma_{BR,i}^2} \right)} \right), \tag{4.45}$$

$$\bar{R}_{AR,i} = \frac{\eta_{coh} - \eta_p}{2\eta_{coh}} \log_2 \left(1 + \frac{\frac{E_u}{N_R^{\alpha-1}}}{\left(\frac{1}{\sigma_{AR,i}^2} + \frac{1}{\sigma_{BR,i}^2} \right)} \right), \tag{4.46}$$

$$\bar{R}_{RA,i} = \frac{\eta_{coh} - \eta_p}{2\eta_{coh}} \log_2 \left(1 + \frac{\frac{E_r}{N_R^{\beta-1}}}{\sum_{j=1}^{K} \left(\frac{1}{\sigma_{AR,j}^2} + \frac{1}{\sigma_{BR,j}^2} \right)} \right). \tag{4.47}$$

Similarly, $\bar{R}_{BR,i}$ and $\bar{R}_{RB,i}$ can be obtained by replacing the subscripts "AR", "BR" in $\bar{R}_{AR,i}$ and $\bar{R}_{RA,i}$ with the subscripts "BR", "AR", respectively.

This case investigates that when both p_u and p_r are scaled with N_R when $N_R \to \infty$, the effects of estimation error and inter-user interference eliminate; thus, only the noise at users and the relay remains to cause imperfection. When we cut down p_u and p_r aggressively, namely, 1) $\alpha > 1$, and $\beta \geq 0$, 2) $\alpha \geq 0$, and $\beta > 1$, 3) $\alpha > 1$, and $\beta > 1$, $\bar{R}_i$ reduces to zero. On the other hand, when we reduce both p_u and p_r moderately, which is, $0 \leq \alpha < 1$ and $0 \leq \beta < 1$, $\bar{R}_i$ grows unboundedly.

Furthermore, for a specific scenario where both the transmit powers of the relay and of each user are scaled with the same speed $\alpha = \beta = 1$, $\bar{R}_i$ converges to a non-zero limit,

$$\bar{R}_{1,i} = \frac{\eta_{coh} - \eta_p}{2\eta_{coh}} \log_2 \left(1 + \frac{2E_u}{\left(\frac{1}{\sigma_{AR,i}^2} + \frac{1}{\sigma_{BR,i}^2} \right)} \right), \tag{4.48}$$

$$\bar{R}_{AR,i} = \bar{R}_{BR,i} = \frac{\eta_{coh} - \eta_p}{2\eta_{coh}} \log_2 \left(1 + \frac{E_u}{\left(\frac{1}{\sigma^2_{AR,i}} + \frac{1}{\sigma^2_{BR,i}} \right)} \right), \tag{4.49}$$

$$\bar{R}_{RA,i} = \bar{R}_{RB,i} = \frac{\eta_{coh} - \eta_p}{2\eta_{coh}} \log_2 \left(1 + \frac{E_r}{\sum_{j=1}^{K} \left(\frac{1}{\sigma^2_{AR,j}} + \frac{1}{\sigma^2_{BR,j}} \right)} \right). \tag{4.50}$$

We can see that the non-zero limit increases with respect to E_u and E_r, while decreasing with respect to the number of user pairs K. Also, if we apply $0 \leq \beta < \alpha = 1$, the approximation of the sum SE is determined by the SE performance in the MAC phase, which means that $\bar{R}_{1,i}$ given by (4.48) determines $\bar{R}_i$ when $N_R \to \infty$. On the other hand, when $0 \leq \alpha < \beta = 1$, the determination of SE appears in the BC phase; thus, $\bar{R}_i$ is determined by $\bar{R}_{RA,i}$ and $\bar{R}_{RB,i}$ given by (4.50).

4.4.3 All Transmit Power Scaling

This is a general case where all transmit powers are scaled, namely, $p_p = \frac{E_p}{N_R^\gamma}$, $p_u = \frac{E_u}{N_R^\alpha}$ and $p_r = \frac{E_r}{N_R^\beta}$. In this case, $\gamma \geq 0$, $\alpha \geq 0$ and $\beta \geq 0$, E_p, E_u and E_r are constants.

Corollary 4: For $p_p = \frac{E_p}{N_R^\gamma}$, $p_u = \frac{E_u}{N_R^\alpha}$, $p_r = \frac{E_r}{N_R^\beta}$ with fixed E_p, E_u, E_r and $\gamma \geq 0$, $\alpha \geq 0$, $\beta \geq 0$, when $N_R \to \infty$, we can obtain

$$R_i - \min(\bar{R}_{1,i}, \bar{R}_{2,i}) \to 0. \tag{4.51}$$

with

$$\bar{R}_{1,i} = \frac{\eta_{coh} - \eta_p}{2\eta_{coh}} \log_2 \left(1 + \frac{2 \times \frac{\eta_p E_p E_u}{N_R^{\alpha+\gamma-1}}}{\left(\frac{1}{\beta^2_{AR,i}} + \frac{1}{\beta^2_{BR,i}} \right)} \right), \tag{4.52}$$

$$\bar{R}_{AR,i} = \frac{\eta_{coh} - \eta_p}{2\eta_{coh}} \log_2 \left(1 + \frac{\frac{\eta_p E_p E_u}{N_R^{\alpha+\gamma-1}}}{\left(\frac{1}{\beta^2_{AR,i}} + \frac{1}{\beta^2_{BR,i}} \right)} \right), \tag{4.53}$$

$$\bar{R}_{RA,i} = \frac{\eta_{coh} - \eta_p}{2\eta_{coh}} \log_2 \left(1 + \frac{\frac{\eta_p E_p E_r}{N_R^{\beta+\gamma-1}}}{\sum_{j=1}^{K} \left(\frac{1}{\beta_{AR,j}^2} + \frac{1}{\beta_{BR,j}^2} \right)} \right). \tag{4.54}$$

Similarly, we can obtain $\bar{R}_{BR,i}$ and $\bar{R}_{RB,i}$ by replacing the subscripts "AR", "BR" with the subscripts "BR", "AR" in $\bar{R}_{AR,i}$ and $\bar{R}_{RA,i}$ in the above expressions, respectively.

As expected, the sum SE depends on the choice of α, β and γ. Additionally, $\alpha + \gamma$ determines the SE in the MAC phase, while $\beta + \gamma$ determines the SE in the BC phase. When $\alpha = \beta > 0$ and $\alpha + \gamma = 1$, the trade-off between the transmit powers of each user/the relay and of each pilot symbol is displayed. In this case, if we reduce the transmit power of each pilot symbol aggressively, the channel estimate is corrupted and in order to compensate this imperfection, the transmit power of each user/the relay should be increased. The non-zero limit of the asymptotic SE under this specific case can be given by

$$\bar{R}_{1,i} = \frac{\eta_{coh} - \eta_p}{2\eta_{coh}} \log_2 \left(1 + \frac{2\eta_p E_p E_u}{\left(\frac{1}{\beta_{AR,i}^2} + \frac{1}{\beta_{BR,i}^2} \right)} \right), \tag{4.55}$$

$$\bar{R}_{AR,i} = \bar{R}_{BR,i} = \frac{\eta_{coh} - \eta_p}{2\eta_{coh}} \log_2 \left(1 + \frac{\eta_p E_p E_u}{\left(\frac{1}{\beta_{AR,i}^2} + \frac{1}{\beta_{BR,i}^2} \right)} \right), \tag{4.56}$$

$$\bar{R}_{RA,i} = \bar{R}_{RB,i} = \frac{\eta_{coh} - \eta_p}{2\eta_{coh}} \log_2 \left(1 + \frac{\eta_p E_p E_r}{\sum_{j=1}^{K} \left(\frac{1}{\beta_{AR,j}^2} + \frac{1}{\beta_{BR,j}^2} \right)} \right). \tag{4.57}$$

Moreover, we can see that when $\alpha > \beta \geq 0$ and $\alpha + \gamma = 1$, the limit of $\bar{R}_i$ is determined by $\bar{R}_{1,i}$ according to (4.55), which means that we can improve the sum SE by increasing E_p and E_u in the MAC phase. In addition, the sum SE of the proposed system is an increasing function of K based on (4.38).

Meanwhile, when $0 \leq \alpha < \beta$ and $\beta + \gamma = 1$, the limit of $\bar{R}_i$ is determined by $\bar{R}_{RA,i}$ and $\bar{R}_{RB,i}$ according to (4.57) existing in the BC phase, which displays the trade-off between the transmit powers of each pilot symbol and of the relay.

4.5 Max-Min Fairness Analysis

With the assistance of the above mentioned SE analysis, and as a further step forward from the power scaling laws, in this sub-chapter, our objective is to harness SE fairness among the user pairs. We achieve this purpose by maximizing the minimum achievable SE among all the user pairs; therefore, providing max-min fairness [105, 112].

4.5.1 Spectral Efficiency Fairness

For analytical simplicity, the large-scale approximation in **Corollary 1** is employed and we assume that the pilot power p_p is determined in advance. Moreover, we define that $\mathbf{p}_A = [p_{A,1}, ..., p_{A,K}]^T$, and $\mathbf{p}_B = [p_{B,1}, ..., p_{B,K}]^T$. In this case, the optimization problem can be formulated as

$$\max_{\mathbf{p}_A, \mathbf{p}_B, p_r} \min_{i \in 1,...,K} \hat{R}_i \tag{4.58a}$$

subject to

$$0 \leq p_r \leq P_r^{max}, 0 \leq p_{A,i} \leq P_u^{max}, 0 \leq p_{B,i} \leq P_u^{max}, \forall i \tag{4.58b}$$

$$\frac{1}{2}\left(\sum_{i=1}^{K} \frac{(\eta_{coh} - \eta_p)\left(p_{A,i} + p_{B,i}\right)}{\eta_{coh}\zeta_u} + \frac{p_r}{\zeta_c}\right) + P_o \leq P^{\max} \tag{4.58c}$$

Here, P^{max} is the total power constraint, P_u^{max} and P_r^{max} are the maximum powers of each user and the relay, respectively and

$$P_o = \frac{1}{2}\left[\frac{2K\eta_p p_p}{\eta_{coh}\zeta_u} + (2K + N_R)(P_{DAC} + P_{mix} + P_{filt}) + (2K+1)P_{syn} + P_{static}\right], \tag{4.59}$$

where P_o is determined in Chapter 4.3.2. According to **Corollary 1**, we can rewrite the optimization problem (4.58) by introducing the auxiliary vari-

ables t, t_1, t_2 as follows

$$\max_{\mathbf{p}_A,\mathbf{p}_B,p_r,t,t_1,t_2} t \tag{4.60a}$$

$$\text{s.t. (4.58b), (4.58c)} \tag{4.60b}$$

$$t_1 + t_2 \geq t \tag{4.60c}$$

$$\frac{\eta_{coh}-\eta_p}{2\eta_{coh}}\log_2\left(1+\frac{\frac{N_R\sigma_{AR,i}^2\sigma_{BR,i}^2}{\sigma_{AR,i}^2+\sigma_{BR,i}^2}\left(p_{A,i}+p_{B,i}\right)}{\sum_{j=1}^{K}\left(p_{A,j}\tilde{\sigma}_{AR,j}^2+p_{B,j}\tilde{\sigma}_{BR,j}^2\right)+1}\right) \geq t, \forall i \tag{4.60d}$$

$$\frac{\eta_{coh}-\eta_p}{2\eta_{coh}}\log_2\left(1+\frac{\frac{N_R\sigma_{AR,i}^2\sigma_{BR,i}^2}{\sigma_{AR,i}^2+\sigma_{BR,i}^2}p_{A,i}}{\sum_{j=1}^{K}\left(p_{A,j}\tilde{\sigma}_{AR,j}^2+p_{B,j}\tilde{\sigma}_{BR,j}^2\right)+1}\right) \geq t_1, \forall i \tag{4.60e}$$

$$\frac{\eta_{coh}-\eta_p}{2\eta_{coh}}\log_2\left(1+\frac{p_rN_R}{\left(p_r\tilde{\sigma}_{BR,i}^2+1\right)\sum_{j=1}^{K}\left(\frac{1}{\sigma_{AR,j}^2}+\frac{1}{\sigma_{AR,j}^2}\right)}\right) \geq t_1, \forall i \tag{4.60f}$$

$$\frac{\eta_{coh}-\eta_p}{2\eta_{coh}}\log_2\left(1+\frac{\frac{N_R\sigma_{AR,i}^2\sigma_{BR,i}^2}{\sigma_{AR,i}^2+\sigma_{BR,i}^2}p_{B,i}}{\sum_{j=1}^{K}\left(p_{A,j}\tilde{\sigma}_{AR,j}^2+p_{B,j}\tilde{\sigma}_{BR,j}^2\right)+1}\right) \geq t_2, \forall i \tag{4.60g}$$

$$\frac{\eta_{coh}-\eta_p}{2\eta_{coh}}\log_2\left(1+\frac{p_rN_R}{\left(p_r\tilde{\sigma}_{AR,i}^2+1\right)\sum_{j=1}^{K}\left(\frac{1}{\sigma_{AR,j}^2}+\frac{1}{\sigma_{AR,j}^2}\right)}\right) \geq t_2, \forall i \tag{4.60h}$$

According to the property of logarithm function $\log(\frac{a}{b}) = \log(a) - \log(b)$, we can observe that the SE of the proposed system can be defined as a difference of two concave functions [121], we can rewrite the constraints with $\hat{R}_i = f(p_{A,i}, p_{B,i}, p_r) - h(p_{A,i}, p_{B,i}, p_r)$, where the specific mathematical expressions for $\mathrm{T}_{X,i}$, $i = 1, ..., K$ and $X = A, B$ can be given by

$$f_1\left(p_{A,i},p_{B,i},p_r\right)=\frac{\eta_{coh}-\eta_p}{2\eta_{coh}}\times \log_2\left(\frac{N_R\sigma_{AR,i}^2\sigma_{BR,i}^2}{\sigma_{AR,i}^2+\sigma_{BR,i}^2}\left(p_{A,i}+p_{B,i}\right)+\sum_{j=1}^{K}\left(p_{A,j}\tilde{\sigma}_{AR,j}^2+p_{B,j}\tilde{\sigma}_{BR,j}^2\right)+1\right), \tag{4.61}$$

$$f_{XR}\left(p_{A,i},p_{B,i},p_r\right)=\frac{\eta_{coh}-\eta_p}{2\eta_{coh}}\times \log_2\left(\frac{N_R\sigma_{AR,i}^2\sigma_{BR,i}^2}{\sigma_{AR,i}^2+\sigma_{BR,i}^2}p_{X,i}+\sum_{j=1}^{K}\left(p_{A,j}\tilde{\sigma}_{AR,j}^2+p_{B,j}\tilde{\sigma}_{BR,j}^2\right)+1\right), \tag{4.62}$$

$$f_{RX}\left(p_{A,i},p_{B,i},p_r\right)=\frac{\eta_{coh}-\eta_p}{2\eta_{coh}}\times\log_2\left(p_rN_R+\left(p_r\tilde{\sigma}_{XR,i}^2+1\right)\sum_{j=1}^{K}\left(\frac{1}{\sigma_{AR,j}^2}+\frac{1}{\sigma_{BR,j}^2}\right)\right), \tag{4.63}$$

$$h_{XR}\left(p_{A,i},p_{B,i},p_r\right)=\frac{\eta_{coh}-\eta_p}{2\eta_{coh}}\times\log_2\left(\sum_{j=1}^{K}\left(p_{A,j}\tilde{\sigma}_{AR,j}^2+p_{B,j}\tilde{\sigma}_{BR,j}^2\right)+1\right), \tag{4.64}$$

$$h_{RX}\left(p_{A,i},p_{B,i},p_r\right)=\frac{\eta_{coh}-\eta_p}{2\eta_{coh}}\times\log_2\left(\left(p_r\tilde{\sigma}_{XR,i}^2+1\right)\sum_{j=1}^{K}\left(\frac{1}{\sigma_{AR,j}^2}+\frac{1}{\sigma_{BR,j}^2}\right)\right). \tag{4.65}$$

Based on **Corollary 1**, it is clear that for $\hat{R}_{1,i}$, $h_1\left(p_{A,i},p_{B,i},p_r\right)=h_{XR}\left(p_{A,i},p_{B,i},p_r\right)$, $X=A,B$. The specific functions $f(p_{A,i},p_{B,i},p_r)$ and $h(p_{A,i},p_{B,i},p_r)$ defined above are jointly concave with respect to $p_{A,i},p_{B,i},p_r$, $i=1,...,K$ [121, 122], and the relaxed problem can be reformulated as

$$\max_{\mathbf{p}_A,\mathbf{p}_B,p_r,t,t_1,t_2} t \tag{4.66a}$$

$$\text{s.t. (58b), (58c), (60c)} \tag{4.66b}$$

$$f_1\left(p_{A,i},p_{B,i},p_r\right)-h_1\left(p_{A,i},p_{B,i},p_r\right)\geq t,\forall i \tag{4.66c}$$

$$f_{AR}\left(p_{A,i},p_{B,i},p_r\right)-h_{AR}\left(p_{A,i},p_{B,i},p_r\right)\geq t_1,\forall i \tag{4.66d}$$

$$f_{RB}\left(p_{A,i},p_{B,i},p_r\right)-h_{RB}\left(p_{A,i},p_{B,i},p_r\right)\geq t_1,\forall i \tag{4.66e}$$

$$f_{BR}\left(p_{A,i},p_{B,i},p_r\right)-h_{BR}\left(p_{A,i},p_{B,i},p_r\right)\geq t_2,\forall i \tag{4.66f}$$

$$f_{RA}\left(p_{A,i},p_{B,i},p_r\right)-h_{RA}\left(p_{A,i},p_{B,i},p_r\right)\geq t_2,\forall i \tag{4.66g}$$

We can find that the difficulty in solving (4.66) lies in the component $h_{XR}\left(p_{A,i}, p_{B,i}, p_r\right)$ and $h_{RX}\left(p_{A,i}, p_{B,i}, p_r\right)$, $X = A, B$. Therefore, the value of $\left(p_{A,i}, p_{B,i}, p_r\right)$ at k-th iteration is supposed to be $\left(p_{A,i}^{(k)}, p_{B,i}^{(k)}, p_r^{(k)}\right)$. Since $h_{XR}\left(p_{A,i}, p_{B,i}, p_r\right)$ and $h_{RX}\left(p_{A,i}, p_{B,i}, p_r\right)$, $X = A, B$ are concave and differentiable on the considered domain, we can easily find the affine function as a Taylor first order approximation near $\left(p_{A,i}^{(k)}, p_{B,i}^{(k)}, p_r^{(k)}\right)$ [121, 122], given by

$$\begin{aligned} h_{XR}^{(k)}\left(p_{A,i}, p_{B,i}, p_r\right) = & \frac{\eta_{coh} - \eta_p}{2\eta_{coh}} \times \log_2\left(\sum_{j=1}^{K}\left(p_{A,j}^{(k)}\tilde{\sigma}_{AR,j}^2 + p_{B,j}^{(k)}\tilde{\sigma}_{BR,j}^2\right) + 1\right) \\ & + \frac{\eta_{coh} - \eta_p}{2\eta_{coh}} \times \frac{\sum_{j=1}^{K}\left(p_{A,j} - p_{A,j}^{(k)}\right)\tilde{\sigma}_{AR,j}^2 + \left(p_{B,j} - p_{B,j}^{(k)}\right)\tilde{\sigma}_{BR,j}^2}{\ln 2\left(\sum_{j=1}^{K}\left(p_{A,j}^{(k)}\tilde{\sigma}_{AR,j}^2 + p_{B,j}^{(k)}\tilde{\sigma}_{BR,j}^2\right) + 1\right)}, \end{aligned} \tag{4.67}$$

$$\begin{aligned} h_{RX}^{(k)}\left(p_{A,i}, p_{B,i}, p_r\right) = & \frac{\eta_{coh} - \eta_p}{2\eta_{coh}} \times \log_2\left(\left(p_r^{(k)}\tilde{\sigma}_{XR,i}^2 + 1\right)\sum_{j=1}^{K}\left(\frac{1}{\sigma_{AR,j}^2} + \frac{1}{\sigma_{BR,j}^2}\right)\right) \\ & + \frac{\eta_{coh} - \eta_p}{2\eta_{coh}} \times \frac{\left(p_r - p_r^{(k)}\right)\tilde{\sigma}_{XR,i}^2 \sum_{j=1}^{K}\left(\frac{1}{\sigma_{AR,j}^2} + \frac{1}{\sigma_{BR,j}^2}\right)}{\ln 2\left(p_r^{(k)}\tilde{\sigma}_{XR,i}^2 + 1\right)\sum_{j=1}^{K}\left(\frac{1}{\sigma_{AR,j}^2} + \frac{1}{\sigma_{BR,j}^2}\right)}. \end{aligned} \tag{4.68}$$

To update the objective in the $(k+1)$-th iteration, we replace $h_{XR}\left(p_{A,i}, p_{B,i}, p_r\right)$ and $h_{RX}\left(p_{A,i}, p_{B,i}, p_r\right)$, $X = A, B$ by their affine functions, respectively. Therefore, the optimization problem (4.66) at iteration $(k+1)$-th with convex con-

straints can be reformulated as

$$\max_{\mathbf{p}_A,\mathbf{p}_B,p_r,t,t_1,t_2} t \tag{4.69a}$$

$$\text{s.t. (58b), (58c), (60c)} \tag{4.69b}$$

$$f_1\left(p_{A,i},p_{B,i},p_r\right)-h_1^{(k)}\left(p_{A,i},p_{B,i},p_r\right)\geq t,\forall i \tag{4.69c}$$

$$f_{AR}\left(p_{A,i},p_{B,i},p_r\right)-h_{AR}^{(k)}\left(p_{A,i},p_{B,i},p_r\right)\geq t_1,\forall i \tag{4.69d}$$

$$f_{RB}\left(p_{A,i},p_{B,i},p_r\right)-h_{RB}^{(k)}\left(p_{A,i},p_{B,i},p_r\right)\geq t_1,\forall i \tag{4.69e}$$

$$f_{BR}\left(p_{A,i},p_{B,i},p_r\right)-h_{BR}^{(k)}\left(p_{A,i},p_{B,i},p_r\right)\geq t_2,\forall i \tag{4.69f}$$

$$f_{RA}\left(p_{A,i},p_{B,i},p_r\right)-h_{RA}^{(k)}\left(p_{A,i},p_{B,i},p_r\right)\geq t_2,\forall i \tag{4.69g}$$

To this end, via solving the optimization problem (4.69), the lower bound of the SE for each user pair can be obtained. Overall, the optimal solutions can be obtained by existing optimization tool (CVX) and the iterative procedure of Max-Min fairness analysis can be summarized in Algorithm 4.2.

Algorithm 4.2 General iterative algorithm

Initialization: Set the iteration index $k=0$, define a tolerance $\iota>0$ and initial values for $p_{A,i}^{(0)}$, $p_{B,i}^{(0)}$ and $p_r^{(0)}$, $i=1,...,K$.

Repeat:

1: Solve optimization problem (4.69) and obtain the solutions $p_{A,i}^{(k)}$, $p_{B,i}^{(k)}$ and $p_r^{(k)}$, $i=1,...K$.

2: Update $(p_{A,i}^{(0)}, p_{B,i}^{(0)}\ p_r^{(0)})$=$(p_{A,i}^{(k)}, p_{B,i}^{(k)}\ p_r^{(k)})$, $i=1,...K$.

3: Set $k=k+1$.

Until:

4: $|t^{(k)}-t^{(k-1)}|<\iota$ or $k\geq L_{max}$ (maximum iteration number).

Output: $p_{A,i}^*$, $p_{B,i}^*$ and p_r^*, $i=1,...,K$ as the solutions.

4.5.2 Complexity Analysis

Recall that in the optimization problem (4.69), logarithmic functions are deployed in the constraints; therefore, the successive approximation method which constructs polynomial approximations for all logarithmic terms is employed in CVX when solving this optimization problem [123]. To the best of our knowledge, the exact complexity of the successive approxima-

tion method in CVX has not been determined in the literature. Accordingly, we consider studying the complexity of the optimization problem with polynomial-approximation constraints to obtain the complexity lower bound of Algorithm 4.2.

Here, we make use of the fact that the optimization problem can be considered as a quadratically constrained quadratic program (QCQP) in epigraph form [124] after constructing polynomial approximations in CVX. With the assistance of previous studies [125, 126], the quadratic constraints can be rewritten as linear matrix inequalities (LMIs). Note that linear constraints can also be considered as LMI constraints. Since Algorithm 4.2 is an iterative process, solving the optimization problem by the interior-point method via CVX, as per the methodology in [127], we can similarly determine the lower bound of the complexity of Algorithm 4.2 via the following two parts:

Iteration Complexity: In Algorithm 4.2, with the given tolerance $\iota > 0$, the number of required iterations to achieve the ι-optimal solution can be given by

$$C_{iter} = \sqrt{\sum_{j=1}^{L_{num}} k_j} \cdot \ln(\frac{1}{\iota}) = \sqrt{6K^2 + 4K + 3} \cdot \ln(\frac{1}{\iota}), \tag{4.70}$$

where L_{num} is the number of LMI constraints and k_j represents the size of the j-th constraint, $j = 1, ..., L_{num}$.

Per-Iteration Complexity: For each iteration, a search direction is generated by solving a system of n linear equations in n unknowns with $n = \mathscr{O}(K^2)$ [127]. To this end, the computation cost per iteration can be obtained by

$$\begin{aligned} C_{per} &= n \cdot \textstyle\sum_{j=1}^{L_{num}} k_j^3 + n^2 \cdot \sum_{j=1}^{L_{num}} k_j^2 + n^3 \\ &= n \cdot (3 + 2K + 8K^3 + 24K^4) + n^2 \cdot (3 + 2K + 4K^2 + 12K^3) + n^3. \end{aligned} \tag{4.71}$$

Hence, the lower bound of the total complexity C_{total} of Algorithm 4.2 can be

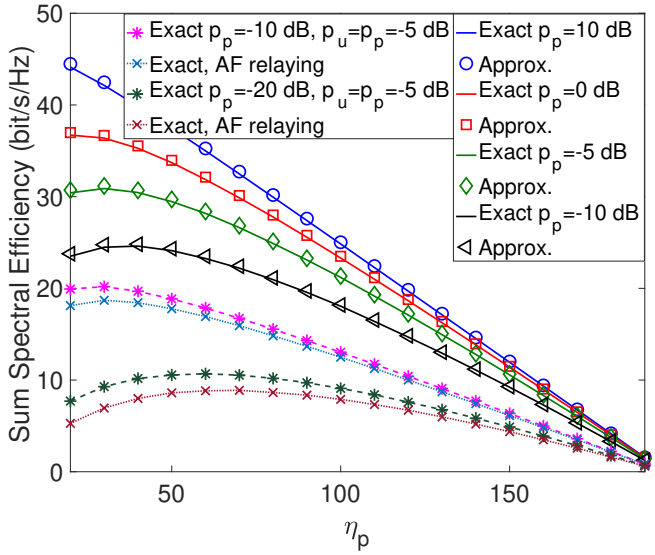

Figure 4.2: Sum SE vs. η_p with ZF processing, $N_R = 400$, $K = 10$, $p_u = 5$ dB and $p_r = 10$ dB.

calculated by combining these two parts,

$$\begin{aligned} C_{total} &= C_{iter} \times C_{per} \\ &= \sqrt{6K^2+3K+4} \cdot \ln(\tfrac{1}{\iota}) \cdot n \cdot [(3+2K++8K^3+24K^4) \\ &+ n \cdot (3+2K+4K^2+12K^3)+n^2]. \end{aligned} \tag{4.72}$$

4.6 Numerical Results

We now present simulation results to verify the above studies. Unless specifically noted, the following parameters are employed in the simulation. We consider a Long-term evolution (LTE) frame introduced in [17] and we assume a coherence time $\eta_{coh} = 196$ (symbols) and the length of the pilot sequences is $\eta_p = 2K$, the minimum requirement. For simplicity, we assume that the large-scale fading parameters are $\beta_{AR,i} = \beta_{BR,i} = 1$ and each user has the same transmit power $p_{A,i} = p_{B,i} = p_u$, $i = 1, \ldots, K$. For the proposed power consumption model, we assume that $\zeta = 0.38$, $P_{DAC} = 7.8$ mW, $P_{mix} = 15.2$ mW, $P_{filt} = 10$ mW, $P_{syn} = 25$ mW and $P_{static} = 2$ W.

4.6.1 Validation of Analytical Expressions

Fig. 4.2 shows the sum SE v.s. the length of pilot sequence η_p (in symbols). Note that the "Approx." (Approximations) curves are obtained via applying **Corollary 1**, and the "Exact" (Exact results) curves are generated by (4.10)-(4.20). We can observe that the large-scale approximations closely match the exact results and the sum SE can be maximized with an optimal η_p^* at low p_p. In contrast, the sum SE is a decreasing function of η_p at moderate and high p_p. To this end, in order to achieve better sum SE performance, $\eta_p = 2K$, the minimum requirement, is deployed in the channel estimation phase. Moreover, AF relaying with ZF processing studied in [128, 129, 130] has been considered here as a benchmark to further illustrate the performance of the proposed DF relaying system. It can be observed that when transmit powers are small resulting in lower SINRs, the performance of DF relaying can outperform that of AF relaying and an optimal η_p^* can be obtained to maximize the sum SE with specific transmit power configurations. Since in our following simulations, we consider a more general power configuration, where SINRs are not small enough for DF relaying to outperform AF relaying; therefore, we only focus on the performance of the proposed DF relaying in the following numerical results.

4.6.2 Power Scaling Laws

4.6.2.1 Pilot Symbol Transmit Power Scaling

It can be easily observed in Fig. 4.3 (a) that the power scaling law breaks down when $\gamma = 0$ and the sum SE grows unboundedly. For Pilot Symbol Transmit Power Scaling, the curves named "Asy" (Asymptotic results) are presented according to **Corollary 2**. When $0 < \gamma < 1$, the sum SE is an increasing function of N_R. In contrast, when $\gamma = 1$, the sum SE progressively reaches a non-zero limit, and when $\gamma > 1$, the sum SE approaches zero gradually. Moreover, the sum SE is a decreasing function of γ; since with larger γ, the system would experience a lower channel estimation accuracy, which

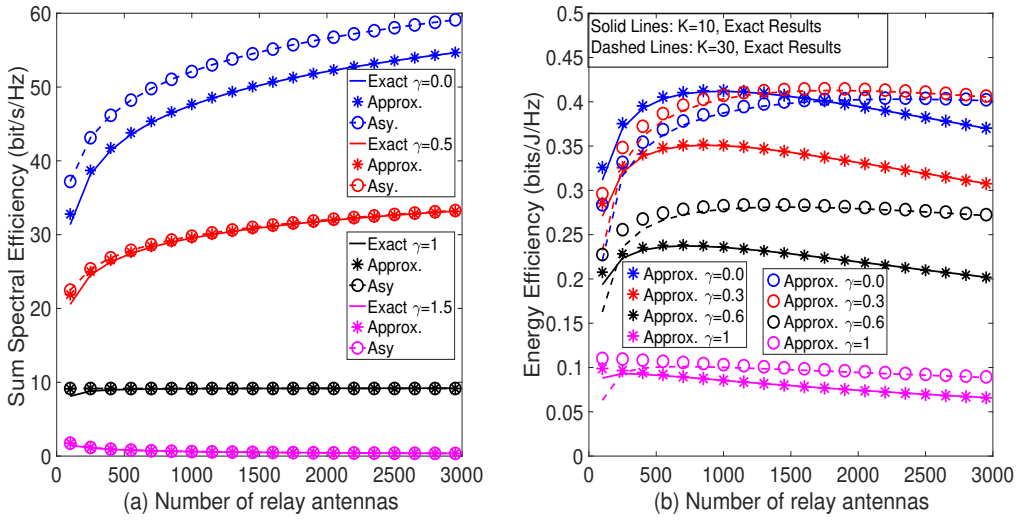

Figure 4.3: (a) Sum SE and (b) EE v.s. number of relay antennas N_R for $K = 10$, $p_u = 5$ dB, $p_r = 10$ dB and $p_p = E_p/N_R^{\gamma}$ with $E_p = 5$ dB.

results in worse system performance.

Fig. 4.3 (b) verifies the impact of N_R on the EE when different K and γ are applied. It is clearly shown that the sum SE saturates when N_R is large, while P_{total} increases linearly with N_R, and accordingly the EE peaks at a certain value of N_R. In this case, an optimal N_R^* within the range $(500, 1500)$ can be selected to maximize the EE, especially when $0 \leq \gamma < 1$. Moreover, the EE decreases more significantly with a smaller K when N_R is large, and we can observe that the power scaling law introduced in **Corollary 2** can achieve the maximum EE while achieving power savings in a larger K scenario. In Fig. 4.3 (b), we can indicate that when $K = 30$, an optimal $\gamma^* = 0.3$ and optimal $N_R^* \approx 1500$ can be selected to achieve the maximum EE≈ 0.4 bits/J/Hz.

4.6.2.2 Relay and User Transmit Power Scaling

Fig. 4.4 (a) investigates how the transmit powers of each user $p_u = E_u/N_R^{\alpha}$ and the relay $p_r = E_r/N_R^{\beta}$ affect the achievable SE. For Relay and User Transmit Power Scaling, the curves named "Asy" (Asymptotic results) are generated by **Corollary 3**. Due to the lack of figure space, the SE performance without power scaling law is displayed in Fig. 4.3 (a). When $\alpha = 1$ and/or $\beta = 1$, the

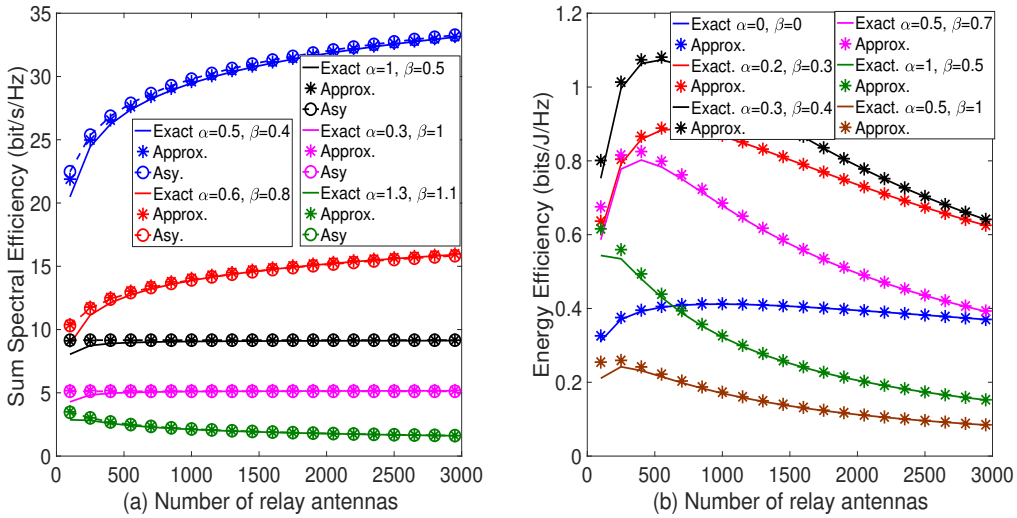

Figure 4.4: (a) Sum SE and (b) EE v.s. number of relay antennas N_R for $K = 10$, $p_p = 5$ dB, $p_u = E_u/N_R^{\alpha}$ with $E_u = 5$ dB and $p_r = E_r/N_R^{\beta}$ with $E_r = 10$ dB.

SE saturates to a non-zero limit. When $\alpha > 1$, $\beta > 1$, the sum SE gradually reduces to zero. On the other hand, when we reduce the transmit powers moderately with $0 \leq \alpha < 1$ and $0 \leq \beta < 1$, the sum SE grows unboundedly. The channel estimation accuracy keeps stable and the transmission phase plays an important role in the SE performance.

The impact of N_R on the EE generated according to **Corollary 3** with different α and β is investigated in Fig. 4.4 (b). We can see that when $0 < \alpha < 1$ and $0 < \beta < 1$, the EE performance can outperform that without power scaling law ($\alpha = \beta = 0$) and an optimal N_R^* can be obtained to maximize the EE. Moreover, the moderate power scaling in the transmission phase can help to optimize the EE performance. Fig. 4.4 (b) shows that when the optimal $N_R^* \approx 500$ is selected, the optimal EE can be achieved, especially when $\alpha = 0.3$ and $\beta = 0.4$, the EE can achieve the maximum value $\varepsilon \approx 1.1$ bits/J/Hz. In contrast, when the transmit powers are reduced aggressively, e.g., $\alpha = 0.5$ and $\beta = 1$, the EE is a completely decreasing function with respect to N_R. With regards to this, by considering the trade-off between scaling parameters, appropriate values of α and β could be selected to optimize the EE performance.

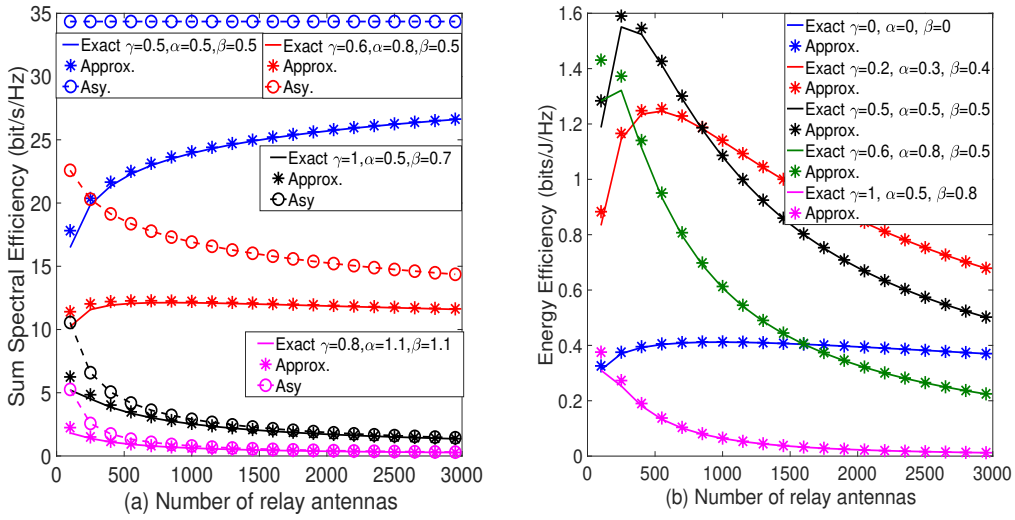

Figure 4.5: (a) Sum SE and (b) EE v.s. number of relay antennas N_R for $K = 10$, $p_p = E_p/N_R^{\gamma}$, $p_u = E_u/N_R^{\alpha}$ with $E_p = E_u = 5$ dB and $p_r = E_r/N_R^{\beta}$ with $E_r = 10$ dB.

4.6.2.3 All Transmit Power Scaling

Fig. 4.5 (a) verifies the trade-off between the transmit powers of each user, the relay and the pilot symbol. For All Transmit Power Scaling, the "Asy" (Asymptotic results) curves are obtained via **Corollary 4**. As a reference, the SE performance without power scaling law is displayed in Fig. 4.3 (a). For the aggressive power-scaling scenario, the sum SE progressively converges to zero, as predicted. Moreover, with the moderate power-scaling parameters, $0 < \gamma < 1$, $0 < \alpha < 1$ and $0 < \beta < 1$, the sum SE increases with respect to N_R.

Fig. 4.5 (b) illustrates the impact of the number of relay antennas on the EE following the power scaling law **Corollary 4**. It is clearly shown that the EE rises and then descends with respect to N_R while applying moderate power-scaling parameters; thus, we can obtain the optimal N_R^* to maximize the EE, e.g., with $\gamma = 0.2$, $\alpha = 0.3$ and $\beta = 0.4$, the maximum EE around 1.25 bits/J/Hz can be obtained when $N_R^* \approx 500$. On the other hand, when we cut down the transmit powers aggressively, the EE approaches to zero straightforwardly. Therefore, it is of crucial importance to determine the scaling

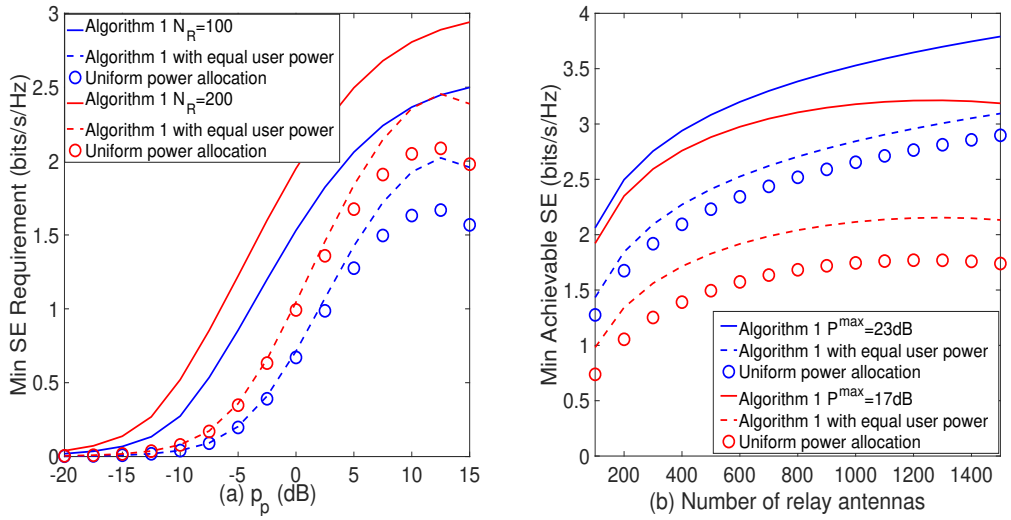

Figure 4.6: Min achievable SE v.s. (a) p_p with $P^{max} = P_r^{max} = 23$ dB and (b) number of relay antennas with $p_p = 5$ dB, $P_r^{max} = P^{max}$ for $K = 10$ and $P_u^{max} = 10$ dB.

parameters to optimize the EE performance in a specific power-limited scenario.

4.6.3 Max-Min Fairness

We consider three optimization scenarios with the minimum achievable SE among all user pairs: 1) Algorithm 4.2; 2) Algorithm 4.2 with equal user power, i.e. $p_{A,i} = p_{B,i} = p_u$, $i = 1,\ldots,K$; 3) Uniform power allocation, i.e. $p_{A,i} = p_{B,i} = p_u$, $i = 1,\ldots,K$, $2Kp_u = p_r$, $\frac{1}{2}\left(\sum_{i=1}^{K} \frac{(\eta_{coh}-\eta_p)(p_{A,i}+p_{B,i})}{\eta_{coh}\zeta_u} + \frac{p_r}{\zeta_c}\right) + P_o = P^{\max}$. For a more practical comparison, all users' large-scale fading parameters are different and can be generated via $\beta_k = \sqrt{\frac{\kappa}{D_k^{\nu}}}$, where κ is the large-scale fading coefficient, D_k is the distance between the k-th user and the relay, ν is the path-loss exponent [39]. Following our benchmark work in [69], we consider

$\beta_{AR} = [0.3188, 0.4242, 0.5079, 0.0855, 0.2625, 0.8010, 0.0292, 0.9289, 0.7303, 0.4886]$,

$\beta_{BR} = [0.5785, 0.2373, 0.4588, 0.9631, 0.5468, 0.5211, 0.2316, 0.4889, 0.6241, 0.6791]$.

Fig. 4.6 (a) shows the minimum achievable SE versus p_p. It can be observed that the minimum achievable SE achieved via Algorithm 4.2 outperforms the other two scenarios, Algorithm 4.2 with equal user power and uni-

form power allocation, especially when p_p is large enough. Moreover, larger number of relay antennas can help to increase the minimum achievable SE with the same total power constraint $P^{\max}$.

Fig. 4.6 (b) shows the minimum achievable SE with increasing number of relay antennas N_R. Similarly, a higher minimum achievable SE can be achieved by Algorithm 4.2 compared with the other two power allocation scenarios. The minimum achievable SE is an increasing function of N_R, especially with a larger total power constraint.

K		2	4	6	8	10
$N_R = 500$	Algorithm 1	9.318	10.021	12.745	13.136	14.721
$P^{max} = 23$dB	Equal power allocation	6.485	9.548	13.233	15.936	16.110
$p_p = 5$dB	Uniform power allocation	4.100	5.529	7.504	8.997	11.298

Table 4.1: Average Run Time (in seconds) for three scenarios of Algorithm 4.2

In Table 4.1, we display the average run time (in seconds) of three optimization scenarios defined above with a given tolerance $\iota = 10^{-5}$. We can observe that, the running times for all three scenarios are increasing with respect to K. Moreover, more constraints will introduce a longer operation time. Then, uniform power allocation has the smallest number of constraints and, therefore, the running time for this scenario is the shortest, while Algorithm 1 experiences the longest running time but the highest minimum achievable SE performance.

4.7 Conclusion

This chapter has studied the sum SE and EE performance of a multi-pair two-way half-duplex DF relaying system with ZF processing and imperfect CSI. Note that this setup extends considerably a stream of recent studies on massive MIMO relaying by leveraging tools of Wishart matrix theory. In particular, a large-scale approximation of the achievable SE was deduced. Meanwhile, a practical power consumption model was characterized to study the EE performance. Furthermore, in view of approximations, three specific

power scaling laws were investigated to present how the transmit powers of each pilot symbol, each user and the relay can be scaled to improve the system performance. These results have their own adding value as they translate mathematical formulations into system design guidelines for power savings. Finally, a formulated optimization problem was studied to optimize the minimum achievable SE among all user pairs. Our numerical results demonstrated emphatically that the proposed system with ZF processing is able to enhance the EE while preserving the SE performance with moderate system configurations. Moreover, the simulation results of the optimization problem demonstrated that our proposed max-min fairness scheme can achieve higher minimum achievable SE among user pairs compared with the benchmark schemes where equal user power and uniform power allocation are applied.

Chapter 5

Space-Constrained Multi-Pair Two-Way Relaying System

This chapter is based on our works in [C1], [C2], [J3].

5.1 Introduction

In the previous chapter, our studies on the multi-pair two-way relaying system focus on the uncorrelated antenna arrays at the relay. However, an excessive number of antennas in physically constrained arrays give rise to increasing spatial correlation. Moreover, the varying channel between transmission frames results in channel aging. Therefore, this chapter focuses on the performance analysis of a space-constrained multi-pair two-way half-duplex DF relaying system via exploiting the spatial correlation and the effect of channel aging.

As a promising technique for next-generation wireless communications, relay technologies can enhance cellular coverage and improve network capacity and throughput in relay-aided communication systems [131, 132]. A two-way relay system where users can exchange information via a shared relay with a shorter required time has been introduced to improve SE [62, 105, 133]. Several relay schemes have been widely studied, such as decode-and-forward (DF), amplify-and-forward (AF), which have been introduced in Chapter 2.4.2 [43, 130, 134]. AF protocol is commonly used in most previous

studies on multi-pair two-way relaying. Normally, the DF two-way relaying can perform separate linear processing on each relaying communication direction [68, 110]. Ideally, the SE of full-duplex two-way massive MIMO relay systems is expected to double compared to half-duplex [62, 135]. However, in practice, due to the immense power difference between the self-loop interference and the desired signal and hardware deficiencies, perfect self-loop interference cancellation is hard to acquire. In this case, half-duplex is considered, where the relay transmits and receives in orthogonal frequency or time resources, having the practical relevance and simplicity of implementation [68, 132].

As introduced in Chapter 2, massive MIMO has been popular because of the ability to achieve higher data rates and improve link reliability by serving numerous users simultaneously and providing large array gains [9, 44]. Therefore, it is of great interest to incorporate massive MIMO into multi-pair two-way relaying. With massive arrays at the relay, the main factor limiting system performance, inter-pair co-channel interference, could be mitigated to improve the system performance and network capacity [9, 99, 106, 131]. Note that deploying a large number of antennas in a physically constrained space would increase the spatial correlation because of insufficient inter-antenna distance [9, 76, 136]. Although both spatial correlation and mutual coupling are widely studied in the MIMO literature [137, 138], we neglect the effects of mutual coupling with the assumption that impedance matching techniques compensate them for tractable analysis [92]. The impacts of spatial correlation on ergodic capacity and symbol error rate (SER) in one-way relay systems with single-antenna nodes are studied in [139, 140, 141, 142]. [143] and [62] derived asymptotic power scaling laws with the Zero-forcing reception/Zero-forcing transmission (ZFR/ZFT) and Maximum ratio combining/Maximum ratio transmission (MRC/MRT), respectively. Both works considered correlated channels while [143] illustrated a single-pair massive MIMO full-duplex relay with only two MIMO users, and

[62] studied a two-way full-duplex multi-pair massive MIMO relay. [144] derived the SE lower-bound for a spatially correlated massive MIMO two-way full-duplex AF relay, valid for an arbitrary number of relay antennas. [145, 146] studies a multi-pair two-way full-duplex AF massive MIMO relaying system with non-negligible direct links between all user pairs. Furthermore, the spatial correlation between adjacent antennas could lead to the similarity among channels. Exploiting spatial correlation may unexpectedly alleviate the requirement of CSI acquisition [17, 147].

Additionally, channel aging making the estimated CSI out of date between transmission frames has also become an interesting topic in the multi-pair massive MIMO relay system, most of the relevant studies are operated in full-duplex AF mode [148, 149, 150] or half-duplex AF mode [148], while multi-pair two-way half-duplex DF relay system with channel aging is overlooked. This can also be analyzed in the device-to-device (D2D) communications. The deployment of a two-way relay allows resource limited device pairs to exchange information with each other simultaneously with the aid of the relay. This deployment improves the SE performance and allows longer distance communication with D2D mode [104, 142, 149, 151].

Because of the above-mentioned considerations, we propose a method that involves deactivating a subset of relay antennas and activating the remaining antennas to acquire CSI at the channel estimation stage. The CSI of deactivated relay antennas is obtained by averaging the instantaneous CSI of adjacent activated antennas by exploiting the similarity between spatially correlated channels. Moreover, the proposed analysis could trade off the computational complexity and power consumption of Radio frequency (RF) chains in the channel estimation stage against the resulting estimation accuracy. This also motivates us to study the effects of the number of relay antennas without explicit CSI on the system performance.

To the best of our knowledge, no previous work has jointly studied incomplete CSI and spatial correlation in the DF multi-pair half-duplex two-

way relay systems. In this case, we focus on a space-constrained multi-pair two-way half-duplex DF relaying system with linear processing and incomplete CSI acquisition [69, 111]. Although our studies can be applied in both Time-division-duplex (TDD) and Frequency-division-duplex (FDD) scenarios, we concentrate on TDD systems in this chapter for their simplicity and practical importance in massive MIMO [9, 152]. A detailed analysis of the sum SE with MRT and Zero-forcing (ZF) processing is presented and we illustrate a practical power consumption model to analyze the EE performance of the proposed relaying system. In addition, incomplete CSI acquisition is studied thoroughly to further make use of the spatial correlation. The effects of channel aging are also presented with MRT processing to evaluate the effects of outdated CSI. Specifically, the main contributions of this chapter can be summarized as

- We study a multi-pair two-way DF relaying massive MIMO system deployed in a physically-constrained space. This gives rise to an interesting trade-off between antenna gain and spatial correlation with an increasing number of antennas. The large-scale approximations of the sum SE with MRT processing and ZF processing are presented with a large but finite number of antennas and imperfect CSI.

- We evaluate the impact of channel aging [148]. We analyze the SE performance of the proposed system by exploiting the spatial correlation and the time correlation generated by channel aging jointly with MRT processing schemes.

- We investigate a practical and common power consumption model derived from [17, 43]. It is employed to analyze the EE performance of the proposed system with different linear processing schemes, and reveal the gains of incomplete CSI acquisition.

- We employ and analyse a low-complexity incomplete CSI acquisition scheme that exploits the spatial correlation in space-constrained mas-

sive MIMO inspired by [17]. We analyze the system performance and derive the computational complexity analysis to reveal the benefits of the incomplete CSI acquisition.

Based on the above contributions, this chapter has also revealed a number of insights which we summarise below:

- The space-constrained deployment of increasing antennas at the relay introduces a trade-off in spatial diversity where, by increasing the numbers of antennas as signal sources diversity is enhanced, while the resulting diminishing inter-antenna spacing introduces spatial correlation and limits the diversity gains;

- The increased spatial correlation due to the space-constrained deployment can be readily exploited through incomplete CSI acquisition, where significant complexity gains in CSI acquisition are traded-off with the impact of inaccurate CSI on the system SE;

- The space-constrained antenna deployment results in saturating gains in SE as the number of antennas increases. As the consumed power persistently increases with the increase in antenna numbers, this results in a concave EE performance with antenna numbers and scenario-dependent optimal numbers of antennas;

- The time correlation is modelled by the channel aging effect as a result of channel variation between transmissions. When the antenna deployment is space-constrained, the degree of spatial correlation due to antenna proximity and time correlation due to channel aging can be jointly tolerated in the massive MIMO regime without significant degradation of performance.

- Incomplete CSI provides higher EE performance with respect to full CSI in such scenarios, while reducing the CSI acquisition complexity and even the total power consumption. To the best of our knowledge,

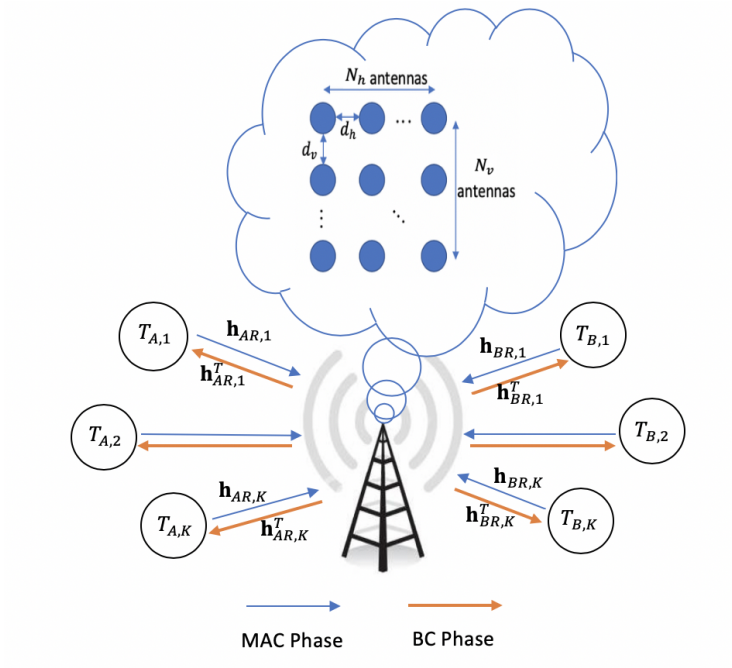

Figure 5.1: Multi-pair two-way DF relaying system with space-constrained massive MIMO relay.

no other previous work has studied CSI relaxation with spatial correlation and a systemic complexity analysis in the proposed scenario. Our results first show that in space-constrained antenna deployment, acquiring CSI for down to half the deployed antennas achieves negligible SE performance loss, while significantly enhancing the system's EE, especially with moderate spatial correlation.

5.2 System Model

5.2.1 Spatially-Correlated Channel Model

As shown in Fig. 5.1, a space-constrained multi-pair two-way half-duplex DF relay system is investigated. K pairs of single-antenna users are defined as $\mathrm{T}_{A,i}$ and $\mathrm{T}_{B,i}$, where subscripts A and B denote the communication nodes in any pair of i, $i = 1, \ldots, K$. User pairs can exchange information with each other via the relay T_R equipped with $N_R \gg K$ closely-spaced antennas. The spatially-correlated Rayleigh fading system under TDD protocol is adopted [56, 113, 153]. The uplink and downlink channels between

$\mathrm{T}_{X,i}$ $(X = A, B)$ and T_R can be defined as $\mathbf{h}_{XR,i} \in \mathbb{C}^{N_R \times 1}$ and $\mathbf{h}_{XR,i}^T$, $i = 1, ..., K$, respectively. Hence, the uplink channel matrix can be further given by $\mathbf{H}_{XR} = [\mathbf{h}_{XR,1}, ..., \mathbf{h}_{XR,K}] \in \mathbb{C}^{N_R \times K}$, where $X = A, B$. In particular, the uplink channel matrix from $\mathrm{T}_{X,i}$ to the relay in the spatially-correlated system can be defined as [56, 154]

$$\mathbf{h}_{XR,i} = \mathbf{A}_i^H \mathbf{g}_{XR,i}, \tag{5.1}$$

where $\mathbf{g}_{XR,i} \sim \mathbb{CN}(0, \beta_{XR,i}\mathbf{I}_{L_i})$ and L_i denotes the number of signal propagation paths with different angles of departure. For simplicity, we consider $L_i = L$ $(i = 1, ..., K)$ in the following. $\beta_{AR,i}$ and $\beta_{BR,i}$ represent the slow large fading effect, composing path loss and shadowing effect. When the uniform linear array (ULAs) topology is applied, where $N_h = N_R$ and $N_v = 1$. In this case, $\mathbf{A}_i \in \mathbb{C}^{L \times N_R}$, the transmit steering matrix at $T_{X,i}$, can be given by [17, 34]

$$\mathbf{A}_i = \tfrac{1}{\sqrt{L}}[\mathbf{a}^{\mathrm{T}}(\theta_{i,1}), ..., \mathbf{a}^{\mathrm{T}}(\theta_{i,L})]^{\mathrm{T}}. \tag{5.2}$$

Here, $\theta_{i,l}$, $l = 1, ..., L$ represents the spreading angle describing the directions of departure. The corresponding steering vectors of ULA topology are in terms of [56]

$$\mathbf{a}(\theta_{i,l}) = [1, e^{j2\pi d sin(\theta_{i,l})}, ..., e^{j2\pi(N_R-1)d sin(\theta_{i,l})}], \tag{5.3}$$

where $d = \frac{D_{tot}}{N_R - 1}$ is the inter-antenna distance with D_{tot}, the total spacing length normalized by the carrier wavelength λ. Similarly, if the topology of uniform rectangular arrays (URAs) is applied, $\mathbf{A}_i \in \mathbb{C}^{L \times N_R}$ is the transmit steering matrix at $T_{X,i}$ given by [34]

$$\mathbf{A}_i = \tfrac{1}{\sqrt{L}}[\mathbf{a}^T(\theta_{i,1}, \phi_{i,1}), ..., \mathbf{a}^T(\theta_{i,L}, \phi_{i,L})]^T, \tag{5.4}$$

while the respective horizontal and vertical array steering vectors can be characterized as [56]

$$\mathbf{a}_h(\theta_{i,l},\phi_{i,l}) = [1, e^{j2\pi[d_h sin(\theta_{i,l})sin(\phi_{i,l})]}, \dots, e^{j2\pi[(N_h-1)d_h sin(\theta_{i,l})sin(\phi_{i,l})]}], \tag{5.5}$$

$$\mathbf{a}_v(\theta_{i,l},\phi_{i,l}) = [1, e^{j2\pi[d_v sin(\theta_{i,l})cos(\phi_{i,l})]}, \dots, e^{j2\pi[(N_v-1)d_v sin(\theta_{i,l})cos(\phi_{i,l})]}], \tag{5.6}$$

where $\theta_{i,l}$ and $\phi_{i,l}$ $(l = 1, ..., L)$ are elevation and azimuth angles of departure respectively [57]. The steering vector $\mathbf{a}(\theta_{i,l},\phi_{i,l})$ for the specific departure direction $(\theta_{i,l},\phi_{i,l})$ at the i-th user can be decomposed as

$$\begin{aligned}\mathbf{a}(\theta_{i,l},\phi_{i,l}) &= \mathrm{vec}\big(\mathbf{a}_h(\theta_{i,l},\phi_{i,l})^{\mathrm{T}}\mathbf{a}_v(\theta_{i,l},\phi_{i,l})\big) \\ &= \Big[1, e^{j2\pi[d_h sin(\theta_{i,l})sin(\phi_{i,l})]}, \dots, e^{j2\pi[(N_h-1)d_h sin(\theta_{i,l})sin(\phi_{i,l})+(N_v-1)d_v sin(\theta_{i,l})cos(\phi_{i,l})]}\Big],\end{aligned} \tag{5.7}$$

where the vector valued operator $\mathrm{vec}(\cdot)$ can map a $m \times n$ matrix to a $mn \times 1$ column vector. The total number of relay antennas can be defined as $N_R = N_h \times N_v$. N_h and N_v stand for the number of antennas deployed in the horizontal and vertical directions respectively. Moreover, $d_{\{h,v\}} = \frac{D_{\{h,v\}}}{N_{\{h,v\}}-1}$ is the inter-antenna distance where $D_{\{h,v\}}$ is the respective horizontal and vertical lengths of the antenna arrays normalized by the carrier wavelength λ. For sake of simplicity, we assume that $d_h = d_v = d$ and $N_h = N_v$. Note that in practice, the inter-user distance is greater than λ, it is readily assumed that there is no receive correlation [56].

5.2.2 Channel Aging

Similar to [148, 149, 150], we assume that the channel varies between transmissions and results in channel aging. To model the time correlation generated by channel aging between consecutive channel instantiations, the time-variant channel vector at the time instant n after the most recent channel estimation can be given by

$$\mathbf{h}_{XR,i}(n) = \rho\mathbf{h}_{XR,i}(n-1) + \mathbf{e}_{XR,i}(n) = \rho^{n-1}\mathbf{h}_{XR,i}(1) + \sum_{k=2}^{n}\rho^{n-k}\mathbf{e}_{XR,i}(k), \tag{5.8}$$

where $\rho \in [0,1]$ is the time correlation parameter and $\mathbf{e}_{XR,i}(n)$ is the channel aging error at the time instant n with zero mean and $\sigma^2_{e_{XR,i}}(n)$. For notational simplicity, we assume that all channel vectors experience the same time correlation parameter. In (5.1), we consider that $\mathbf{g}_{XR,i}$ varies between transmissions and $\mathbf{A}_i$ is assumed to be fixed during all time instants at $T_{X,i}$, $X = A, B$, $i = 1, ..., K$. In addition, the channel matrix at the time instant n can be further defined as $\mathbf{H}_{XR}(n) = [\mathbf{h}_{XR,1}(n), ..., \mathbf{h}_{XR,K}(n)] \in \mathbb{C}^{N_R \times K}$, $X = A, B$.

5.2.3 Multiple Access Broadcast Transmission Process

5.2.3.1 Fundamental Transmission Process

In our study, the data transmission process consists of two equal time-slot phases, and this two-phase protocol is called Multiple Access Broadcast (MABC) protocol [68]. In the Multiple Access Channel (MAC) phase, all users transmit signals to the relay at the same time, and then the received signal at the relay is obtained as [43, 69, 155]

$$\mathbf{y}_r = \sum_{i=1}^{K} \left(\sqrt{p_{A,i}} \mathbf{h}_{AR,i} x_{AR,i} + \sqrt{p_{B,i}} \mathbf{h}_{BR,i} x_{BR,i} \right) + \mathbf{n}_R, \tag{5.9}$$

where $x_{XR,i}$ is the Gaussian signal with zero mean and unit power transmitted by the i-th user $T_{X,i}$. $p_{X,i}$ is the transmit power of $\mathrm{T}_{X,i}$ $(X = A, B)$. $\mathbf{n}_R$ represents the Additive White Gaussian noise (AWGN) vector with (i.i.d) $\mathbb{CN}(0,1)$ elements at the relay. We assume low-complexity linear processing at the relay, with which the transformed signal is expressed as

$$\mathbf{z}_r = \mathbf{F}_{MAC} \mathbf{y}_r \ , \tag{5.10}$$

where $\mathbf{F}_{MAC} \in \mathbb{C}^{2K \times N_R}$ is the linear receiver matrix.

Then, in the Broadcast Channel (BC) phase, the relay decodes the received signal and then encodes and broadcasts the information to users [69]. The linear precoding matrix $\mathbf{F}_{BC} \in \mathbb{C}^{N_R \times 2K}$ is deployed to generate the trans-

mit signal of the relay as

$$\mathbf{y}_t = \rho_{DF}\mathbf{F}_{BC}\mathbf{x}, \tag{5.11}$$

where $\mathbf{x} = \begin{bmatrix} \mathbf{x}_A \\ \mathbf{x}_B \end{bmatrix}$ displays the decoded signal and ρ_{DF} is the normalization coefficient related to the relay power constraint $E\left\{||\mathbf{y}_t||^2\right\} = p_r$. To this end, the received signals at $\mathrm{T}_{X,i}$ $(X = A, B)$ can be given by

$$z_{X,i} = \mathbf{h}_{XR,i}^T\mathbf{y}_t + n_{X,i}, \tag{5.12}$$

and considering the standard AWGN at $T_{X,i}$, $n_{X,i} \sim \mathbb{CN}(0,1)$, where $X = A, B$.

5.2.3.2 Transmission Process with Channel aging

As per the MABC protocol [68], the two-way relayed data transmission process is also divided into two stages with equal time slots. At the time instant n, all devices transmit signals to the relay simultaneously in the MAC phase and the received signal at the relay is given by [69, 150, 155]

$$\mathbf{y}_r(n) = \sum_{i=1}^{K}\sum_{X=A,B}\left(\sqrt{p_{X,i}}\mathbf{h}_{XR,i}(n)s_{XR,i}(n)\right) + \mathbf{n}_R(n), \tag{5.13}$$

where $s_{XR,i}(n)$ is the Gaussian signal with zero mean and unit power transmitted by the i-th device $T_{X,i}$ at the time instant n, $p_{X,i}$ is the average transmit power of $\mathrm{T}_{X,i}$, $X = A, B$. $\mathbf{n}_R(n)$ is the vector of AWGN with elements satisfying (i.i.d) $\mathbb{CN}(0,1)$. Assuming low-complexity linear processing at the relay, the transformed signal can be given by

$$\mathbf{z}_r(n) = \mathbf{F}_{MAC}(n)\mathbf{y}_r(n)\ . \tag{5.14}$$

Here, $\mathbf{F}_{MAC}(n) \in \mathbb{C}^{2K\times N_R}$ is the linear receiver matrix.

In the BC phase, the relay first decodes the received information, then encodes and broadcasts it to device pairs [69]. The linear precoding matrix $\mathbf{F}_{BC}(n) \in \mathbb{C}^{N_R\times 2K}$ in the BC phase is applied to obtain the transmit signal of

the relay

$$\mathbf{y}_t(n) = \rho_{DF}(n)\mathbf{F}_{BC}(n)\mathbf{s}(n), \tag{5.15}$$

where $\mathbf{s}(n) = \left[\mathbf{s}_A^T(n), \mathbf{s}_B^T(n)\right]^T$ denotes the decoded signal at the time instant n and $\rho_{DF}(n)$ is the normalization coefficient determined by the average relay power $\mathbb{E}\left\{||\mathbf{y}_t(n)||^2\right\} = p_r$. With the standard AWGN $n_{X,i}(n) \sim \mathbb{CN}(0,1)$, the received signal at the i-th device $T_{X,i}$ $(i = 1, ..., K, X = A, B)$ is given by

$$z_{X,i}(n) = \mathbf{h}_{XR,i}^T(n)\mathbf{y}_t(n) + n_{X,i}(n). \tag{5.16}$$

5.2.4 Linear Processing and Channel Estimation

5.2.4.1 Linear Processing

We consider two linear processing methods, namely, MRT and ZF processing. For brevity, we assume $\mathbf{F}_{MAC}$ and $\mathbf{F}_{BC}$ in (5.10)-(5.11) as the general linear processing matrices in the MAC phase and BC phase respectively. Further respective calculations of $\mathbf{F}_{MAC} \in \mathbb{C}^{2K \times N_R}$ and $\mathbf{F}_{BC} \in \mathbb{C}^{N_R \times 2K}$ for MRT and ZF processing are studied in Chapter 5.3.2. First, the MRT and ZF processing matrices for the proposed system are given by

MRT Processing: The linear receiver matrix in the MAC phase can be given by

$$\mathbf{F}_{MAC} = \left[\hat{\mathbf{H}}_{AR}, \hat{\mathbf{H}}_{BR}\right]^H, \tag{5.17}$$

while the linear precoding matrix in the BC phase can be defined as

$$\mathbf{F}_{BC} = \left[\hat{\mathbf{H}}_{BR}, \hat{\mathbf{H}}_{AR}\right]^*. \tag{5.18}$$

Moreover, the respective MRC/MRT processing matrices $\mathbf{F}_{MAC}(n) \in \mathbb{C}^{2K \times N_R}$ and $\mathbf{F}_{BC}(n) \in \mathbb{C}^{N_R \times 2K}$ with channel aging at the time instant n can be given by

$$\mathbf{F}_{MAC}(n) = \left[\hat{\mathbf{H}}_{AR}(n), \hat{\mathbf{H}}_{BR}(n)\right]^H, \tag{5.19}$$

$$\mathbf{F}_{BC}(n) = \left[\hat{\mathbf{H}}_{BR}(n), \hat{\mathbf{H}}_{AR}(n)\right]^*. \tag{5.20}$$

Here, $\hat{\mathbf{H}}_{XR}(n)$ represents the CSI estimates at the time instant n, $X = A, B$. For notational simplicity, we define that $\mathbf{F}_{MAC}^{AR}(n) \in \mathbb{C}^{K \times N_R}$, $\mathbf{F}_{MAC}^{BR}(n) \in \mathbb{C}^{K \times N_R}$ are the first K rows and the rest K rows of $\mathbf{F}_{MAC}(n)$, respectively. $\mathbf{F}_{BC}^{RB}(n) \in \mathbb{C}^{N_R \times K}$, $\mathbf{F}_{BC}^{RA}(n) \in \mathbb{C}^{N_R \times K}$ represent the first K columns of and the second K columns of $\mathbf{F}_{BC}(n)$, respectively.

ZF Processing: The linear receiver matrix in the MAC phase is mathematically presented as

$$\mathbf{F}_{MAC} = \left(\left[\hat{\mathbf{H}}_{AR}, \hat{\mathbf{H}}_{BR} \right]^H \left[\hat{\mathbf{H}}_{AR}, \hat{\mathbf{H}}_{BR} \right] \right)^{-1} \left[\hat{\mathbf{H}}_{AR}, \hat{\mathbf{H}}_{BR} \right]^H, \tag{5.21}$$

meanwhile, the linear precoding matrix in the BC phase can be written as

$$\mathbf{F}_{BC} = \left[\hat{\mathbf{H}}_{BR}, \hat{\mathbf{H}}_{AR} \right]^* \left(\left[\hat{\mathbf{H}}_{BR}, \hat{\mathbf{H}}_{AR} \right]^T \left[\hat{\mathbf{H}}_{BR}, \hat{\mathbf{H}}_{AR} \right]^* \right)^{-1}, \tag{5.22}$$

here, in both MRT and ZF processing expressions (5.17)-(5.18) and (5.21)-(5.22), $\hat{\mathbf{H}}_{XR}, X = A, B$ represents the estimated channel matrices which would be defined later.

Furthermore, with the expression of the linear precoding matrix $\mathbf{F}_{BC}$, the normalization coefficient in the BC phase with (5.11) can be given by

$$\rho_{DF} = \sqrt{\frac{p_r}{E\left\{ \left|\left| \mathbf{F}_{BC} \right|\right|_{\mathrm{F}}^2 \right\}}}. \tag{5.23}$$

Similarly, the normalization coefficient in the BC phase with channel aging at the time instant n presented in (5.15) can be expressed as

$$\rho_{DF}(n) = \sqrt{\frac{p_r}{E\left\{ \left|\left| \mathbf{F}_{BC}(n) \right|\right|_{\mathrm{F}}^2 \right\}}}. \tag{5.24}$$

5.2.4.2 Channel Estimation

In addition to linear processing methods, imperfect CSI is also considered as perfect CSI is not attainable in practical applications. To obtain channel estimation at the relay, transmitting pilot symbols is employed in TDD sys-

tems [17, 69]. In this case, η_p symbols are used as pilots for channel estimation in each coherence interval with η_{coh} symbols. Accordingly, we apply an minimum mean square error (MMSE) channel estimator in which case the channel estimates are given by [50, 99]

$$\mathbf{h}_{XR,i} = \hat{\mathbf{h}}_{XR,i} + \Delta\mathbf{h}_{XR,i} = \mathbf{A}_i^H \hat{\mathbf{g}}_{XR,i} + \mathbf{A}_i^H \mathbf{q}_{XR,i}, \tag{5.25}$$

where $\hat{\mathbf{h}}_{XR,i}$ and $\Delta\mathbf{h}_{XR,i}$ are the i-th columns of the estimated matrices $\hat{\mathbf{H}}_{XR}$ and estimation error matrices $\Delta\mathbf{H}_{XR}, X = A, B$, respectively. Remark that $\hat{\mathbf{g}}_{XR,i}$, derived from $\mathbf{g}_{XR,i}$ defined in (5.1), is uncorrelated with $\mathbf{q}_{XR,i}$. The elements in $\hat{\mathbf{g}}_{XR,i}$ and $\mathbf{q}_{XR,i}$ are Gaussian random variables with zero mean, variance $\sigma^2_{XR,i} = \frac{\eta_p p_p \beta^2_{XR,i}}{1+\eta_p p_p \beta_{XR,i}}$ and $\tilde{\sigma}^2_{XR,i} = \frac{\beta_{XR,i}}{1+\eta_p p_p \beta_{XR,i}}$ $(X = A, B,\ i = 1, ..., K)$ respectively, while p_p is the transmit power of pilot symbol [69].

Similarly, we can obtain the channel estimates for all time instants by applying the MMSE estimator. In this chapter, we assume that CSI is only estimated at the time instant 1 and explore the SE degradation in the following time instants; therefore, the channel estimates at the time instant 1 can be expressed as

$$\mathbf{h}_{XR,i}(1) = \hat{\mathbf{h}}_{XR,i}(1) + \Delta\mathbf{h}_{XR,i}(1) = \mathbf{A}_i^H \hat{\mathbf{g}}_{XR,i}(1) + \mathbf{A}_i^H \mathbf{q}_{XR,i}(1), \tag{5.26}$$

$\hat{\mathbf{h}}_{XR,i}(1)$ and $\Delta\mathbf{h}_{XR,i}(1)$ are the estimated channel vector and the estimation error vector at the i-th device respectively. Furthermore, the respective estimated channel matrix and estimation error matrix at the time instant 1 can be given by $\hat{\mathbf{H}}_{XR}(1)$ and $\Delta\mathbf{H}_{XR}(1)$. The elements in $\hat{\mathbf{g}}_{XR,i}(1)$ and $\mathbf{q}_{XR,i}(1)$ are Gaussian random variables with zero mean, variance $\sigma^2_{XR,i}(1)$ and $\sigma^2_{\Delta h_{XR,i}}(1)$, $X = A, B$, $i = 1, ..., K$, respectively. Supported by (5.26) and the effect of time correlation defined in (5.8), the respective estimated channel vectors and estimation error vectors of the i-th device $T_{XR,i}$ $(X = A, B,\ i = 1, ..., K)$ in the

following time instants can be further simplified as

$$\hat{\mathbf{h}}_{XR,i}(n) = \rho^{n-1}\hat{\mathbf{h}}_{XR,i}(1) = \rho^{n-1}\mathbf{A}_i^H\hat{\mathbf{g}}_{XR,i}(1), \tag{5.27}$$

$$\Delta\mathbf{h}_{XR,i}(n) = \rho^{n-1}\Delta\mathbf{h}_{XR,i}(1) = \rho^{n-1}\mathbf{A}_i^H\mathbf{q}_{XR,i}(1), \tag{5.28}$$

while the relevant channel estimates at the time instant n could be obtained via (5.8), (5.27)-(5.28) and the detailed expression can be given by

$$\mathbf{h}_{XR,i}(n) = \rho^{n-1}\mathbf{A}_i^H\hat{\mathbf{g}}_{XR,i}(1) + \rho^{n-1}\mathbf{A}_i^H\mathbf{q}_{XR,i}(1) + \sum_{k=2}^{n}\rho^{n-k}\mathbf{e}_{XR,i}(k). \tag{5.29}$$

5.3 System Performance Analysis

5.3.1 Exact results of Spectral Efficiency

5.3.1.1 Numerical expressions

In this sub-chapter, the sum SE performance of the proposed system is investigated. In the MAC phase, based on (5.9)-(5.10), the transformed signal at the relay associated with the i-th user pair is given by

$$z_{R,i} = z_{r,i}^A + z_{r,i}^B, \tag{5.30}$$

where $z_{r,i}^X$ is defined as

$$\begin{aligned} z_{r,i}^X = &\underbrace{\sqrt{p_{X,i}}\left(\mathbf{F}_{MAC,i}^{AR} + \mathbf{F}_{MAC,i}^{BR}\right)\hat{\mathbf{h}}_{XR,i}x_{X,i}}_{\text{desired signal}} \\ &+ \underbrace{\sqrt{p_{X,i}}\left(\mathbf{F}_{MAC,i}^{AR} + \mathbf{F}_{MAC,i}^{BR}\right)\Delta\mathbf{h}_{XR,i}x_{X,i}}_{\text{estimation error}} \\ &+ \underbrace{\sum_{j\neq i}\sqrt{p_{X,j}}\left(\mathbf{F}_{MAC,i}^{AR} + \mathbf{F}_{MAC,i}^{BR}\right)\mathbf{h}_{XR,j}x_{X,j}}_{\text{inter-user interference}} + \underbrace{\mathbf{F}_{MAC,i}^{XR}\mathbf{n}_R}_{\text{noise}}, \end{aligned} \tag{5.31}$$

and $\mathbf{z}_r = \begin{bmatrix} \mathbf{z}_r^A \\ \mathbf{z}_r^B \end{bmatrix} \in \mathbb{C}^{2K\times 1}$, with $\mathbf{z}_r^X \in \mathbb{C}^{K\times 1}$ $(X = A, B)$ as shown in (5.10).

Meanwhile, the transformed signal vector at the relay can be expressed as $\mathbf{z}_R = (\mathbf{z}_r^A + \mathbf{z}_r^B) \in \mathbb{C}^{K\times 1}$. With the assistance of (5.30)-(5.31), we can specify the power of the estimation error, inter-user interference and compound noise in $z_{R,i}$ as

$$A_i = \sum_{X=A,B} p_{X,i} \left(\left|\mathbf{F}_{MAC,i}^{AR} \Delta\mathbf{h}_{XR,i}\right|^2 + \left|\mathbf{F}_{MAC,i}^{BR} \Delta\mathbf{h}_{XR,i}\right|^2 \right), \tag{5.32}$$

$$B_i = \sum_{X=A,B} \sum_{j\neq i} p_{X,j} \left(\left|\mathbf{F}_{MAC,i}^{AR} \mathbf{h}_{XR,j}\right|^2 + \left|\mathbf{F}_{MAC,i}^{BR} \mathbf{h}_{XR,j}\right|^2 \right), \tag{5.33}$$

$$C_i = \left|\left|\mathbf{F}_{MAC,i}^{AR}\right|\right|^2 + \left|\left|\mathbf{F}_{MAC,i}^{BR}\right|\right|^2, \tag{5.34}$$

respectively. With the expressions of desired signals in (5.31), the signal-to-noise-plus-interference ratio (SINR) from $T_{X,i}$ $(X = A,B)$ to the relay can be obtained as

$$\mathrm{SINR}_{XR,i} = \frac{p_{X,i} \left(\left|\mathbf{F}_{MAC,i}^{AR} \hat{\mathbf{h}}_{XR,i}\right|^2 + \left|\mathbf{F}_{MAC,i}^{BR} \hat{\mathbf{h}}_{XR,i}\right|^2 \right)}{A_i + B_i + C_i}. \tag{5.35}$$

In addition, this chapter applies the standard lower capacity bound related to the worst-case uncorrelated additive noise [37, 69]. The lower bounding method was suggested in [156] and to avoid repetition, a more systematic study is leaning on the studies from [156]. To this end, the achievable SE of the i-th user pair in the MAC phase can be given by

$$R_{1,i} = \frac{\eta_{coh} - \eta_p}{2\eta_{coh}} \times \mathbb{E}\left\{ \log_2 \left(1 + \frac{p_{A,i}\left(\left|\mathbf{F}_{MAC,i}^{AR} \hat{\mathbf{h}}_{AR,i}\right|^2 + \left|\mathbf{F}_{MAC,i}^{BR} \hat{\mathbf{h}}_{AR,i}\right|^2 \right) + p_{B,i}\left(\left|\mathbf{F}_{MAC,i}^{AR} \hat{\mathbf{h}}_{BR,i}\right|^2 + \left|\mathbf{F}_{MAC,i}^{BR} \hat{\mathbf{h}}_{BR,i}\right|^2 \right)}{A_i + B_i + C_i} \right) \right\}. \tag{5.36}$$

Meanwhile, the SE of the user $T_{X,i}$ (where $X = A,B$) to the relay can be expressed as

$$R_{XR,i} = \frac{\eta_{coh} - \eta_p}{2\eta_{coh}} \times \mathbb{E}\left\{ \log_2(1 + \mathrm{SINR}_{XR,i}) \right\}. \tag{5.37}$$

In the BC phase, $\mathbf{F}_{BC}$ is applied to generate the relay's transmit signal, and then the received signal at $T_{X,i}$ can be obtained by (5.12). For a more detailed description, $z_{A,i}$ can be given by

$$\begin{aligned} z_{A,i} = & \underbrace{\rho_{DF}\hat{\mathbf{h}}_{AR,i}^{T}\mathbf{F}_{BC,i}^{RA}x_{B,i}}_{\text{desired signal}} + \underbrace{\rho_{DF}\Delta\mathbf{h}_{AR,i}^{T}\mathbf{F}_{BC,i}^{RA}x_{B,i}}_{\text{estimation error}} \\ & \underbrace{+\rho_{DF}\sum_{j=1}^{K}\mathbf{h}_{AR,i}^{T}\mathbf{F}_{BC,j}^{RB}x_{A,j} + \rho_{DF}\sum_{j\neq i}\mathbf{h}_{AR,i}^{T}\mathbf{F}_{BC,j}^{RA}x_{B,j}}_{\text{inter-user interference}} + \underbrace{n_{A,i}}_{\text{noise}}. \end{aligned} \tag{5.38}$$

Similarly, to obtain $z_{B,i}$, the subscripts "AR", "BR" in the channel vectors and estimation error vectors, the subscripts "RA", "RB" in linear precoding vectors, and "A", "B" in signal and noise terms can be replaced with the subscripts "BR", "AR", the subscripts "RB", "RA", and "B", "A" in $z_{A,i}$, respectively. With the assistance of (5.38), we can obtain the $\text{SINR}_{RX,i}$ from the relay to $T_{X,i}$ $(X = A, B)$ straightforward,

$$\text{SINR}_{RX,i} = \frac{\left|\hat{\mathbf{h}}_{XR,i}^{T}\mathbf{F}_{BC,i}^{RX}\right|^2}{\left|\Delta\mathbf{h}_{XR,i}^{T}\mathbf{F}_{BC,i}^{RX}\right|^2 + \sum_{j=1}^{K}\left(\left|\mathbf{h}_{XR,i}^{T}\mathbf{F}_{BC,j}^{RA}\right|^2 + \left|\mathbf{h}_{XR,i}^{T}\mathbf{F}_{BC,j}^{RB}\right|^2\right) - \left|\mathbf{h}_{XR,i}^{T}\mathbf{F}_{BC,i}^{RX}\right|^2 + \frac{1}{\rho_{DF}^2}}. \tag{5.39}$$

Consequently, the SE of the relay to the i-th user $T_{X,i}$ $(X = A, B)$ is given by

$$R_{RX,i} = \frac{\eta_{coh} - \eta_p}{2\eta_{coh}} \times \mathbb{E}\Big\{\log_2(1 + \text{SINR}_{RX,i})\Big\}. \tag{5.40}$$

Moreover, the SE of the i-th user pair in the BC phase is obtained by the minimum sum of the end-to-end SE from $T_{A,i}$ to $T_{B,i}$ and the end-to-end SE from $T_{B,i}$ to $T_{A,i}$ [69],

$$R_{2,i} = \min\left(R_{AR,i}, R_{RB,i}\right) + \min\left(R_{BR,i}, R_{RA,i}\right). \tag{5.41}$$

Based on the above, the sum SE of the proposed system can be summed as

the total SE of all user pairs

$$R = \sum_{i=1}^{K} R_i = \sum_{i=1}^{K} \min\left(R_{1,i}, R_{2,i}\right), \tag{5.42}$$

where R_i for the i-th user pair is determined by the minimum SE in the two phases [103, 109].

5.3.1.2 Numerical expressions with Channel aging

Inspired by Chapter 5.3.1.1, we focus on the SE performance with channel aging. First, in the MAC phase, the transformed signals are obtained by applying the linear processing matrix $\mathbf{F}_{MAC}(n)$ to the received signals at the time instant n. Thus, the power of desired signals at $\mathrm{T}_{X,i}$, $(i = 1, ..., K, X = A, B)$ at the time instant n can be given by

$$\mathbb{X}_i^{MAC}(n) = p_{X,i}\left|\hat{\mathbf{h}}_{AR,i}^H(n)\hat{\mathbf{h}}_{XR,i}(n)\right|^2 + p_{X,i}\left|\hat{\mathbf{h}}_{BR,i}^H(n)\hat{\mathbf{h}}_{XR,i}(n)\right|^2, \tag{5.43}$$

where $\mathbb{X} = A, B$. The respective power of estimation and channel aging error, inter-device interference of the post-processing signals $\mathbf{z}_r(n)$ for the i-th device pair at the time instant n can be expressed as

$$\begin{aligned} C_i^{MAC}(n) = &\sum_{X=A,B} p_{X,i}\left(\left|\hat{\mathbf{h}}_{XR,i}^H(n)\Delta\mathbf{h}_{XR,i}(n)\right|^2 + \sum_{j=2}^{n}\left|\rho^{n-j}\hat{\mathbf{h}}_{XR,i}^H(n)\mathbf{e}_{XR,i}(j)\right|^2\right) \\ &+ p_{A,i}\left(\left|\hat{\mathbf{h}}_{BR,i}^H(n)\Delta\mathbf{h}_{AR,i}(n)\right|^2 + \sum_{j=2}^{n}\left|\rho^{n-j}\hat{\mathbf{h}}_{BR,i}^H(n)\mathbf{e}_{AR,i}(j)\right|^2\right) \\ &+ p_{B,i}\left(\left|\hat{\mathbf{h}}_{AR,i}^H(n)\Delta\mathbf{h}_{BR,i}(n)\right|^2 + \sum_{j=2}^{n}\left|\rho^{n-j}\hat{\mathbf{h}}_{AR,i}^H(n)\mathbf{e}_{BR,i}(j)\right|^2\right), \end{aligned} \tag{5.44}$$

$$\begin{aligned} D_i^{MAC}(n) = &\sum_{k\neq i}\sum_{X=A,B} p_{A,k}\left[\left|\hat{\mathbf{h}}_{XR,i}^H(n)\hat{\mathbf{h}}_{AR,k}(n)\right|^2 + \left|\hat{\mathbf{h}}_{XR,i}^H(n)\Delta\mathbf{h}_{AR,k}(n)\right|^2\right] \\ &+ \sum_{k\neq i}\sum_{X=A,B} p_{A,k}\left[\sum_{j=2}^{n}\left|\rho^{n-j}\hat{\mathbf{h}}_{XR,i}^H(n)\mathbf{e}_{AR,k}(j)\right|^2\right] \\ &+ \sum_{k\neq i}\sum_{X=A,B} p_{B,k}\left[\left|\hat{\mathbf{h}}_{XR,i}^H(n)\hat{\mathbf{h}}_{BR,k}(n)\right|^2 + \left|\hat{\mathbf{h}}_{XR,i}^H(n)\Delta\mathbf{h}_{BR,k}(n)\right|^2\right] \\ &+ \sum_{k\neq i}\sum_{X=A,B} p_{B,k}\left[\sum_{j=2}^{n}\left|\rho^{n-j}\hat{\mathbf{h}}_{XR,i}^H(n)\mathbf{e}_{BR,k}(j)\right|^2\right], \end{aligned} \tag{5.45}$$

and the compound noise power is given by

$$E_i^{MAC}(n) = \left|\hat{\mathbf{h}}_{AR,i}^H(n)\right|^2 + \left|\hat{\mathbf{h}}_{BR,i}^H(n)\right|^2. \tag{5.46}$$

In the following, we define that $\chi(1) = \frac{\eta_{coh}-\eta_p}{2\eta_{coh}}$ and $\chi(n) = \frac{1}{2}$ $(n \neq 1)$ with η_{coh} and η_p representing the coherence interval length and pilot sequence length respectively, since CSI is only estimated at the time instant 1. Additionally, supported by (5.43)-(5.46) and the standard lower capacity bound with the worst-case uncorrelated additive noise [155, 156], the respective SE of the i-th device pair and the SE of the device $T_{X,i}$ $(X = A, B,\ i = 1, ..., K)$ to the relay are defined as

$$R_{1,i}(n) = \chi(n) \times \mathbb{E}\left\{\log_2\left(1 + \frac{\sum\limits_{\mathbb{X}=A,B} \mathbb{X}_i^{MAC}(n)}{C_i^{MAC}(n) + D_i^{MAC}(n) + E_i^{MAC}(n)}\right)\right\}. \tag{5.47}$$

$$R_{XR,i}(n) = \chi(n) \times \mathbb{E}\left\{\log_2\left(1 + \frac{\mathbb{X}_i^{MAC}(n)}{C_i^{MAC}(n) + D_i^{MAC}(n) + E_i^{MAC}(n)}\right)\right\}. \tag{5.48}$$

In the BC phase, $\mathbf{F}_{BC}(n)$ is applied to generate the transmit signal of the relay and then the received signals are obtained at $T_{X,i}$ at the time instant n. In the following, we take the relevant terms at $T_{A,i}$ $(i = 1, ..., K)$ for details. We can obtain the power of desired signal, estimation and channel aging error respectively,

$$A_i^{BC}(n) = \left|\hat{\mathbf{h}}_{AR,i}^T(n)\hat{\mathbf{h}}_{AR,i}^*(n)\right|^2, \tag{5.49}$$

$$B_i^{BC}(n) = \left|\Delta\mathbf{h}_{AR,i}^T(n)\hat{\mathbf{h}}_{AR,i}^*(n)\right|^2 + \sum_{j=2}^{n}\left|\rho^{n-j}\mathbf{e}_{AR,i}^T(j)\hat{\mathbf{h}}_{AR,i}^*(n)\right|^2. \tag{5.50}$$

Meanwhile, the the inter-user interference power and the noise power can

be given by

$$\begin{aligned} C_i^{BC}(n) = &\sum\nolimits_{k\neq i}\left[\left|\hat{\mathbf{h}}_{AR,i}^T(n)\hat{\mathbf{h}}_{AR,k}^*(n)\right|^2 + \left|\Delta\mathbf{h}_{AR,i}^T(n)\hat{\mathbf{h}}_{AR,k}^*(n)\right|^2\right] \\ &+\sum\nolimits_{k\neq i}\left[\sum\nolimits_{j=2}^{n}\left|\rho^{n-j}\mathbf{e}_{AR,i}^T(j)\hat{\mathbf{h}}_{AR,k}^*(n)\right|^2\right] \\ &+\sum\nolimits_{k=1}^{K}\left[\left|\hat{\mathbf{h}}_{AR,i}^T(n)\hat{\mathbf{h}}_{BR,k}^*(n)\right|^2 + \left|\Delta\mathbf{h}_{AR,i}^T(n)\hat{\mathbf{h}}_{BR,k}^*(n)\right|^2\right] \\ &+\sum\nolimits_{k=1}^{K}\left[\sum\nolimits_{j=2}^{n}\left|\rho^{n-j}\mathbf{e}_{AR,i}^T(j)\hat{\mathbf{h}}_{BR,k}^*(n)\right|^2\right], \end{aligned} \tag{5.51}$$

$$D_i^{BC}(n) = \frac{1}{\rho_{DF}^2(n)} = 1/\left(\sqrt{\frac{p_r}{\mathbb{E}\left\{||\mathbf{F}_{BC}(n)||_{\mathrm{F}}^2\right\}}}\right)^2. \tag{5.52}$$

Therefore, the SE of the relay to the i-th device $T_{A,i}$ at the time instant n is given by

$$R_{RA,i}(n) = \chi(n)\times\mathbb{E}\left\{\log_2\left(1+\frac{A_i^{BC}(n)}{B_i^{BC}(n)+C_i^{BC}(n)+D_i^{BC}(n)}\right)\right\}. \tag{5.53}$$

Similarly, $R_{RB,i}(n)$ can be obtained by replacing AR, BR with BR, AR in (5.49)-(5.53). The sum SE of the i-th device pair in the BC phase is denoted as the sum of the end-to-end SE from $T_{A,i}$ to $T_{B,i}$ and the end-to-end SE from $T_{B,i}$ to $T_{A,i}$, which can be expressed as

$$R_{2,i}(n) = \min\left(R_{AR,i}(n), R_{RB,i}(n)\right) + \min\left(R_{BR,i}(n), R_{RA,i}(n)\right). \tag{5.54}$$

Based to [69, 103], the sum SE at the time instant n can be obtained by

$$R(n) = \sum_{i=1}^{K}\min\left(R_{1,i}(n), R_{2,i}(n)\right). \tag{5.55}$$

The average SE of the whole transmission process with channel aging can be further given by

$$R_{avr} = \frac{1}{N_{total}}\sum_{n=1}^{N_{total}} R(n), \tag{5.56}$$

where N_{total} is the number of total time instants.

5.3.2 Large-scale Approximations of Spectral Efficiency

This sub-chapter studies the respective large-scale approximations of the sum SE with two linear processing methods in the case of N_R increasing to large but finite numbers.

5.3.2.1 Maximum Ratio Method

First, we study the SE approximations of the system with MRT processing. The linear processing matrices defined in (5.17)-(5.18) can be rewritten as

$$\mathbf{F}_{MAC} = \begin{bmatrix} \hat{\mathbf{H}}_{AR}^{H} \\ \hat{\mathbf{H}}_{BR}^{H} \end{bmatrix}, \tag{5.57}$$

$$\mathbf{F}_{BC} = \left[\hat{\mathbf{H}}_{BR}^{*}, \hat{\mathbf{H}}_{AR}^{*}\right], \tag{5.58}$$

respectively. The approximation of the normalization coefficient ρ_{DF} in (5.23) is obtained by

$$\rho_{DF}^{MRT} = \sqrt{\frac{p_r}{\sum\limits_{i=1}^{K}\left(\sigma_{AR,i}^2 + \sigma_{BR,i}^2\right)\sum\limits_{m=1}^{L}\sum\limits_{n=1}^{N_R}|\mathbf{A}_{m,n}|^2}}. \tag{5.59}$$

When N_R increases to large but finite numbers, the approximations of the achievable SE in the MAC phase and the SE between the relay and user pairs defined in (5.32)-(5.37), (5.39)-(5.40) can be expressed as

$$\hat{R}_{1,i}^{MRT} = \frac{\eta_{coh} - \eta_p}{2\eta_{coh}} \times \log_2\left(1 + \frac{\mathbb{Y}_{A,i} + \mathbb{Y}_{B,i}}{\mathbb{Z}_i}\right), \tag{5.60}$$

$$\hat{R}_{AR,i}^{MRT} = \frac{\eta_{coh} - \eta_p}{2\eta_{coh}} \times \log_2\left(1 + \frac{\mathbb{Y}_{A,i}}{\mathbb{Z}_i}\right), \tag{5.61}$$

$$\hat{R}_{RA,i}^{MRT} = \frac{\eta_{coh} - \eta_p}{2\eta_{coh}} \times \log_2\left(1 + \frac{\left(N_R^2 + \sum\limits_{a=1}^{L}\sum\limits_{\substack{b=1 \\ b\neq a}}^{L}|\Theta(a,b)|^2\right)\cdot\sigma_{AR,i}^4\cdot p_r}{\mathbb{T}_i}\right), \tag{5.62}$$

with

$$\mathbb{Y}_{X,i} = p_{X,i}\left(\left(N_R^2 + \sum_{a=1}^{L}\sum_{\substack{b=1\\b\neq a}}^{L}|\Theta(a,b)|^2\right)\cdot\sigma_{XR,i}^4 + \sigma_{AR,i}^2\sigma_{BR,i}^2\sum_{m=1}^{L}\sum_{n=1}^{L}|\Theta_{m,n}|^2\right), \tag{5.63}$$

$$\begin{aligned}\mathbb{Z}_i = &\left(p_{A,i}\tilde{\sigma}_{AR,i}^2 + p_{B,i}\tilde{\sigma}_{BR,i}^2\right)\left(\sigma_{AR,i}^2 + \sigma_{BR,i}^2\right)\sum_{m=1}^{L}\sum_{n=1}^{L}|\Theta_{m,n}|^2\\ &+\sum_{j\neq i}\left(p_{A,j}\beta_{AR,j} + p_{B,j}\beta_{BR,j}\right)\left(\sigma_{AR,i}^2 + \sigma_{BR,i}^2\right)\sum_{m=1}^{L}\sum_{n=1}^{L}|\Theta_{m,n}|^2\\ &+N_R\left(\sigma_{AR,i}^2 + \sigma_{BR,i}^2\right),\end{aligned} \tag{5.64}$$

$$\begin{aligned}\mathbb{T}_i = &\, p_r\left(\sigma_{AR,i}^2\tilde{\sigma}_{AR,i}^2 + \sum_{j\neq i}\beta_{AR,i}\sigma_{AR,j}^2 + \sum_{j=1}^{K}\beta_{AR,i}\sigma_{BR,j}^2\right)\sum_{m=1}^{L}\sum_{n=1}^{L}|\Theta_{m,n}|^2\\ &+\sum_{j=1}^{K}\left(\sigma_{AR,j}^2 + \sigma_{BR,j}^2\right)\sum_{m=1}^{L}\sum_{n=1}^{N_R}|A_{m,n}|^2,\end{aligned} \tag{5.65}$$

where $X = A, B$. For simplicity, we assume $\Theta = \mathbf{A}\mathbf{A}^{\mathrm{H}}$ and $\mathbf{A}_i = \mathbf{A}_j$ $(i, j = 1, ..., K)$, which are also applied in the following simulations. Based on (5.61)-(5.65), $\hat{R}_{BR,i}$ and $\hat{R}_{RB,i}$ can be obtained by using $p_{B,i}$, $p_{A,i}$, and the subscripts "BR", "AR" to replace $p_{A,i}$, $p_{B,i}$, and the subscripts "AR", "BR" in $\hat{R}_{AR,i}$ and $\hat{R}_{RA,i}$, respectively. Thus, the SE approximation in the BC phase can be obtained by

$$\hat{R}_{2,i} = \min\left(\hat{R}_{AR,i}, \hat{R}_{RB,i}\right) + \min\left(\hat{R}_{BR,i}, \hat{R}_{RA,i}\right). \tag{5.66}$$

According to the above expressions, the approximations of the sum SE of the proposed system $\hat{R}$ associated with $\hat{R}_i$ and the respective SE approximations in the MAC and BC phases, while $R_i - \hat{R}_i \to 0$, $R_{1,i} - \hat{R}_{1,i} \to 0$ and $R_{2,i} - \hat{R}_{2,i} \to 0$, is given by

$$\hat{R} = \sum_{i=1}^{K}\hat{R}_i = \sum_{i=1}^{K}\min\left(\hat{R}_{1,i}, \hat{R}_{2,i}\right). \tag{5.67}$$

Proof: Please see Appendix C.

5.3.2.2 Maximum Ratio Method with Channel Aging

Note that $\hat{\mathbf{G}}_{XR}(1) = [\hat{\mathbf{g}}_{XR,1}(1), ..., \hat{\mathbf{g}}_{XR,K}(1)] \in \mathbb{C}^{L\times K}$ based on (5.26), $X = A, B$. When N_R increases to a large number, the vectors in $\hat{\mathbf{G}}_{XR}(1)$ could be assumed to become asymptotically mutually orthogonal. Therefore, $\hat{\mathbf{G}}_{XR}^H(1)\hat{\mathbf{G}}_{XR}(1)$ approaches a diagonal matrix [76]. In this case, the approximations of corresponding SE terms of the power of desired signals, the power of estimation and channel aging error in the MAC phase at the time instant n defined in Chapter 5.3.1.2 can be given by,

$$\begin{aligned}\tilde{A}_i^{MAC}(n) = p_{A,i}\rho^{4(n-1)} \times \sigma_{AR,i}^4 \left(\sum_{a=1}^{L} \sum_{\substack{b=1\\ b\neq a}}^{L} |\Theta(a,b)|^2 + \sum_{a=1}^{L}\sum_{b=1}^{L} \Theta(a,a)\Theta(b,b) \right) \\ + p_{A,i}\rho^{4(n-1)} \times \sigma_{AR,i}^2\sigma_{BR,i}^2 \sum_{a=1}^{L}\sum_{b=1}^{L} |\Theta(a,b)|^2,\end{aligned} \tag{5.68}$$

$$\begin{aligned}\tilde{B}_i^{MAC}(n) = p_{B,i}\rho^{4(n-1)} \times \sigma_{BR,i}^4 \left(\sum_{a=1}^{L} \sum_{\substack{b=1\\ b\neq a}}^{L} |\Theta(a,b)|^2 + \sum_{a=1}^{L}\sum_{b=1}^{L} \Theta(a,a)\Theta(b,b) \right) \\ + p_{B,i}\rho^{4(n-1)} \times \sigma_{AR,i}^2\sigma_{BR,i}^2 \sum_{a=1}^{L}\sum_{b=1}^{L} |\Theta(a,b)|^2,\end{aligned} \tag{5.69}$$

$$\begin{aligned}\tilde{C}_i^{MAC}(n) = \rho^{4(n-1)} \left(\sigma_{AR,i}^2 + \sigma_{BR,i}^2\right) \cdot \sum_{a=1}^{L}\sum_{b=1}^{L} |\Theta(a,b)|^2 \times \\ \left[\left(p_{A,i}\sigma_{\Delta h_{AR,i}}^2 + p_{B,i}\sigma_{\Delta h_{BR,i}}^2\right) + \sum_{j=2}^{n} \rho^{2(1-j)} \left(p_{A,i}\sigma_{e_{AR,i}}^2(j) + p_{B,i}\sigma_{e_{BR,i}}^2(j)\right) \right],\end{aligned} \tag{5.70}$$

while the approximations of the inter-user interference and the compound noise power is given by

$$\begin{aligned}\tilde{D}_i^{MAC}(n) = \rho^{4(n-1)} \left(\sigma_{AR,i}^2 + \sigma_{BR,i}^2\right) \cdot \sum_{a=1}^{L}\sum_{b=1}^{L} |\Theta(a,b)|^2 \times \\ \sum_{k\neq i} \left[\left(p_{A,k}\beta_{AR,k} + p_{B,k}\beta_{BR,k}\right) + \sum_{j=2}^{n} \rho^{2(1-j)} \left(p_{A,k}\sigma_{e_{AR,k}}^2(j) + p_{B,k}\sigma_{e_{BR,k}}^2(j)\right) \right],\end{aligned} \tag{5.71}$$

$$\tilde{E}_i^{MAC}(n) = \rho^{2(n-1)} \left(\sigma_{AR,i}^2 + \sigma_{BR,i}^2\right) \cdot \sum_{a=1}^{L} \Theta(a,a). \tag{5.72}$$

Supported by (5.47)-(5.48) and (5.68)-(5.72), we can obtain the SE ap-

proximations $\tilde{R}_{1,i}(n)$ and $\tilde{R}_{XR,i}(n)$,

$$\tilde{R}_{1,i}(n) = \chi(n) \times \mathbb{E}\left\{\log_2\left(1 + \frac{\sum\limits_{\mathbb{X}=A,B} \tilde{\mathbb{X}}_i^{MAC}(n)}{\tilde{C}_i^{MAC}(n) + \tilde{D}_i^{MAC}(n) + \tilde{E}_i^{MAC}(n)}\right)\right\}. \tag{5.73}$$

$$\tilde{R}_{XR,i}(n) = \chi(n) \times \mathbb{E}\left\{\log_2\left(1 + \frac{\tilde{\mathbb{X}}_i^{MAC}(n)}{\tilde{C}_i^{MAC}(n) + \tilde{D}_i^{MAC}(n) + \tilde{E}_i^{MAC}(n)}\right)\right\}. \tag{5.74}$$

where $i = 1, ..., K$, $\mathbb{X} = A,\ B$.

Meanwhile, in the BC phase, the approximated normalization coefficient $\tilde{\rho}_{DF}(n)$ can be expressed as

$$\tilde{\rho}_{DF}(n) = \sqrt{\frac{p_r}{\rho^{2(n-1)} \sum\limits_{j=1}^{K} \left(\sigma_{AR,j}^2 + \sigma_{BR,j}^2\right) \sum\limits_{m=1}^{L} \sum\limits_{n=1}^{N_R} |\mathbf{A}_{m,n}|^2}} \tag{5.75}$$

Moreover, the approximations of the SE terms at $T_{AR,i}$ in the BC phase at the time instant n defined in Chapter 5.3.1.2 can be given as

$$\tilde{A}_i^{BC}(n) = \rho^{4(n-1)} \cdot \sigma_{AR,i}^4 \left(\sum_{a=1}^{L} \sum_{b=1}^{L} \Theta^*(a,a)\Theta^*(b,b) + \sum_{a=1}^{L} \sum_{\substack{b=1 \\ b\neq a}}^{L} |\Theta(a,b)|^2\right), \tag{5.76}$$

$$\tilde{B}_i^{BC}(n) = \rho^{4(n-1)} \cdot \sigma_{AR,i}^2 \left(\sigma_{\Delta h_{AR,i}}^2 + \sum_{j=2}^{n} \rho^{2(1-j)} \sigma_{e_{AR,i}}^2(j)\right) \sum_{a=1}^{L} \sum_{b=1}^{L} |\Theta(a,b)|^2, \tag{5.77}$$

$$\tilde{C}_i^{BC}(n) = \rho^{4(n-1)} \cdot \sum_{a=1}^{L} \sum_{b=1}^{L} |\Theta(a,b)|^2 \times \left\{\sigma_{AR,i}^2 \Big(\sum_{k\neq i} \beta_{AR,k} + \sum_{k=1}^{K} \beta_{BR,k}\Big) + \sum_{j=2}^{n} \rho^{2(1-j)} \sigma_{e_{AR,i}}^2(j) \Big(\sum_{k\neq i} \sigma_{AR,k}^2 + \sum_{k=1}^{K} \sigma_{BR,k}^2\Big)\right\}, \tag{5.78}$$

$$\tilde{D}_i^{BC}(n) = \frac{\rho^{2(n-1)}}{p_r} \sum_{j=1}^{K} \left(\sigma_{AR,j}^2 + \sigma_{BR,j}^2\right) \sum_{m=1}^{L} \sum_{n=1}^{N_R} |\mathbf{A}_{m,n}|^2. \tag{5.79}$$

Therefore, $\tilde{R}_{RA,i}(n)$ can be obtained by (5.53) and (5.75)-(5.79), and expressed as,

$$\tilde{R}_{RA,i}(n) = \chi(n) \times \mathbb{E}\left\{\log_2\left(1 + \frac{\tilde{A}_i^{BC}(n)}{\tilde{B}_i^{BC}(n) + \tilde{C}_i^{BC}(n) + \tilde{D}_i^{BC}(n)}\right)\right\}. \tag{5.80}$$

Similarly, $\tilde{R}_{RB,i}(n)$ can be obtained by replacing AR, BR with BR, AR in (5.75)-(5.79). With the assistance of all approximation terms derived above, the SE approximation in the BC phase can be expressed as

$$\tilde{R}_{2,i}(n) = \min\left(\tilde{R}_{AR,i}(n), \tilde{R}_{RB,i}(n)\right) + \min\left(\tilde{R}_{BR,i}(n), \tilde{R}_{RA,i}(n)\right). \tag{5.81}$$

Moreover, the sum SE approximation of the proposed system at the time instant n can be obtained by

$$\tilde{R}(n) = \sum_{i=1}^{K} \min\left(\tilde{R}_{1,i}(n), \tilde{R}_{2,i}(n)\right). \tag{5.82}$$

The approximation of the average SE of the whole transmission process with channel aging can be further given by

$$\tilde{R}_{avr} = \frac{1}{N_{total}} \sum_{n=1}^{N_{total}} \tilde{R}(n), \tag{5.83}$$

where N_{total} is the number of total time instants.

5.3.2.3 Zero Forcing Method

In this sub-chapter, the SE approximations of the system with ZF processing are studied. Recall that $\hat{\mathbf{G}}_{XR} = [\hat{\mathbf{g}}_{XR,1}, ..., \hat{\mathbf{g}}_{XR,K}] \in \mathbb{C}^{L\times K}$ and $\hat{\mathbf{g}}_{XR,i} \sim \mathbb{CN}(0, \sigma_{XR,i}\mathbf{I}_L)$, $X = A, B$; moreover, $\hat{\mathbf{g}}_{XR,i}$ and $\hat{\mathbf{g}}_{XR,j}$ $(i \neq j)$ are uncorrelated. When N_R increases to large number, the inner product of any two columns in $\hat{\mathbf{G}}_{XR}$ can be simplified as [76, 98, 118]

$$\frac{1}{N_R} \cdot \hat{\mathbf{g}}_{XR,i}^H \hat{\mathbf{g}}_{XR,j} \rightarrow \begin{cases} \sigma_{XR,i}^2, & i = j \\ 0, & i \neq j \end{cases}. \tag{5.84}$$

Therefore, when the number of relay antennas goes to a large number, the inner product of any two columns in estimated channel matrices $\hat{\mathbf{H}}_{XR}$

$(X = A, B)$ can be approximated as

$$\hat{\mathbf{h}}_{XR,i}^{H}\hat{\mathbf{h}}_{XR,j} \rightarrow \begin{cases} \hat{\mathbf{g}}_{XR,i}^{H}\Theta\hat{\mathbf{g}}_{XR,j}, & i = j \\ 0, & i \neq j \end{cases}. \tag{5.85}$$

With (5.85), the ZF linear processing matrices $\mathbf{F}_{MAC}$ and $\mathbf{F}_{BC}$ defined in (5.21)-(5.22) can be approximated as

$$\mathbf{F}_{MAC} \rightarrow \begin{bmatrix} \left(\hat{\mathbf{H}}_{AR}^{H}\hat{\mathbf{H}}_{AR}\right)^{-1}\hat{\mathbf{H}}_{AR}^{H} \\ \left(\hat{\mathbf{H}}_{BR}^{H}\hat{\mathbf{H}}_{BR}\right)^{-1}\hat{\mathbf{H}}_{BR}^{H} \end{bmatrix}, \tag{5.86}$$

$$\mathbf{F}_{BC} \rightarrow \left[\hat{\mathbf{H}}_{BR}^{*}\left(\hat{\mathbf{H}}_{BR}^{T}\hat{\mathbf{H}}_{BR}^{*}\right)^{-1}, \hat{\mathbf{H}}_{AR}^{*}\left(\hat{\mathbf{H}}_{AR}^{T}\hat{\mathbf{H}}_{AR}^{*}\right)^{-1}\right], \tag{5.87}$$

respectively. The approximation of normalization coefficient ρ_{DF} can be given by

$$\rho_{DF}^{ZF} = \sqrt{\frac{N_R^2 \cdot p_r}{\sum\limits_{i=1}^{K}\left(\frac{1}{\sigma_{AR,i}^2} + \frac{1}{\sigma_{BR,i}^2}\right)\sum\limits_{m=1}^{L}\sum\limits_{n=1}^{N_R}|\mathbf{A}_{m,n}|^2}}. \tag{5.88}$$

According to the above analysis and highlighting the properties of ZF processing of eliminating inter-channel interference [119], the approximations of the SE in the MAC phase and the corresponding approximations of the SE between the relay and user pairs are given by

$$\hat{R}_{1,i}^{ZF} = \frac{\eta_{coh} - \eta_p}{2\eta_{coh}} \times \log_2\left(1 + \frac{p_{A,i} + p_{B,i}}{\text{denominator}}\right), \tag{5.89}$$

$$\hat{R}_{AR,i}^{ZF} = \frac{\eta_{coh} - \eta_p}{2\eta_{coh}} \times \log_2\left(1 + \frac{p_{A,i}}{\text{denominator}}\right), \tag{5.90}$$

$$\hat{R}_{RA,i}^{ZF} = \frac{\eta_{coh} - \eta_p}{2\eta_{coh}} \times \log_2\left(1 + \frac{N_R^2 p_r}{p_r\sum\limits_{j=1}^{K}\left(\frac{\tilde{\sigma}_{AR,i}^2}{\sigma_{AR,j}^2} + \frac{\tilde{\sigma}_{AR,i}^2}{\sigma_{BR,j}^2}\right)\sum\limits_{m=1}^{L}\sum\limits_{n=1}^{L}|\Theta_{m,n}|^2 + \sum\limits_{j=1}^{K}\left(\frac{1}{\sigma_{AR,j}^2} + \frac{1}{\sigma_{BR,j}^2}\right)\sum\limits_{m=1}^{L}\sum\limits_{n=1}^{N_R}|A_{m,n}|^2}\right), \tag{5.91}$$

respectively. In (5.89)-(5.90), denominator can be expressed as with

$$\begin{aligned}\text{denominator} = &\sum_{j=1}^{K} p_{A,j}\left(\frac{\tilde{\sigma}_{AR,j}^2}{N_R^2\sigma_{AR,i}^2}+\frac{\tilde{\sigma}_{AR,j}^2}{N_R^2\sigma_{BR,i}^2}\right)\sum_{m=1}^{L}\sum_{n=1}^{L}|\Theta_{m,n}|^2\\ &+\sum_{j=1}^{K} p_{B,j}\left(\frac{\tilde{\sigma}_{BR,j}^2}{N_R^2\sigma_{AR,i}^2}+\frac{\tilde{\sigma}_{BR,j}^2}{N_R^2\sigma_{BR,i}^2}\right)\sum_{m=1}^{L}\sum_{n=1}^{L}|\Theta_{m,n}|^2\\ &+\left(\frac{1}{N_R\sigma_{AR,i}^2}+\frac{1}{N_R\sigma_{BR,i}^2}\right)\end{aligned} \tag{5.92}$$

Based on (5.90)-(5.92), $\hat{R}_{BR,i}$ and $\hat{R}_{RB,i}$ can be obtained by replacing the transmit powers $p_{A,i}$, $p_{B,i}$, and the subscripts "AR", "BR" in $\hat{R}_{AR,i}$ and $\hat{R}_{RA,i}$ with the transmit powers $p_{B,i}$, $p_{A,i}$, and the subscripts "BR", "AR", respectively. Then, the SE approximation in the BC phase can be expressed as

$$\hat{R}_{2,i} = \min\left(\hat{R}_{AR,i}, \hat{R}_{RB,i}\right) + \min\left(\hat{R}_{BR,i}, \hat{R}_{RA,i}\right). \tag{5.93}$$

Accordingly, the approximations of the sum SE $\hat{R}$ related to $\hat{R}_i$ and the SE approximations in the MAC and BC phases with $R_{1,i} - \hat{R}_{1,i} \to 0$ and $R_{2,i} - \hat{R}_{2,i} \to 0$, respectively, while $R_i - \hat{R}_i \to 0$, is given by

$$\hat{R} = \sum_{i=1}^{K} \hat{R}_i = \sum_{i=1}^{K} \min\left(\hat{R}_{1,i}, \hat{R}_{2,i}\right), \tag{5.94}$$

Proof: Please see Appendix C.

5.3.3 Energy Efficiency

In general, the EE can be defined as the ratio of the sum SE to the total power consumption of the system, given by [44, 120],

$$\varepsilon = \frac{R}{P_{\text{tot}}}, \tag{5.95}$$

where R represents the sum SE defined in (5.42) and P_{tot} represents the total power consumption by particularizing (2.19),

$$P_{tot} = \sum_{i=1}^{K} (P_{A,i} + P_{B,i}) + P_r + P_{static}. \tag{5.96}$$

In practice, the total power consumption of the two-way relay system defined by (2.19) consists of the transmit powers, the powers consumed by static circuits, and the RF components in all RF chains. Typically, one antenna is connected to one RF chain by digital beamforming architecture [44, 157]. Moreover, P_{static} is the power consumption of all static circuits in the system [44]. In this chapter, we consider a common power consumption model referring to the model introduced in Chapter 2.2.3 and developed in Chapter 4.3.2 where the respective power consumption terms can be referred to (4.33)-(4.36). Similar to Chapter 4.3.2, we consider that $\zeta_i = \zeta_r = \zeta$, $P_{DAC,i} = P_{DAC,r} = P_{DAC}$, $P_{mix,i} = P_{mix,r} = P_{mix}$, $P_{filt,i} = P_{filt,r} = P_{filt}$ and $P_{syn,i} = P_{syn,r} = P_{syn}$ for $i = 1, 2, ..., K$ in the following simulations for sake of simplicity.

5.4 Incomplete CSI Acquisition

In practical massive MIMO relay systems, the dense deployment of relay antennas leads to an increasing spatial correlation between adjacent antennas. Higher spatial correlation can obtain greater similarity between the channels of these closely spaced antennas [9, 17]. Therefore, apart from imperfect CSI, we implement incomplete CSI acquisition by collecting the CSI for a subset of relay antennas during the channel estimation stage and generating the CSI of the rest antennas via the averaging method. This may take advantage of the similarity of channels, and dramatically reduce CSI overhead in transmission.

As illustrated in Chapter 3.2.2, the example of the active antenna distribution is displayed by Fig. 5.2. Similarly, let $\mathscr{B}$ and $\mathscr{C}$ represent the subsets of indices for active and inactive relay antennas during the channel estima-

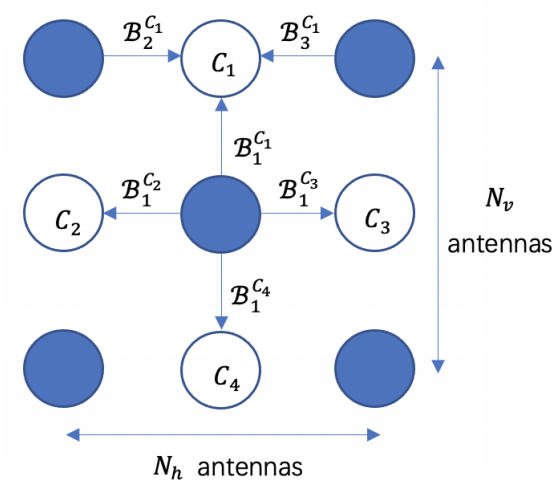

Figure 5.2: Example CSI distribution pattern for a URA with $N_t = 9$, $N_c = 5$. Colored and white elements represent antennas with and without CSI acquisition respectively.

tion stage respectively with $|\mathscr{B}| = N_c$, and $|\mathscr{C}| = N_R - N_c$ [17, 158]. Moreover, we express the design of the CSI distribution pattern as

- 1) First, to guarantee that each inactive relay antenna could have at least one adjacent active antenna, $N_c/N_R > 0.3$ is considered.
- 2) The basic number of antennas with CSI each row should be $\lfloor N_c/N_v \rfloor$ and evenly distributed.
- 3) Then, we shift the patterns circularly to determine the CSI distribution in the following rows.
- 4) When $N_c > N_v \times \lfloor N_c/N_v \rfloor$, the additional antennas $N_c - N_v \times \lfloor N_c/N_v \rfloor$ with CSI should be added from the last row with the same even distribution pattern.

This CSI distribution ensures that the antennas with CSI are evenly distributed and that each inactive antenna has at least one adjacent active antenna. For the sake of simplicity, the channel estimates for active antennas in $\mathscr{B}$ can be obtained by (5.25) and the channel estimates of inactive antennas in $\mathscr{C}$ are obtained by averaging the estimated vectors of adjacent active

antennas

$$\hat{\mathbf{h}}_{XR,i\mathscr{C}_j} = \frac{1}{N_{\mathscr{C}_j}} \sum_{a=1}^{N_{\mathscr{C}_j}} \hat{\mathbf{h}}_{XR,i\mathscr{B}_a^{\mathscr{C}_j}}, \tag{5.97}$$

where $N_{\mathscr{C}_j}$ represents the number of antennas with instantaneous CSI that is used to approximate the CSI of the inactive antenna $\mathscr{C}_j$. Intuitively, the CSI of the $\mathscr{C}_j$-th antenna is computed through averaging the CSI of its closest active antennas, $\mathscr{B}_a^{\mathscr{C}_j}$, $a = 1,...,N_{\mathscr{C}_j}$. With the averaging method, the actual channel estimate of inactive antenna $\mathscr{C}_j$ can also be derived via averaging the actual channel estimate of active antennas,

$$\begin{aligned}
\mathbf{h}_{XR,i\mathscr{C}_j} &= \frac{1}{N_{\mathscr{C}_j}} \sum_{a=1}^{N_{\mathscr{C}_j}} \mathbf{h}_{XR,i\mathscr{B}_a^{\mathscr{C}_j}} \\
&= \frac{1}{N_{\mathscr{C}_j}} \sum_{a=1}^{N_{\mathscr{C}_j}} \left(\hat{\mathbf{h}}_{XR,i\mathscr{B}_a^{\mathscr{C}_j}} + \Delta\mathbf{h}_{XR,i\mathscr{B}_a^{\mathscr{C}_j}} \right) \\
&= \hat{\mathbf{h}}_{XR,i\mathscr{C}_j} + \frac{1}{N_{\mathscr{C}_j}} \sum_{a=1}^{N_{\mathscr{C}_j}} \Delta\mathbf{h}_{XR,i\mathscr{B}_a^{\mathscr{C}_j}}.
\end{aligned} \tag{5.98}$$

5.4.1 Power Consumption Model

Considering both the total power consumption model defined in Chapter 5.3.3 and the proposed incomplete CSI acquisition model, we note that only N_c RF chains are required to generate the transmit signals. Therefore, the power consumption of RF components in RF chains for the relay with N_c active antennas can be given by

$$P_{RF,r} = N_c(P_{DAC} + P_{mix} + P_{filt}) + P_{syn}. \tag{5.99}$$

With the assistance of (5.96), (5.99) and (4.33)-(4.35), the proposed incomplete CSI acquisition model can achieve power reductions in the total power

consumption as

$$\begin{aligned} P_{tot} &= \sum_{i=1}^{K}(P_{A,i}+P_{B,i})+P_r+P_{sta} \\ &= \sum\nolimits_{X=A,B}\sum\nolimits_{i=1}^{K}\left(\frac{(\eta_{coh}-\eta_p)p_{X,i}+\eta_p p_p}{2\eta_{coh}\zeta}\right)+\frac{p_r}{2\zeta} \\ &+\left(K+\frac{N_c}{2}\right)\cdot\left(P_{DAC}+P_{mix}+P_{filt}\right)+\left(K+\frac{1}{2}\right)P_{syn}+P_{sta}. \end{aligned} \tag{5.100}$$

5.4.2 Complexity Analysis

In this sub-chapter, we study the total computational complexity of the proposed system and analyze the complexity reduction achieved by the incomplete CSI strategy. Based on the system model in Chapter 5.2, the signal processing operations performed in the proposed multi-pair two-way TDD relaying system can be divided into three phases, namely, channel estimation phase, the MAC phase and the BC phase. To this end, the total complexity of the proposed system can be expressed as follows.

5.4.2.1 Channel Estimation Phase

The main computational complexity of the MMSE estimator lies in computing the matrix inversion [50]. For simplicity, long-term statistics are assumed to remain constant, and the effect of channel coherence time is taken into account. Therefore, the complexity can be simplified as [50, 159]

$$C_{MMSE}^{est} = N_c \cdot 2K \cdot (2N_c\eta_p - 1), \tag{5.101}$$

where η_p is the length of the pilot sequence. Meanwhile, since the CSI of inactive antennas is obtained by averaging the CSI of adjacent active antennas, the additional flops are related to the number of adjacent active antennas $N_{\mathscr{C}_j}$ for $\mathscr{C}_j$-th inactive antenna. As a more general introduction, we assume that all inactive antennas have an equal number of adjacent active antennas. Accordingly, additional operation flops with two complex-scalar additions

are considered [160]

$$C_{avr}^{est} = 2K \cdot 4\left(N_R - N_c\right). \tag{5.102}$$

Here we assume that each complex-scalar addition requires two real flops. Remark that the division by $N_{\mathscr{C}_j}$ shown in (5.98) does not introduce extra complexity. In this case, the complexity of the channel estimation phase can be stated by

$$C^{est} = C_{MMSE}^{est} + C_{avr}^{est}. \tag{5.103}$$

5.4.2.2 MAC phase

The overall complexity of the MAC phase depends on the operations involved in generating the precoding matrix and calculating the transformed signals. First, the complexity of implementing the precoding matrix can be given by [97]

$$C_{imp}^{MAC} = N_c \cdot 2K \cdot \eta_{MAC}, \tag{5.104}$$

where η_{MAC} is the number of symbols in the MAC phase. Moreover, compared with MRT processing, ZF processing introduces extra computational complexity related to the conventional singular value decomposition (SVD) approach used to compute the pseudo-inverse precoding matrix [159, 160]. Thus, the complexity of this process is given by [158]

$$C_{inv}^{MAC} = 24 \cdot (2K)^3 + 16N_R \cdot (2K)^2 + 2K + 4KN_R + 8N_R \cdot (2K)^2. \tag{5.105}$$

Subsequently, the generated precoding matrix is multiplied with the symbols to generate the transformed signal. The complexity of computing the transformed signal in (5.10) is given by

$$C_{comp}^{MAC} = \left[8N_c \cdot 2K + 2\left(N_R - N_c\right)\right] \cdot \eta_{MAC}. \tag{5.106}$$

Hence, with MRT processing, the complexity of MAC phase is given by

$$C_{MRT}^{MAC} = C_{imp}^{MAC} + C_{comp}^{MAC}. \tag{5.107}$$

The complexity of MAC phase for ZF processing is given by

$$C_{ZF}^{MAC} = C_{imp}^{MAC} + C_{comp}^{MAC} + C_{inv}^{MAC}. \tag{5.108}$$

5.4.2.3 BC phase

The BC phase also generates a precoding matrix and computes the precoded signal. Moreover, decoding the received information at the relay introduces additional complexity. The complexity of decoding is given by [97]

$$C_{dec}^{BC} = N_c \cdot 2K \cdot \eta_{BC}, \tag{5.109}$$

where η_{BC} is the number of symbols in the BC phase. Besides, the complexity of implementing precoding matrix is given by

$$C_{imp}^{BC} = N_c \cdot 2K \cdot \eta_{BC}. \tag{5.110}$$

As with the MAC phase, when ZF processing is applied, the SVD approach is applied to calculate the pseudo-inverse precoding matrix. Therefore, the complexity of this process is

$$C_{inv}^{BC} = 24 \times (2K)^3 + 16N_R \times (2K)^2 + 2K + 4KN_R + 8N_R \times (2K)^2. \tag{5.111}$$

Furthermore, the complexity of computing the transmit signal in (5.11) can be expressed as

$$C_{comp}^{BC} = [8N_c \cdot 2K + 2(N_R - N_c)] \cdot \eta_{BC}. \tag{5.112}$$

Thus, the complexity of the BC phase can be given by

$$C_{MRT}^{BC} = C_{dec}^{BC} + C_{imp}^{BC} + C_{comp}^{BC}, \tag{5.113}$$

$$C_{ZF}^{BC} = C_{dec}^{BC} + C_{imp}^{BC} + C_{comp}^{BC} + C_{inv}^{BC}, \tag{5.114}$$

for MRT processing and ZF processing respectively.

5.4.2.4 Total Complexity

The total complexity of the proposed system with different processing methods ($X =$ MRT, ZF) can be given by

$$C_X^{tot} = C^{est} + C_X^{MAC} + C_X^{BC}. \tag{5.115}$$

5.5 Numerical Results

In this chapter, numerical results are presented to evaluate the system performance of the proposed space-constrained two-way relaying system. The following parameters are employed until otherwise stated. We consider a standard Long Term Evolution (LTE) frame with coherence interval length $\eta_{coh} = 196$ (symbols) and pilot sequence length $\eta_p = 2K$ [69]. An equal number of angular directions $L = 200$ is applied until specifically stated, and the angle spreads of the azimuth and elevation angles of departure are fixed to $\pi/4$ and $\pi/3$ radians respectively. For the power consumption model, we assume that $p_{A,i} = p_{B,i} = p_u$, $i = 1, ..., K$, $P_{DAC} = 7.8$mW, $P_{mix} = 15.2$mW, $P_{filt} = 10$mW, $P_{syn} = 25$mW and $P_{sta} = 2$W [99]. With considered path loss model, all users' slow large-scale fading parameters are different and can be arbitrarily achieved by $\beta_k = (\frac{\kappa}{D_k^\nu})^{\frac{1}{2}}$, where κ represents the shadowing effect with typical values ranging from 2 to 6, D_k is the distance between the k-th user and the relay, and ν is the path loss exponent [38, 39]. It is assumed that the relay is located in the center of a cell and all users are randomly

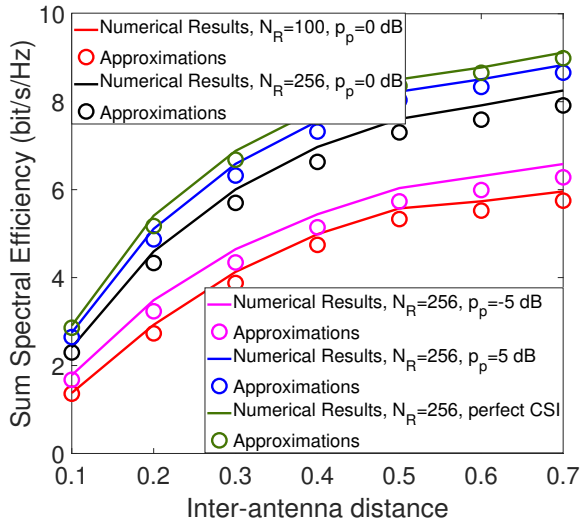

Figure 5.3: Sum SE vs. inter-antenna distance d with MRT processing for $K = 5$, $p_p = 0$ dB and $p_r = 5$dB.

distributed within the cell. To make the results more practical, we consider $\beta_{AR} = [0.3188, 0.4242, 0.5079, 0.8550, 0.2625, 0.8010, 0.2920, 0.9289, 0.7303, 0.4886]$, $\beta_{BR} = [0.5785, 0.2373, 0.4588, 0.9631, 0.5468, 0.5211, 0.2316, 0.4889, 0.6241, 0.6791]$.

5.5.1 Large-scale Approximations

5.5.1.1 MRT Processing

Fig. 5.3 shows the sum SE v.s. inter-antenna distance d. Note that the "Approximations" are obtained by applying (5.60)-(5.67), and the "Numerical Results" are generated according to (5.32)-(5.37) and (5.39)-(5.42). We can observe that large-scale approximations closely match the numerical results, and the sum SE increases with increasing inter-antenna distance while experiencing a smaller spatial correlation. However, the growth trend decelerates when $d > 0.5\lambda$. The larger transmit power of pilot symbols can achieve a better sum SE performance due to the estimation accuracy enhancement, and the performance can gradually approach the ideal one with perfect CSI. In addition, the growing number of relay antennas also has a positive impact.

In Fig. 5.4 (a), simulation results are presented to show the effects of an increasing number of relay antennas on the sum SE. With the increase of

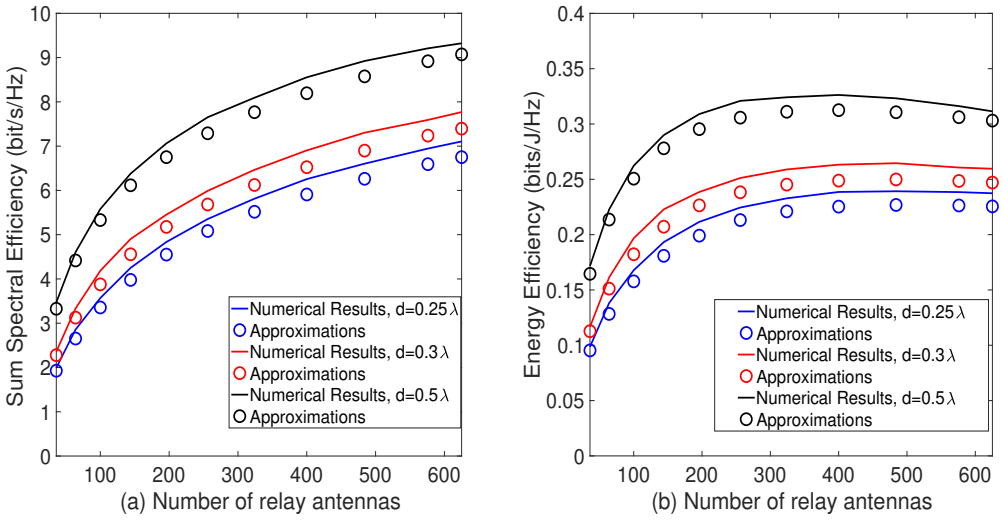

Figure 5.4: (a) Sum SE and (b) EE vs. number of relay antennas N_R with MRT processing for $K = 5$, $p_p = p_u = 0$ dB and $p_r = 5$ dB.

N_R, the sum SE grows without limit as there is no pilot contamination. Similar to Fig. 5.3, a larger inter-antenna distance can help to obtain a better SE performance. However, it is critical to note that in all cases, as N_R increases, the benefits of adding further antennas decline. Fig. 5.4 (b) particularly pronounces the relationship between the EE and the number of relay antennas N_R. The power consumption increases linearly with the number of antennas, while the growth trend of the SE gains decrease to large N_R. Accordingly, it is shown in Fig. 5.4 (b) that the EE performance would be saturated after reaching a particular EE value. We can find that when $N_R \approx 300$, an optimal EE can be achieved, especially, when $d = 0.5\lambda$, the maximum EE around 0.3 bits/J/Hz is obtained. To this end, with a fixed inter-antenna distance, the EE performance can be optimized with specific N_R while reducing power consumption and sacrificing a specific SE performance.

5.5.1.2 MRT Processing with Channel Aging

For the imperfect channel estimation, the CSI is only estimated at the time instant 1 with $\sigma^2_{XR,k}(1) = \frac{10}{11}$, $\sigma^2_{\Delta h_{XR,k}}(1) = \frac{1}{11}$, $X = A, B$, $k = 1, \ldots, K$. For channel aging, the variance of channel aging error is $\sigma^2_{e_{XR,k}}(n) = 0.1$, $X = A, B$, $k = 1, \ldots, K$, in all time instants and the time correlation parameter is $\rho = 0.8$ until

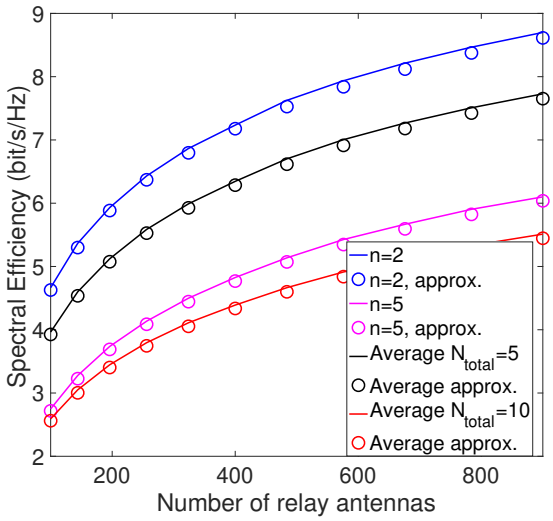

Figure 5.5: SE v.s. number of relay antennas N_R with MRT processing and channel aging for $K = 5$, $d = 0.3\lambda$, $p_p = p_u = 0$ dB and $p_r = 10$ dB.

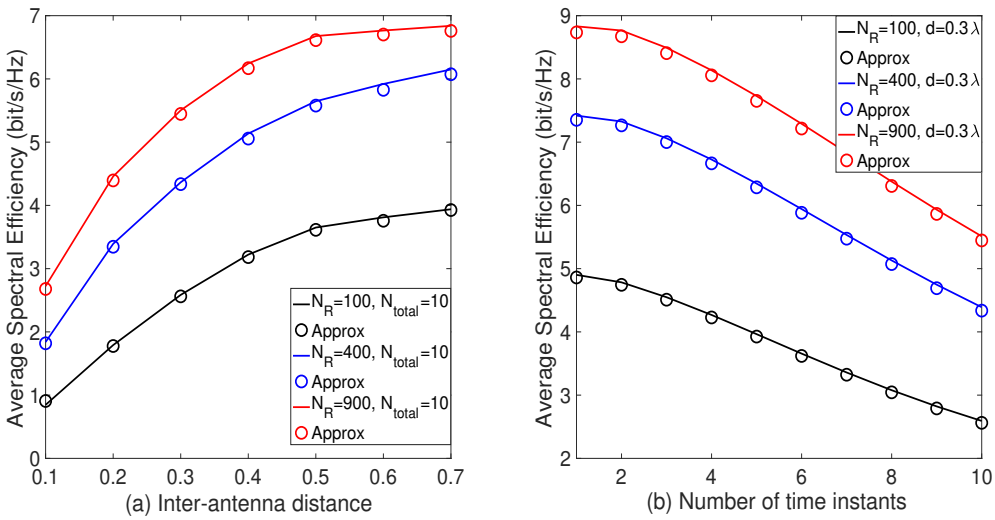

Figure 5.6: Average SE v.s. a) inter-antenna distance d and b) number of time instants N_{total} with MRT processing and channel aging for $K = 5$, $p_p = p_u = 0$ dB and $p_r = 10$ dB.

otherwise stated. Moreover, for simplicity, the large-scale fading parameters are defined as $\beta_{AR,i} = \beta_{BR,i} = 1$, $i = 1, \ldots, K$.

Fig. 5.5 shows the instantaneous SE at the selected time instant n after the most recent channel estimation and the average SE for all time instants v.s. the number of relay antennas respectively. The "Approx." (Approximations) are obtained by (5.68)-(5.83). Moreover, numerical results are gener-

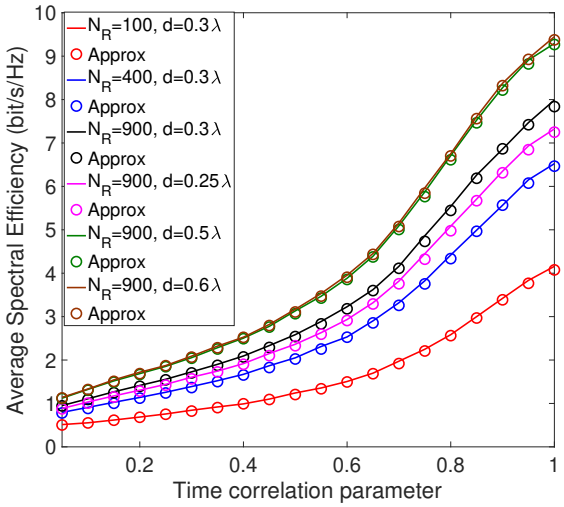

Figure 5.7: Average SE v.s. time correlation parameter ρ with MRT processing and channel aging for $K = 5$, $N_{total} = 10$, $p_p = p_u = 0$ dB and $p_r = 10$ dB.

ated by (5.43)-(5.56). It can be observed that the large-scale approximations can match the numerical results closely. We can also observe that both the average SE and the instantaneous SE for the selected time instant n grow unboundedly with increasing N_R. Moreover, both larger N_{total} and n could reduce the average SE and the SE at the selected time instant due to the effect of channel aging respectively.

Fig. 5.6, the direct effect of spatial and time correlation is explored, where we show the average SE with increasing inter-antenna distance and the total number of time instants, with the CSI estimated at the time instant 1. Similar to Fig. 5.5, larger N_R can help to achieve a better SE performance. In Fig. 5.6 (a), the average SE increases with inter-antenna distance and starts to saturate especially when $d \geq 0.5\lambda$ with moderate spatial correlation. Meanwhile, Fig. 5.6 (b) shows that the total number of time instants plays a negative role on the average SE. Nevertheless, it is important to note that significant performance degradation only appears for inter-antenna spacing $d < 0.3\lambda$, and for channel aging more than 4 to 5 time instants. This can be exploited for significant physical space savings and channel estimation relaxation.

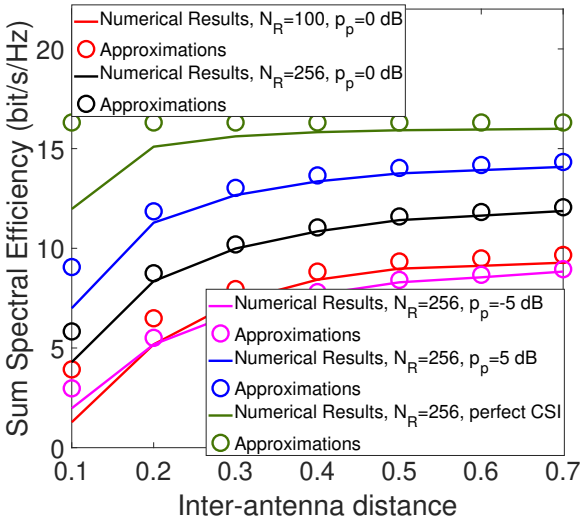

Figure 5.8: Sum SE vs. inter-antenna distance d with ZF processing for $K = 5$, $p_p = p_u = 0$ dB and $p_r = 5$ dB.

In Fig. 5.7, the effect of the time correlation parameter on the average SE is illustrated. It is obviously shown that the average SE would increase with growing time correlation parameter ρ which represents increasingly retained channel accuracy and similar to Fig. 5.5, larger N_R has positive effects on the average SE. Moreover, Fig. 5.7 can further clarify that increasing d has positive effects, however when d is large enough to achieve moderate even low spatial correlation, the average SE could tend to saturate. This can show that the joint spatial and time correlation could be tolerated in terms of the SE performance.

5.5.1.3 ZF Processing

Fig. 5.8 shows the sum SE v.s. inter-antenna distance d with ZF processing. Note that the "Approximations" are obtained by applying (5.89)-(5.94), and the "Numerical Results" are generated by (5.32)-(5.37) and (5.39)-(5.42). We can see that the sum SE increases as the inter-antenna distance increases and begins to saturate when $d > 0.5\lambda$. Furthermore, compared with Fig. 5.3, ZF processing can outperform MRT processing by eliminating inter-user and inter-pair interference. Moreover, increasing channel estimation accuracy with higher transmit power of pilot symbols is beneficial for the SE perfor-

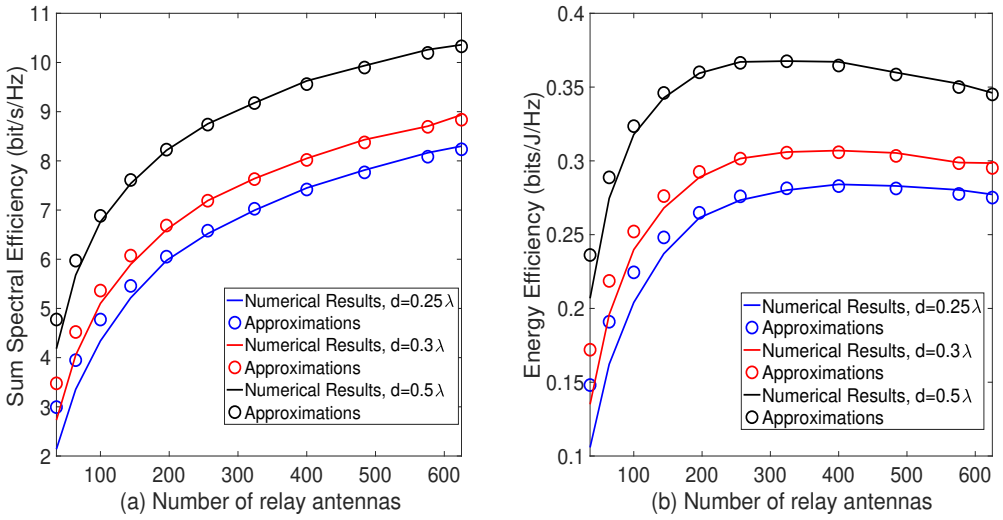

Figure 5.9: (a) Sum SE and (b) EE vs. number of relay antennas N_R with ZF processing for $K = 5$, $p_p = p_u = 0$ dB and $p_r = 5$ dB.

mance to achieve the perfect CSI performance. The greater N_R is beneficial to the performance of sum SE.

Fig. 5.9 (a) displays the relation of the sum SE to the number of relay antennas. The sum SE grows unboundedly with increasing N_R. Similar to Fig. 5.8, a greater inter-antenna distance is beneficial to the SE performance. The power consumption increases linearly while the growth trend of the SE decreases at increasing N_R. Thus, in Fig. 5.9 (b), we can observe that the EE performance would slowly decline after achieving an optimal EE with a specific N_R, especially, the optimal EE around 0.37 bits/J/Hz can be achieved with $N_R \approx 250$ when $d = 0.5\lambda$. In this case, $N_R \approx 250$ can be selected to be the optimal number of relay antennas to improve the EE performance. Compared with Fig. 5.4, system performances of ZF processing can outperform those of MRT processing, which is clarified by Fig. 5.8. Furthermore, the ideal approximations of matrix inversion in ZF processing result in less accuracy when N_R is small. In the non-asymptotic regime, the numerical results could closely match approximations when N_R becomes larger.

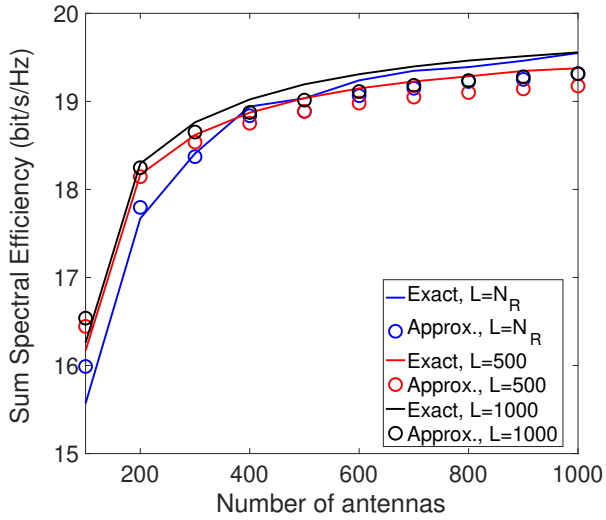

Figure 5.10: Sum SE v.s. number of relay antennas N_R with ZF processing and varying path number for $K = 5$, $p_p = p_u = 5$ dB and $p_r = 10$ dB.

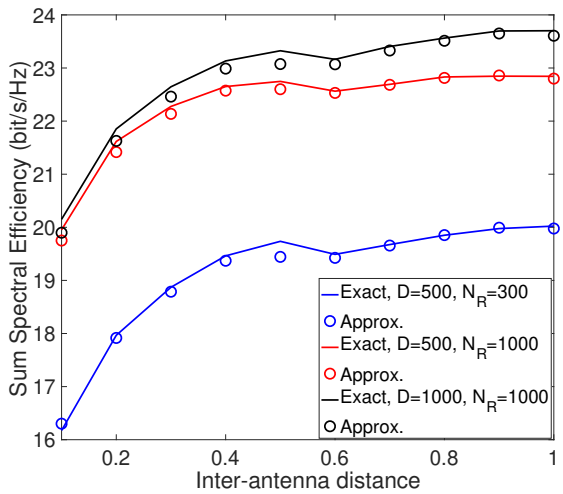

Figure 5.11: Sum SE v.s. inter-antenna distance d with ZF processing and varying path number for $K = 5$, $p_p = p_u = 5$ dB and $p_r = 10$ dB.

5.5.1.4 ZF Processing with Varying Path Number

For simplicity, the large-scale fading parameters are defined as $\beta_{AR,i} = \beta_{BR,i} = 1$, $i = 1, ..., K$, to better evaluate the effect of spatial correlation on the system performance.

Fig. 5.10 shows the sum SE vs the number of relay antennas N_R with different settings of the signal propagation path number L. Note that the "Approx." (Approximations) are obtained by applying (5.89)-(5.94), and

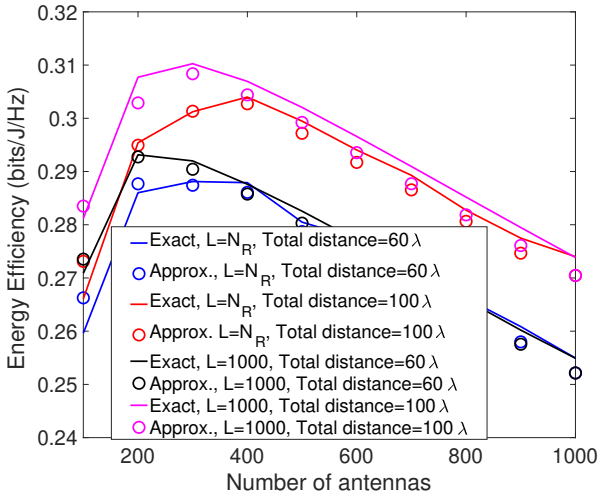

Figure 5.12: EE v.s. number of relay antennas N_R with ZF processing and varying path number for $K = 5$, $p_p = p_u = 5$ dB and $p_r = 10$ dB.

the "Exact" (Numerical results) are generated according to (5.32)-(5.37) and (5.39)-(5.42). We can observe that the sum SE grows unboundedly with respect to N_R, Moreover, larger number of L can help to achieve better sum SE, especially when N_R is small.

As shown in Fig. 5.11, simulation results are presented to display the relationship between the sum SE and the inter-antenna distance d of the proposed physically constrained system. Similar with Fig. 5.10, larger L can help to achieve a better SE performance; moreover, $d = 0.5$ normalized by the carrier wavelength λ can be selected to make better use of spatial correlation to achieve greater sum SE while antennas are closely spaced.

Fig. 5.12 represents the relationship between EE and the number of antennas N_R. It is clearly shown that after achieving an optimal EE performance, EE would decrease with respect to N_R, and larger L has a positive effect on EE when N_R is small. Moreover, we can observe that when $D_{tot} = 100$ normalized by the carrier wavelength λ, the optimal EE can be achieved when $N_R = 300$ while $d = D_{tot}/N_R = \frac{1}{3}$, similarly, when $D_{tot} = 60$, the optimal EE is achieved when $N_R = 200$ with $d = D_{tot}/N_R = 0.3$. In this specific case we considered here, $d \approx 0.3$ can be determined to achieve an optimal EE in the proposed physically spaced system.

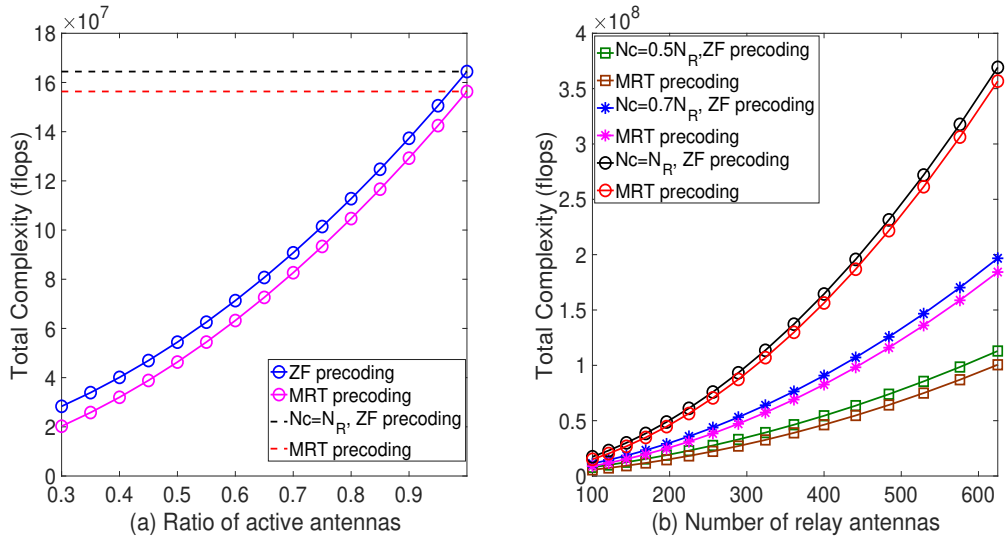

Figure 5.13: (a) Total Complexity vs. ratio of active antennas N_c/N_R with $N_R = 400$ and (b) Total Complexity vs. number of relay antennas N_R, $K = 10$, $\eta_p = 2K$, $\eta_{MAC} = \eta_{coh} - \eta_p$, $\eta_{BC} = \eta_{coh}$.

5.5.2 Incomplete CSI Acquisition

5.5.2.1 Complexity Analysis

The development of total complexity is studied in Fig. 5.13. It is shown that Fig. 5.13 (a) explores the complexity of an incomplete CSI strategy with an increasing ratio of active antennas and compares it with the complexity of a complete CSI acquisition. First, the matrix inversion in ZF processing could generate additional computational complexity; therefore, the system proposed with ZF processing experiences higher complexity than the system with MRT processing. We can observe that the incomplete CSI strategy can reduce the total complexity of the proposed method. Fig. 5.13 (b) shows that total complexity increases dramatically as the number of relay antennas increases. Similar to Fig. 5.13 (a), a smaller ratio of active antennas achieves computational complexity reductions.

5.5.2.2 MRT processing

The effect of the inter-antenna distance on the sum SE and EE performance with incomplete CSI acquisition and MRT processing is shown in Fig. 5.14.

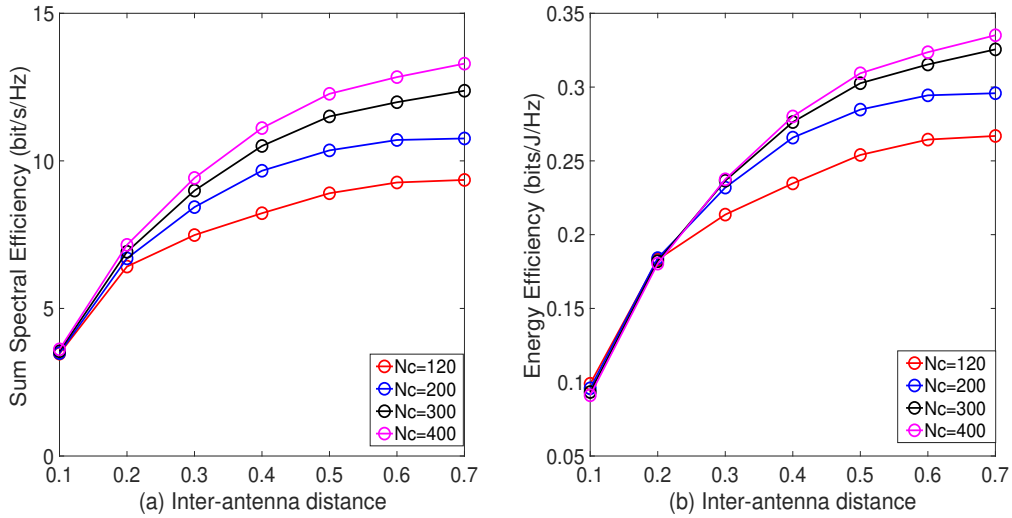

Figure 5.14: (a) Sum SE and (b) EE vs. inter-antenna distance d with MRT processing, $N_R = 400$, $K = 10$, $p_p = p_u = 0$ dB, $p_r = 5$ dB.

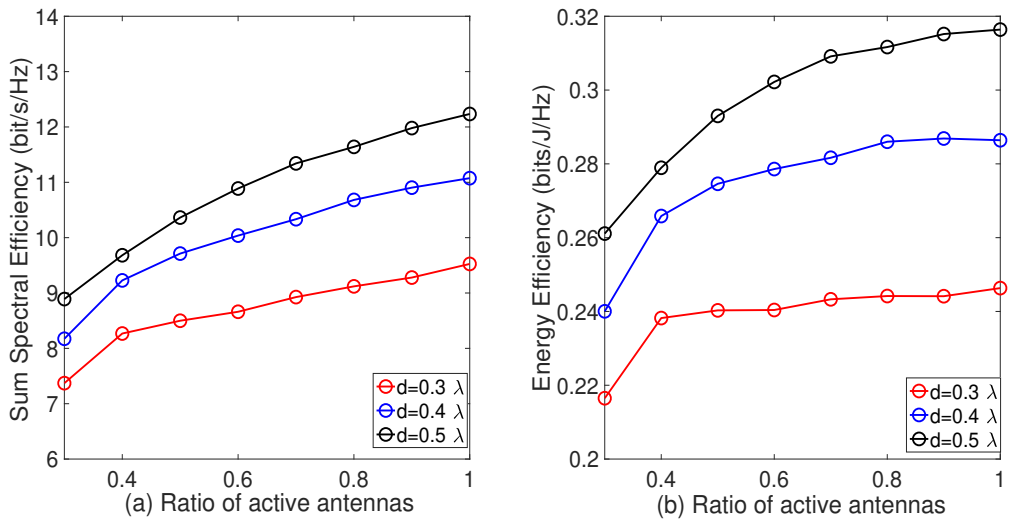

Figure 5.15: (a) Sum SE and (b) EE vs. ratio of active antennas N_c/N_R with MRT processing, $N_R = 400$, $K = 10$, $p_p = p_u = 0$ dB, $p_r = 5$ dB.

Fig. 5.14 (a) shows that an increasing inter-antenna distance plays a positive role in the sum SE performance. Moreover, a larger number of active antennas help achieve a higher sum SE, and the sum SE meets a saturation when $d > 0.5\lambda$, especially when $N_c \leq 0.5 \times N_R$. The EE performance is demonstrated in Fig. 5.14 (b). It can be observed that when d is small, namely,

higher spatial correlation, a smaller number of active antennas with CSI can closely achieve the EE performance with full CSI. When $d > 0.5\lambda$, the EE would also approach a saturation with incomplete CSI acquisition. To this end, spatial correlation, and incomplete CSI acquisition can jointly attain potential EE benefits and complexity reduction.

Fig. 5.15 shows the effect of the ratio of active antennas on the sum SE and EE performance. Fig. 5.15 (a) underlines that the sum SE increases with the increasing ratio of active antennas. It can also be observed that more antennas with CSI are required as the inter-antenna distance increases to attain the ultimate performance achieved by the full CSI acquisition. The EE performance is studied in Fig. 5.15 (b). We can observe that the EE growth rate would start to slow down when $N_c \approx 0.5 \times N_R$, especially when d is small. In this case, when relay antennas are strongly correlated, the proposed scheme could select a specific ratio of active antennas to achieve the desired EE performance. Therefore, the proposed incomplete CSI acquisition can help maintain the required system performance and reduce complexity.

5.5.2.3 ZF Processing

In Fig. 5.16, the relationship between the inter-antenna distance and the system performance with ZF processing is examined. First, compared with Fig. 5.14, it can be seen that ZF processing can significantly outperform MRT processing in this proposed system. Moreover, the results in Fig. 5.16 (a) show that increasing the inter-antenna distance benefits the sum SE. The sum SE could begin to saturate when $d > 0.4\lambda$, especially with fewer active antennas. However, larger N_c could help achieve a higher sum SE with increasing d. In Fig. 5.16 (b), the performance of EE is illustrated, where the EE increases and then saturates for d. Additionally, we can observe that the reduction in the number of active antennas with CSI can benefit EE, especially when $d \leq 0.5\lambda$, this will be further clarified by Fig. 5.17. Therefore, when d is small to achieve a high spatial correlation, a moderate incomplete

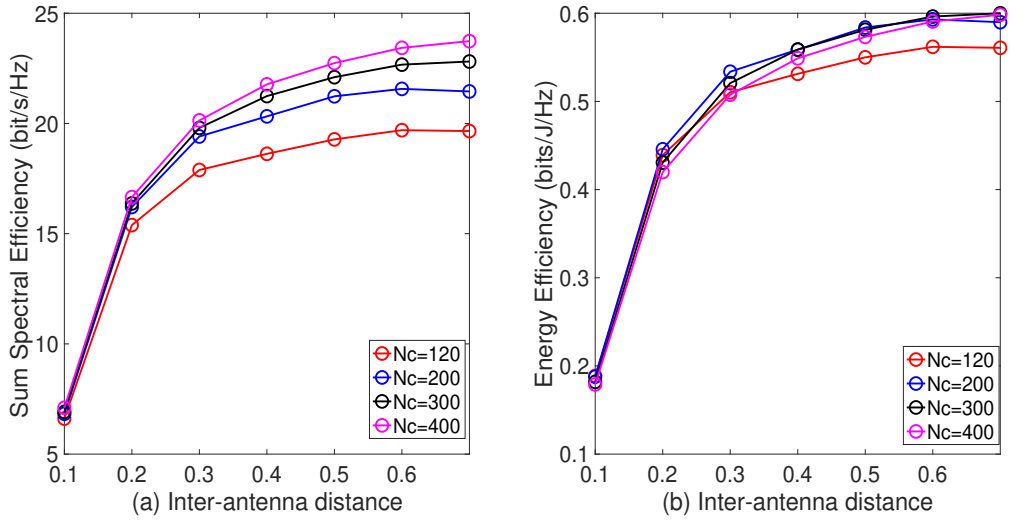

Figure 5.16: (a) Sum SE and (b) EE vs. inter-antenna distance d with ZF processing, $N_R = 400$, $K = 10$, $p_p = p_u = 0$ dB, $p_r = 5$ dB.

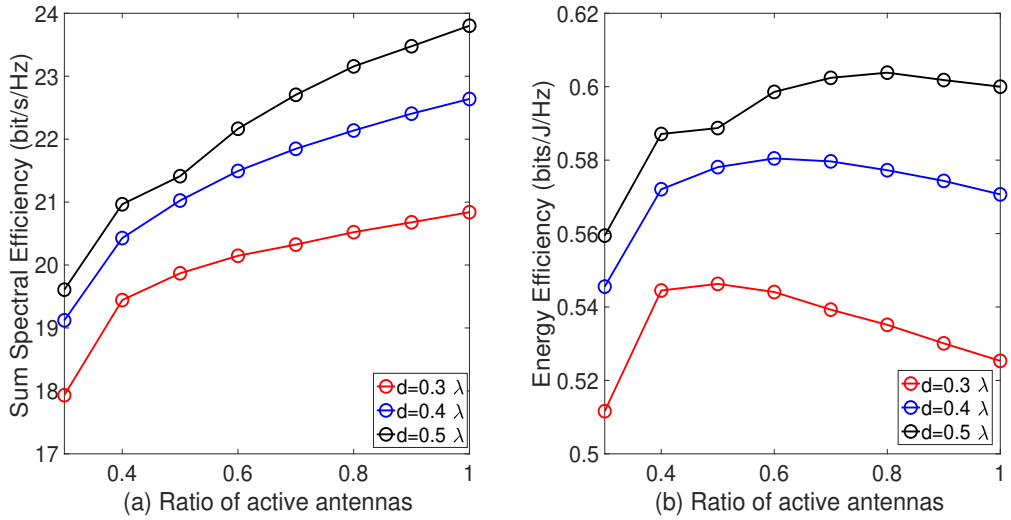

Figure 5.17: (a) Sum SE and (b) EE vs. ratio of active antennas N_c/N_R with ZF processing, $N_R = 400$, $K = 10$, $p_p = p_u = 0$ dB, $p_r = 5$ dB.

CSI acquisition can help enhance the EE performance while maintaining the SE performance.

Fig. 5.17 shows the effect of the ratio of active antennas on the sum SE and EE performance. Specifically, Fig. 5.17 (a) indicates that the sum SE increases with an increasing ratio of active antennas. Similar to Fig. 5.16, a

greater inter-antenna distance achieves a better sum SE performance. The EE performance is studied in Fig. 5.17 (b). It can be observed that an increasing number of active antennas could play a negative role in EE performance after achieving an optimal result. It shows that when relay antennas are highly correlated, an optimal EE can be obtained with $N_c = 0.5 \times N_R$. Moreover, when inter-antenna distance is large, like $d = 0.5\lambda$ with lower spatial correlation, the EE would approach the maximum when more than half antennas are active, which is also clarified in Fig. 5.16 (b). Intuitively, this occurs because the small loss in the SE is compensated by the substantial reduction in the power consumption. Therefore, $N_c = 0.5 \times N_R$ could be the benchmark number of active antennas to maximize the EE while maintaining a required sum SE in moderate and high spatial correlation scenarios.

5.6 Conclusion

This chapter has studied the sum SE and EE performance of a space-constrained multi-pair two-way half-duplex DF relaying system with linear processing methods, incomplete CSI and the effect of channel aging. In particular, the large-scale approximations of the achievable SE with MRT and ZF processing were derived respectively. Meanwhile, a practical power consumption model was characterized to study the EE performance. To exploit spatial correlation, an incomplete CSI approach was introduced and analysed. Our analysis and results demonstrated the important design guidelines for the studied scenario and verified that the proposed system with spatial correlation and linear processing methods is able to enhance the EE while preserving the sum SE performance with specific system configurations. Moreover, the closed-form large-scale approximations of the SE with channel aging are investigated to show that both space savings and channel estimation relaxation can be exploited to maintain system performance while reducing costs. Supported by the above-mentioned results, our analysis shows that the moderate spatial correlation and channel aging can be

tolerated at the relay in the massive MIMO regime.

Chapter 6

Two-stage Alignment Method Design for Beam Alignment

This chapter is based on our works published in [C3].

6.1 Introduction

Millimeter-Wave (mmWave) communication is a promising domain for future wireless communication because of its ample frequency spectrum availability and the throughput enhancements it can offer to cellular communication [21, 73, 74]. The advantages of mmWave communication include the high data rates thanks to the large bandwidth with mmWave frequencies and the line-of-sight (LOS) communication nature which is key to control interference between systems [75]. The short wavelength of the mmWave allows large-scale antenna arrays to be implemented in a small physical space [161]. However, a fundamental challenge in mmWave communication is severe path loss. To compensate for this challenge, high-gain beamforming together with accurate transmitter (Tx) and receiver (Rx) beam alignment is required to acquire large antenna array gains [162, 163].

Several theoretical beam alignment techniques for mmWave communications to achieve high antenna gains have been developed in previous studies. The work in [75] has studied hard-alignment algorithms for uniform linear array (ULA) scenarios and extended to dual-polarized array in [164],

while a soft-alignment algorithm scanning the channel subspace with dual-polarized antennas has been presented in [162]. The iterative search has been studied in [165, 166], in which the beam codebook is pre-designed and independent of the beam-alignment protocol; this results in sub-optimal performance. The beam alignment techniques presented in [167, 168, 169] can be employed in single-user ULA mmWave system to investigate a promising channel estimation performance of the angle of departure (AoD) and angle of arrival (AoA). Another common technique studied in [75, 170] is beam training achieved by spatial scanning; however, this is generally applied to the one-sided scenario. In this case, a conventional approach to adjust Tx and Rx beams jointly is performing an exhaustive method by examining all potential beam pairs in the given angle range and determining the best beam pair that maximizes the antenna gain [171, 172]. A tree-fashion hierarchical beam codebook design with ULA arrays compared to conventional exhaustive search has been illustrated in [20], and [173] has proposed wider beams to speed up beam scanning. The work in [161] has exploited the exhaustive method to propose a pseudo-exhaustive beam training method with full beam search. However, significant computational complexity and signalling overheads might occur when a great number of beam pairs are steered or suffers losses in the antenna gain if the scan interval is large.

This work focuses on a detailed electromagnetic simulation of the antenna arrays at the Tx and Rx, based on NEC's commercial-level simulation environment. To provide a scalable trade-off between the complexity and antenna gain discussed above, we propose two-stage alignment methods starting with wider beams achieved by deactivating antennas at the Tx and Rx to speed up the coarse beam scanning, and then refined with a precise estimate of the direction range to attain both required performance and potential measurement and complexity reduction. To further achieve low-complexity beam alignment, we propose a further two-stage alignment method, that also starts with a wider-beam coarse scanning, and at the second stage em-

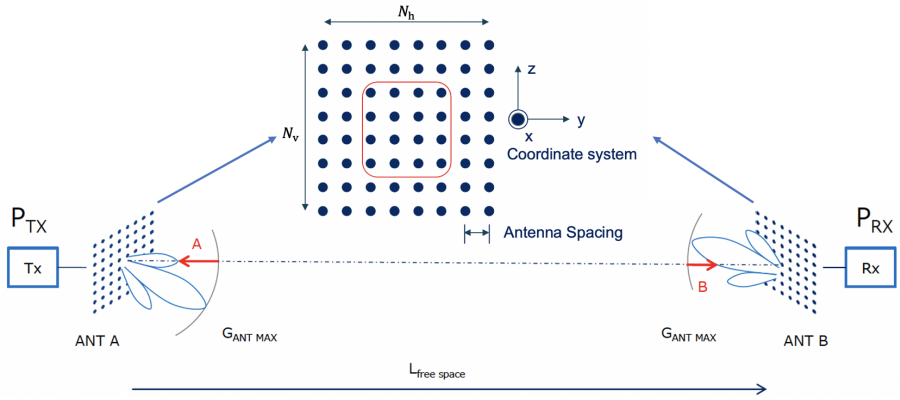

Figure 6.1: Free Space Communication Link with *yz*-plane planar array

ploys an algorithmic approach based on the gain difference generated by adjacent beams and the known beam pattern of our transceiver antenna arrays. Our methods are supported by a steerable, hybrid antenna array architecture with massive multiple-input multiple-output (MIMO) arrays at the Tx and Rx. The performance of the proposed beam-alignment methods is analyzed in terms of achievable total Tx-Rx antenna gain, beam misalignment probability, number of measurements, and total complexity. Numerical results avail complexity-performance trade-offs by tuning key scanning parameters of the methods governing the performance and demonstrate the effectiveness of our proposed alignment methods under the considered practical scenario.

6.2 System model

6.2.1 Free Space Propagation Model

We consider an xHaul point-to-point link as shown in Fig. 6.1, which is typically dominated by a strong LOS component [75]. To simplify our electromagnetic simulation, we employ the free space propagation model to model the LOS path incurred in a free space environment between the Tx and Rx in mmWave communication. We further assume that the Tx and Rx antennas are matched in impedance to their connecting transmission lines with identical and aligned polarizations [78, 82]. According to the well known

Friis formulation, we calculate the received signal power in free space at a distance $\mathfrak{R}$ from the Tx as [73, 79]

$$P_{Rx} = P_{Tx}\frac{G_{Tx}G_{Rx}\lambda^2}{(4\pi\mathfrak{R})^2}, \tag{6.1}$$

where P_{Rx} and P_{Tx} are the received power and transmit power respectively. G_{Rx} and G_{Tx} are the receive and transmit antenna gains. $\mathfrak{R}$ is the Tx-Rx separation distance and $\lambda = c/f$ is the carrier wavelength where f is the mmWave frequency and $c = 3 \times 10^8\ m/s$ is the speed of light. A convenient dB-form of (6.1) reads as

$$\begin{aligned} P_{Rx}(\text{dBm}) = P_{Tx}(\text{dBm}) + G_{Tx}(\text{dB}) + G_{Rx}(\text{dB}) - 20\log\mathfrak{R}(\text{km}) \\ - 20\log f(\text{MHz}) - 32.44, \end{aligned} \tag{6.2}$$

where, $\text{L}_{\text{free space}} = -20\log\mathfrak{R}(\text{km}) - 20\log f(\text{MHz}) - 32.44$ represents the free space path loss. (6.2) indicates the way to quantify the link performance, and the determination of the received power $P_{Rx}(\text{dBm})$ for a given mmWave frequency f relies on three key system factors: transmit power $P_{Tx}(\text{dBm})$, transmit antenna gain $G_{Tx}(\text{dB})$, and receive antenna gain $G_{Rx}(\text{dB})$. To validate the communication link, the actual received power should be greater than the minimum required received signal level; the gap between the minimum received signal level and the received power is called the link margin [78, 82].

Moreover, as shown in Fig. 6.1, $G_{ANT}^{TX}\ (dB)$ and $G_{ANT}^{RX}\ (dB)$ are optimal antenna gains acquired by ideal beam alignment, $A+B$ is the gain loss caused by misalignment. Then, the optimal antenna gain can be defined as

$$G_{opt}\ (dB) = G_{ANT}^{TX}\ (dB) + G_{ANT}^{RX}\ (dB). \tag{6.3}$$

While, the achievable Tx-Rx antenna gain in (6.2) can be extended to

$$G\ (dB) = G_{Tx}\ (dB) + G_{Rx}\ (dB) = G_{ANT}^{TX}\ (dB) + G_{ANT}^{RX}\ (dB) - (A+B). \tag{6.4}$$

In our studies, the target is to achieve close-to-optimal antenna gain by improving the achievable G (dB) and satisfying the required $A+B$.

6.2.2 Antenna Array and Antenna Gain

We define the array factor as $AF(\theta,\phi)$ in massive MIMO antenna arrays, where (θ,ϕ) denotes the angle coordinates of elevation and azimuth directions of AoD/AoA. By controlling the progressive phase difference between antennas, the maximum radiation can be targeted toward the desired direction to form a scanning array [80]. In the phase-shifted antenna array, we assume that each antenna element is excited with a signal at an amplitude of 1. However, the phase shift of each antenna achieved by analog beamforming where the phase excitation is done at the phase control unit will be different due to various transmission paths between antennas [174]. Therefore, the phase-shifted array factor of the $N_v \times N_h$ uniform planar array (UPA), shown in Fig. 6.1, can be written as [78, 82, 83]

$$AF(\theta,\phi) = \sum_{n=1}^{N_h}\sum_{m=1}^{N_v} e^{j(2\pi\hat{\mathbf{r}}\cdot\mathbf{r}_{mn}+\beta_{mn})}. \tag{6.5}$$

Here, β_{mn} is the phase shift for the mn-th antenna. N_v and N_h are the number of antennas deployed in the vertical and horizontal directions respectively. $\hat{\mathbf{r}}$ is the unit vector pointing in AoD/AoA [78, 82]:

$$\hat{\mathbf{r}} = \sin\theta\cos\phi\,\hat{\mathbf{x}} + \sin\theta\sin\phi\,\hat{\mathbf{y}} + \cos\theta\,\hat{\mathbf{z}}. \tag{6.6}$$

The antennas for a three-dimensional array are located with position vectors normalised by carrier wavelength from the origin to the mn-th antenna:

$$\mathbf{r}_{mn} = x_{mn}\hat{\mathbf{x}} + y_{mn}\hat{\mathbf{y}} + z_{mn}\hat{\mathbf{z}}. \tag{6.7}$$

Fig. 6.1 shows an example of a planar array, where the antennas are arranged uniformly along a rectangular grid in the yz-plane [78, 82]. Moreover, z represents elevation direction, and y represents azimuth direction. The phase-

shifted array factor of yz-plane planar array can be expanded from (6.5) to

$$AF(\theta,\phi) = \sum_{n=1}^{N_h}\sum_{m=1}^{N_v} e^{j2\pi(y_{mn}\sin\theta\sin\phi + z_{mn}\cos\theta - y_{mn}\sin\theta_0\sin\phi_0 - z_{mn}\cos\theta_0)}, \tag{6.8}$$

where $\beta_{mn} = -(y_{mn}\sin\theta_0\sin\phi_0 + z_{mn}\cos\theta_0)$ is the phase shift defined in (6.5). θ_0 and ϕ_0 are the elevation and azimuth phase excitation achieved by Intermediate Frequency (IF) phase control in NEC's mmWave radio unit. Note that the phase-shifted antenna array using analog beamforming where the phase adjustment is done at RF or IF frequencies and there is one set of data converters for the entire antenna. Generally, by tuning θ_0 and ϕ_0 on each side to match the optimal values, we can achieve beam alignment [78]. For simplicity, we assume $N_v = N_h = N$ in the following studies.

In general, the actual antenna elements do not have isotropic patterns. Therefore, the field pattern of a single antenna is defined as a product of an element factor and a pattern factor [78, 82]. Similarly, the complete array pattern can be acquired by pattern multiplication as the product of the element pattern and the phase-shifted array factor [78, 80, 82] with the expression

$$F(\theta,\phi) = g(\theta,\phi)AF(\theta,\phi). \tag{6.9}$$

Here, we employ the element pattern provided by NEC's equipment

$$g(\theta,\phi) = -\min\Big[12(\frac{\cos^{-1}(\cos\theta\sin\phi)}{HPBW})^2, SLL\Big], \tag{6.10}$$

where, $HPBW$ is the half-power beamwidth (HPBW) with inter-antenna distance d normalized by the carrier wavelength λ,

$$HPBW = \frac{50.8}{Nd}. \tag{6.11}$$

SLL is the side lobe level (SLL) introducing the information of how large (or

how small) is the ratio of the side lobe compared to the main lobe [80, 175]

$$SLL = 20 \cdot 1\log_{10}\Big(\frac{\text{the maximum value of largest side lobe}}{\text{the maximum value of main lobe}}\Big). \tag{6.12}$$

The antenna directivity is the ratio of the radiation intensity in a given direction from the antenna to the radiation intensity averaged over all directions. The average radiation intensity is equal to the total power radiated by the antenna divided by 4π [80]. In mathematical form, it can be written as

$$D(\theta,\phi) = \frac{4\pi U(\theta,\phi)}{P_{rad}}, \tag{6.13}$$

here, $D(\theta,\phi)$ is the dimensionless directivity. $U(\theta,\phi) = |F(\theta,\phi)|^2$ is the radiation intensity in terms of the power radiated from an antenna per unit solid angle [78, 82]. P_{rad} is the total radiated power with the mathematical form

$$P_{rad} = \int_0^{2\pi}\int_0^{\pi} U(\theta,\phi) sin(\theta) d\theta d\phi. \tag{6.14}$$

Then, (6.13) can be re-written as

$$D(\theta,\phi) = 4\pi \frac{U(\theta,\phi)}{\int_0^{2\pi}\int_0^{\pi} U(\theta,\phi) sin(\theta) d\theta d\phi}. \tag{6.15}$$

The antenna gain, applied in the communication link, is defined as 4π times the ratio of the radiation intensity in a given direction to the power input by the antenna [78, 80]. The total radiated power is related to the total input power by $P_{rad} = e_r \cdot P_{in}$. Then, the antenna gain can be given by

$$G(\theta,\phi) = 4\pi \frac{U(\theta,\phi)}{P_{in}} = e_r \cdot D(\theta,\phi), \tag{6.16}$$

where e_r is the antenna radiation efficiency. For simplicity, we assume $e_r = 1$. Later, 10 log would be applied to acquire the dB-form antenna gain defined in (6.2)-(6.4).

6.3 Design of Two-Stage Alignment Methods

In this chapter, we propose the design of two-stage alignment methods by exploiting an antenna deactivating approach [17, 20] and the theoretical beam pattern. The proposed beam alignment methods focus on achieving measurement and complexity reductions while satisfying the minimum antenna gain requirement.

6.3.1 Fundamental Techniques

Before the method design, we first introduce the deactivating approach, the scanning approach and the S-curve generation, which are applied in the design and will support the alignment methods.

6.3.1.1 Deactivating Approach

As shown in Fig. 6.1, we assume $N \times N$-element antenna arrays in yz-plane for both Tx and Rx, and each circle represents one antenna element. The antenna-position vectors for yz-plane planar array defined in (6.7) can be extended to

$$\mathbf{r}_{mn} = y_{mn}\hat{\mathbf{y}} + z_{mn}\hat{\mathbf{z}}, m = 1, ..., N, n = 1, ..., N, \tag{6.17}$$

where y_{mn} and z_{mn} are the mn-th elements in $\mathbf{y}.*\mathbf{I}_N$ and $\mathbf{z}.*\mathbf{I}_N$, respectively. Since the origin is the center $(0,0)$, then, the initial position coordinates $\mathbf{y} = \mathbf{z} = \mathbf{P} \in \mathbb{C}^{1\times N}$ can be given by

$$\mathbf{P} = 2d \cdot [-(N-1), -(N-3), ..., (N-1)], \tag{6.18}$$

where d is the normalised inter-antenna distance. If deactivating approach is applied in the $N \times N$ antenna array with only $N_{active} \times N_{active}$ antennas active for beam scanning, the determination of the position coordinates of active antennas is expressed as

$$\mathbf{P}_{active} = \mathbf{P}(5 + \frac{\upsilon - N_{active}}{2} : 4 + \frac{\upsilon + N_{active}}{2}), \tag{6.19}$$

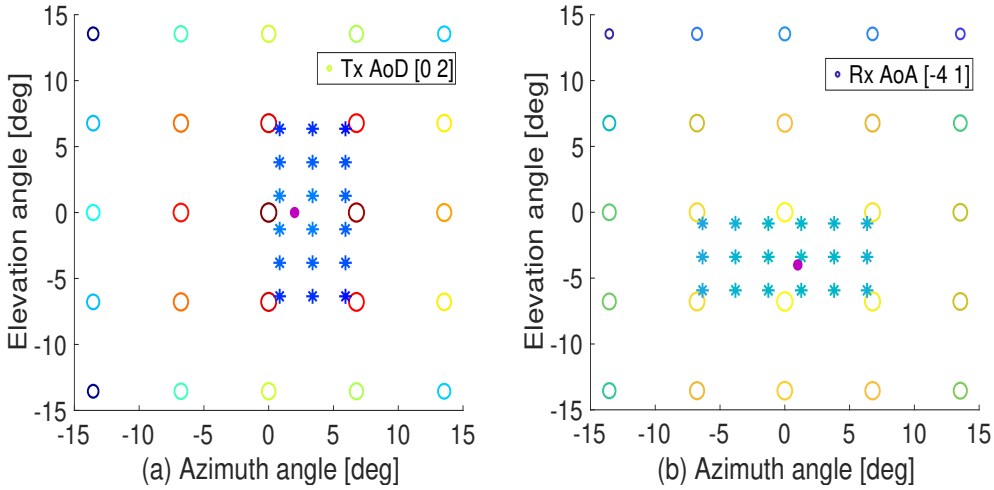

Figure 6.2: Scan range in square grid array with DD-BA. 6×6 active antennas in Stage 1, initial scan range $= [-15, 15]$, scan interval $= 0.4 \cdot HPBW$, red points represent the optimal AoD and AoA.

where, $\upsilon = \lceil N_{active} \rceil - \lfloor N_{active} \rfloor$. Thus, $\mathbf{y}_{active} = \mathbf{z}_{active} = \mathbf{P}_{active}$ will help to acquire the position vectors of active antennas according to (6.17).

6.3.1.2 Scanning Approach

With the assumption that the link's optimal AoD (θ_{Tx}, ϕ_{Tx}) and AoA (θ_{Rx}, ϕ_{Rx}) remain constant at Tx and Rx during the alignment phase, we steer the phase excitation achieved by IF phase control within the given scan range to match the optimal AoD and AoA. The Tx and Rx antennas can be aimed toward each other to form the maximum gain. In this case, the angle variables (φ^X, μ^X), $X = Tx,\ Rx$ represents the phase excitation in the following. Moreover, φ^X and μ^X stands for the elevation and azimuth phase excitation, respectively.

The initial elevation and azimuth scan ranges for Tx and Rx are defined as $[-\varphi_X, \varphi_X]$ and $[-\mu_X, \mu_X]$, $X = Tx,\ Rx$, respectively. The scan interval is $a \cdot HPBW$ to determine the coordinates of scanning points with a, the tunable scan interval parameter. Fig. 6.2 displays an example of scan range in a square grid array with a specific Dual-Deactivating Alignment Method (DD-BA) which will be introduced in the coming chapters. In Fig. 6.2, the empty circles are the coordinates of phase excitation (φ^X, μ^X) in Stage 1, while

the stars are the coordinates of phase excitation in Stage 2. Each scanning point will achieve its own antenna gain $G_X(\varphi^X, \mu^X)$, $X = Tx,\ Rx$, according to (6.16). The process of the scanning approach to generate the table matrices displaying the gain acquisition can be obtained by

Step 1: The table matrix for Tx is defined as $\mathbf{H}_{Tx} \in \mathbb{C}^{M_{Tx} \times 3}$, where $M_{Tx} = M_{\varphi}^{Tx} M_{\mu}^{Tx}$ is the total number of scanning points, M_{φ}^{Tx} and M_{μ}^{Tx} are the number of phase excitation in elevation and azimuth direction respectively. The coordinate of scanning point $(\varphi_i^{Tx}, \mu_j^{Tx})$ and its relevant antenna gain $G_{Tx}(\varphi_i^{Tx}, \mu_j^{Tx})$, $i = 1, ..., M_{\varphi}^{Tx}, j = 1, ..., M_{\mu}^{Tx}$ can be obtained. The generation process can follow the instructions in Algorithm 6.3.

Step 2: Similarly, the table matrix for Rx is defined as $\mathbf{H}_{Rx} \in \mathbb{C}^{M_{Rx} \times 3}$, where $M_{Rx} = M_{\varphi}^{Rx} M_{\mu}^{Rx}$ is the total number of scanning points and M_{φ}^{Rx} and M_{μ}^{Rx} are the number of phase excitation in elevation and azimuth direction respectively. The coordinate of scanning point $(\varphi_i^{Rx}, \mu_j^{Rx})$ and its relevant antenna gain $G_{Rx}(\varphi_i^{Rx}, \mu_j^{Rx})$, $i = 1, ..., M_{\varphi}^{Rx}, j = 1, ..., M_{\mu}^{Rx}$ can be obtained. Similarly, the generation process can be instructed by Algorithm 6.3.

Step 3: Now we focus on the gains of scanning point pairs as $G\ (dB) = G_{Tx}\ (dB) + G_{Rx}\ (dB)$ defined in Chapter 6.2. If we observe Tx with a specific phase excitation $(\varphi_i^{Tx}, \mu_j^{Tx})$, all phase excitation at Rx will be scanned, namely, M_{Rx} scanning point pairs will be steered to select the phase excitation team which can achieve the maximum $G\ (dB)$. This process will be repeated for all phase excitation at Tx; thus, an updated table matrix $\mathbf{H}_{Tx}^{\text{up}} \in \mathbb{C}^{M_{Tx} \times 7}$ will be obtained, which is further instructed by Algorithm 6.3.

Step 4: This step applies a similar process at Rx. If we observe Rx with a fixed phase excitation $(\varphi_i^{Rx}, \mu_j^{Rx})$, we will scan all phase excitation at Tx to steer M_{Tx} scanning point pairs for the selection of the phase excitation team achieving maximum antenna gain $G\ (dB)$. This process will also be repeated for all phase excitation at Rx; thus, an updated table matrix $\mathbf{H}_{Rx}^{\text{up}} \in \mathbb{C}^{M_{Rx} \times 7}$ will be obtained according to Algorithm 6.3.

Step 5: Based on the above-mentioned updated table matrices, we can

find the specific Tx and Rx phase excitation to achieve the maximum antenna gain or the narrowed range in which the optimal AoD and AoA are located to promote the beam alignment.

6.3.1.3 S-curve Generation

The generation of the gain difference between adjacent beams can be obtained off-line using the theoretical beam patterns produced by the Tx or Rx arrays. Owing to its shape, we denote this theoretical function as the *S-curve*, which is the key of the Deactivating S-curve Alignment Method (DS-BA). The S-curve is one-dimensional; therefore, we have to obtain the elevation and azimuth S-curves separately. Fig. 6.3 shows the elevation S-curve generation, and we take this elevation S-curve generation as an example. We assume that the estimated elevation direction is φ_0 and the angle error between φ_0 and the optimal AoD/AoA is ς, which equates to $\theta_X = \varphi_0 + \varsigma$, $X = Tx, Rx$.

Algorithm 6.3 Table matrix generation at Tx and Rx

Input: M_X, M_φ^X, M_μ^X, $\varphi_X \in \mathbb{C}^{M_\varphi^X \times 1}$, $\mu_X \in \mathbb{C}^{M_\mu^X \times 1}$, $X = Tx,\ Rx$.
Output: $\mathbf{H}_X \in \mathbb{C}^{M_X \times 3}$,$\mathbf{H}_X^{\text{up}} \in \mathbb{C}^{M_X \times 7}$, $X = Tx,\ Rx$.
Tx/Rx Table matrix:
1: index $= 0$
2: **for** $i = 1 : M_\varphi^X$ **do**
3: **for** $j = 1 : M_\mu^X$ **do**
4: index $=$ index $+ 1$;
5: $\mathbf{H}_X(\text{index}, 1) = \varphi_X(i)$;
6: $\mathbf{H}_X(\text{index}, 2) = \mu_X(j)$;
7: $\mathbf{H}_X(\text{index}, 3) = 10\log_{10} G_X(\varphi_i^X, \mu_j^X)$, here dB-form is applied and $G_X(\varphi_i^X, \mu_j^X)$ is obtained by (6.16).
8: **end for**
9: **end for**
Updated Table matrix:
10: $\mathbf{H}_X^{\text{up}}(:, 1:3) = \mathbf{H}_X$
11: **for** $i = 1 : M_X$ **do**
12: $[m] = \text{find}(\mathbf{H}_X(i,3) + \mathbf{H}_Y(:,3) == \max(\mathbf{H}_X(i,3) + \mathbf{H}_Y(:,3)))$;
13: $\mathbf{H}_X^{\text{up}}(i, 4:6) = \mathbf{H}_Y(m, :)$;
14: $\mathbf{H}_X^{\text{up}}(i, 7) = \mathbf{H}_X(i,3) + \mathbf{H}_Y(m,3)$;
15: **end for**
16: Note: If $X = Tx$, $Y = Rx$, vice versa.

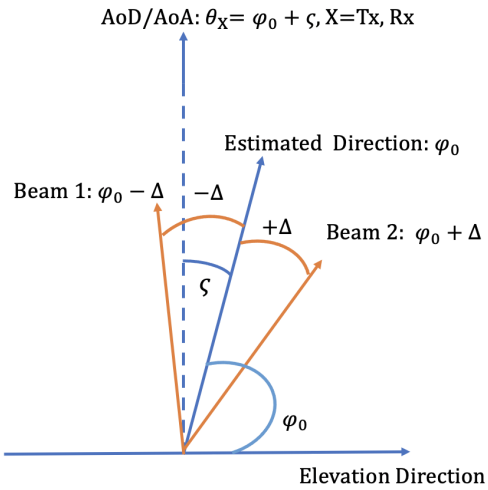

Figure 6.3: S-curve generation of elevation direction

Two beam angles are sampled with measured beam gains $G(\varphi_0+\Delta,\mu)(dB)$ and $G(\varphi_0-\Delta,\mu)(dB)$, where Δ is the interval between the sampled beam angles and the estimated direction φ_0. Therefore, the S-curve can be obtained prospectively as a function of ς by calculating the gain difference between the two sampled beams,

$$\begin{aligned} G_{diff}(\varsigma)\ (dB) &= G(\varphi_0+\Delta,\mu^X)\ (dB) - G(\varphi_0-\Delta,\mu^X)\ (dB) \\ &= G(\theta_X-\varsigma+\Delta,\mu^X)\ (dB) - G(\theta_X-\varsigma-\Delta,\mu^X)\ (dB), \end{aligned} \tag{6.20}$$

where $X = Tx,\ Rx$. In general, the directions of the two sampled beams should be within the range of the main lobe to guarantee the alignment accuracy; thus, we can set up the angle error range, $\varsigma \in [\Delta - HPBW, HPBW - \Delta]$ with $0 < \Delta < HPBW$. The mathematical extensions of $G_{diff}(\varsigma)$ for elevation

direction can be given by

$$
\begin{aligned}
G_{diff}^{\varphi}(\varsigma) = 10\log_{10}&\left(\frac{\sum_{m=1}^{N\times N}\sum_{n=1}^{N\times N} g_{+}(\varsigma)^2 e^{2\pi jNu_{\varphi,+\Delta}}}{\sum_{a=1}^{\text{length}(\hat{\theta})}\sum_{b=1}^{\text{length}(\hat{\phi})}\sum_{m=1}^{N\times N}\sum_{n=1}^{N\times N}\chi(a)g(a,b)^2 e^{2\pi jDe_{\varphi,+\Delta}}}\right)\\
-10\log_{10}&\left(\frac{\sum_{m=1}^{N\times N}\sum_{n=1}^{N\times N} g_{-}(\varsigma)^2 e^{2\pi jNu_{\varphi,-\Delta}}}{\sum_{a=1}^{\text{length}(\hat{\theta})}\sum_{b=1}^{\text{length}(\hat{\phi})}\sum_{m=1}^{N\times N}\sum_{n=1}^{N\times N}\chi(a)g(a,b)^2 e^{2\pi jDe_{\varphi,-\Delta}}}\right),
\end{aligned}
\tag{6.21}
$$

with

$$
\begin{aligned}
Nu_{\varphi,+\Delta} &= (\sin\theta_X \sin\phi_X - \sin(\theta_X - \varsigma + \Delta)\sin\mu^X)\cdot(\mathbf{y}(m)-\mathbf{y}(n))\\
&\quad + (\cos\theta_X - \cos(\theta_X - \varsigma + \Delta))\cdot(\mathbf{z}(m)-\mathbf{z}(n))\\
De_{\varphi,+\Delta} &= (\sin\hat{\theta}(a)\sin\hat{\phi}(b) - \sin(\theta_X - \varsigma + \Delta)\sin\mu^X)\cdot(\mathbf{y}(m)-\mathbf{y}(n))\\
&\quad + (\cos\hat{\theta}(a) - \cos(\theta_X - \varsigma + \Delta))\cdot(\mathbf{z}(m)-\mathbf{z}(n)),
\end{aligned}
\tag{6.22}
$$

$$
\begin{aligned}
Nu_{\varphi,-\Delta} &= (\sin\theta_X \sin\phi_X - \sin(\theta_X - \varsigma - \Delta)\sin\mu^X)\cdot(\mathbf{y}(m)-\mathbf{y}(n))\\
&\quad + (\cos\theta_X - \cos(\theta_X - \varsigma - \Delta))\cdot(\mathbf{z}(m)-\mathbf{z}(n))\\
De_{\varphi,-\Delta} &= (\sin\hat{\theta}(a)\sin\hat{\phi}(b) - \sin(\theta_X - \varsigma - \Delta)\sin\mu^X)\cdot(\mathbf{y}(m)-\mathbf{y}(n))\\
&\quad + (\cos\hat{\theta}(a) - \cos(\theta_X - \varsigma - \Delta))\cdot(\mathbf{z}(m)-\mathbf{z}(n)).
\end{aligned}
\tag{6.23}
$$

Similarly, the S-curve of azimuth direction will be generated via the above-mentioned process and expressed as

$$
\begin{aligned}
G_{diff}^{\mu}(\varsigma) = 10\log_{10}&\left(\frac{\sum_{m=1}^{N\times N}\sum_{n=1}^{N\times N} \gamma_{+}(\varsigma)^2 e^{2\pi jNu_{\mu,+\Delta}}}{\sum_{a=1}^{\text{length}(\hat{\theta})}\sum_{b=1}^{\text{length}(\hat{\phi})}\sum_{m=1}^{N\times N}\sum_{n=1}^{N\times N}\chi(a)g(a,b)^2 e^{2\pi jDe_{\mu,+\Delta}}}\right)\\
-10\log_{10}&\left(\frac{\sum_{m=1}^{N\times N}\sum_{n=1}^{N\times N} \gamma_{-}(\varsigma)^2 e^{2\pi jNu_{\mu,-\Delta}}}{\sum_{a=1}^{\text{length}(\hat{\theta})}\sum_{b=1}^{\text{length}(\hat{\phi})}\sum_{m=1}^{N\times N}\sum_{n=1}^{N\times N}\chi(a)g(a,b)^2 e^{2\pi jDe_{\mu,-\Delta}}}\right),
\end{aligned}
\tag{6.24}
$$

with

$$\begin{aligned} Nu_{\mu,+\Delta} &= (\sin\theta_X \sin\phi_X - \sin\varphi^X \sin(\phi_X - \varsigma + \Delta)) \cdot (\mathbf{y}(m) - \mathbf{y}(n)) \\ &\quad + (\cos\theta_X - \cos\varphi^X) \cdot (\mathbf{z}(m) - \mathbf{z}(n)) \\ De_{\mu,+\Delta} &= (\sin\hat{\theta}(a)\sin\hat{\phi}(b) - \sin\varphi^X \sin(\phi_X - \varsigma + \Delta)) \cdot (\mathbf{y}(m) - \mathbf{y}(n)) \\ &\quad + (\cos\hat{\theta}(a) - \cos\varphi^X) \cdot (\mathbf{z}(m) - \mathbf{z}(n)) \end{aligned} \tag{6.25}$$

$$\begin{aligned} Nu_{\mu,-\Delta} &= (\sin\theta_X \sin\phi_X - \sin\varphi^X \sin(\phi_X - \varsigma - \Delta)) \cdot (\mathbf{y}(m) - \mathbf{y}(n)) \\ &\quad + (\cos\theta_X - \cos\varphi^X) \cdot (\mathbf{z}(m) - \mathbf{z}(n)) \\ De_{\mu,-\Delta} &= (\sin\hat{\theta}(a)\sin\hat{\phi}(b) - \sin\varphi^X \sin(\phi_X - \varsigma - \Delta)) \cdot (\mathbf{y}(m) - \mathbf{y}(n)) \\ &\quad + (\cos\hat{\theta}(a) - \cos\varphi^X) \cdot (\mathbf{z}(m) - \mathbf{z}(n)). \end{aligned} \tag{6.26}$$

Moreover, the expressions of relevant element patterns in (6.21) and (6.24), can be given by

$$g_{\pm}(\varsigma) = -\min\Big[12(\frac{\cos^{-1}(\cos(\theta_X - \varsigma \pm \Delta)\sin\mu^X)}{HPBW})^2, SLL\Big], \tag{6.27}$$

$$\gamma_{\pm}(\varsigma) = -\min\Big[12(\frac{\cos^{-1}(\cos\varphi^X \sin(\phi_X - \varsigma \pm \Delta))}{HPBW})^2, SLL\Big], \tag{6.28}$$

$$g(a,b) = -\min\Big[12(\frac{\cos^{-1}(\cos\hat{\theta}(a)\hat{\phi}(b))}{HPBW})^2, SLL\Big]. \tag{6.29}$$

Here, $\hat{\theta} \in (0, \pi)$ and $\hat{\phi} \in (-\pi/2, \pi/2)$ are applied to calculate the total radiated power with intervals Δ_θ and Δ_ϕ, respectively. Note that $\chi(a) = \sin\hat{\theta}(a)\frac{\Delta_\theta \Delta_\phi (\pi/180)^2}{4\pi}$ is defined and applied in (6.21) and (6.24).

Fig. 6.4 shows the example elevation and azimuth S-curves for AoD =[0 2] and AoA=[-4 1] generated by (6.21)-(6.26) as functions of the angle error ς (deg). Both elevation and azimuth S-curves for Tx and Rx share the same curve as we assume a symmetric antenna array at both the Tx and the Rx.

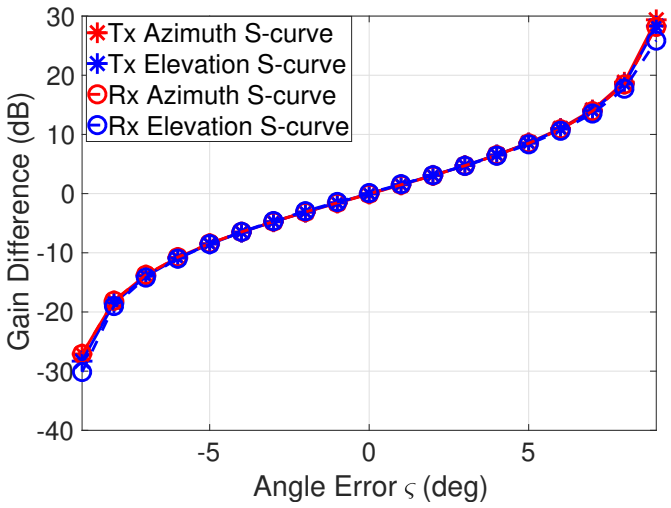

Figure 6.4: S-Curve v.s. Angle error, AoD=[0 2] and AoA=[-4 1].

6.3.2 Two-stage Beam Alignment Methods

6.3.2.1 Deactivating-Activating Alignment Method (DA-BA)

In this method, we deactivate a subset of antennas at Stage 1 to obtain a wider beam and a first approximate scan of the angle range. Then in Stage 2 we activate all antennas to obtain a finer scan over a narrowed scan range and maximize the total link gain.

Stage 1: The deactivating approach with $N_{active} \times N_{active}$ antennas is employed within the scan range of $[-\varphi_X, \varphi_X]$ and $[-\mu_X, \mu_X]$, $X = Tx,\ Rx$. The scan interval, $a \cdot HPBW_1$ with $HPBW_1 = 50.8/(N_{active}d)$, is applied to determine the scanning point coordinates. If the maximum antenna gain obtained in Stage 1 is $G^1_{max}\ (dB)$, the narrowed scan range would be determined by selecting the phase excitation pairs with $G\ (dB) > G^1_{max}\ (dB) - \delta\ (dB)$ referring to the table matrices, where $\delta\ (dB)$ is the threshold in the observed link gain that is used to determine the narrowed scan range. Thus, the narrowed scan range can be summarised as $[\varphi_X^{\text{low}}, \varphi_X^{\text{upper}}]$ and $[\mu_X^{\text{low}}, \mu_X^{\text{upper}}]$, $X = Tx,\ Rx$.

Stage 2: All $N \times N$ antennas are active to steer within the narrowed scanning range obtained by Stage 1. $b \cdot HPBW_2$ with $HPBW_2 = 50.8/(Nd)$ and b, a new tunable scan interval parameter, is used as the scan interval to determine the scanning points in Stage 2. After steering all scanning point pairs

in Stage 2 and obtaining the table matrices of Stage 2. Then, we can get the achievable maximum antenna gain G_{max} (dB) and its relevant Tx/Rx phase excitation.

6.3.2.2 Dual-Deactivating Alignment Method (DD-BA)

In this method, the deactivating approach is applied in both stages with the same number of active antennas.

Stage 1: The scanning process in this stage is the same as Stage 1 in the DA-BA method, where the scan interval is $a \cdot HPBW_1$ with $HPBW_1 = 50.8/(N_{active}d)$. In this case, the narrowed scan range can be obtained as $[\varphi_X^{\text{low}}, \varphi_X^{\text{upper}}]$ and $[\mu_X^{\text{low}}, \mu_X^{\text{upper}}]$, $X = Tx, Rx$, with selecting all phase excitation pairs in the table matrices to satisfy $G\ (dB) > G_{max}^1\ (dB) - \delta\ (dB)$. The completion of the scanning approach and generation of table matrices support this process.

Stage 2: Deactivating approach with $N_{active} \times N_{active}$ active antennas is still applied to complete the scanning within the narrowed scan range obtained by Stage 1. $b \cdot HPBW_2$ with $HPBW_2 = 50.8/(N_{active}d)$ is used as the scan interval to determine the new scanning points in Stage 2. After steering all scanning point pairs in Stage 2 and obtaining the table matrices of Stage 2, we can find the optimal angles of the Tx and Rx phase excitation. Then, all antennas are activated to point to the selected directions with maximum Tx-Rx antenna gain G_{max} (dB).

6.3.2.3 Deactivating S-curve Alignment Method (DS-BA)

In the DS-BA method, we deactivate a subset of antennas at Stage 1 to obtain a wider beam and a first approximate scan of the estimated directions. Then in Stage 2, we activate all antennas to exploit the S-curves generated in Chapter 6.3.1.3 for linear interpolation and maximize the total Tx-Rx antenna gain.

Stage 1: The scanning process in this stage is the same as Stage 1 in the DA-BA and DD-BA methods. In this case, if the maximum antenna gain obtained in Stage 1 is G_{max}^1 (dB); then the scanning points attaining G_{max}^1 (dB)

will be selected, i.e., $(\varphi_{X,i}^{\text{stage1}}, \mu_{X,i}^{\text{stage1}})$ will be selected, $X = Tx,\ Rx$, $i = 1, \ldots, N_{p,X}$ with $N_{p,X}$, the total number of scanning points achieving $G_{max}^{1}\ (dB)$. Then, an averaging method will be applied to obtain

$$\bar{\varphi}_X^{\text{stage1}} = \frac{1}{N_{p,X}} \sum_{i=1}^{N_{p,X}} \varphi_{X,i}^{\text{stage1}}, \tag{6.30}$$

$$\bar{\mu}_X^{\text{stage1}} = \frac{1}{N_{p,X}} \sum_{i=1}^{N_{p,X}} \mu_{X,i}^{\text{stage1}}, \tag{6.31}$$

where, $X = Tx,\ Rx$. $\bar{\varphi}_X^{\text{stage1}}$ and $\bar{\mu}_X^{\text{stage1}}$ will be used as the estimated directions to apply off-line S-curves and accomplish the gain difference interpolation in Stage 2.

Stage 2: All $N \times N$ antennas are active in this stage, and off-line elevation and azimuth S-curves generated by (6.20)-(6.26) will be exploited to accomplish gain difference interpolation; thus, the process is:

- Step 1: We first calculate the gain difference in the elevation direction by $G_{diff}^{\varphi}\ (dB) = G(\bar{\varphi}_X^{\text{stage1}} + \Delta, \bar{\mu}_X^{\text{stage1}})\ (dB) - G(\bar{\varphi}_X^{\text{stage1}} - \Delta, \bar{\mu}_X^{\text{stage1}})\ (dB)$.

- Step 2: We interpolate the elevation gain difference $G_{diff}^{\varphi}\ (dB)$ obtained in Step 1 to S-curve by using Matlab function interp1() to obtain the elevation angle error ς_φ and then the achievable elevation direction equates to $\bar{\varphi}_X = \bar{\varphi}_X^{\text{stage1}} + \varsigma_\varphi$.

- Step 3: Similarly, we then calculate the gain difference in the azimuth direction by $G_{diff}^{\mu}\ (dB) = G(\bar{\varphi}_X^{\text{stage1}}, \bar{\mu}_X^{\text{stage1}} + \Delta)\ (dB) - G(\bar{\varphi}_X^{\text{stage1}}, \bar{\mu}_X^{\text{stage1}} - \Delta)\ (dB)$.

- Step 4: We interpolate the azimuth gain difference $G_{diff}^{\mu}\ (dB)$ obtained in Step 3 to S-curve by using Matlab function interp1() to obtain the azimuth angle error ς_μ and then the achievable azimuth direction equates to $\bar{\mu}_X = \bar{\mu}_X^{\text{stage1}} + \varsigma_\mu$.

- Step 5: If $G(\bar{\varphi}_{Tx}, \bar{\mu}_{Tx})\ (dB) + G(\bar{\varphi}_{Rx}, \bar{\mu}_{Rx})\ (dB) < G_{opt}\ (dB) - \varkappa\ (dB)$, the new estimated directions $\bar{\varphi}_X$ and $\bar{\mu}_X$, $X = Tx,\ Rx$, will be applied to

repeat Step 1-4 until $G_{max}\ (dB) = G(\bar{\varphi}_{Tx}, \bar{\mu}_{Tx})\ (dB) + G(\bar{\varphi}_{Rx}, \bar{\mu}_{Rx})\ (dB) \geq G_{opt}\ (dB) - \varkappa\ (dB)$. This repetition might last for L times.

The summary of the key system parameters applied in the two-stage alignment methods is in Table 6.1. Note that when comparing the achievable maximum antenna gain $G_{max}\ (dB)$ with the optimal antenna gain $G_{opt}\ (dB)$, if $G_{opt}\ (dB) - G_{max}\ (dB) < \varkappa\ (dB)$, where $\varkappa\ (dB)$ is the maximum acceptable gain loss, the target of required antenna gain can be attained.

6.4 Performance Metrics

6.4.1 Misalignment Probability

The Probability of misalignment of the two-stage alignment methods is defined as probability that the achievable Tx-Rx antenna gain is smaller than a certain threshold [75, 171, 176],

$$P_{miss} = \text{Prob}(G_{max} < G_{opt} - \varkappa) = \int_{-\infty}^{G_{opt}-\varkappa} f(x)dx. \tag{6.32}$$

Here, G_{max} is the antenna gain acquired by the two-stage alignment methods, and G_{opt} is the optimal antenna gain, $f(x)$ is the probability density function of G_{max}. Typically, G_{max} can be admitted as a noncentral chi-square random variable of two degrees of freedom with non-centrality parameter λ_{max} [74] and $\varkappa$ is the threshold which equals to the maximum acceptable gain loss.

Description		Stage 1	Stage 2	Note
Deactivating-Activating Beam Alignment (DA-BA)	No. active antennas	$N_1 = N_{active}$	$N_2 = N$	$1 \leq N_{active} \leq N$
	Scanning interval	$a \cdot HPBW_1$	$b \cdot HPBW_2$	$HPBW_1 \geq HPBW_2; a \geq b$
	Scanning range	Pre-defined	Narrowed Range	Determined by Stage 1
Dual-Deactivating Beam Alignment (DD-BA)	No. active antennas	$N_1 = N_{active}$	$N_2 = N_{active}$	$1 \leq N_{active} \leq N$
	Scanning interval	$a \cdot HPBW_1$	$b \cdot HPBW_2$	$HPBW_1 = HPBW_2; a \geq b$
	Scan range	Pre-defined	Narrowed Range	Determined by Stage 1
Deactivating S-curve Beam Alignment (DS-BA)	No. active antennas	$N_1 = N_{active}$	$N_2 = N$	$1 \leq N_{active} \leq N$
	Scanning interval	$a \cdot HPBW_1$	/	/
	Scan range	Pre-defined	$(\bar{\varphi}_X^{\text{stage1}}, \bar{\mu}_X^{\text{stage1}})$	Determined by Stage 1

Table 6.1: Two-stage Alignment Method Summary

Referring to [75, 171], we can simplify the mathematical form of misalignment probability as

$$P_{miss} = 1 - Q_1(\sqrt{\lambda_{max}}, \sqrt{G_{opt} - \varkappa}), \tag{6.33}$$

$Q_1(x, y)$ is the first-order Marcum Q function. We refer readers to [75, 171] for a more systematic study to avoid repetition. Note that, G_{max} and $G_{opt} - \varkappa$ are symbolic expressions in dB-form, actual mathematical calculations employ the dimensionless form transferred from dB-form.

6.4.2 Number of Measurements and Complexity

6.4.2.1 Number of Measurements

In our studies, we consider that one scanning point pair equates to one measurement until specifically stated, where scanning points are determined by scan range and scan interval as shown in Fig. 6.2. In Stage 1, the predefined scan ranges are the same for both directions; thus, both Tx and Rx have the same number of scanning points M_{scan}. Then, the total number of scanning point pairs in Stage 1, in other words, the total number of measurements, is $M_{scan} \cdot M_{scan}$. For the DA-BA and DD-BA methods, in Stage 2, the scan ranges are narrowed by the scanning in Stage 1; thus, both Tx and Rx have their respective number of scanning points, which are, M_{Tx} and M_{Rx}, due to different narrowed scan ranges. The number of measurements in Stage 2 is $M_{Tx} \cdot M_{Rx}$. In this case, we can obtain the general mathematical expression of the number of total measurements of the DA-BA and DD-BA methods by,

$$M_{total} = M_{scan}^2 + M_{Tx} \cdot M_{Rx}. \tag{6.34}$$

For the DS-BA method, the gain difference interpolation in Stage 2 employs two sampled beams, namely, two scanning points for both elevation and azimuth directions. We assume one scanning point equates to one measurement for S-curve interpolation. Therefore, when the process of S-curve in-

terpolation at Tx and Rx repeat for L times, the total measurements of the DS-BA method can be given by

$$M_{total} = M_{scan}^2 + 2 \times 4L. \tag{6.35}$$

6.4.2.2 Complexity

The computational complexity shows how many flops are needed to complete the gain measurements [81, 97], and the overall complexity of our methods depends on the operations required to calculate antenna gains and attain the table matrices. We recall that the power consumption of digital signal processors (DSP) in RF chains dedicated to antennas is positively determined by the computational flops [81]. In this case, computational complexity reduction becomes a vital topic in achieving power consumption reduction and energy efficiency [177]. Both stages in the DA-BA and DD-BA methods have a similar process with different numbers of active antennas and scanning points; then, we can provide a general expression of complexity. In this case, for Stage x, $x \in [1,2]$, the complexity of implementing $N_x \times N_x$ phase-shifting matrix to achieve phase-shifted antenna array at both Tx and Rx, $y = Tx,\ Rx$, can be given by [81, 97]

$$C_{p-af}^{x,y} = 10N_x \times N_x \times M, \tag{6.36}$$

where M is the number of scanning points. In our studies, we consider the element pattern in (6.10) for pattern multiplication, the calculation of element pattern increases the complexity as [81]

$$C_{\mathrm{ep}}^{x,y} = \frac{5}{2} M \log_2(M). \tag{6.37}$$

Subsequently, we come to calculate the radiation intensity, and then antenna gains. The complexity of this process turns to

$$C_{\text{ap}}^{\text{x,y}} = 8M. \tag{6.38}$$

After obtaining antenna gains for all scanning points, the generation of table matrices defined in Chapter 6.3.1.2 will introduce extra complexity

$$C_{\text{table}}^{\text{x}} = 3M_{tot}. \tag{6.39}$$

The total complexity for the DA-BA and DD-BA methods can be expressed as

$$C_{\text{total}} = \sum_{x=1,2} \sum_{y=Tx,Rx} \left(C_{p-af}^{\text{x,y}} + C_{\text{ep}}^{\text{x,y}} + C_{\text{ap}}^{\text{x,y}}\right) + C_{\text{table}}^{\text{x}}. \tag{6.40}$$

Note that $M = M_{scan}$ for both Tx and Rx with $M_{tot} = M_{scan}^2$ in Stage 1, $M = M_{Tx}$ for Tx complexity and $M = M_{Rx}$ for Rx complexity with $M_{tot} = M_{Tx}M_{Rx}$ in Stage 2.

Similarly, the DS-BA method employs the same Stage 1, and the complexity difference compared with the DA-BA and DD-BA methods relies on Stage 2. In Stage 2, (6.36)-(6.38) are operated with $M = 2$ and $N_2 = N$ for both elevation and azimuth directions at Tx and Rx. Note that no table matrices are generated in Stage 2 of the DS-BA method. Meanwhile, the complexity of linear interpolation equates to four flops [178]. If the process of S-curve interpolation at Tx and Rx repeat for L times, the total complexity for the DS-BA method can be expressed as

$$C_{\text{total}} = \sum_{y=Tx,Rx} \left(C_{p-af}^{1,\text{y}} + C_{\text{ep}}^{1,\text{y}} + C_{\text{ap}}^{1,\text{y}}\right) + C_{\text{table}}^{1} + 4L(20N^2 + 25). \tag{6.41}$$

6.5 Numerical Results

Our setup involves an 8×8-element antenna array. For deactivating approach, $N_{active}^2/N^2 \geq 1/3$ is required to obtain a satisfactory performance in realistic massive MIMO systems [17]. The inter-antenna distance $D = 3.15\ mm$ and the mmWave frequency $f = 47.619\ GHz$; then the normalized inter-antenna distance $d = D/(c/f) = 0.5$. The interval parameter in Stage 2 of both DA-BA and DD-BA methods is fixed to be $b = 0.05$. We propose $\varkappa\,(dB) = 0.03$ dB as the maximum acceptable gain loss for the DS-BA method according to NEC's simulation requirement. The values of AoD and AoA at Tx and Rx are randomly selected from $[-5, 5]$ (deg) in both elevation and azimuth directions to evaluate the average performance by Monte-Carlo simulation. The parameters of NEC's experimental communication link are given in Table 6.2. In our current experimental scenario, the initial scan range is $[-15, 15]$ (deg) for elevation and azimuth directions. The interval between the sampled beam angles and the estimated direction in the DS-BA method is $\Delta = 5$ (deg).

6.5.1 DA-BA and DD-BA

Fig. 6.5 shows the effect of the interval parameter a in Stage 1 on the achievable antenna gain with different values of δ (dB). We can observe that both DA-BA and DD-BA methods can outperform the conventional one-stage exhaustive method with varying interval parameters. Moreover, the achievable antenna gain matches the maximum value, for the region of $a \leq 0.3$ for

Parameters	
Tx power	18.0 dBm
Distance	500 m
Path loss	-123.6 dB
$G_{opt} = G_{ANT}^{TX} + G_{ANT}^{RX}$	45.3213 dB
Minimum Rx Power	-80 dBm
Acceptable Gain loss	$\tau \leq 19.7213$ dB

Table 6.2: Parameters of Experimental Communication Link

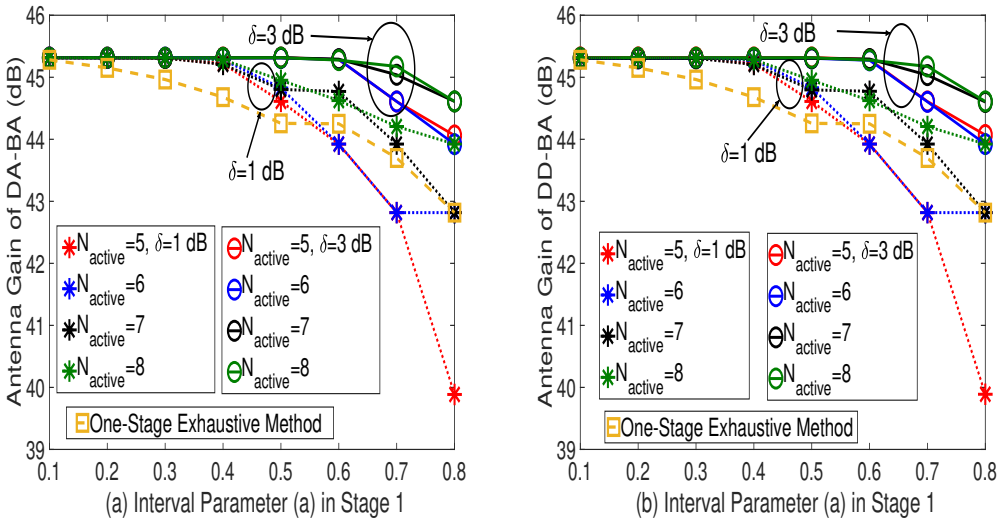

Figure 6.5: Antenna Gain G_{max} (dB) v.s. Interval parameter a in Stage 1.

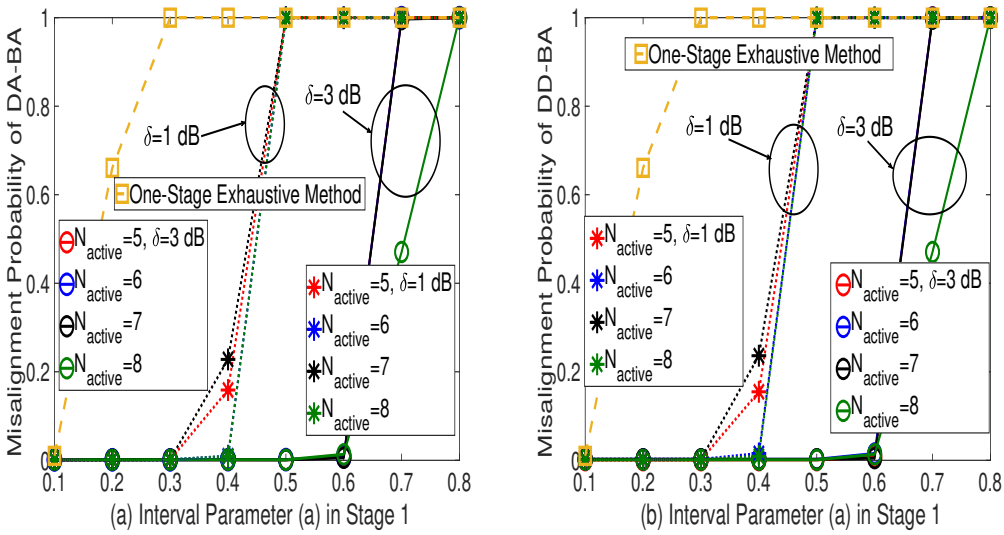

Figure 6.6: Misalignment probability P_{miss} v.s. Interval parameter a in Stage 1, $\varkappa = 0.15$ (dB).

both methods with varying N_{active} and varying δ (dB). Nevertheless, the achievable antenna gain drops rapidly when $a > 0.3$ with $\delta = 1(dB)$ and $a > 0.6$ with $\delta = 3(dB)$. Larger scan intervals and smaller δ (dB) can jointly result in potential misalignment since these two parameters can increase the possibility that the optimal AoD and AoA are outside the narrowed scan range of Stage 2.

The misalignment probability v.s. interval parameter a in Stage 1 is dis-

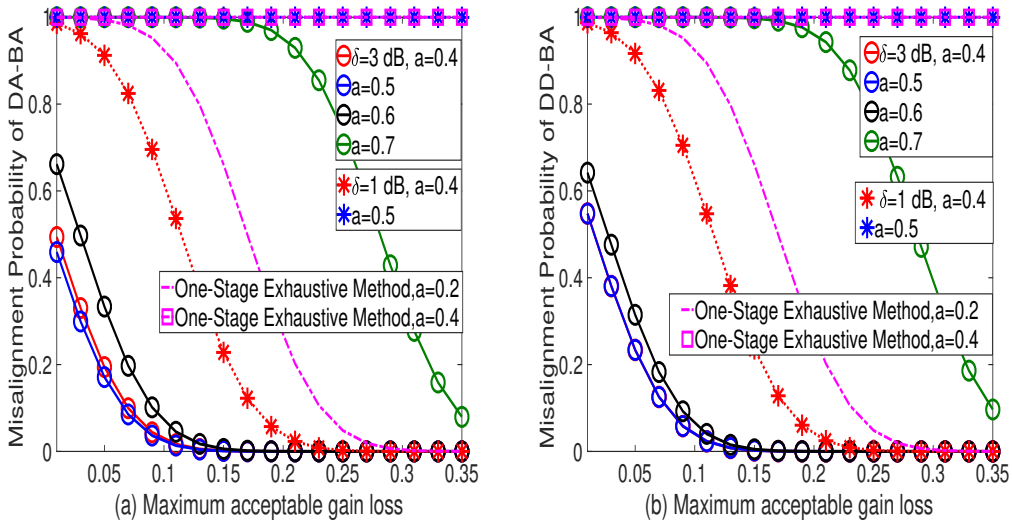

Figure 6.7: Misalignment probability P_{miss} v.s. Maximum acceptable gain loss $\varkappa$ (dB), $N_{active} = 7$.

played in Fig. 6.6 with the maximum acceptable gain loss $\varkappa = 0.15$ (dB). For simplicity, we assume $\lambda_{max} = G_{max}$ is applied in (6.33) according to [75, 171]. We can observe that both DA-BA and DD-BA methods can outperform the conventional one-stage exhaustive method when the interval parameter $a > 0.1$. It also shows that when $a \leq 0.3$ with $\delta = 1$ (dB) and $a < 0.6$ with $\delta = 3$ (dB), both methods with varying N_{active} can satisfy the acceptable gain loss $\varkappa$ and achieve close to zero misalignment probability. As clarified in Fig. 6.5, smaller δ (dB) and larger a can jointly result in potential misalignment; therefore, smaller δ (dB) has a negative impact on misalignment probability when a is increasing.

Fig. 6.7 examines the relationship between the misalignment probability and the maximum acceptable gain loss $\varkappa$ (dB). We can observe that a higher value of $\varkappa$ (dB) achieves a larger tolerance to the loss in the link gain, and the misalignment probability will significantly reduce for both DA-BA and DD-BA methods. The conventional one-stage exhaustive method obtains a larger misalignment probability compared with both proposed methods. Moreover, smaller δ (dB) can increase the misalignment probability when other key parameters are the same, because smaller δ (dB) may cause the opti-

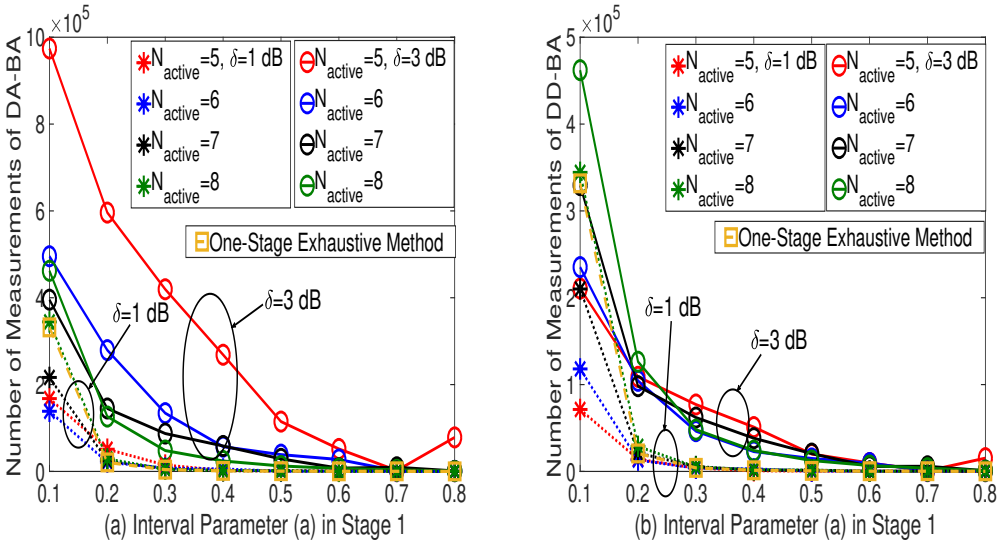

Figure 6.8: Number of Measurements M_{total} v.s. Interval parameter a in Stage 1.

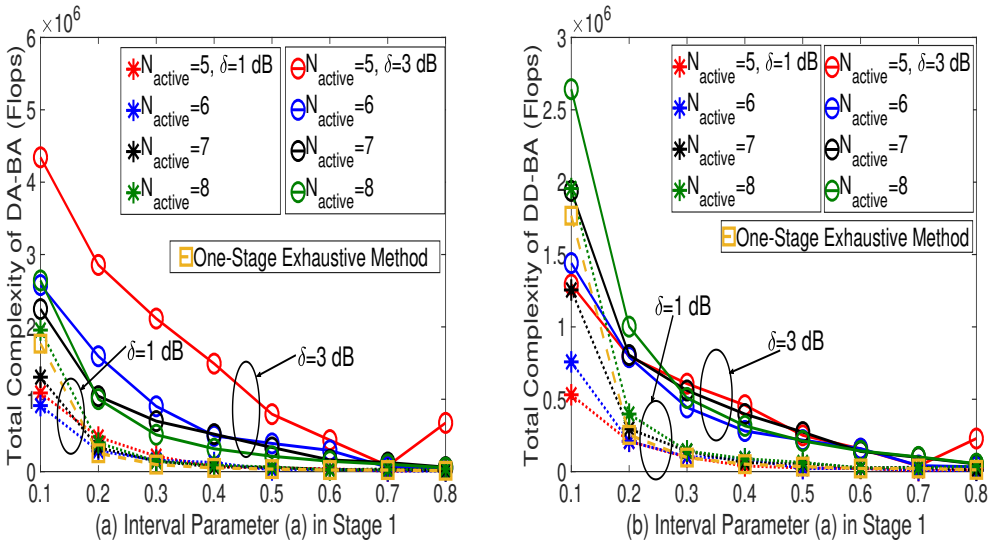

Figure 6.9: Total complexity C_{total} v.s. Interval parameter a in Stage 1.

mal AoD and AoA out of the narrowed scan range in Stage 2, as clarified in Fig. 6.5. We can observe that $\varkappa = 0.15$ (dB) and $\varkappa = 0.25$ (dB) in respective moderate and small interval parameter scenarios, i.e., $\delta = 3$ (dB) with $a < 0.6$, $\delta = 1$ (dB) with $a < 0.4$, can be selected for both proposed methods to achieve close-to-zero misalignment probability.

The number of measurements and total complexity of the DA-BA and DD-BA methods are examined in Fig. 6.8 and Fig. 6.9. It shows that the DD-BA method offers reduced measurements and complexity compared to the

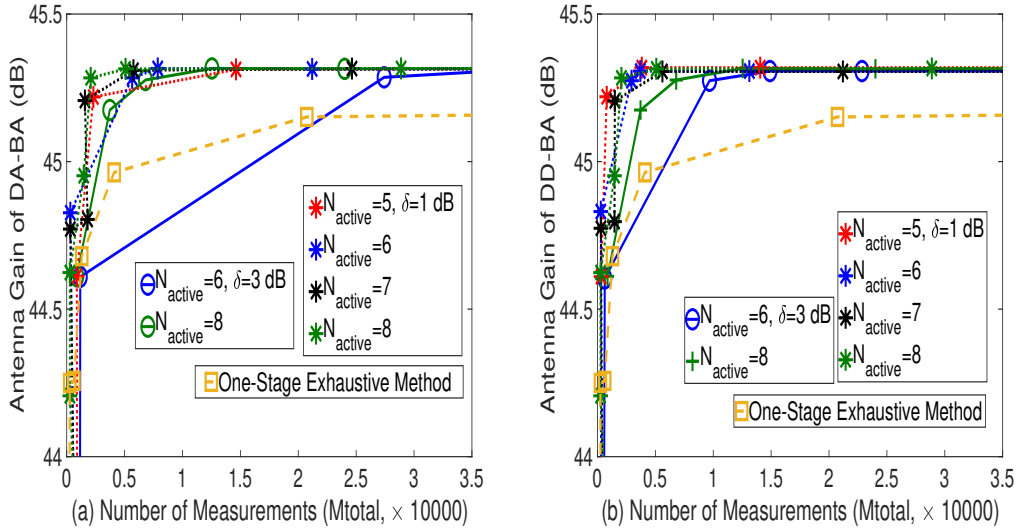

Figure 6.10: Antenna Gain G_{max} (dB) v.s. Number of measurements M_{total}

DA-BA method, especially when $a \leq 0.6$. This occurs because the deactivating approach in Stage 2 of the DD-BA method has a wider interval to decrease the number of measurements and complexity. It can be observed that, in Fig. 6.9, based on Section 6.4.2, the total complexity is entirely determined by the number of measurements and N_{active}, especially the number of measurements. Moreover, a smaller δ (dB) benefits the measurement and complexity reductions because it leads to a narrower scan range for Stage 2. Thus, by tuning key parameters of the beam scanning process, both DA-BA and DD-BA methods can offer measurement and complexity reductions while satisfying the antenna gain requirements.

Fig. 6.10 shows the direct performance-complexity trade-off in terms of the achievable antenna gain and the number of measurements of both DA-BA and DD-BA methods. It shows that a larger number of measurements can benefit the achievable antenna gain. Nevertheless, both methods can approach their respective achievable maximum antenna gains within a low-measurement/complexity regime, especially when $M_{total} < 1 \times 10^4$ and $M_{total} < 0.5 \times 10^4$ for the DA-BA and DD-BA methods with $\delta = 1$ (dB) respectively. It should be noted that power consumption is positively associated with computational complexity. Our proposed two-stage beam align-

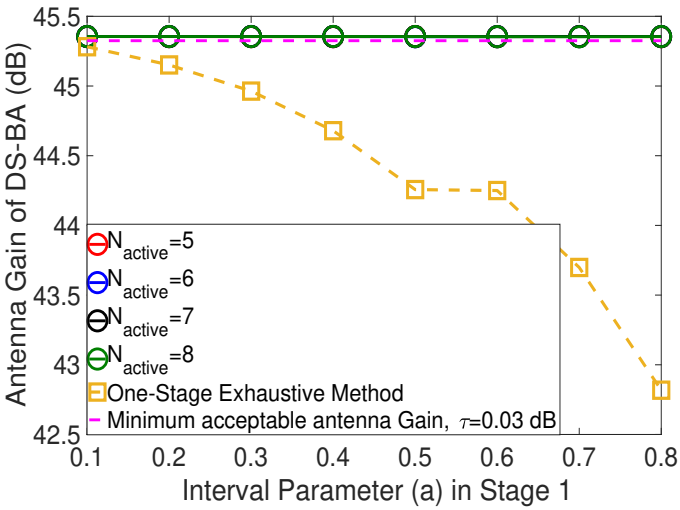

Figure 6.11: Antenna Gain G_{max} (dB) v.s. Interval parameter a in Stage 1 of the DS-BA method, $\varkappa = 0.03$ dB.

ment methods can offer significant antenna gain benefits and reductions in the number of measurements/complexity, extending their range of application to the energy efficiency enhancement and other complicated mmWave scenarios where the computational cost is cumbersome. Referring to the results, when the interval parameter is small or moderate, DA-BA experiences a smaller misalignment probability than DD-BA, while DD-BA achieves higher complexity/measurement reduction than DA-BA. Therefore, when the target is to maintain the achievable antenna gain stably, DA-BA will be applied. On the other hand, DD-BA can achieve better complexity reduction even energy efficiency enhancement.

6.5.2 DS-BA

Fig. 6.11 shows the relationship between the achievable antenna gain and the interval parameter a in Stage 1. It can be observed that the DS-BA method can outperform the one-stage exhaustive method and meet the antenna gain requirement regardless of the varying interval parameter. This is because the configuration of Step 5 in Stage 2 guarantees that the required gain loss $\varkappa = 0.03$ (dB) will be satisfied. According to these results, the DS-BA method could be considered as a close-to-optimal beam alignment method to cer-

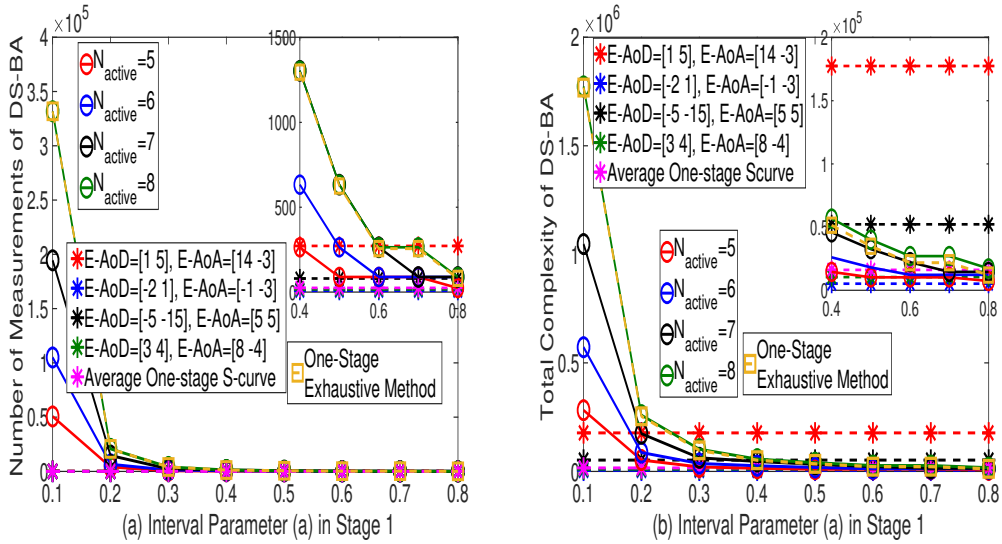

Figure 6.12: a) Number of Measurements M_{total} and b) Total complexity C_{total} of DS-BA method, AoD=[0 2] and AoA=[-4 1] for One-stage S-curve method.

tainly achieve the antenna gain requirement by exploiting the theoretical beam pattern. Moreover, it is crucial to study DS-BA's benefits on the measurement and complexity reductions, which can further evaluate the performance of the DS-BA method.

Fig. 6.12 illustrates the number of measurements and total complexity of the DS-BA method. First, "E-" in the legends indicates the randomly estimated directions. The results of the one-stage S-curve method (i.e. applying the S-curve approach without a preceding coarse beam scanning) with AoD=[0 2] and AoA=[-4 1] indicate that the linear interpolation to S-curve helps to closely match the optimal AoD and AoA. However, the S-curve interpolation will be repeated $L > 1$ times if smaller $\varkappa(dB)$ is required, or the estimated directions for the S-curve interpolation are outside the main lobe range, where the main lobe range consists of $\varphi \in [\theta_X - HPBW + \Delta, \theta_X + HPBW - \Delta]$ and $\mu \in [\phi_X - HPBW + \Delta, \phi_X + HPBW - \Delta]$, $X = Tx, Rx$. Therefore, the randomness of the estimated directions has an impact on the number of measurements and complexity. It can be observed that the DS-BA method can outperform both the one-stage S-curve method and the one-stage exhaustive method, especially when both N_{active} and a are small.

Moreover, compared with Fig. 6.8 and Fig. 6.9, when off-line S-curves are generated in advance, DS-BA can significantly reduce the complexity while achieving the antenna gain requirement. This is because the deactivating approach in the DS-BA method can guarantee the estimated directions are in the main lobe range and leads to $L = 1$, i.e., Stage 2 will be processed only once to achieve further measurement and complexity reductions. Therefore, $N_{active} = 5$ and $a = 0.8$ can be selected for the DS-BA method to attain the required antenna gain with the minimum number of measurements and complexity in our experimental scenarios. According to these results, the DS-BA method could be considered as a close-to-optimal beam alignment method to completely achieve the antenna gain requirement with the highest complexity/measurement reductions when the knowledge of beam pattern is known.

6.6 Conclusion

This chapter has studied the design of low-complexity two-stage beam alignment methods in LOS mmWave systems. The DA-BA and DD-BA methods achieve coarse steering in Stage 1 by deactivating antennas and relatively fine steering in Stage 2 to match the optimal AoD/AoA. The DS-BA alignment method obtain the estimated directions in Stage 1 by deactivating antennas and utilizes them to complete linear interpolation supported by off-line S-curves exploiting the beam pattern. Our performance evaluation has demonstrated that proposed two-stage beam alignment methods could attain the target of antenna gain satisfaction and measurement/complexity reduction with properly selected parameters. Channel models with non-LOS paths and other noises, including but not limited to wind or rain, will also be explored in the future.

Chapter 7

Conclusions and Future Work

This Thesis demonstrated that energy efficiency improvements are essential to the realistic implementation of future wireless communications systems. Simultaneously, an increase in the number of antennas appears necessary to meet the increasing spectral efficiency requirements of serving a large number of mobile devices simultaneously. Accordingly, this Thesis has proposed and studied several schemes to enhance the energy efficiency and reduce the computational complexity of massive MIMO communication systems with compact antenna arrays. A number of practical insights have been revealed.

7.1 Conclusions

In this Thesis, a general overview of energy-efficient multi-antenna systems is provided in Chapter 2. Conventional precoding schemes and channel models are described, followed by a fundamental description of cooperative communication and mmWave communication, a description of general strategies in relay-aided multiple antenna systems. The characteristics of antennas applied in multi-antenna systems are also presented. After identifying the above techniques and highlighting areas that need further investigation, the main contributions of this Thesis are presented in Chapter 3 - Chapter 6. More specifically:

- Both the increasing spatial correlation experienced by closely-spaced antenna arrays and the temporal correlation among channels of adja-

cent transmission frames determined by user mobility were leveraged in Chapter 3 by partial CSI acquisition for reducing the complexity of massive MIMO systems and enhancing their energy efficiency. Specifically, a simultaneous reduction of hardware and signal processing complexity was demonstrated by exploiting the spatial correlation and temporal correlation existing in physically-constrained massive MIMO systems. The reduced number of RF chains and transmission frames required by the proposed scheme facilitates the deployment of massive MIMO systems in communication channels with high spatial and temporal correlations. The central results within this chapter are:

C3.1 The proposed scheme is studied in the moderate SNR range SNR=15 dB with inter-antenna spacing $d = 0.3\lambda$ for the massive MIMO systems considered in this Thesis and without incorporating the effect of mutual coupling. These user mobilities are those where there is sufficient temporal correlation to employ the proposed strategy without a significant spectral efficiency performance degradation, but the energy efficiency can be enhanced. Intuitively, if the effect of mutual coupling is considered, these ranges should not be significantly modified with the generally pronounced impact for the small inter-antenna distance [179].

- The objective of Chapter 4 is to improve the performance of a relay-aided massive MIMO system in the scenario of the half-duplex decode-and-forward protocol with zero-forcing processing. Power scaling laws and max-min optimisation for efficient power distribution have been investigated. The proposed studies also consider the imperfect acquisition of CSI, and therefore a robust operation under realistic conditions has been ensured. The following specific remarks can be derived from the results of this chapter:

C4.1 With a general multi-pair massive MIMO two-way relay-aided

system employing the DF protocol, a new large-scale approximation of the SE with ZF processing and imperfect CSI when the number of relay antennas approaches infinity has been presented. A practical power consumption model is also studied to analyze the EE performance of the proposed system.

C4.2 The chapter investigates three power scaling laws to illustrate the trade-off between the transmit powers of each user, each pilot symbol and the relay; in this case, the same SE, even the same EE, can be achieved with different configurations of the power-scaling parameters. Generally, when the scaling parameters of transmit powers of the user, relay and pilot symbol satisfying $0 < \alpha, \beta, \gamma < 1$ and properly selected, the EE performance can outperform the performance without power scaling law. This provides excellent flexibility in the practical design of the system and forms a roadmap to select optimal parameters to maximize the EE performance in specific scenarios.

C4.3 An optimisation problem is formulated to maximize the minimum achievable SE among all user pairs with imperfect CSI to improve the sum SE and achieve fairness across all user pairs. It shows that when the transmit powers of the user, relay and pilot symbol are all independent to complete the optimisation, the better performance of minimum achievable SE could be achieved. The analysis of the complexity of the proposed optimisation problem has also been studied and shows that improved optimisation performance has a higher cost of time.

- The considerations and results described in Chapter 3 and Chapter 4 have motivated the studies in Chapter 5. Here, the incomplete and imperfect CSI acquisition is performed to achieve complexity reduction and CSI relaxation. The consideration of space-constrained BSs and the path loss model leads to the exploitation of the spatial correlation. At

the same time, technical specifications such as channel aging have been analyzed. The main contributions of the chapter can be highlighted in the following list:

C5.1 A multi-pair two-way DF relaying massive MIMO system is deployed in a physically constrained space. This gives rise to an interesting trade-off between system performance and spatial correlation when the number of antennas grows large. The large-scale approximations of the sum SE with MRT and ZF processing are presented with a large but finite number of antennas since a large but finite number of antennas attracts attention due to its practicability. However, the orthogonal characteristics obtained by an infinite number of antennas can still be used in theoretical studies.

C5.2 It is essential to investigate a practical and standard power consumption model to evaluate the system energy efficiency characteristics. Different processing schemes are considered, where the performance of ZF processing can outperform that of MRT processing due to the potential of better interference cancellation. In addition, the study is evaluated by revealing the gains of incomplete CSI acquisition. The low-complexity incomplete CSI acquisition scheme that exploits the spatial correlation in space-constrained massive MIMO is studied. Obviously, the incomplete CSI benefits the computational complexity reduction. The number of active antennas $N_c = 0.5 \cdot M$ could be the benchmark number of active antennas to maximize the EE while maintaining the required sum SE in moderate and high spatial correlation scenarios.

C5.3 In general, the channel aging problem might reduce the accuracy with a more significant channel aging parameter ρ causing outdated channel estimation. The effect of channel aging is studied with MRT processing. At the same time, it can be observed that when channel aging exists, a higher spatial correlation between

adjacent antennas might also worsen the system performance. Moreover, the number of transmit steering vectors in the steering matrix plays a positive role in the performance since more paths can help to strengthen the received level. Different degrees of spatial correlation are adjusted by varying the angle spread.

- The development of two-stage beam alignment methods exploiting antenna gains in mmWave communication systems is illustrated in Chapter 6. Analytical and numerical results show that the proposed methods avail measurements and complexity reductions compared to the existing exhaustive scheme while maintaining the essential antenna gain requirement.

  C6.1 Two-stage alignment methods are studied to manage beam alignment by evaluating the achievable antenna gain and the total number of measurements/complexity in the communication links. The methods apply the deactivating approach with only $N_{active} \times N_{active}$ active antennas to achieve wider beams for beam scanning in the $N \times N$ antenna array in the first stage and the second stage applies either deactivating or exhaustive approaches. Compared with conventional exhaustive methods, the proposed two-stage alignment methods greatly benefit measurements/complexity reduction and satisfy the required antenna gain. The trade-off between performance and complexity forms a guideline to select optimal key parameters of two-stage alignment methods to improve the performance in practical cases.

  C6.2 Another two-stage beam alignment method exploiting the knowledge of beam patterns is also evaluated, where the gain difference between adjacent beams can be obtained off-line and this theoretical function is denoted as the *S-curve*. This method can further reduce the measurements/complexity and attain close-to-optimal

antenna gains, while extending their range of application to other complicated mmWave scenarios.

7.2 Future Work

The studies in this Thesis have presented the foundation for future works and motivated further investigations that aim at increasing the energy efficiency of multiple-antenna systems, especially in the area of future massive MIMO systems. In particular, the following research lines of work are of interest for future work:

- **Partial CSI acquisition under different channel and propagation models:** The scheme introduced in Chapter 3 was applied to exploit the spatial correlation resulting from insufficient inter-antenna distance and the temporal correlation of the channels between adjacent transmission frames. The partial CSI acquisition could be extended to generic scenarios by considering the specific structure of the channel statistics and the practical vehicle velocity playing a fundamental role in the channel estimation quality. The study of the implications of the partial CSI in FDD massive MIMO systems for improving energy efficiency is worthwhile. The employment of alternative channel models and the potential effect of vehicle velocity on channel models also have their research value. In addition, more intricate and efficient strategies to determine the antennas with CSI and how to interpolate the information will be one of the subjects of our future work.

- **Relay-aided Massive MIMO in D2D communications:** The power scaling laws and max-min fairness analysis developed in Chapter 4 aim at enhancing the energy efficiency performance of the proposed system. The key parameters govern the performance, and this provides excellent flexibility in practical system design. Moreover, the incomplete CSI acquisition supporting by the shareable similarity between channels due to high spatial correlation could facilitate attain-

ing complexity reduction and potential EE improvement in Chapter 5. Based on current works, relay-aided systems can be applied in device-to-device (D2D) communications in Internet of Things (IoT) environments supporting multiple pairs of resource-limited and long-distance spaced devices to achieve performance improvements while allowing longer distance communication [151]. Compared with a conventional relay-aided system, the direct link between user pairs plays an important role. Meanwhile, the system can also be considered as a wireless-powered communication network where the relay transfers power to all devices. Therefore, the subsequent work could illustrate the performance of this proposed D2D system and relevant power transfer scheme based on incorporating prior knowledge to indicate energy-efficient strategies or power scaling methods in achieving power consumption reduction and EE improvement jointly.

- **Beam Alignment Extension in mmWave communication systems:** Two-stage beam alignment methods exploiting deactivating approach and beam pattern in Chapter 6 are studied to manage beam alignment by evaluating the achievable antenna gain in the communication links. Compared to the conventional exhaustive method, the proposed two-stage alignment methods can significantly improve the measurement/complexity reductions and attain the maximum gain loss requirement. The results motivate further research aimed at developing more energy-efficient and effective alignment methods for beam management. In addition, a detailed study of alternative channel patterns with non-LOS propagation paths and noise caused by wind or obstacles will be valuable. Similarly, to achieve energy-efficient beam alignment, a method designed to minimize power consumption while maintaining the required gains seems potential to investigate relevant contributions.

To finally summarise, this Thesis has presented several energy efficient

schemes, each designed for a specific multiple antenna system structure. It is hoped that the results and observations from this Thesis may serve to improve the realistic implementation and enhance the system energy efficiency in multiple antenna systems for the future 5G and beyond wireless communications.

Appendices

Appendix A: Proof of Lemma 1–Asymptotic Channel Orthogonality

In this appendix, we provide the calculations of **Lemma 1**. With the assumption that all estimated channels with $\hat{\mathbf{h}}_{XR,i} \sim \mathbb{CN}\left(\mathbf{0}, \tilde{\sigma}^2_{XR,i}\mathbf{I}_{N_R}\right)$ and $\hat{\mathbf{h}}_{XR,j} \sim \mathbb{CN}\left(\mathbf{0}, \tilde{\sigma}^2_{XR,j}\mathbf{I}_{N_R}\right)$ are mutually independent when $i \neq j$, $i, j = 1, ..., K$. When $N_R \to \infty$, we can have

If $i = j$,

$$\frac{1}{N_R}\hat{\mathbf{h}}^H_{XR,i}\hat{\mathbf{h}}_{XR,i} = \frac{1}{N_R}\left|\hat{\mathbf{h}}_{XR,i}\right|^2 = \frac{1}{N_R} \cdot N_R\tilde{\sigma}^2_{XR,i} = \tilde{\sigma}^2_{XR,i}, \tag{A.1}$$

If $i \neq j$,

$$\frac{1}{N_R}\hat{\mathbf{h}}^H_{XR,i}\hat{\mathbf{h}}_{XR,j} = 0. \tag{A.2}$$

With the computation of (A.1)-(A.2), we can obtain **Lemma 1** in (4.21).

Appendix B: Derivation for SE approximations in uncorrelated relaying system

In this appendix, we present the detailed derivation for $\hat{R}_{1,i}$ and $\hat{R}_{RX,i}$, while $\hat{R}_{XR,i}$ can be obtained in a straightforward way. At first, some useful results widely used in the calculation are given in **Lemma 2**.

Lemma 2: Assume that $\mathbf{h}_i \sim \mathbb{CN}\left(\mathbf{0}, \sigma_i^2\mathbf{I}_{N_R}\right)$ and $\mathbf{h}_j \sim \mathbb{CN}\left(\mathbf{0}, \sigma_j^2\mathbf{I}_{N_R}\right)$ are

mutually independent when $i \neq j$, $i, j = 1, ..., K$. Therefore, we have

$$\frac{\left|\mathbf{h}_i^H \mathbf{h}_j\right|^2}{N_R^2} \rightarrow \begin{cases} \sigma_i^4, & i = j \\ \frac{1}{N_R}\sigma_i^2\sigma_j^2, & i \neq j \end{cases}, \tag{B.1}$$

With the assistance of (4.22)-(4.25), **Lemma 1** and **Lemma 2**, we derive the calculation of the corresponding approximations in the following. First, we focus on $\hat{R}_{1,i}$, $\hat{R}_{XR,i}$, $X = A, B$ in the MAC phase, consisting of four terms defined above. When $N_R \rightarrow \infty$, we can have

1) Desired signal power of $T_{X,i}$, $X = A, B$,

$$\begin{aligned} & p_{X,i}\left(\left|\mathbf{F}_{MAC,i}^{AR}\hat{\mathbf{h}}_{XR,i}\right|^2 + \left|\mathbf{F}_{MAC,i}^{BR}\hat{\mathbf{h}}_{XR,i}\right|^2\right) \\ & \rightarrow \begin{cases} p_{A,i}\left|\mathbf{F}_{MAC,i}^{AR}\hat{\mathbf{h}}_{AR,i}\right|^2 \\ p_{B,i}\left|\mathbf{F}_{MAC,i}^{BR}\hat{\mathbf{h}}_{BR,i}\right|^2 \end{cases} \rightarrow \begin{cases} p_{A,i}\left|\frac{1}{N_R\sigma_{AR,i}^2}\hat{\mathbf{h}}_{AR,i}^H\hat{\mathbf{h}}_{AR,i}\right|^2 \\ p_{B,i}\left|\frac{1}{N_R\sigma_{BR,i}^2}\hat{\mathbf{h}}_{BR,i}^H\hat{\mathbf{h}}_{BR,i}\right|^2 \end{cases} \rightarrow \begin{cases} p_{A,i}, & X = A \\ p_{B,i}, & X = B \end{cases}, \end{aligned} \tag{B.2}$$

2) Estimation Error A_i,

$$\begin{aligned} A_i & \rightarrow \sum_{X=A,B} p_{X,i}\left(\left|\frac{1}{N_R\sigma_{AR,i}^2}\hat{\mathbf{h}}_{AR,i}^H\Delta\mathbf{h}_{XR,i}\right|^2 + \left|\frac{1}{N_R\sigma_{BR,i}^2}\hat{\mathbf{h}}_{BR,i}^H\Delta\mathbf{h}_{XR,i}\right|^2\right) \\ & \rightarrow \frac{\left(p_{A,i}\tilde{\sigma}_{AR,i}^2 + p_{B,i}\tilde{\sigma}_{BR,i}^2\right)}{N_R}\left(\frac{1}{\sigma_{AR,i}^2} + \frac{1}{\sigma_{BR,i}^2}\right), \end{aligned} \tag{B.3}$$

3) Inter-user Interference B_i,

$$\begin{aligned} B_i & = \sum_{X=A,B}\sum_{j\neq i} p_{X,j}\left(\left|\mathbf{F}_{MAC,i}^{AR}\left(\hat{\mathbf{h}}_{XR,j} + \Delta\mathbf{h}_{XR,j}\right)\right|^2 + \left|\mathbf{F}_{MAC,i}^{BR}\left(\hat{\mathbf{h}}_{XR,j} + \Delta\mathbf{h}_{XR,j}\right)\right|^2\right) \\ & \rightarrow \sum_{X=A,B}\sum_{j\neq i} p_{X,j}\left(\left|\mathbf{F}_{MAC,i}^{AR}\Delta\mathbf{h}_{XR,j}\right|^2 + \left|\mathbf{F}_{MAC,i}^{BR}\Delta\mathbf{h}_{XR,j}\right|^2\right) \\ & \rightarrow \sum_{X=A,B}\sum_{j\neq i} p_{X,j}\left(\left|\frac{1}{N_R\sigma_{AR,i}^2}\hat{\mathbf{h}}_{AR,i}^H\Delta\mathbf{h}_{XR,j}\right|^2 + \left|\frac{1}{N_R\sigma_{BR,i}^2}\hat{\mathbf{h}}_{BR,i}^H\Delta\mathbf{h}_{XR,j}\right|^2\right) \\ & \rightarrow \frac{1}{N_R}\left(\frac{1}{\sigma_{AR,i}^2} + \frac{1}{\sigma_{BR,i}^2}\right)\sum_{j\neq i}\left(p_{A,j}\tilde{\sigma}_{AR,j} + p_{B,j}\tilde{\sigma}_{BR,j}\right), \end{aligned} \tag{B.4}$$

4) Noise C_i,

$$C_i \to \left|\left|\frac{1}{N_R\sigma_{AR,i}^2}\hat{\mathbf{h}}_{AR,i}^H\right|\right|^2 + \left|\left|\frac{1}{N_R\sigma_{BR,i}^2}\hat{\mathbf{h}}_{BR,i}^H\right|\right|^2 \to \frac{1}{N_R}\left(\frac{1}{\sigma_{AR,i}^2} + \frac{1}{\sigma_{BR,i}^2}\right). \tag{B.5}$$

Substituting (B.2)-(B.5) into (4.13)-(4.15), we can obtain $\hat{R}_{1,i}$, $\hat{R}_{XR,i}$, $X = A, B$ in (4.28), (4.30). Then, we focus on $\hat{R}_{RX,i}$, $X = A, B$, in the BC phase. Similarly, the corresponding terms in $\hat{R}_{RX,i}$ can be computed as following when $N_R \to \infty$,

1) Normalization coefficient,

$$\begin{aligned}\rho_{DF} &= \sqrt{\frac{p_r}{E\left\{\left|\left|\mathbf{F}_{BC}\right|\right|^2\right\}}} = \sqrt{\frac{p_r}{E\left\{\sum_{i=1}^{N_R}\sum_{j=1}^{2K}\left|\mathbf{F}_{BC}(i,j)\right|^2\right\}}} \\ &\to \sqrt{\frac{p_r}{\sum_{i=1}^{K}\left(\frac{1}{N_R\sigma_{AR,i}^2} + \frac{1}{N_R\sigma_{BR,i}^2}\right)}}.\end{aligned} \tag{B.6}$$

2) Desired signal,

$$\left|\hat{\mathbf{h}}_{XR,i}^T\mathbf{F}_{BC,i}^{RX}\right|^2 \to \left|\hat{\mathbf{h}}_{XR,i}^T\frac{1}{N_R\sigma_{XR,i}^2}\hat{\mathbf{h}}_{XR,i}^*\right|^2 \to 1, \tag{B.7}$$

3) Estimation error,

$$\left|\Delta\mathbf{h}_{XR,i}^T\mathbf{F}_{BC,i}^{RX}\right|^2 \to \left|\Delta\mathbf{h}_{XR,i}^T\frac{1}{N_R\sigma_{XR,i}^2}\hat{\mathbf{h}}_{XR,i}^*\right|^2 \to \frac{\tilde{\sigma}_{XR,i}^2}{N_R\sigma_{XR,i}^2}, \tag{B.8}$$

4) Inter-user interference,

$$\begin{aligned}
&\sum_{j=1}^{K}\left(\left|\mathbf{h}_{XR,i}^{T}\mathbf{F}_{BC,j}^{RA}\right|^{2}+\left|\mathbf{h}_{XR,i}^{T}\mathbf{F}_{BC,j}^{RB}\right|^{2}\right)-\left|\mathbf{h}_{XR,i}^{T}\mathbf{F}_{BC,i}^{RX}\right|^{2}\\
&=\sum_{j=1}^{K}\left(\left|\left(\hat{\mathbf{h}}_{XR,i}^{T}+\Delta\mathbf{h}_{XR,i}^{T}\right)\mathbf{F}_{BC,j}^{RA}\right|^{2}+\left|\left(\hat{\mathbf{h}}_{XR,i}^{T}+\Delta\mathbf{h}_{XR,i}^{T}\right)\mathbf{F}_{BC,j}^{RB}\right|^{2}\right)-\left|\left(\hat{\mathbf{h}}_{XR,i}^{T}+\Delta\mathbf{h}_{XR,i}^{T}\right)\mathbf{F}_{BC,i}^{RX}\right|^{2}\\
&\rightarrow\begin{cases}\sum\limits_{j=1}^{K}\left|\Delta\mathbf{h}_{AR,i}^{T}\mathbf{F}_{BC,j}^{RB}\right|^{2}+\sum\limits_{j\neq i}\left|\Delta\mathbf{h}_{AR,i}^{T}\mathbf{F}_{BC,j}^{RA}\right|^{2}\\ \sum\limits_{j=1}^{K}\left|\Delta\mathbf{h}_{BR,i}^{T}\mathbf{F}_{BC,j}^{RA}\right|^{2}+\sum\limits_{j\neq i}\left|\Delta\mathbf{h}_{BR,i}^{T}\mathbf{F}_{BC,j}^{RB}\right|^{2}\end{cases}\rightarrow\begin{cases}\sum\limits_{j=1}^{K}\left|\Delta\mathbf{h}_{AR,i}^{T}\frac{\hat{\mathbf{h}}_{BR,j}^{*}}{N_R\sigma_{BR,j}^{2}}\right|^{2}+\sum\limits_{j\neq i}\left|\Delta\mathbf{h}_{AR,i}^{T}\frac{\hat{\mathbf{h}}_{AR,j}^{*}}{N_R\sigma_{AR,j}^{2}}\right|^{2}\\ \sum\limits_{j=1}^{K}\left|\Delta\mathbf{h}_{BR,i}^{T}\frac{\hat{\mathbf{h}}_{AR,j}^{*}}{N_R\sigma_{AR,j}^{2}}\right|^{2}+\sum\limits_{j\neq i}\left|\Delta\mathbf{h}_{BR,i}^{T}\frac{\hat{\mathbf{h}}_{BR,j}^{*}}{N_R\sigma_{BR,j}^{2}}\right|^{2}\end{cases}\\
&\rightarrow\begin{cases}\sum\limits_{j=1}^{K}\frac{\tilde{\sigma}_{AR,i}^{2}}{N_R\sigma_{BR,j}^{2}}+\sum\limits_{j\neq i}\frac{\tilde{\sigma}_{AR,i}^{2}}{N_R\sigma_{AR,j}^{2}}, & X=A\\ \sum\limits_{j=1}^{K}\frac{\tilde{\sigma}_{BR,i}^{2}}{N_R\sigma_{AR,j}^{2}}+\sum\limits_{j\neq i}\frac{\tilde{\sigma}_{BR,i}^{2}}{N_R\sigma_{BR,j}^{2}}, & X=B\end{cases}.
\end{aligned}\tag{B.9}$$

By applying (B.6)-(B.9) to (4.17)-(4.18), we can obtain $\hat{R}_{RX,i}$, $X=A,B$, in (4.31). With other additional computations, we complete the proof of the SE approximations shown in **Corollary 1**.

Appendix C: Derivation of SE approximations in correlated relaying system

In this appendix, we present the respective detailed derivation of all SE terms for two linear processing methods. With the assumption that $\Theta=\mathbf{A}\mathbf{A}^{H}$ and $\bar{\Theta}=\mathbf{A}^{H}\mathbf{A}$, we can have the following derivations.

7.2.1 MRT Processing

With the assistance of (5.57)-(5.58), the calculation of the relevant approximations is derived as follows. First, in MAC phase, the four terms in $\hat{R}_{1,i}$ and $\hat{R}_{XR,i}$ $(X=A,B)$ are given by

1) Desired signal power of $T_{X,i}$, $X = A, B$,

$$p_{X,i}\left(\left|\mathbf{F}_{MAC,i}^{AR}\hat{\mathbf{h}}_{XR,i}\right|^2 + \left|\mathbf{F}_{MAC,i}^{BR}\hat{\mathbf{h}}_{XR,i}\right|^2\right) = p_{X,i}\left(\left|\hat{\mathbf{g}}_{AR,i}^H\Theta\hat{\mathbf{g}}_{XR,i}\right|^2 + \left|\hat{\mathbf{g}}_{BR,i}^H\Theta\hat{\mathbf{g}}_{XR,i}\right|^2\right)$$
$$\rightarrow p_{X,i}\left(\sigma_{XR,i}^4 \cdot \left(\sum_{a=1}^{L}\sum_{\substack{b=1\\b\neq a}}^{L}|\Theta(a,b)|^2 + \sum_{a=1}^{L}\sum_{b=1}^{L}\Theta(a,a)\Theta(b,b)\right)\right)$$
$$+ p_{X,i}\left(\sigma_{AR,i}^2\sigma_{BR,i}^2\sum_{a=1}^{L}\sum_{b=1}^{L}|\Theta(a,b)|^2\right), \tag{C.1}$$

2) Estimation Error A_i,

$$\begin{aligned}A_i &= \textstyle\sum_{X=A,B} p_{X,i}\left(\left|\mathbf{F}_{MAC,i}^{AR}\Delta\mathbf{h}_{XR,i}\right|^2 + \left|\mathbf{F}_{MAC,i}^{BR}\Delta\mathbf{h}_{XR,i}\right|^2\right)\\ &= \textstyle\sum_{X=A,B} p_{X,i}\left(\left|\hat{\mathbf{g}}_{AR,i}^H\Theta\mathbf{q}_{XR,i}\right|^2 + \left|\hat{\mathbf{g}}_{BR,i}^H\Theta\mathbf{q}_{XR,i}\right|^2\right)\\ &\rightarrow \textstyle\sum_{X=A,B} p_{X,i}\left[\left(\sigma_{AR,i}^2\tilde{\sigma}_{XR,i}^2 + \sigma_{BR,i}^2\tilde{\sigma}_{XR,i}^2\right)\sum_{a=1}^{L}\sum_{b=1}^{L}|\Theta(a,b)|^2\right],\end{aligned} \tag{C.2}$$

3) Inter-user Interference B_i,

$$\begin{aligned}B_i &= \sum_{X=A,B}\sum_{j\neq i} p_{X,j}\left(\left|\mathbf{F}_{MAC,i}^{AR}\mathbf{h}_{XR,j}\right|^2 + \left|\mathbf{F}_{MAC,i}^{BR}\mathbf{h}_{XR,j}\right|^2\right)\\ &= \sum_{X=A,B}\sum_{j\neq i} p_{X,j}\left(\left|\mathbf{F}_{MAC,i}^{AR}\left(\hat{\mathbf{h}}_{XR,j} + \Delta\mathbf{h}_{XR,j}\right)\right|^2 + \left|\mathbf{F}_{MAC,i}^{BR}\left(\hat{\mathbf{h}}_{XR,j} + \Delta\mathbf{h}_{XR,j}\right)\right|^2\right)\\ &\rightarrow \sum_{X=A,B}\sum_{j\neq i} p_{X,j}\left(\left(\sigma_{AR,i}^2\sigma_{XR,j}^2 + \sigma_{AR,i}^2\tilde{\sigma}_{XR,j}^2\right)\textstyle\sum_{a=1}^{L}\sum_{b=1}^{L}|\Theta(a,b)|^2\right)\\ &+ \sum_{X=A,B}\sum_{j\neq i} p_{X,j}\left(\left(\sigma_{BR,i}^2\sigma_{XR,j}^2 + \sigma_{BR,i}^2\tilde{\sigma}_{XR,j}^2\right)\textstyle\sum_{a=1}^{L}\sum_{b=1}^{L}|\Theta(a,b)|^2\right),\end{aligned} \tag{C.3}$$

4) Noise C_i,

$$\begin{aligned}C_i &= \left|\left|\mathbf{F}_{MAC,i}^{AR}\right|\right|^2 + \left|\left|\mathbf{F}_{MAC,i}^{BR}\right|\right|^2 = \left|\left|\hat{\mathbf{g}}_{AR,i}^H\mathbf{A}\right|\right|^2 + \left|\left|\hat{\mathbf{g}}_{BR,i}^H\mathbf{A}\right|\right|^2\\ &\rightarrow \left(\sigma_{AR,i}^2 + \sigma_{BR,i}^2\right)\cdot\textstyle\sum_{a=1}^{L}\Theta(a,a).\end{aligned} \tag{C.4}$$

Substituting (C.1)-(C.4) into (5.35)-(5.37), we can obtain $\hat{R}_{1,i}$, $\hat{R}_{XR,i}$ (where $X = A, B$) in (5.60), (5.61), (5.63) and (5.64). Then, we focus on $\hat{R}_{RX,i}$ in the

BC phase. Similarly, the relevant terms in $\hat{R}_{RX,i}$, $X = A, B$ can be computed as following when N_R increases to large number,

1) Normalization coefficient,

$$\rho_{DF}^{MRT} = \sqrt{\frac{p_r}{E\left\{\left|\left|\mathbf{F}_{BC}\right|\right|_F^2\right\}}} = \sqrt{\frac{p_r}{E\left\{\sum_{i=1}^{N_R}\sum_{j=1}^{2K}\left|\mathbf{F}_{BC}(i,j)\right|^2\right\}}}$$
$$\rightarrow \sqrt{\frac{p_r}{\sum_{i=1}^{N_R}\sum_{j=1}^{K}(\sigma_{AR,j}^2+\sigma_{BR,j}^2)\bar{\Theta}(i,i)}}. \tag{C.5}$$

2) Desired signal,

$$\left|\hat{\mathbf{h}}_{XR,i}^T\mathbf{F}_{BC,i}^{RX}\right|^2 = \left|\hat{\mathbf{h}}_{XR,i}^T\hat{\mathbf{h}}_{XR,i}^*\right|^2$$
$$\rightarrow \sigma_{XR,i}^4\left(\sum_{a=1}^{L}\sum_{\substack{b=1\\b\neq a}}^{L}|\Theta(a,b)|^2+\sum_{a=1}^{L}\sum_{b=1}^{L}\Theta^*(a,a)\Theta^*(b,b)\right), \tag{C.6}$$

3) Estimation error,

$$\left|\Delta\mathbf{h}_{XR,i}^T\mathbf{F}_{BC,i}^{RX}\right|^2 = \left|\Delta\mathbf{h}_{XR,i}^T\hat{\mathbf{h}}_{XR,i}^*\right|^2 \rightarrow \sigma_{XR,i}^2\tilde{\sigma}_{XR,i}^2\sum_{a=1}^{L}\sum_{b=1}^{L}|\Theta(a,b)|^2, \tag{C.7}$$

4) Inter-user interference,

$$\sum_{j=1}^{K}\left(\left|\mathbf{h}_{XR,i}^T\mathbf{F}_{BC,j}^{RA}\right|^2+\left|\mathbf{h}_{XR,i}^T\mathbf{F}_{BC,j}^{RB}\right|^2\right)-\left|\mathbf{h}_{XR,i}^T\mathbf{F}_{BC,i}^{RX}\right|^2$$
$$=\sum_{j=1}^{K}\left(\left|\left(\hat{\mathbf{h}}_{XR,i}^T+\Delta\mathbf{h}_{XR,i}^T\right)\hat{\mathbf{h}}_{AR,j}^*\right|^2+\left|\left(\hat{\mathbf{h}}_{XR,i}^T+\Delta\mathbf{h}_{XR,i}^T\right)\hat{\mathbf{h}}_{BR,j}^*\right|^2\right)-\left|\left(\hat{\mathbf{h}}_{XR,i}^T+\Delta\mathbf{h}_{XR,i}^T\right)\hat{\mathbf{h}}_{XR,i}^*\right|^2$$
$$\rightarrow\begin{cases}\sum\limits_{j=1}^{K}\left|\left(\hat{\mathbf{h}}_{AR,i}^T+\Delta\mathbf{h}_{AR,i}^T\right)\hat{\mathbf{h}}_{BR,j}^*\right|^2+\sum\limits_{j\neq i}\left|\left(\hat{\mathbf{h}}_{AR,i}^T+\Delta\mathbf{h}_{AR,i}^T\right)\hat{\mathbf{h}}_{AR,j}^*\right|^2, & X=A\\ \sum\limits_{j=1}^{K}\left|\left(\hat{\mathbf{h}}_{BR,i}^T+\Delta\mathbf{h}_{BR,i}^T\right)\hat{\mathbf{h}}_{AR,j}^*\right|^2+\sum\limits_{j\neq i}\left|\left(\hat{\mathbf{h}}_{BR,i}^T+\Delta\mathbf{h}_{BR,i}^T\right)\hat{\mathbf{h}}_{BR,j}^*\right|^2, & X=B\end{cases}$$
$$\rightarrow\begin{cases}\left\{\sum\limits_{j=1}^{K}\beta_{AR,i}\sigma_{BR,j}^2+\sum\limits_{j\neq i}\beta_{AR,i}\sigma_{AR,j}^2\right\}\cdot\sum\limits_{a=1}^{L}\sum\limits_{b=1}^{L}|\Theta(a,b)|^2, & X=A\\ \left\{\sum\limits_{j=1}^{K}\beta_{BR,i}\sigma_{AR,j}^2+\sum\limits_{j\neq i}\beta_{BR,i}\sigma_{BR,j}^2\right\}\cdot\sum\limits_{a=1}^{L}\sum\limits_{b=1}^{L}|\Theta(a,b)|^2, & X=B\end{cases}. \tag{C.8}$$

By applying (C.5)-(C.8) to (5.39)-(5.40), $\hat{R}_{RX,i}$ $(X = A, B)$ in (5.62) and (5.65) is obtained and the proof completes.

7.2.2 ZF Processing

First, we derive the matrix inversion in ZF processing. With the assistance of (5.84)-(5.85), the matrix derivation can be described as

$$\begin{aligned}
\left(\hat{\mathbf{H}}_{XR}^{H}\hat{\mathbf{H}}_{XR}\right)^{-1} &\rightarrow \begin{bmatrix} \hat{\mathbf{g}}_{XR,1}^{H}\Theta\hat{\mathbf{g}}_{XR,1} & \cdots & \hat{\mathbf{g}}_{XR,1}^{H}\Theta\hat{\mathbf{g}}_{XR,K} \\ \vdots & \ddots & \vdots \\ \hat{\mathbf{g}}_{XR,K}^{H}\Theta\hat{\mathbf{g}}_{XR,1} & \cdots & \hat{\mathbf{g}}_{XR,K}^{H}\Theta\hat{\mathbf{g}}_{XR,K} \end{bmatrix}^{-1} \\
&\rightarrow \begin{bmatrix} \hat{\mathbf{g}}_{XR,1}^{H}\Theta\hat{\mathbf{g}}_{XR,1} & \cdots & 0 \\ \vdots & \ddots & \vdots \\ 0 & \cdots & \hat{\mathbf{g}}_{XR,K}^{H}\Theta\hat{\mathbf{g}}_{XR,K} \end{bmatrix}^{-1} \\
&\rightarrow \begin{bmatrix} \frac{1}{\sigma_{XR,1}^{2}\sum_{a=1}^{L}\Theta(a,a)} & \cdots & 0 \\ \vdots & \ddots & \vdots \\ 0 & \cdots & \frac{1}{\sigma_{XR,K}^{2}\sum_{a=1}^{L}\Theta(a,a)} \end{bmatrix}.
\end{aligned} \tag{C.9}$$

Moreover, according to (5.86)-(5.87) and (C.9), we can derive the calculation of the relevant SE approximations. First, $\hat{R}_{1,i}$, $\hat{R}_{XR,i}$, $X = A,B$ are derived. When N_R grows to large number, we can obtain the approximations,

1) Desired signal power of $T_{X,i}$, $X = A,B$,

$$\begin{aligned}
&p_{X,i}\left(\left|\mathbf{F}_{MAC,i}^{AR}\hat{\mathbf{h}}_{XR,i}\right|^{2} + \left|\mathbf{F}_{MAC,i}^{BR}\hat{\mathbf{h}}_{XR,i}\right|^{2}\right) \\
&\rightarrow p_{X,i}\left(\left|\frac{\hat{\mathbf{g}}_{AR,i}^{H}\Theta\hat{\mathbf{g}}_{XR,i}}{\sigma_{AR,i}^{2}\sum_{a=1}^{L}\Theta(a,a)}\right|^{2} + \left|\frac{\hat{\mathbf{g}}_{BR,i}^{H}\Theta\hat{\mathbf{g}}_{XR,i}}{\sigma_{BR,i}^{2}\sum_{a=1}^{L}\Theta(a,a)}\right|^{2}\right) \rightarrow p_{X,i},
\end{aligned} \tag{C.10}$$

2) Estimation Error A_i

$$\begin{aligned}
A_i &= \sum_{X=A,B} p_{X,i}\left(\left|\mathbf{F}_{MAC,i}^{AR}\Delta\mathbf{h}_{XR,i}\right|^{2} + \left|\mathbf{F}_{MAC,i}^{BR}\Delta\mathbf{h}_{XR,i}\right|^{2}\right) \\
&\rightarrow \sum_{X=A,B} p_{X,i}\left(\left|\frac{\hat{\mathbf{g}}_{AR,i}^{H}\Theta\mathbf{q}_{XR,i}}{\sigma_{AR,i}^{2}\sum_{a=1}^{L}\Theta(a,a)}\right|^{2} + \left|\frac{\hat{\mathbf{g}}_{BR,i}^{H}\Theta\mathbf{q}_{XR,i}}{\sigma_{BR,i}^{2}\sum_{a=1}^{L}\Theta(a,a)}\right|^{2}\right) \\
&\rightarrow \sum_{X=A,B} p_{X,i}\left[\left(\frac{\tilde{\sigma}_{XR,i}^{2}}{\sigma_{AR,i}^{2}} + \frac{\tilde{\sigma}_{XR,i}^{2}}{\sigma_{BR,i}^{2}}\right)\frac{\sum_{a=1}^{L}\sum_{b=1}^{L}|\Theta(a,b)|^{2}}{\sum_{a=1}^{L}\sum_{b=1}^{L}\Theta(a,a)\Theta(b,b)}\right],
\end{aligned} \tag{C.11}$$

3) Inter-user Interference B_i,

$$
\begin{aligned}
B_i &= \sum_{X=A,B}\sum_{j\neq i} p_{X,j}\left(\left|\mathbf{F}^{AR}_{MAC,i}\mathbf{h}_{XR,j}\right|^2+\left|\mathbf{F}^{BR}_{MAC,i}\mathbf{h}_{XR,j}\right|^2\right)\\
&\to \sum_{X=A,B}\sum_{j\neq i} p_{X,j}\left(\left|\frac{\hat{\mathbf{g}}^H_{AR,i}\mathbf{A}\left(\hat{\mathbf{h}}_{XR,j}+\Delta\mathbf{h}_{XR,j}\right)}{\sigma^2_{AR,i}\sum_{a=1}^{L}\Theta(a,a)}\right|^2+\left|\frac{\hat{\mathbf{g}}^H_{BR,i}\mathbf{A}\left(\hat{\mathbf{h}}_{XR,j}+\Delta\mathbf{h}_{XR,j}\right)}{\sigma^2_{BR,i}\sum_{a=1}^{L}\Theta(a,a)}\right|^2\right)\\
&\to \sum_{X=A,B}\sum_{j\neq i} p_{X,j}\left(\left(\frac{\tilde{\sigma}_{XR,j}}{\sigma^2_{AR,i}}+\frac{\tilde{\sigma}_{XR,j}}{\sigma^2_{BR,i}}\right)\cdot\frac{\sum_{a=1}^{L}\sum_{b=1}^{L}|\Theta(a,b)|^2}{\sum_{a=1}^{L}\sum_{b=1}^{L}\Theta(a,a)\Theta(b,b)}\right),
\end{aligned}
\tag{C.12}
$$

4) Noise C_i,

$$
\begin{aligned}
C_i &= \left|\left|\mathbf{F}^{AR}_{MAC,i}\right|\right|^2+\left|\left|\mathbf{F}^{BR}_{MAC,i}\right|\right|^2\\
&\to \left|\left|\frac{\hat{\mathbf{g}}^H_{AR,i}\mathbf{A}}{\sigma^2_{AR,i}\sum_{a=1}^{L}\Theta(a,a)}\right|\right|^2+\left|\left|\frac{\hat{\mathbf{g}}^H_{BR,i}\mathbf{A}}{\sigma^2_{BR,i}\sum_{a=1}^{L}\Theta(a,a)}\right|\right|^2\\
&\to \frac{1}{\sigma^2_{AR,i}\cdot\sum_{a=1}^{L}\Theta(a,a)}+\frac{1}{\sigma^2_{BR,i}\cdot\sum_{a=1}^{L}\Theta(a,a)}.
\end{aligned}
\tag{C.13}
$$

Substituting (C.10)-(C.13) into (5.35)-(5.37), $\hat{R}_{1,i}$, $\hat{R}_{XR,i}$, $X=A,B$ in (5.89)-(5.90) and (5.92) are proofed. Then, we focus on $\hat{R}_{RX,i}$ in the BC phase. $\hat{R}_{RX,i}$, $X=A,B$ can be obtained with the following calculation when N_R increase to large number,

1) Normalization coefficient,

$$
\begin{aligned}
\rho^{ZF}_{DF} &= \sqrt{\frac{p_r}{E\left\{\left|\left|\mathbf{F}_{BC}\right|\right|^2_F\right\}}}=\sqrt{\frac{p_r}{E\left\{\sum_{i=1}^{N_R}\sum_{j=1}^{2K}\left|\mathbf{F}_{BC}(i,j)\right|^2\right\}}}\\
&\to \sqrt{\frac{p_r}{\sum_{i=1}^{N_R}\sum_{j=1}^{K}\left(\frac{1}{\sigma^2_{AR,j}}+\frac{1}{\sigma^2_{BR,j}}\right)\frac{\bar{\Theta}(i,i)}{\sum_{a=1}^{L}\sum_{b=1}^{L}\Theta(a,a)\Theta(b,b)}}},
\end{aligned}
\tag{C.14}
$$

2) Desired signal,

$$
\left|\hat{\mathbf{h}}^T_{XR,i}\mathbf{F}^{RX}_{BC,i}\right|^2\to\left|\frac{\hat{\mathbf{h}}^T_{XR,i}\mathbf{A}^{\mathbf{T}}\hat{\mathbf{g}}^*_{XR,i}}{\sigma^2_{XR,i}\sum_{a=1}^{L}\Theta^*(a,a)}\right|^2\to 1,
\tag{C.15}
$$

3) Estimation error,

$$\left|\Delta\mathbf{h}_{XR,i}^{T}\mathbf{F}_{BC,i}^{RX}\right|^2 \to \left|\frac{\Delta\mathbf{h}_{XR,i}^{T}\mathbf{A}^{\mathbf{T}}\hat{\mathbf{g}}_{XR,i}^{*}}{\sigma_{XR,i}^2\sum\limits_{a=1}^{L}\Theta^*(a,a)}\right|^2 \to \frac{\tilde{\sigma}_{XR,i}^2}{\sigma_{XR,i}^2}\frac{\sum\limits_{a=1}^{L}\sum\limits_{b=1}^{L}|\Theta(a,b)|^2}{\sum\limits_{a=1}^{L}\sum\limits_{b=1}^{L}\Theta(a,a)\Theta(b,b)}, \tag{C.16}$$

4) Inter-user interference can be obtained by

$$\begin{aligned}
&\sum_{j=1}^{K}\left(\left|\mathbf{h}_{XR,i}^{T}\mathbf{F}_{BC,j}^{RA}\right|^2+\left|\mathbf{h}_{XR,i}^{T}\mathbf{F}_{BC,j}^{RB}\right|^2\right)-\left|\mathbf{h}_{XR,i}^{T}\mathbf{F}_{BC,i}^{RX}\right|^2\\
&\to\sum_{j=1}^{K}\left(\left|\frac{\mathbf{h}_{XR,i}^{T}\mathbf{A}^{\mathbf{T}}\hat{\mathbf{g}}_{AR,j}^{*}}{\sigma_{AR,j}^2\sum_{a=1}^{L}\Theta^*(a,a)}\right|^2+\left|\frac{\mathbf{h}_{XR,i}^{T}\mathbf{A}^{\mathbf{T}}\hat{\mathbf{g}}_{BR,j}^{*}}{\sigma_{BR,j}^2\sum_{a=1}^{L}\Theta^*(a,a)}\right|^2\right)-\left|\frac{\mathbf{h}_{XR,i}^{T}\mathbf{A}^{\mathbf{T}}\hat{\mathbf{g}}_{XR,i}^{*}}{\sigma_{XR,i}^2\sum_{a=1}^{L}\Theta^*(a,a)}\right|^2\\
&\to\begin{cases}\left\{\sum\limits_{j=1}^{K}\left(\dfrac{\tilde{\sigma}_{AR,i}^2}{\sigma_{BR,j}^2}\right)+\sum_{j\neq i}\left(\dfrac{\tilde{\sigma}_{AR,i}^2}{\sigma_{AR,j}^2}\right)\right\}\cdot\left(\dfrac{\sum_{a=1}^{L}\sum_{b=1}^{L}|\Theta(a,b)|^2}{\sum_{a=1}^{L}\sum_{b=1}^{L}\Theta(a,a)\Theta(b,b)}\right), & X=A\\
\left\{\sum\limits_{j=1}^{K}\left(\dfrac{\tilde{\sigma}_{BR,i}^2}{\sigma_{AR,j}^2}\right)+\sum_{j\neq i}\left(\dfrac{\tilde{\sigma}_{BR,i}^2}{\sigma_{BR,j}^2}\right)\right\}\cdot\left(\dfrac{\sum_{a=1}^{L}\sum_{b=1}^{L}|\Theta(a,b)|^2}{\sum_{a=1}^{L}\sum_{b=1}^{L}\Theta(a,a)\Theta(b,b)}\right), & X=B\end{cases}.
\end{aligned} \tag{C.17}$$

By applying (C.14)-(C.17) to (5.39)-(5.40), we can obtain $\hat{R}_{RX,i}$ $(X=A,B)$ in (5.91) and the proof completes.

Bibliography

[1] S. Sesia *et al.*, *LTE - The UMTS Long Term Evolution*, 2nd ed. John Wiley and Sons, Aug. 2011.

[2] G. Y. Li *et al.*, "Energy-efficient wireless communications: tutorial, survey, and open issues," *IEEE Wireless Commun.*, vol. 18, no. 6, pp. 28–35, 2011.

[3] Z. Hasan *et al.*, "Green cellular networks: A survey, some research issues and challenges," *IEEE Commun. Surveys Tut.*, vol. 13, no. 4, pp. 524–540, 2011.

[4] E. Björnson *et al.*, "Optimal design of energy-efficient multi-user MIMO systems: Is massive MIMO the answer?" *IEEE Trans. Wireless Commun.*, vol. 14, no. 6, pp. 3059–3075, June 2015.

[5] I. P. Chochliouros *et al.*, "Energy efficiency concerns and trends in future 5G network infrastructures," *Energies*, vol. 14, no. 17, 2021.

[6] J. G. Andrews *et al.*, "What will 5G be?" *IEEE J. Sel. Areas Commun.*, vol. 32, no. 6, pp. 1065–1082, June 2014.

[7] Y. Chen *et al.*, "Fundamental trade-offs on green wireless networks," *IEEE Commun. Mag.*, vol. 49, no. 6, pp. 30–37, 2011.

[8] J. Wu *et al.*, *Green communications: Theoretical fundamentals, algorithms,and applications*, 09 2012.

[9] F. Rusek *et al.*, "Scaling up MIMO: Opportunities and challenges with very large arrays," *IEEE Sig. Process. Mag.*, vol. 30, no. 1, pp. 40–60,

Jan 2013.

[10] K. Zheng *et al.*, "Survey of large-scale MIMO systems," *IEEE Commun. Surveys Tut.*, vol. 17, no. 3, pp. 1738–1760, third quarter 2015.

[11] A. o. Puglielli, "Design of energy- and cost-efficient massive MIMO arrays," *Proceedings of the IEEE*, vol. 104, no. 3, pp. 586–606, 2016.

[12] E. Björnson *et al.*, "Massive MIMO: ten myths and one critical question," *IEEE Commun. Mag.*, vol. 54, no. 2, pp. 114–123, 2016.

[13] W. Roh *et al.*, "Millimeter-wave beamforming as an enabling technology for 5G cellular communications: theoretical feasibility and prototype results," *IEEE Commun. Mag.*, vol. 52, no. 2, pp. 106–113, 2014.

[14] M. Di Renzo *et al.*, "Spatial modulation for generalized MIMO: Challenges, opportunities, and implementation," *Proceedings of the IEEE*, vol. 102, no. 1, pp. 56–103, 2014.

[15] S. Sanayei and A. Nosratinia, "Capacity of MIMO channels with antenna selection," *IEEE Trans. Inf. Theory*, vol. 53, no. 11, pp. 4356–4362, 2007.

[16] L. Yang *et al.*, "Efficient channel estimation for millimeter wave MIMO with limited RF chains," in *Proc. IEEE ICC*, 2016, pp. 1–6.

[17] A. Garcia-Rodriguez and C. Masouros, "Exploiting the increasing correlation of space constrained massive MIMO for CSI relaxation," *IEEE Trans. Commun.*, vol. 64, no. 4, pp. 1572–1587, April 2016.

[18] A. Gorokhov *et al.*, "Receive antenna selection for MIMO flat-fading channels: theory and algorithms," *IEEE Trans. Inf. Theory*, vol. 49, no. 10, pp. 2687–2696, 2003.

[19] A. Molisch *et al.*, "Capacity of MIMO systems with antenna selection," *IEEE Trans. Wireless Commun.*, vol. 4, no. 4, pp. 1759–1772, 2005.

[20] Z. Xiao *et al.*, "Hierarchical codebook design for beamforming training

in millimeter-wave communication," *IEEE Trans. Wireless Commun.*, vol. 15, no. 5, pp. 3380–3392, 2016.

[21] S. Haghighatshoar and G. Caire, "The beam alignment problem in-mmwave wireless networks," in *Proc. IEEE ACSSC*, 2016, pp. 741–745.

[22] J. Brady *et al.*, "Beamspace MIMO for millimeter-wave communications: System architecture, modeling, analysis, and measurements," *IEEE Trans. Ant. Propag.*, vol. 61, no. 7, pp. 3814–3827, 2013.

[23] D. Tse and P. Viswanath, *Fundamentals of Wireless Communications.* Cambridge University Press, 2005.

[24] L. Zheng and D. Tse, "Diversity and multiplexing: a fundamental tradeoff in multiple-antenna channels," *IEEE Trans. Inf. Theory*, vol. 49, no. 5, pp. 1073–1096, 2003.

[25] C. Oestges and B. Clerckx, *MIMO wireless communications: From real-world propagation to space-time code design.* Academic Press, 2010.

[26] C. Windpassinger *et al.*, "Precoding in multiantenna and multiuser communications," *IEEE Trans. Wireless Commun.*, vol. 3, no. 4, pp. 1305–1316, 2004.

[27] C. Masouros, "Correlation rotation linear precoding for MIMO broadcast communications," *IEEE Trans. Sig. Process.*, vol. 59, no. 1, pp. 252–262, 2011.

[28] S. M. Razavi *et al.*, "Transmit-power efficient linear precoding utilizing known interference for the multiantenna downlink," *IEEE Trans. Veh.Tech.*, vol. 63, no. 9, pp. 4383–4394, 2014.

[29] T. L. Marzetta, "Noncooperative cellular wireless with unlimited numbers of base station antennas," *IEEE Trans. Wireless Commun.*, vol. 9, no. 11, pp. 3590–3600, November 2010.

[30] H. Q. Ngo *et al.*, "Energy and spectral efficiency of very large multiuser MIMO systems," *IEEE Trans. Commun.*, vol. 61, no. 4, pp. 1436–1449,

Apr. 2013.

[31] T. Lo, "Maximum ratio transmission," *IEEE Trans. Commun.*, vol. 47, no. 10, pp. 1458–1461, 1999.

[32] Q. Spencer *et al.*, "Zero-forcing methods for downlink spatial multiplexing in multiuser MIMO channels," *IEEE Trans. Sig. Process.*, vol. 52, no. 2, pp. 461–471, 2004.

[33] C. Peel *et al.*, "A vector-perturbation technique for near-capacity multiantenna multiuser communication-part I: channel inversion and regularization," *IEEE Trans. Commun.*, vol. 53, no. 1, pp. 195–202, 2005.

[34] C. Masouros *et al.*, "Large-scale MIMO transmitters in fixed physical spaces: The effect of transmit correlation and mutual coupling," *IEEE Trans. Commun.*, vol. 61, no. 7, pp. 2794–2804, July 2013.

[35] Q. Wang and Y. Jing, "Performance analysis and scaling law of MRC/MRT relaying with CSI error in multi-pair massive MIMO systems," *IEEE Trans. Wireless Commun.,* vol. 16, no. 9, pp. 5882–5896, Sept. 2017.

[36] S. Rangan *et al.*, "Millimeter-wave cellular wireless networks: Potentials and challenges," *Proceedings of the IEEE*, vol. 102, no. 3, pp. 366–385, 2014.

[37] J. Hoydis *et al.*, "Massive MIMO in the UL/DL of cellular networks: How many antennas do we need?" *IEEE J. Sel. Areas Commun.*, vol. 31,no. 2, pp. 160–171, February 2013.

[38] G. N. Kamga *et al.*, "Channel modeling and capacity analysis of large MIMO in real propagation environments," in *Proc. IEEE ICC*, 2015, pp. 1447–1452.

[39] A. Yang *et al.*, "The role of large-scale fading in uplink massive MIMO systems," *IEEE Trans. Veh. Tech.*, vol. 65, no. 1, pp. 477–483, Jan 2016.

[40] F. Heliot *et al.*, "On the energy efficiency-spectral efficiency trade-off over the MIMO rayleigh fading channel," *IEEE Trans. Commun.*, vol. 60, no. 5, pp. 1345–1356, 2012.

[41] A. Salh *et al.*, "A study on the achievable data rate in massive MIMO system," vol. 1883, 09 2017, p. 020014.

[42] D. Ha *et al.*, "Energy efficiency analysis with circuit power consumption in massive MIMO systems," in *Proc. IEEE PIMRC*, Sept 2013, pp. 938–942.

[43] H. Yu *et al.*, "The analysis of the energy efficiency for the decode-and-forward two-way relay networks," in *Proc. IEEE WCNC*, Apr. 2013, pp. 2823–2827.

[44] Z. Zhang *et al.*, "Spectral and energy efficiency of multipair two-way full-duplex relay systems with massive MIMO," *IEEE J. Sel. Areas Commun.*, vol. 34, no. 4, pp. 848–863, Apr. 2016.

[45] J. Xu and L. Qiu, "Energy efficiency optimization for MIMO broadcast channels," *IEEE Trans. Wireless Commun.*, vol. 12, no. 2, pp. 690–701, 2013.

[46] G. Miao, "Energy-efficient uplink multi-user MIMO," *IEEE Trans. Wireless Commun.*, vol. 12, no. 5, pp. 2302–2313, 2013.

[47] A. Kammoun *et al.*, "Linear precoding based on polynomial expansion: Large-scale multi-cell MIMO systems," *IEEE J. Sel. Topics Sig. Process.*, vol. 8, no. 5, pp. 861–875, Oct 2014.

[48] N. Shariati *et al.*, "Low-complexity polynomial channel estimation in large-scale MIMO with arbitrary statistics," *IEEE J. Sel. Topics Sig. Process.*, vol. 8, no. 5, pp. 815–830, Oct 2014.

[49] H. Q. Ngo *et al.*, "The multicell multiuser MIMO uplink with very large antenna arrays and a finite-dimensional channel," *IEEE Trans. Commun.*, vol. 61, no. 6, pp. 2350–2361, 2013.

[50] C. Wang and R. D. Murch, "Adaptive downlink multi-user MIMO wireless systems for correlated channels with imperfect CSI," *IEEE Trans. Wireless Commun.*, vol. 5, no. 9, pp. 2435–2446, September 2006.

[51] T. Marzetta *et al.*, *Fundamentals of Massive MIMO.* United Kingdom: Cambridge University Press, 2016.

[52] M. Chavan *et al.*, "Multipath fading channel modeling and performance comparison of wireless channel models," *Int. J. electron. commun. eng.*, vol. 4, no. 2, pp. 189–203, 2011.

[53] R. Ertel *et al.*, "Overview of spatial channel models for antenna array communication systems," *IEEE Personal Commun.*, vol. 5, no. 1,pp. 10–22, 1998.

[54] Y. S. Cho *et al.*, *MIMO-OFDM wireless communications with MATLAB,* Singapore: IEEE Press., 2010.

[55] A. Forenza *et al.*, "Simplified spatial correlation models for clustered MIMO channels with different array configurations," *IEEE Trans. Veh. Tech.*, vol. 56, no. 4, pp. 1924–1934, 2007.

[56] S. Biswas *et al.*, "Performance analysis of large multiuser MIMO systems with space-constrained 2-D antenna arrays," *IEEE Trans. Wireless Commun.*, vol. 15, no. 5, pp. 3492–3505, May 2016.

[57] C. T. Neil *et al.*, "On the performance of spatially correlated large antenna arrays for millimeter-wave frequencies," *IEEE Trans. Ant. Propag.*, vol. 66, no. 1, pp. 132–148, Jan. 2018.

[58] N. Ebaid *et al.*, "Performance enhancement of cooperative cognitive relay network using multi antennas multi hopping techniques," *International Journal of Computer Applications*, vol. 144, pp. 18–22, 06 2016.

[59] C. Li *et al.*, "Multi-user scheduling of the full-duplex enabled two-way relay systems," *IEEE Trans. Wireless Commun.*, vol. 16, no. 2, pp. 1094–1106, 2017.

[60] Z. Zhang *et al.*, "Full-duplex two-way and one-way relaying: Average rate, outage probability, and tradeoffs," *IEEE Trans. Wireless Commun.*, vol. 15, no. 6, pp. 3920–3933, 2016.

[61] N. Shende *et al.*, "Half-duplex or full-duplex relaying: A capacity analysis under self-interference," in *Proc. IEEE CISS*, 2013, pp. 1–6.

[62] J. Feng *et al.*, "Power scaling of full-duplex two-way massive MIMO relay systems with correlated antennas and MRC/MRT processing," *IEEE Trans. Wireless Commun.*, vol. 16, no. 7, pp. 4738–4753, July 2017.

[63] X. Xia *et al.*, "Hardware impairments aware transceiver for full-duplex massive MIMO relaying," *IEEE Trans. Sig. Process.*, vol. 63, no. 24, pp. 6565–6580, 2015.

[64] H. Alves *et al.*, "On the performance of two-way half-duplex and one-way full-duplex relaying,"" in *Proc. IEEE SPAWC*, 2013, pp. 56–60.

[65] S. Berger, "Coherent cooperative relaying in low mobility wireless multiuser networks," *ETH ZURICH*, 2010.

[66] A. Marczak, "Overview of cooperative communication methods," *Scientific Journal of Polish Naval Academy*, vol. 210, pp. 1–1, 09 2017.

[67] B. Rankov and A. Wittneben, "Distributed spatial multiplexing in a wireless network," in *Proc. IEEE ACSSC*, 2004., vol. 2, 2004, pp. 1932–1937 Vol. 2.

[68] S. J. Kim *et al.*, "Achievable rate regions and performance comparison of half duplex bi-directional relaying protocols," *IEEE Trans. Inf. Theory*, vol. 57, no. 10, pp. 6405–6418, Oct. 2011.

[69] C. Kong *et al.*, "Multipair two-way half-duplex DF relaying with massive arrays and imperfect CSI," *IEEE Trans. Wireless Commun.*, vol. 17, no. 5, pp. 3269–3283, May 2018.

[70] G. Kramer *et al.*, "Cooperative strategies and capacity theorems for relay networks," *IEEE Trans. Inf. Theory*, vol. 51, no. 9, pp. 3037–3063,

2005.

[71] S. Simoens *et al.*, "Compress-and-forward cooperative relaying in MIMO-OFDM systems," in *Proc. IEEE SPWAC*, 2006, pp. 1–5.

[72] R. Nabar *et al.*, "Fading relay channels: performance limits and space-time signal design," *IEEE J. Sel. Areas. Commun.*, vol. 22, no. 6, pp. 1099–1109, 2004.

[73] R. W. Heath *et al.*, "An overview of signal processing techniques for millimeter wave MIMO systems," *IEEE J. Sel. Topics Sig. Process.*,vol. 10, no. 3, pp. 436–453, 2016.

[74] M. Hussain and N. Michelusi, "Energy-efficient interactive beam alignment for millimeter-wave networks," *IEEE Trans. Wireless Commun.*, vol. 18, no. 2, pp. 838–851, 2019.

[75] S. Hur *et al.*, "Millimeter wave beamforming for wireless backhaul and access in small cell networks," *IEEE Trans. Commun.*, vol. 61, no. 10, pp.4391–4403, 2013.

[76] C. Masouros and M. Matthaiou, "Space-constrained massive MIMO: Hitting the wall of favorable propagation," *IEEE Commun. Lett.*, vol. 19, no. 5, pp. 771–774, May 2015.

[77] A. Alkhateeb *et al.*, "Limited feedback hybrid precoding for multi-user millimeter wave systems," *IEEE Trans. Wireless Commun.*, vol. 14, no. 11, pp. 6481–6494, 2015.

[78] W. L. Stutzman and G. A. Thiele, *Antenna Theory and Design.* John Wiley & Sons, Inc., Hoboken, New Jersey., 2012.

[79] H. Friis, "A note on a simple transmission formula," *Proceedings of the IRE*, vol. 34, no. 5, pp. 254–256, 1946.

[80] C. A. Balanis, *Antenna Theory: Analysis and Design.* John Wiley & Sons, Inc., Hoboken, New Jersey., 2005.

[81] M. D. Foegelle, *Antenna pattern measurement: Concepts and techniques,* Compliance Engineering, 2002.

[82] S. V. Hum, *Radio and Microwave Wireless Systems.* University of Toronto., 2007.

[83] J. Carl B. Dietrich, *Adaptive Arrays and Diversity Antenna Configurations for Handheld Wireless Communication Terminals.* Academic Press, 2000.

[84] Y. Li *et al.*, "Exploiting temporal channel correlation in data-assisted massive MIMO uplink detection," *IEEE Commun. Lett.*, vol. 21, no. 2, pp. 430–433, Feb 2017.

[85] L. Sanguinetti *et al.*, "Toward Massive MIMO 2.0: Understanding Spatial Correlation, Interference Suppression, and Pilot Contamination," *IEEE Trans. Commun.*, vol. 68, no. 1, pp. 232-257, Jan. 2020.

[86] M.A. Naser *et al.*, "The Role of Correlation in the Performance of Massive MIMO Systems," *Appl. Syst. Innov.*, 2021, 4, 54.

[87] Y. Fang *et al.*, "Asymptotic Equivalent Performance of Uplink Massive MIMO Systems With Spatial–Temporal Correlation," *IEEE Trans. Veh. Tech.*, vol. 68, no. 5, pp. 4615-4624, May 2019.

[88] B. Lee *et al.*, "Antenna grouping based feedback compression for FDD-based massive MIMO systems," *IEEE Trans. Commun.*, vol. 63, no. 9, pp. 3261–3274, Sept 2015.

[89] G. J. Byers and F. Takawira, "Spatially and temporally correlated MIMO channels: modeling and capacity analysis," *IEEE Trans. Veh. Tech.*, vol. 53, no. 3, pp. 634–643, May 2004.

[90] P. Harris *et al.*, "Performance characterization of a real-time massive MIMO system with LOS mobile channels," *IEEE J. Sel. Areas Commun.*,vol. 35, no. 6, pp. 1244–1253, June 2017.

[91] H. Tataria *et al.*, "Uplink analysis of large MU-MIMO systems with space-constrained arrays in Ricean fading," in *Proc. IEEE ICC*, May

2017, pp. 1–7.

[92] K. F. Warnick and M. A. Jensen, "Optimal noise matching for mutually coupled arrays," *IEEE Trans. Ant. Propag.*, vol. 55, no. 6, pp. 1726–1731, June 2007.

[93] D. Ying *et al.*, "Kronecker product correlation model and limited feedback codebook design in a 3D channel model," in *Proc. IEEE ICC*, June 2014, pp. 5865–5870.

[94] K. T. Truong and R. W. Heath, "Effects of channel aging in massive MIMO systems," *J. Commun. Networks*, vol. 15, no. 4, pp. 338–351, Aug 2013.

[95] R. H. Clarke, "A statistical theory of mobile-radio reception," *The Bell System Technical Journal*, vol. 47, no. 6, pp. 957–1000, July 1968.

[96] J. Zhang *et al.*, "Block diagonalization in the MIMO broadcast channel with delayed CSIT," in *Proc. IEEE GLOBECOM*, Nov 2009, pp. 1–6.

[97] H. Yang and T. L. Marzetta, "Performance of conjugate and zero-forcing beamforming in large-scale antenna systems," *IEEE J. Sel. Areas Commun.*, vol. 31, no. 2, pp. 172–179, February 2013.

[98] X. Sun *et al.*, "Multi-pair two-way massive MIMO AF full-duplex relaying with ZFR/ZFT and imperfect CSI," in *Proc. IEEE ISCIT*, Sept. 2016, pp. 27–32.

[99] H. Q. Ngo *et al.*, "Multipair full-duplex relaying with massive arrays and linear processing," *IEEE J. Sel. Areas Commun.*, vol. 32, no. 9, pp. 1721–1737, Sept. 2014.

[100] X. Xia *et al.*, "Full-duplex massive MIMO AF relaying with semiblind gain control," *IEEE Trans. Veh. Tech.*, vol. 65, no. 7, pp. 5797–5804, July 2016.

[101] C. Li *et al.*, "Outage analysis of the full-duplex decode-and-forward two-way relay system," *IEEE Trans. Veh. Tech.*, vol. 66, no. 5, pp.

4073–4086, May 2017.

[102] F. Tan *et al.*, "Power allocation optimization for energy-efficient massive MIMO aided multi-pair decode-and-forward relay systems," *IEEE Trans. Commun.*, vol. 65, no. 6, pp. 2368–2381, June 2017.

[103] B. Rankov and A. Wittneben, "Spectral efficient protocols for half-duplex fading relay channels," *IEEE J. Sel. Areas Commun.*, vol. 25, no. 2, pp. 379–389, Feb. 2007.

[104] H. Cui *et al.*, "Multi-pair two-way amplify-and-forward relaying with very large number of relay antennas," *IEEE Trans. Wireless Commun.*, vol. 13, no. 5, pp. 2636–2645, May 2014.

[105] M. Tao and R. Wang, "Linear precoding for multi-pair two-way MIMO relay systems with max-min fairness," *IEEE Trans. Sig. Process.*, vol. 60,no. 10, pp. 5361–5370, Oct. 2012.

[106] C. Li *et al.*, "Performance analysis of the full-duplex enabled decode-and-forward two-way relay system," in *Proc. IEEE ICC,* May 2016, pp. 559–564.

[107] E. Chiu and V. K. N. Lau, "Cellular multiuser two-way MIMO AF relaying via signal space alignment: Minimum weighted SINR maximization," *IEEE Trans. Sig. Process.*, vol. 60, no. 9, pp. 4864–4873, Sept. 2012.

[108] M. Chen and A. Yener, "Multiuser two-way relaying: detection and interference management strategies," *IEEE Trans. Wireless Commun.*, vol. 8, no. 8, pp. 4296–4305, Aug. 2009.

[109] J. Gao *et al.*, "Sum-rate maximization with minimum power consumption for MIMO DF two-way relaying— part I: Relay optimization," *IEEE Trans. Sig. Process.*, vol. 61, no. 14, pp. 3563–3577, July 2013.

[110] K. Song *et al.*, "Performance analysis of antenna selection in two-way relay networks," *IEEE Trans. Sig. Process.*, vol. 63, no. 10, pp.

2520–2532, May 2015.

[111] C. Kong *et al.*, "Multi-pair two-way AF relaying systems with massive arrays and imperfect CSI," in *Proc. IEEE ICASSP*, Mar. 2016, pp. 3651–3655.

[112] X. Sun *et al.*, "Relay beamforming for multi-pair two-way MIMO relay systems with max-min fairness," in *Proc. IEEE WCSP*, Oct. 2015, pp.1–4.

[113] H. Q. Ngo *et al.*, "Massive MU-MIMO downlink TDD systems with linear precoding and downlink pilots," in *Proc. Allerton*, Oct. 2013, pp. 293–298.

[114] F. Liu *et al.*, "An efficient manifold algorithm for constructive interference based constant envelope precoding," *IEEE Sig. Process. Lett.*, vol. 24, no. 10, pp. 1542–1546, Oct. 2017.

[115] Z. Shi *et al.*, "Achievability of the channel reciprocity and its benefit in TDD system," in *Proc. IEEE ICST*, Aug 2010, pp. 1–4.

[116] A. Li *et al.*, "Massive MIMO 1-bit DAC transmission: A low-complexity symbol scaling approach," *IEEE Trans. Wireless Commun.*, vol. 17, no. 11, pp. 7559–7575, Nov. 2018.

[117] E. Sharma *et al.*, "Multi-pair two way AF full-duplex massive MIMO relaying with ZFR/ZFT processing," in *Proc. IEEE PIMRC*, Oct 2017, pp. 1–7.

[118] Q. Zhang *et al.*, "Power scaling of uplink massive MIMO systems with arbitrary-rank channel means," *IEEE J. Sel. Topics Signal Process.*, vol. 8, no. 5, pp. 966–981, Oct. 2014.

[119] P. V. Amadori and C. Masouros, "Low RF-complexity millimeter-wave beamspace-MIMO systems by beam selection," *IEEE Trans. Commun.*, vol. 63, no. 6, pp. 2212–2223, June 2015.

[120] A. Garcia-Rodriguez *et al.*, "Hybrid analog–digital precoding revisited under realistic RF modeling," *IEEE Wireless Commun. Lett.*, vol. 5, no. 5, pp. 528–531, Oct. 2016.

[121] D. Nguyen *et al.*, "On the spectral efficiency of full-duplex small cell wireless systems," *IEEE Trans. Wireless Commun.*, vol. 13, no. 9, pp. 4896–4910, Sept. 2014.

[122] S. Boyd and L. Vandenberghe, *Convex Optimization.* New York, NY, USA: Cambridge University Press, 2004.

[123] M. Grant and S. Boyd, *CVX: Matlab software for disciplined convex programming,* http://cvxr.com/cvx/, Dec. 2018.

[124] J. Park and S. Boyd, "General heuristics for nonconvex quadratically constrained quadratic programming," https://arxiv.org/abs/1703.07870, Mar. 2017.

[125] C. Sun and R. Dai, "An iterative method for nonconvex quadratically constrained quadratic programs," https://arxiv.org/abs/1609.02609, Sep. 2016.

[126] A. Beck, "Quadratic matrix programming," *SIAM J. Optim*, vol. 17, no. 4, pp. 1224–1238, 2007.

[127] K. Wang *et al.*, "Outage constrained robust transmit optimization for multiuser MISO downlinks: Tractable approximations by conic optimization," *IEEE Trans. Sig. Process.*, vol. 62, no. 21, pp. 5690–5705, Nov 2014.

[128] G. Amarasuriya *et al.*, "Sum rate analysis of two-way MIMO AF relay networks with zero-forcing," *IEEE Trans. Wireless Commun.*, vol. 12, no. 9, pp. 4456–4469, Sep. 2013.

[129] D. Singh Gurjar and P. K. Upadhyay, "Impact of channel estimation error on zero-forcing-based multiple-input–multiple-output two-way relaying," *IET Sig. Process.*, vol. 10, no. 3, pp. 210–217, 2016.

[130] S. Jin *et al.*, "Ergodic rate analysis for multipair massive MIMO two-way relay networks," *IEEE Trans. Wireless Commun.*, vol. 14, no. 3, pp. 1480–1491, Mar. 2015.

[131] E. Sharma *et al.*, "Spectral- and energy-efficiency of massive MIMO two-way half-duplex hybrid processing AF relay," *IEEE Wireless Commun. Lett.*, vol. 7, no. 5, pp. 876–879, Oct. 2018.

[132] E. Sharma *et al.*, "Full-duplex massive MIMO multi-pair two-way AF relaying: Energy efficiency optimization," *IEEE Trans. Commun.*, vol. 66, no. 8, pp. 3322–3340, Aug. 2018.

[133] H. A. Suraweera *et al.*, "Multi-pair amplify-and-forward relaying with very large antenna arrays," in *Proc. IEEE ICC*, June 2013, pp. 4635–4640.

[134] Z. Peng *et al.*, "Multi-Pair Two-Way Massive MIMO DF Relaying Over Rician Fading Channels Under Imperfect CSI," *IEEE Wireless Commun. Letters*, vol. 11, no. 2, pp. 225-229, Feb. 2022.

[135] Y. Shim *et al.*, "Beamforming design for full-duplex two-way amplify-and-forward MIMO relay," *IEEE Trans. Wireless Commun.*, vol. 15, no. 10, pp. 6705–6715, 2016.

[136] A. Garcia-Rodriguez *et al.*, "Reduced switching connectivity for large scale antenna selection," *IEEE Trans. Commun.*, vol. 65, no. 5, pp. 2250–2263, May 2017.

[137] A. Tulino *et al.*, "Impact of antenna correlation on the capacity of multiantenna channels," *IEEE Trans. Inf. Theory*, vol. 51, no. 7, pp. 2491–2509, 2005.

[138] V. Raghavan and A. M. Sayeed, "Sublinear capacity scaling laws for sparse MIMO channels," *IEEE Trans. Inf. Theory*, vol. 57, no. 1, pp. 345–364, 2011.

[139] R. H. Louie *et al.*, "Performance analysis of beamforming in two hop

amplify and forward relay networks with antenna correlation," *IEEE Trans. Wireless Commun.*, vol. 8, no. 6, pp. 3132–3141, 2009.

[140] P. Dharmawansa *et al.*, "Ergodic capacity and beamforming optimality for multi-antenna relaying with statistical CSI," *IEEE Trans. Commun.*, vol. 59, no. 8, pp. 2119–2131, 2011.

[141] H. Liang *et al.*, "Wireless powered dual-hop multi-antenna relaying systems: Impact of CSI and antenna correlation," *IEEE Trans. Wireless Commun.*, vol. 16, no. 4, pp. 2505–2519, 2017.

[142] L. Melki *et al.*, "System performance of two-way decode-and-forward relaying assisted D2D communication underlaying cellular networks," in *Proc. IEEE ISIVC*, 2016, pp. 270–275.

[143] J. Feng *et al.*, "Impact of antenna correlation on full-duplex two-way massive MIMO relaying systems," *IEEE Trans. Wireless Commun.*, vol. 17, no. 6, pp. 3572–3587, 2018.

[144] D. N. Amudala *et al.*, "Spectral efficiency optimization of spatially-correlated multi-pair full-duplex massive MIMO relaying," *IEEE Trans. Commun.*, vol. 67, no. 12, pp. 8346–8364, 2019.

[145] M. Zaher *et al.*, "Performance of multi-pair two-way full-duplex massive MIMO relay systems with direct link," in *Proc. IEEE SPECTS*, 2019, pp. 1–8.

[146] M. Zaher and A. El-Mahdy, "Two-Way Full-Duplex Massive MIMO Relaying with Correlated Multi-Antenna User Pairs," in *Proc. IEEE ICFSP*, 2019, pp. 57-61.

[147] B. Lee *et al.*, "Antenna grouping based feedback reduction for FDD-based massive MIMO systems," in *Proc. IEEE ICC*, June 2014, pp. 4477–4482.

[148] L. Li *et al.*, "Spectral- and energy-efficiency of multi-pair two-way massive MIMO relay systems experiencing channel aging," *IEEE Access*,

vol. 7, pp. 46 014–46 032, 2019.

[149] J. Feng *et al.*, "Sum rate of full-duplex two-way massive MIMO relay systems with channel aging," in *Proc. IEEE ICCS*, Dec 2016, pp. 1–6.

[150] J. He *et al.*, "Multi-pair bidirectional relaying with full-duplex massive MIMO experiencing channel aging," in *Proc. IEEE GLOBECOM*, Dec 2017, pp. 1–6.

[151] J. Huang and H. Gharavi, "Performance analysis of relay-based two-way D2D communications with network coding," *IEEE Trans. Veh. Tech.*, vol. 67, no. 7, pp. 6642–6646, 2018.

[152] L. Lu *et al.*, "An overview of massive MIMO: Benefits and challenges," *IEEE J. Sel. Topics Sig. Process.*, vol. 8, no. 5, pp. 742–758, Oct 2014.

[153] N. Fatema *et al.*, "Massive MIMO linear precoding: A survey," *IEEE Systems Journal*, pp. 1–12, 2018.

[154] J. Qian and C. Masouros, "On the performance of physically constrained multi-pair two-way massive MIMO relaying with zero forcing," in *Proc. IEEE PIMRC*, Sept. 2019, pp. 1–6.

[155] J. Qian *et al.*, "Multi-pair two-way massive MIMO relaying with zero forcing: Energy efficiency and power scaling laws," *IEEE Trans. Commun.*, vol. 68, no. 3, pp. 1417-1431, March 2020.

[156] B. Hassibi and B. Hochwald, "How much training is needed in multiple-antenna wireless links?" *IEEE Trans. Inf. Theory*, vol. 49,no. 4, pp. 951–963, 2003.

[157] G. Auer *et al.*, "How much energy is needed to run a wireless network?" *IEEE Wireless Commun.*, vol. 18, no. 5, pp. 40–49, Oct. 2011.

[158] J. Qian *et al.*, "Partial CSI acquisition for size-constrained massive MIMO systems with user mobility," *IEEE Trans. Veh. Tech.*, vol. 67, no. 9, pp. 9016–9020, Sep. 2018.

[159] M. Arakawa, *Computational workloads for commonly used signal processing kernels*, 2006.

[160] A. Garcia-Rodriguez and C. Masouros, "Exploiting the tolerance of massive MIMO to incomplete CSI for low-complexity transmission," in *Proc. IEEE GLOBECOM*, Dec. 2015, pp. 1–6.

[161] J. Palacios *et al.*, "Tracking mm-wave channel dynamics: Fast beam training strategies under mobility," in *Proc. IEEE INFOCOM*, 2017, pp. 1–9.

[162] J. Song *et al.*, "Adaptive millimeter wave beam alignment for dual-polarized MIMO systems," *IEEE Trans. Wireless Commun.*, vol. 14, no. 11, pp. 6283–6296, 2015.

[163] Z. Pi and F. Khan, "An introduction to millimeter-wave mobile broadband systems," *IEEE Commun. Mag.*, vol. 49, no. 6, pp. 101–107, 2011.

[164] J. Song *et al.*, "Millimeter wave beamforming for multiuser dual-polarized MIMO systems," in *Proc. IEEE GlobalSIP*, 2013, pp. 719–722.

[165] V. Desai *et al.*, "Initial beamforming for mmwave communications," in *Proc. IEEE ACSSC*, 2014, pp. 1926–1930.

[166] S. Noh *et al.*, "Multi-resolution codebook and adaptive beamforming sequence design for millimeter wave beam alignment," *IEEE Trans. Wireless Commun.*, vol. 16, no. 9, pp. 5689–5701, 2017.

[167] D. Zhang *et al.*, "Exploring AoA/AoD dynamics in beam alignment of mobile millimeter wave MIMO systems," *IEEE Trans. Veh. Tech.*, vol. 68, no. 6, pp. 6172–6176, 2019.

[168] T. Kim and D. J. Love, "Virtual AoA and AoD estimation for sparse millimeter wave MIMO channels," in *Proc. IEEE SPAWC*, 2015, pp.146–150.

[169] A. Alkhateeb *et al.*, "Channel estimation and hybrid precoding for millimeter wave cellular systems," *IEEE J. Sel. Topics Sig. Process.*, vol.

8,no. 5, pp. 831–846, 2014.

[170] C. Liu *et al.*, "Millimeter-wave small cells: Base station discovery, beama lignment, and system design challenges," *IEEE Wireless Commun.*, vol. 25, no. 4, pp. 40–46, 2018.

[171] C. Liu *et al.*, "Millimeter wave beam alignment: Large deviations analysis and design insights," *IEEE J. Sel. Areas Commun.*, vol. 35, no. 7, pp. 1619–1631, 2017.

[172] M. R. Akdeniz *et al.*, "Millimeter wave channel modeling and cellular capacity evaluation," *IEEE J. Sel. Areas Commun.*, vol. 32, no. 6, pp. 1164–1179, 2014.

[173] J. Wang *et al.*, "Beam codebook based beamforming protocol for multi-gbps millimeter-wave WPAN systems," *IEEE J. Sel. Areas Commun.*, vol. 27, no. 8, pp. 1390–1399, 2009.

[174] M. Hashemi *et al.*, "Efficient Beam Alignment in Millimeter Wave Systems Using Contextual Bandits," *Proc. IEEE INFOCOM*, 2018, pp. 2393-2401.

[175] M. Uysal, *Cooperative Communications for Improved Wireless Network Transmission: Framework for Virtual Antenna Array Applications*, 2009.

[176] A. A. Farid and S. Hranilovic, "Diversity gain and outage probability for MIMO free-space optical links with misalignment," *IEEE Trans. Commun.*, vol. 60, no. 2, pp. 479–487, 2012.

[177] D. Schneider, "Could supercomputing turn to signal processors (again)?," *IEEE Spectrum*, vol. 49, no. 10, pp. 13-14, October 2012.

[178] O. Guven *et al.*, "Computationally efficient real-time interpolation algorithm for non-uniform sampled biosignals," *Healthcare Technology Letters*, vol. 3, pp. 105 – 110, 2016.

[179] B. Clerckx *et al.*, "Impact of antenna coupling on 2×2 MIMO communications," *IEEE Trans. Veh. Tech.*, vol. 56, no. 3, pp. 1009–1018, 2007.